THE GRAIN COARSENING AND SUBSEQUENT TRANSFORMATION OF AUSTENITE IN THE HSLA STEEL DURING HIGH TEMPERATURE THERMOMECHANICAL PROCESSING

by

Khaled F. Al-Hajeri

B.S., Mechanical Engineering, King Saud University, Riyadh, Saudi Arabia, 1993

M.S., Metallurgy, University of Sheffield, Sheffield, UK, 1999

Submitted to the Graduate Faculty of

School of Engineering in partial fulfillment

of the requirements for the degree of

Doctor of Philosophy

University of Pittsburgh

2005

UNIVERSITY OF PITTSBURGH

SCHOOL OF ENGINEERING

This dissertation was presented

by

Khaled F. Al-Hajeri

It was defended on

April 13, 2005

and approved by

Mary Grace Burke, Bechtel Bettis, Inc.

Ian Nettelship, Associate Professor, Department of Materials Science and Engineering

Luis E. Vallejo, Professor, Department of Civil and Environmental Engineering

Calixto Isaac Garcia, Research Professor, Department of Materials Science and Engineering

Thesis Advisor: Anthony J. DeArdo, William Keplar Whiteford Professor, Department of Materials Science and Engineering

THE GRAIN COARSENING AND SUBSEQUENT TRANSFORMATION OF AUSTENITE IN THE HSLA STEEL DURING HIGH TEMPERATURE THERMOMECHANICAL PROCESSING

Khaled F. Al-Hajeri, PhD

University of Pittsburgh, 2005

In heavy steel sections, fundamental properties such as strength and toughness are improved remarkably by refining and homogenizing the final ferrite microstructure. Conventionally, the microstructural refinement of the final ferrite depends mainly on the austenite grain size, morphology and composition prior to the phase transformation as well as the cooling rate during the transformation. The production of heavy sections by universal-type rolling mills takes place at elevated temperature (above 1200 ºC) followed by low cooling rates (<0.1 ºC/sec). These processing conditions produce coarse austenite grains and subsequently coarse ferrite grains in addition to other undesirable low temperature transformation products. In heavy steel sections, therefore, the refinement of the ferrite microstructure through modern TMP techniques is not feasible.

The main objective of this study is to investigate the feasibility of refining the ferrite microstructure and eliminate the high-carbon low transformation products in heavy steel sections using the particle-stimulated nucleation, PSN, mechanism to enhance the nucleation of the intragranular ferrite, IGF.

In this investigation, the MnS and Ti-oxide inclusions were used to promote the intragranular ferrite (IGF) nucleation mechanism in a typical ASTM A572 grade 50 Steel. This work included the study of the decomposition behavior of coarse grained austenite and nucleation of the IGF as

a function of very slow cooling rate. In addition, the effects of the inclusions type, size and volume fraction on the kinetics (nucleation and growth) of IGF were investigated.

The main findings of this research were that the refining of ferrite microstructure is achieved, successfully, through enhancing the IGF nucleation with implementing of the PSN mechanism. Additionally, the efficiency of the inclusion as an IGF nucleation site is mainly related to the inclusion size and type.

TABLE OF CONTENTS

LIST OF TABLES

LIST OF FIGURES

ACKNOWLEDGMENTS

All thanks to Almighty Allah (God) for giving me the ability and strength to accomplish this work.

I would like to express my appreciation and gratitude to my advisors Prof. A. J. DeArdo and Prof. C. I. Garcia for their creative suggestions and guidance along the way.

I would like to extend my gratitude to Dr. K. M. Goldman for this wise advice, and for taking the time to review this thesis.

Gratitude is expressed to all my BAMPRI colleagues for their support and encouragement throughout my stay at the University of Pittsburgh. Special thanks to Mr. W. Gao for his patience and help specially with the MTS and dilatometer, and to Dr. M. J. Hua for his help in STEM. Thanks are also due to the staff and faculty members of the Department of Materials Science and Engineering for their constant support.

I would like to express my gratitude to my employer, Saudi Basic Industries Corporation (SABIC), for sponsoring my graduate studies, and to Dr. S. Niaz for his unlimited support and understanding.

Finally, my deepest regards to my father Fakrodeen and my brother Mohammed for their unconditional love and support, to my wife Nada for her patience, love and support, and to my lovely kids, Abdullah, Faisal and Najla. I dedicate this thesis to them.

1.0 INTRODUCTION

Fundamental properties such as strength, toughness and weldability, in addition to some specific properties like fire resistance or elevated-temperature strength are required in heavy steel sections. Most of these properties improve remarkably with refining and homogenizing the final ferrite microstructure. In hot rolled steels, the fine ferrite microstructure depends mainly on the austenite grain size and composition prior to transformation as well as the cooling rate during transformation. Under normal circumstances, several types of thermomechanical processing (TMP) are successfully implemented to condition austenite prior to transformation. Interrupted accelerated cooling (IAC) could also be applied during transformation to facilitate the grain refining process [1, 2, 3, 4]. However, most of the traditional TMP and IAC techniques are not efficient means of ferrite grain refinement in heavy sections where the thickness is normally larger than 40 mm [5].

The hot rolling of heavy H-beams is normally produced through universal mills which usually have limited deformation power. Thus, rolling of these shapes is often characterized by large numbers of individual passes with small reductions per pass, at elevated temperature and relatively long interpass times [6]. These parameters, in addition to the low cooling rate of the heavy sections, result in coarse austenite grains and subsequently coarse ferrite grains and other undesirable low temperature transformation microstructural products. Since grain refinement associated with austenite grain size is limited, further refinement of the ferrite microstructure could be achieved through enhancing the intragranular ferrite (IGF) nucleation. In this approach,

workers proposed using second phase particles to stimulate the nucleation of ferrite intragranularly [4, 6, 7, 8, 9, 10, 11, 12, 13, 14, 15, 16, 17].

In this study, the use of second phase particles is proposed to promote the IGF nucleation mechanism. Steels with a proper composition and volume fraction of second phase particles (TiO and MnS) were designed to study the effect of the selected types of particles on the IGF nucleation. Since the mechanism by which inclusions nucleate IGF is as yet unclear, one of the main objectives of this study is to investigate the mechanism by which nucleation takes place. Moreover, this work includes the study of the decomposition behavior of coarse grained austenite as a function of very slow cooling rate. In addition, attempts were made to differentiate and quantify the nucleation of ferrite grains taking place at γ/γ, γ/α and inclusion interfaces.

2.0 BACKGROUND

Recently, the intergranular and intragranular nucleation of ferrite has received great attention in an attempt to improve both the toughness and strength in the steel, especially when conventional austenite grain refinement techniques are not effective.

This background presents a brief discussion of heavy steel sections and their classification, properties and applications. It also covers the conditioning processes of austenite prior to phase transformation and common strengthening mechanisms. Furthermore, the decomposition mechanisms of austenite and ferrite grain refinement are reviewed based on classical nucleation theory, where attention is being focused on the IGF nucleation with implementation of the particle-stimulated nucleation (PSN) mechanism.

2.1 HEAVY STEEL SECTIONS

Steel is one of the most widely used materials for structural applications. The heavy steel sections application includes, but is not necessarily limited to, the structure of buildings, bridges and towers. Henry [18] showed that the term heavy section fits any steel section when size and weight restrain its ability to respond to conventional heat treatments. This restriction certainly results in technological difficulties to enhance the properties of heavy sections. The source of this limitation is due to the local differences in thickness between flanges, web and fillet which

in turn give large variations in strain, strain rate and temperature during hot rolling and subsequent cooling rates across the section, hence leading to large variation in through thickness microstructure. The effect of these variations is a key factor in controlling the mechanical properties of heavy sections. However, special TMP are sometimes implemented to overcome such effects [4].

There are nearly ten grades of American Society for Testing and Materials, (ASTM), structural steels available in hot rolled structural shapes, plates and bars. The common ASTM specification for structural steel products are A992, A572 grade 50 and A36. Recently, ASTM A992 grade 50 steel has become the dominant material specification for wide-flange shapes, solidly displacing other types [19]. Table 2-1 shows the ASTM standard property specification for these three types of steel.

Table 2-1: ASTM A992, A572 and 36 standard specifications for structural steel shapes [19].

ASTM	Tensile strength, min, ksi (MPa)	Yield strength, ksi (MPa)	Yield to tensile ratio, max.
A 36	58–80 (400-550)	36 (250)	-
A 572 Gr 50	65 (450)	50 (345)	-
A 992	65 (450)	50-65 (345-450)	0.85

Heavy steel sections come in a wide variety of shapes. Among these shapes, wide-flange sections or H-beams are the most commonly used ones for building construction [20]. As shown in Figure 2.1, the H-beam is a doubly symmetrical shape consisting of two rectangular-shaped flanges connected by a rectangular web plate. The width and thickness of the flange could be up to about 515 mm and 90 mm, respectively, and the web could be around 610 mm wide and 50 mm thick. These special dimensions make the conventional thermomechanical processing impractical. Moreover, the maximum ratio in thickness between flange and web that could be reached is 3. Thus, during the hot rolling process, large differences in temperature, reduction ratio and cooling rate could take place among flange, web and their intersection, which is known as a fillet [4].

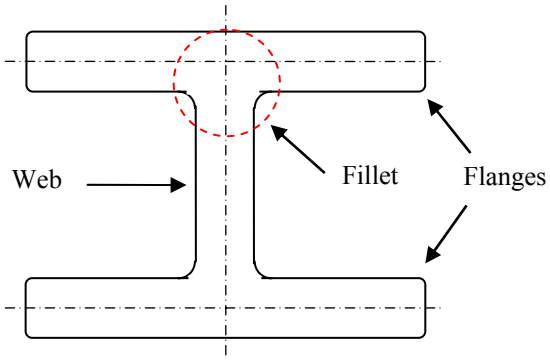

Figure 2.1: Schematic of wide flange section (H-beam).

2.2 STRENGTHENING MECHANISMS

Strength is one of the fundamental properties of steels, where a significant benefit of producing high strength steel is reducing the cost per unit strength as a result of material saving.

Strengthening constitutes increasing the resistance to plastic deformation that results from the change in the metal structure that impedes the motion of dislocations. Dissolved interstitial and substitutional atoms, work hardening and the interactions of dislocations with grain boundaries or second phase particles all reduce the ability of dislocations to move and, hence, strengthen the structure. Based on the type of these obstacles, the yield strength, σ_y, of microalloyed steels can be expressed as a generalized form of the Hall-Petch equation [21, 22, 23], assuming linear additive:

$$\sigma_y = \sigma_o + \sigma_{SS} + \sigma_{pptn.} + \sigma_{dis} + \sigma_{texture} + \sigma_{GB} \qquad (2\text{-}1)$$

where σ_o is the lattice friction or Peierl's-Nabarro stress, which represents the stress required to move a dislocation into a perfect lattice [24], σ_{ss} is the solid solution strengthening, σ_{ppt} is the precipitation strengthening, σ_{GB} is the grain boundary strengthening, $\sigma_{dis.}$ is the dislocation strengthening and $\sigma_{texture}$ is the texture hardening.

The contributions of these strengthening mechanisms are briefly discussed in the following sections.

2.2.1 Solid Solution Strengthening

The presence of substitutional and interstitial solid solutions tends to increase the yield strength. The amount of substitutional solid solution strengthening depends mainly on the difference in

size between the solute and solvent atoms. The substitutional solute atoms cause a localized symmetrical distortion of the solvent lattice which leads to the strengthening effects [25].

Interstitial solutes, such as carbon and nitrogen, introduce an asymmetric lattice distortion which produces strengthening effects that are 10 – 100 times that of substitutional elements [21, 26, 27].

In the addition to the size effect, the difference in the elastic modulus and the electronegativity of the solvent and solute are other sources of solid solution strengthening. The contribution of these strengthening mechanisms is very limited [27].

2.2.2 Precipitation Strengthening

The presence of the precipitates impedes the dislocation movement and increases the strength. This resistance is primarily dependant on the morphology, distribution and volume fraction of the precipitate particles, and their coherency or misfit with the matrix. Based on these factors, dislocation could glide through particles and shear them (Friedel mechanism) or loop between particles and bypass them (Orowan mechanism). For incoherent, semi-coherent and hard coherent particles, Orowan looping or cross slip mechanisms predominate [28, 29, 30]. Figure 2.2 shows the interaction between the dislocations and precipitates based on their coherency or misfit. The strong carbides, nitrides and carbonitrides forming elements such as Ti, Nb, V and Mo can have a remarkable effect on strength.

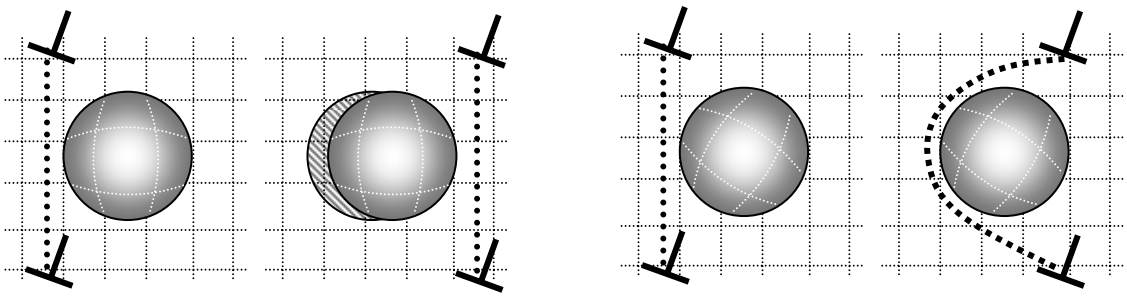

Figure 2.2: Interaction between dislocations and precipitate particles. (a) Dislocations glide through the slip plane and shear the particles (Friedel). (b) Dislocations loop around the particles (Orowan) or may cross slip or climb around them.

2.2.3 Grain Boundary Strengthening

Grain refining is an effective means of strengthening which results from blockage of dislocation motion by the grain boundaries. Thus, decreasing the grain size will increase the grain boundary area per unit volume and reduce the free path for continuous slip. Further motion then requires higher stresses to unlock or generate new dislocations in the neighboring grain [25,31].

The quantitative relationship between yield strength and grain size has been proposed by Hall [32] and Petch [33] as follows:

$$\sigma_y = \sigma_i + k\, d^{-1/2} \qquad (2\text{-}2)$$

where σi is the friction stress opposing the movement of dislocation in the grains, d is the grain diameter, and k is a constant, which represents the difficulty required to unlock or generate dislocations in the neighboring grains.

Grain refining is the most desirable strengthening mechanism since it is the only strengthening mechanism that can enhance both strength and Charpy toughness, as shown in Figure 2.3.

In addition to their role in precipitation strengthening, microalloying elements (MAE) such as Ti, V and Nb, are found to be very effective grain refiners [21, 34, 35]. The variation of the yield strength as a function of grain size for both mild and HSLA steels is shown in Figure 2.4. It shows that HSLA steels gain extra strength, ΔY, as a function of the precipitation strengthening associated with microalloying [36]. The role of the MAE in HSLA steels will be discussed later.

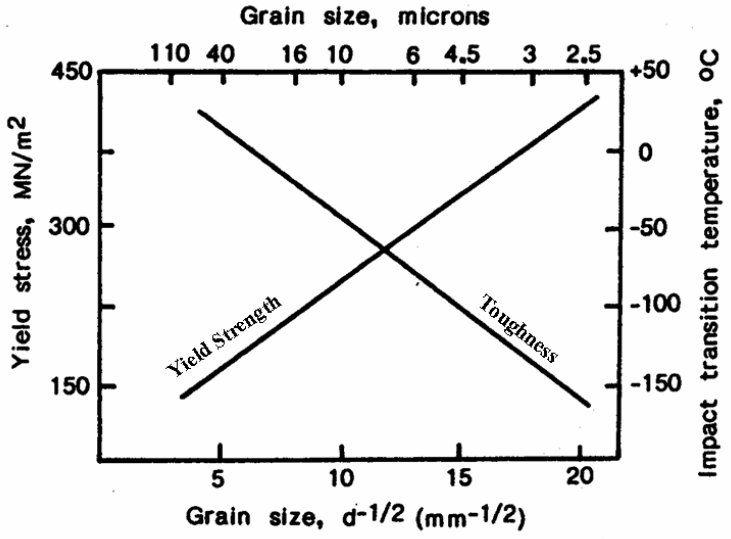

Figure 2.3: Effect of grain size of ferrite on yield stress and impact transition temperature [21].

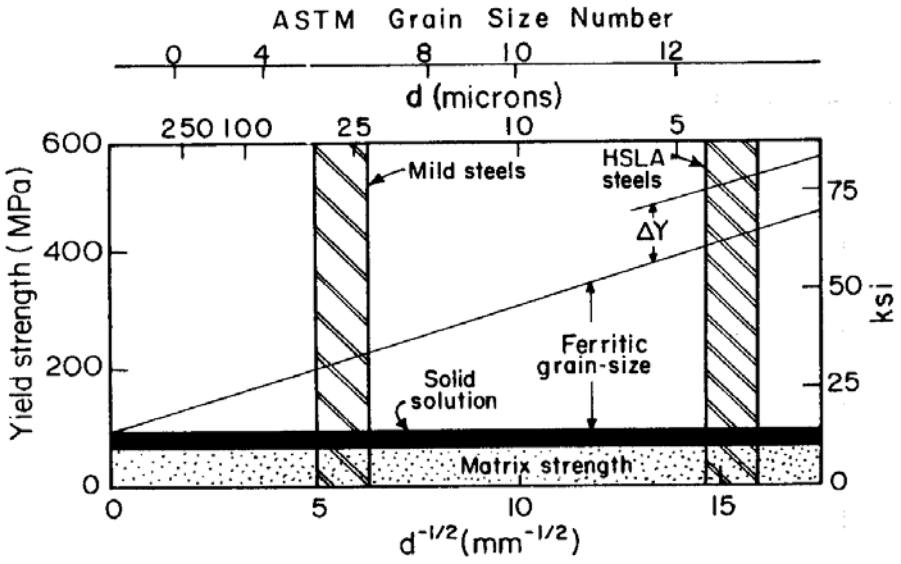

Figure 2.4: The effect of the grain size and other strengthening mechanisms on the yield strength in low-carbon and HSLA steels [36].

2.2.4 Dislocation or Work Hardening Strengthening

The flow stress will increase as a function of dislocation density in a given structure. Dislocations may be introduced by cold working, quenching strain, differences in thermal expansion between particles and the matrix, volume changes accompanying precipitation and strains produced during low temperature transformations [21].

The contribution of dislocation strengthening is negligible in most of the hot rolled steels that have polygonal ferrite microstructure with low dislocation densities [26].

2.3 MICROSTRUCTURAL CONTROL OF AUSTENITE

It is well-known that a fine and uniform ferrite structure is required for excellent strength and toughness of the steels in the as-rolled condition. Production of fine ferritic grains and control of properties in as-rolled HSLA steels are governed by the prior austenite composition and morphology as well as the austenite-to-ferrite transformation characteristics.

The austenite solute composition and grain morphology, i.e., the state of recrystallization prior to transformation, is determined by the selection of the TMP, and on recrystallization and growth rates of austenite. These rates are governed by the amount of reduction, strain rate and deformation temperature as well as the amount of microalloying elements, MAE, in solid solution and as precipitates in austenite. On the other hand, the austenite-to-ferrite transformation mechanism is a function of ferrite nucleation and growth rates as well as chemical composition. These rates are influenced by the morphology of the prior austenite, alloying elements and process variables [36, 37, 38, 39].

2.3.1 Conditioning of Austenite

The conditioning of austenite aims to give the hot rolled austenite prior to transformation the proper microstructure and composition to allow the desired final ferrite microstructure to be formed after transformation. High rates of ferrite nucleation result from having a large number of potential nucleation sites and a high nucleation rate per site. The sites for ferrite nucleation include grain boundaries, incoherent twin boundaries and deformation bands. As will be shown later, the austenite grain boundaries are considered to be the most preferable sites for ferrite nucleation. Hence, maximizing the density of these effective sites per unit volume, S_V, just prior

to the austenite-ferrite transformation, will increase the nucleation rate of ferrite and consequently refine the final microstructure [2, 39, 40, 41].

The final conditioned austenite microstructure prior to transformation is a direct result of several up-stream treatments and reactions. In general, conventional hot rolling (CHR) and thermomechanical processing (TMP) are two different approaches of hot rolling that affect the metallurgical condition of austenite prior to transformation [34, 37, 38, 39, 42, 43].

2.3.2 Conventional Hot Rolling (CHR)

The traditional hot-rolling process for plain carbon steels, as shown in Figure 2.5, is a sequence of recrystallization and growth of austenite grains during multi-passes deformation at high temperature. The main part of the deformation processes takes place at elevated temperatures where recrystallization and subsequent grain growth are relatively rapid, resulting in a coarse austenite grain size, $D\gamma$, prior to transformation. On cooling, these coarse austenite grains result in the formation of coarse ferrite grain size, $D\alpha$, and other undesirable low temperature transformation products. Thus, a fine ferrite microstructure can only be obtained by additional heat treatments such as normalizing [1, 42].

2.3.3 Thermomechanical Processing (TMP)

The principal goal of TMP, as discussed by several workers [1, 34, 44, 45], is to achieve a predetermined austenite microstructure prior to transformation to insure the finest ferrite

microstructure. The austenite grain refinement in the TMP is obtained from controlling the recrystallization and subsequent grain coarsening in a multi-pass rolling schedule.

Tanaka [1] showed that TMP generally consists of the controlled rolling process followed by interrupted accelerated cooling (IAC). The major purpose of controlled rolling process is to produce deformed austenite to increase the density of ferrite nucleation sites, while IAC enhances the ferrite nucleation rate.

Based on where the deformation occurs relative to certain material critical temperatures and condition of austenite, controlled rolling could be divided into three types [1, 34, 46]:

1) Recrystallization controlled rolling, RCR,

2) Conventional controlled rolling, CCR, and

3) Intensified controlled rolling, ICR.

In general, deformations at high temperature above the recrystallization start temperature, T95%, are representative of an RCR process whereas a CCR process implies deformations at low temperatures, below the recrystallization stop temperature, TRXN, or T5%. These critical temperatures and the changing of the austenitic microstructure as a function of deformation temperature and strain is schematically illustrated in Figure 2.6 for constant interpass time [47].

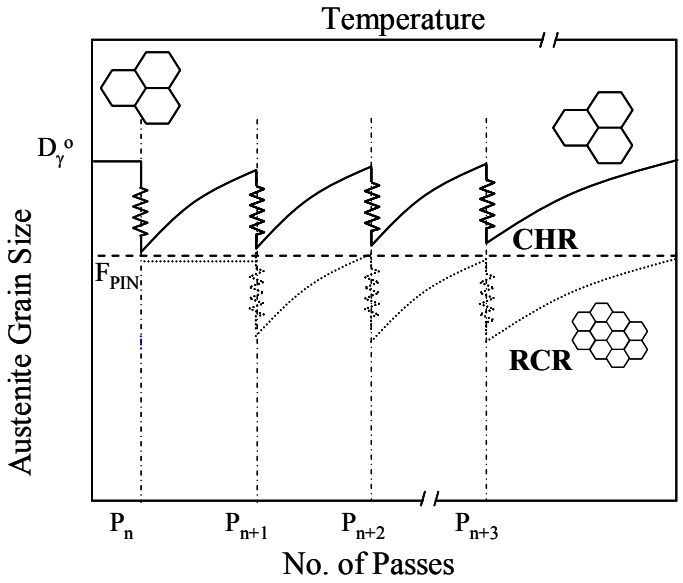

Figure 2.5: Schematic illustration of the differences in the grain size evolution during deformation in both conventional and recrystallization controlled rolling [35].

RCR is a high temperature deformation process that consists of rapid recrystallization followed by inhibiting grain coarsening within the interpass time, as shown in Figure 2.5. In this process, the magnitude of the pinning force, F_{PIN}, of the MAE precipitates must be small enough to permit recrystallization of austenite to occur, but large enough to suppress grain coarsening. In this case, the original equiaxed austenite grains are replaced with a new set of smaller recrystallized grains during each pass. The value of S_V increases as a result of an increase in the grain boundary area per unit volume which is caused by a decrease in average grain volume, as illustrated schematically in Figure 2.7 [34, 37].

Cuddy [39] and Sekine, et al.[48] showed the limitation of structure refinement that can be achieved by using the RCR process. Accordingly, further conditioning of austenite through the CCR process is required to increase the ferrite nucleation sites. The CCR process involves flattening of the recrystallized austenite grains and formation of intragranular planar defects,

such as twin boundaries and deformation bands, as a result of repeated deformation in the non-recrystallization region below the $T_{5\%}$. In this case, the S_V value increases as a result of increasing the grain boundary area per unit volume that arise from a change in grain shape and through the addition of the intragranular planar defects, as shown in Figure 2.7.

On the other hand, deformations which take place in the austenite-ferrite two phase regions are classified as the intensified controlled rolling process. The differences in the deformation schedule between these processes are illustrated in Figure 2.8.

TMP is also applied to the heavy steel sections to condition the austenite prior to the transformation and to homogenize the properties across the section. However, the process is modified to meet the special behavior of large thickness during the rolling and to overcome the limitation of variation in cooling and reduction rates across the section.

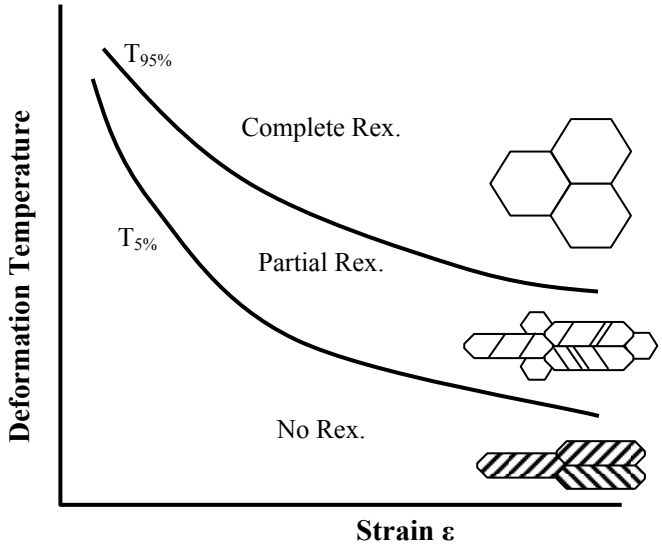

Figure 2.6: Schematic illustration of austenite microstructures results from various deformation conditions [47].

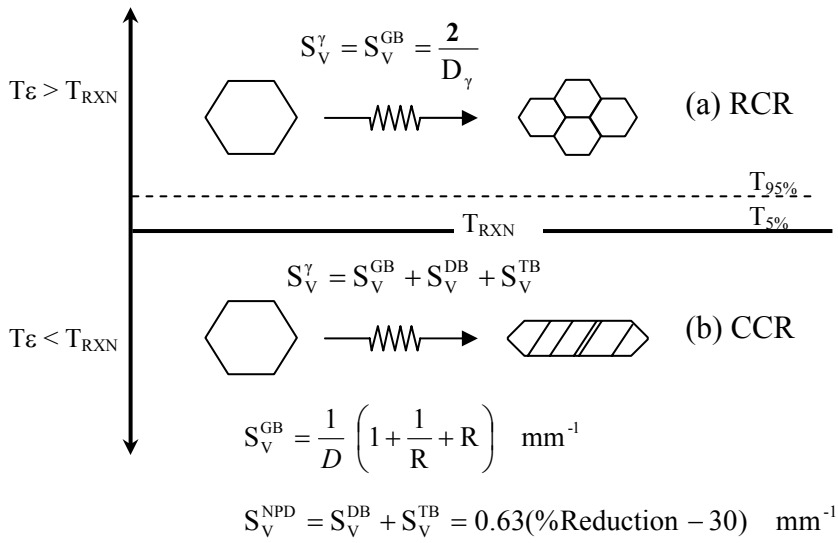

Figure 2.7: Schematic representation of austenite microstructure when deformed above or below the recrystallization stop temperature, T_{RXN}, of austenite. Note that the superscripts GB, DB, TB and NPD denote the contribution to total S_V from grain boundaries, deformation bands, twin boundaries and near planar defects. Moreover, D is the cube edge length and R is the rolling reduction ratio [49].

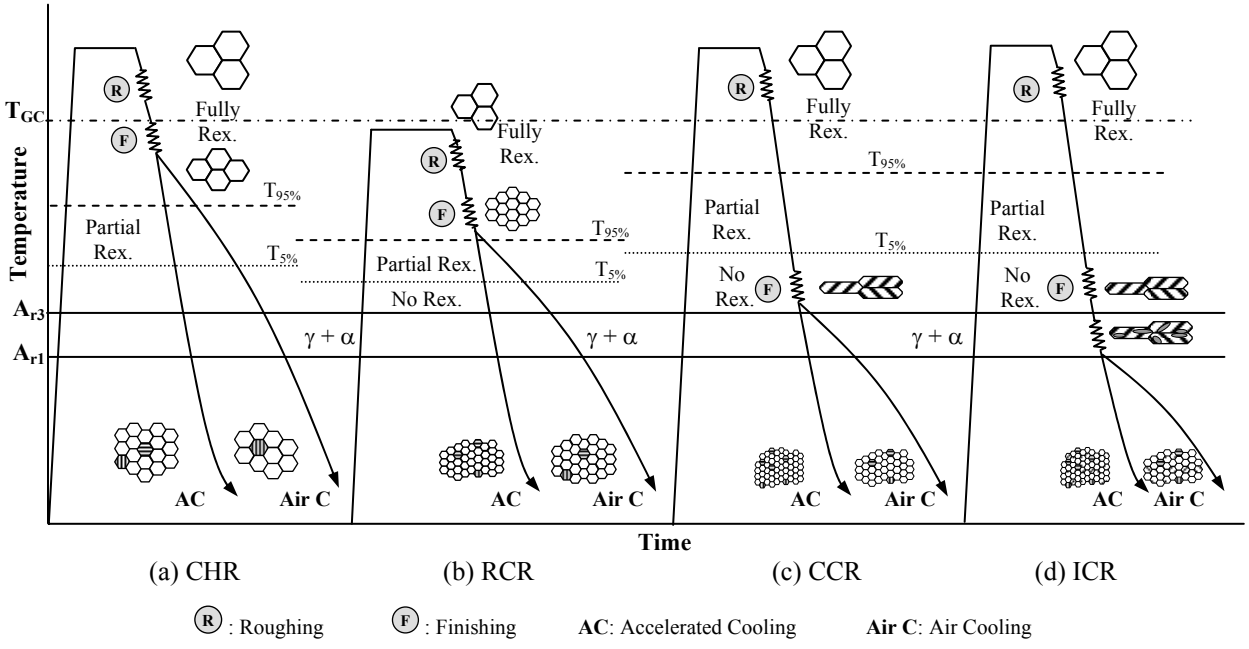

Figure 2.8: Schematic illustration of the hot rolling processes: (a) Conventional hot rolling CHR, (b) Recrystallization controlled rolling RCR, (c) conventional controlled rolling CCR and (d) Intensified controlled rolling ICR.

2.3.4 TMP of Heavy Steel Sections

The desirable fine ferrite microstructure can be acquired with a combination of a large reduction at temperature below $T_{5\%}$ and accelerating cooling during phase transformation. These conditions are typical of plate products, 20 mm or less in thickness.

In the case of heavy plates where the final thickness is larger than 40 mm, the effects of controlled rolling and accelerated cooling will not be spread equally over the whole thickness of the plate. This could give a large variation in the final microstructure and produce a coarse grain structure and deteriorating strength and toughness at mid-thickness of the plate section. The limitation of applying the traditional TMP in the case of heavy sections is based on three main reasons. One is the regional differences in the thickness which give a large variation in rolling temperature and reduction ratio among the different regions of the given section during the hot rolling process. The second reason is due to the limitation of the rolling equipment, i.e., motors, gears and stands, to give large reduction per pass for such heavy sections as required in the traditional TMP. The third source of limitation comes from the difficulty of applying accelerated cooling processes to these heavy sections. This is because of the difference between the cooling rate at both the center and the surface will lead to different transformation products and, consequently, different mechanical properties. Moreover, the transformation of coarse $D\gamma$ under rapid cooling rate could result in undesirable high carbon non-polygonal ferrite microstructures of high yield-to-tensile ratio and lower notch toughness [4, 5, 7, 20].

The production of heavy sections by universal-type rolling mills, which are limited in capacity, create a special environment of high deformation temperature with small reduction per pass, large interpass time and large number of passes. All these processing parameters contribute

to coarsening the equiaxed recrystallized austenite grains prior to the transformation, i.e. > 100 μm. Considering the final product thickness, Figure 2.9 shows schematically the conditions under which fine ferrite grains can be obtained from a given austenite grain size. Clearly, the two main parameters that affect the final ferrite grain size are the microstructural state of the austenite prior to the phase transformation and the cooling rate through the phase transformation.

Based on the previous discussion, it seems to be impossible to produce fine ferrite microstructures in heavy sections by using the conventional, well-established TMP approach which depends on the effective austenite conditioning and accelerated cooling. Therefore, another approach is implemented to refine the final ferrite structure through using particle-stimulated nucleation, PSN, which leads to the formation of intragranular ferrite, IGF. Adding active second phase particles to steel increases the S_V value beyond that associated with austenite grain boundaries and provides additional nucleation sites to form fine ferrite grain size during transformation [4, 6, 7, 8 , 9, 10, 11, 12, 13, 14, 20].

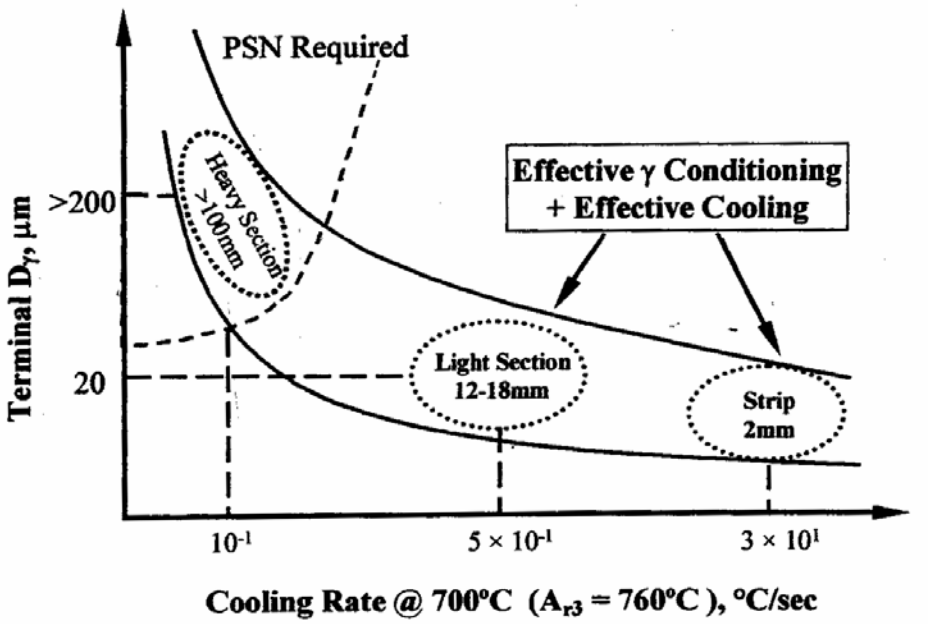

Figure 2.9: The relation between the austenite grain size and cooling rates for achieving fine ferrite (Dα=15μm) [7].

2.3.5 The Role of Microalloying Elements (MAE) in Austenite Conditioning

The presence of the MAE in modern HSLA steels renders austenite very amenable to beneficial austenite conditioning. The influence of MAE such as Nb, Ti and V on the response of austenite to TMP can be understood by the way in which MAE can influence the three critical temperatures of austenite [49]; 1) The grain coarsening temperature (T_{GC}), 2) The recrystallization stop temperature ($T_{5\%}$), and the transformation temperature (Ar_3). The effects of the MAE in these three critical temperatures are discussed in the following sections.

2.3.5.1 The Role of MAE on the Grain Coarsening Temperature The grain coarsening temperature, TGC, is defined as that temperature above which grain coarsening by secondary recrystallization or abnormal grain coarsening commences and relates to the temperature above which the undissolved precipitates can no longer suppress grain coarsening. Since the TGC is related to the dissolution temperature of the pinning precipitate, the choice of the reheat temperature relative to the grain coarsening temperature determines the amount of MAE dissolved as well as the starting grain size [50]. The influence of various MAE on grain coarsening during reheating is shown in Figure 2.10. The hatched region on the curves represents the coarsening temperature region for each type of steel.

The principle of inhibiting the grain growth by fine particles was developed by Zener [51]. The original model proposed that a portion of the migrated grain boundary is eliminated when it intersects a particle. The effective energy of the grain boundary would be lowered due to that elimination. Therefore, the movement of the boundary away from the particle requires the creation of additional grain boundary area that was eliminated by the particle. The unpinning process requires extra energy or driving force. This force is required for grain coarsening. The original work of Zener was later expanded by Gladman[52, 53] who considered the motion of a grain boundary through a regular array of spherical particles per unit area, N_A. Hence, the total pining force, F_{PIN}, that an array of particles of radius, r, exerted on a migration boundary, was expressed as:

$$F_{PIN} = 4\, r\, \sigma\, N_A \qquad (2\text{-}3)$$

where σ is the interfacial energy per unit area of austenite grain boundary ($\sigma = 0.8$ J/m^2). Three models have been suggested to calculate the N_A value [52, 54, 55, 56]. The rigid boundary model assuming that the motion of a rigid grain boundary interacts only with

those particles lying within ± r from the boundary [52]. In contrast, the flexible boundary model assuming that an infinitely flexible boundary interacts with every available particle within a single plane of a three dimensional array [55, 56]. The third model is the subgrain boundary model which is considered as the most realistic assumption. The subgrain boundary model considers the effect of precipitate distribution on the austenite subgrain boundaries prior to the recrystallization process [54]. Therefore, a large number of fine precipitates with small interparticle spacing would lead to a higher F_{PIN}.

Gladman [52] derived an expression for the critical size of particles, r_C, below which grain boundaries are pinned:

$$r_C = \frac{6R_o V_f}{\pi}.\left[\frac{3}{2} - \frac{2}{z}\right]^{-1} \tag{2-4}$$

where R_o is the mean radius of the matrix grain, V_f is the volume fraction of second phase particles and Z is the ratio of the radii of growing and matrix grains. Hillert [57] has deduced that Z can range in value between $\sqrt{2}$ to 2 through the grain growth process. In the system where particle size $r > r_c$, grain growth would proceed with a reduction in energy. On the other hand, systems where $r < r_c$, grain growth would result in an increase in energy and the grain boundaries will be effectively pinned.

The required energy for the growth process per unit area of the growing grain, F_D, or the driving force for grain growth increases with decreasing the grain size, and is given by[58]:

$$F_D = \left[\frac{2}{Z} - \frac{3}{2}\right]\frac{\sigma}{R} \tag{2-5}$$

At temperatures below the T_{GC}, the pinning force exerted by the particles is sufficient to prevent grain coarsening through secondary recrystallization or abnormal grain growth. At temperatures above T_{GC}, the particle size exceeds the critical size required to suppress coarsening; thus, grain coarsening can occur [34, 50, 59]. In plain carbon steels, the grain size systematically increases with increasing temperature while maintaining a consistently normal distribution.

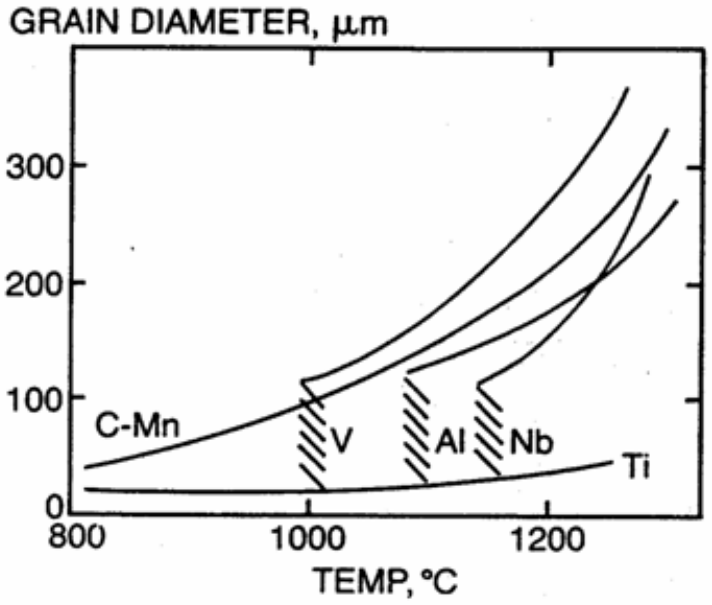

Figure 2.10: Austenitic grain growth characteristics in steels containing various MA additions [34].

2.3.5.2 The Role of MAE on the Recrystallization Stop Temperature Perhaps the most important effect of MAE is in controlling the recrystallization stop temperature, TRXN. Any deformation below this temperature results in fully unrecrystallized austenite grains whereas above this temperature, partially or fully recrystallized grains may be present. This is schematically illustrated in Figure 2.6.

Cuddy [56] illustrated the influence of several MAE on the recrystallization temperature, as shown in Figure 2.11. Niobium shows the most profound effect in increasing the recrystallization temperature and this accounts for its selection as the primary MAE in the controlled rolled steels.

Conditioning HSLA steels using RCR requires a precise selection of the MAE to ensure a low recrystallization temperature to allow a large processing window for several passes between the reheating and finishing, $T_{95\%}$, temperatures, Figure 2.6. On the other hand, steels processed using the CCR technique require an adequate addition of MAE that ensures the highest T_{RXN}. The high T_{RXN} allows accumulation of as much deformation as possible to occur in the non-recrystallization region [7, 34, 37, 45].

2.3.5.3 The Role of MAE on the Transformation Temperature The phase transformation temperature, Ar3, in hypoeutectoid steel is defined as the temperature where the cooling rate intersects the start of the polygonal ferrite nucleation on continuous cooling transformation. The Ar3 temperature is a function of the cooling rate and the hardenability of the steel. The final ferrite microstructure is directly related to the transformation temperature, where lower Ar3 temperatures result in higher nucleation rates and lower growth and coarsening rates. Therefore, Sv and Ar3 have a major effect on ferrite grain size.

The effect of the MAE on the Ar_3 temperature is based on the hardenability concept. At high temperature, where most of the MAE are in solution in austenite, the Ar_3 temperature is relatively low. On other hand, when most of the MAE are precipitated, the Ar_3 temperature is relatively high [60]. Moreover, the Ar_3 temperature increases with increasing the nucleation sites per unit volume, i.e. S_V value.

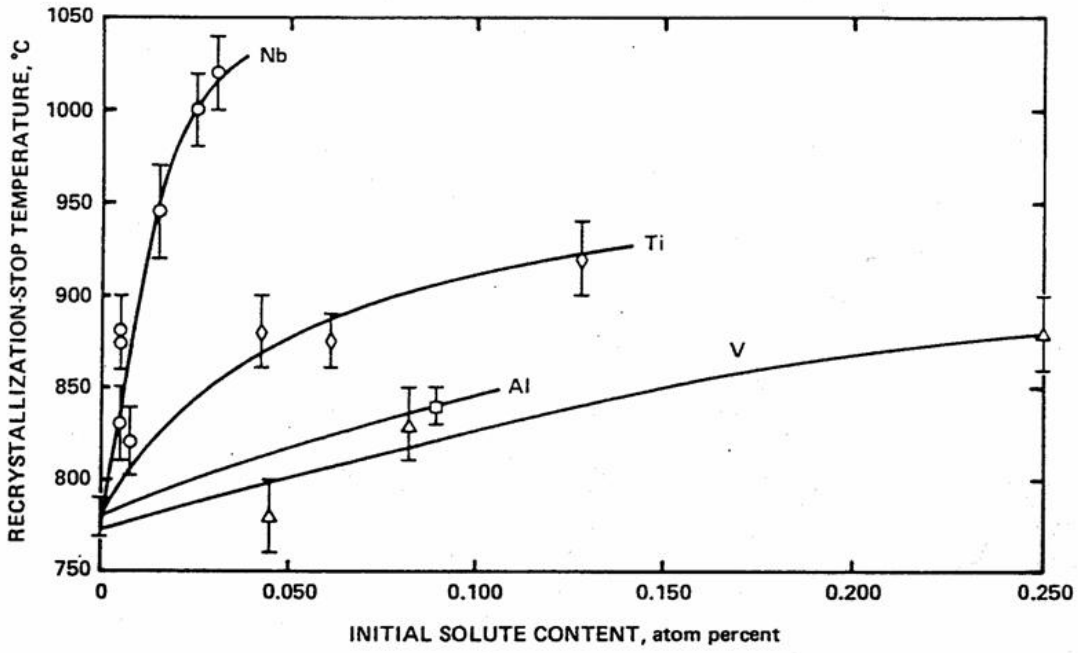

Figure 2.11: Effect of MAE elements in the recrystallization stop temperature [56].

2.4 NUCLEATION AND GROWTH THEORY

The formation of ferrite from of the decomposition of austenite is a phase transformation that depends mainly on nucleation and growth phenomena. The nucleation and growth process starts with the formation of stable nuclei of a new phase inside the matrix of the parent phase, followed by the growth of these nuclei. Nucleation and growth occur simultaneously until the phase transformation is completed. Depending on the nature of the phase transformation, the growth process could be followed by coarsening (Ostwald ripening) of the new phase. In addition to the phase transformation in metals, solidification, precipitation and recrystallization all involve nucleation and growth phenomena.

Based on the thermodynamic stability, phase transformation may be classified into two categories [61]:

1) Continuous or homogenous transformation that takes place simultaneously in all parts of a phase. In this case, the transformation has a small compositional fluctuation with large spatial extent.
2) Discontinuous or heterogeneous transformation where the transformation has a large compositional fluctuation but with small extent. The following discussion is based on this category since the nucleation and growth transformation falls under this type of transformation.

In the present section, the classical nucleation and growth theory in addition to the nucleation theory in solid-solid transformation, are reviewed [40, 61, 62, 63, 64, 65, 66, 67, 68, 69, 70, 71, 72]. These theories are considered to form the basis for understanding the microstructural changes during the austenite-ferrite transformation.

2.4.1 Nucleation Phenomena

Based on Gibbs' thermodynamics [73], a classical theory of nucleation was proposed by Volmer and Weber [74] and developed by Becker and Döring [75] and Turnbull, Fischer and Hollomon [76, 77]. A basic assumption in this theory is that, by random thermal fluctuation, tiny particles of a new stable phase are created within the matrix of the parent phase. These particles are assumed to have the same surface and thermodynamic properties as those of the bulk product phase. A sharp boundary that delineates the particle from the matrix is formed by such an event. The surface energy that is associated with the newly formed boundary will act as a barrier to the phase transformation. This surface energy between the two phases is known as interfacial energy, γ. The size of this barrier is directly proportional to the number of atoms in the surface sites of the new particles. There is always a critical particle size, r*, where the probability of growing or decaying the new particle is equal. Above the critical size, $r > r^*$, the particle grows with a decrease in energy and then becomes stable and forms a nucleus. This nucleus has enough energy to overcome the barrier of the critical free energy of nucleation, ΔG^*. On the other hand, below the critical size, $r < r^*$, the particles are normally called embryos and may disappear completely.

Nucleation takes place either homogenously or heterogeneously. In the homogenous nucleation the new phase forms uniformly throughout the bulk of the parent phase, while in the heterogeneous nucleation, the new phase nucleates preferentially at energy intensive inhomogeneities in the parent phase, i.e., at grain boundaries, inclusions and dislocations.

According to the classical nucleation theory, the free energy of nucleation of solid or liquid, ΔG, is given by [63]:

$$\Delta G = \Delta G_V + \Delta G_A \tag{2-6}$$

where ΔG_A is the interfacial free energy that represents the free energy of the surface area created between the two phases, i.e., the embryo and the matrix, and $\Delta G_V = G_V^{\alpha} - G_V^{\beta}$ is the free energy associated with transformation of the volume of the product phase, where G_V^{α} and G_V^{β} are the free energies per unit volume of parent and new phase, respectively. ΔG_V is always negative while ΔG_A is positive. In the liquid-solid phase transformation, the equation could be expanded as [63]:

$$\Delta G = V_S \Delta G_V + A_{L/S}\gamma_{L/S} \tag{2-7}$$

where V_S is the volume of new phase, $A_{L/S}$ is the interfacial area between the two phases, and $\gamma_{L/S}$ is the solid/liquid interfacial free energy. The relationship between these two phases is schematically illustrated in Figure 2.12.

In the absence of strain during solid/liquid transformation, the nucleated particle tends to have a spherical shape to minimize its surface energy. For a particle of radius r, Equation 2-7 is rewritten as [63,70]:

$$\Delta G = \frac{4}{3}\pi r^3 \Delta G_V + 4\pi r^2 \gamma \tag{2-8}$$

These free energies are schematically plotted in Figure 2.13 as a function of the nucleus radius, r. It is clearly shown that the interfacial term increases as r^2 whereas the volume free energy released increases as r^3. Therefore, the influence of the second term of Equation 2-8 will become less as r increases. In the equilibrium state, the saddle point or the maximum is obtained when $\partial \Delta G / \partial r = 0$ at r = r*, which gives the critical values of r* and ΔG^* as [63, 70]:

$$r^* = -\frac{2\gamma}{\Delta G_V} \tag{2-9}$$

and

$$\Delta G^* = \frac{16\pi\gamma^3}{3\Delta G_V^2} \tag{2-10}$$

The temperature dependency of the surface energy term, γ, is small enough to be neglected, while ΔG_V is strongly dependent on the temperature, as illustrated in the following equation [63]:

$$\Delta G_V = \frac{H_V \Delta T}{T_o} \tag{2-11}$$

where To is the equilibrium temperature, ΔT is the degree of undercooling, ΔT = T - To, and ΔHV is the enthalpy change per unit volume of the product formed. Based on this relation, ΔGV is negligible at the equilibrium temperature where T = To, and it becomes more negative with increasing ΔT. The effect of ΔT on both r* and ΔG* is shown schematically in Figure 2.14 It is clearly shown that the probability of the forming of a critical nuclei increases with increasing the degree of under cooling.

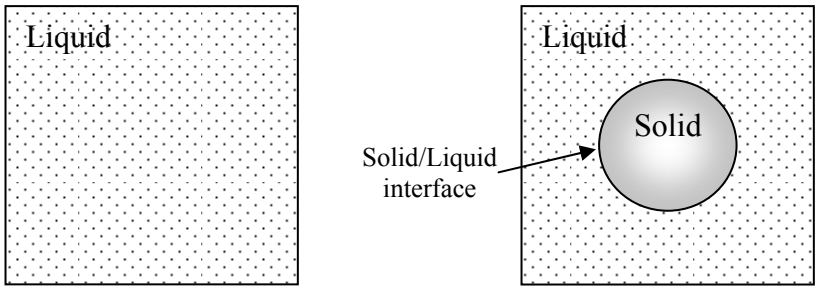

$$G_L = V_L G_V^L + \cancel{V_S G_V^S}$$

$$\Rightarrow G_L = V_L G_V^L$$

$$G_{SL} = G_L + \Delta G \quad \text{,and}$$

$$G_{SL} = V_L G_V^L + V_S G_V^S + A_{S/L}\gamma_{S/L}$$

$$\Delta G = G_{SL} - G_L = V_L G_V^L + V_S G_V^S + A_{S/L}\gamma_{S/L} - V_L G_V^L$$

$$\Rightarrow \boxed{\Delta G = V_S G_V^S + A_{S/L}\gamma_{S/L}}$$

Figure 2.12: Solid/liquid homogenous nucleation [63].

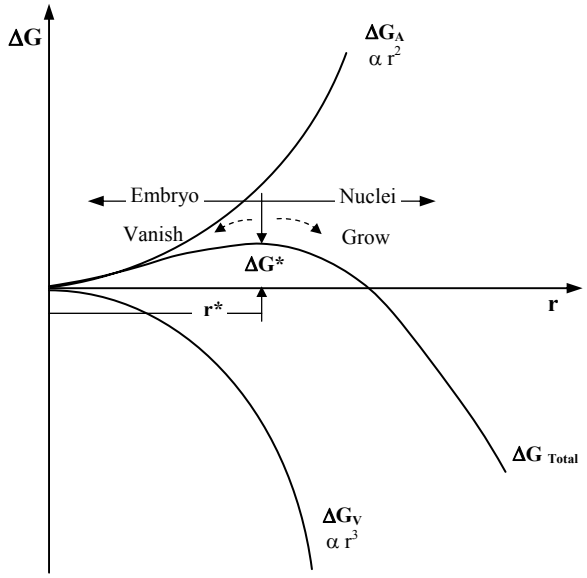

Figure 2.13: Free energy changes associated with homogenous nucleation of a spherical particle of radius, r [63].

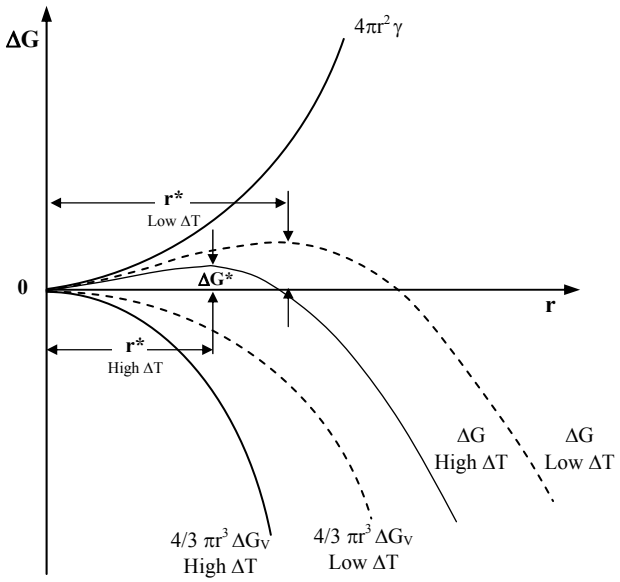

Figure 2.14: Effect of temperature on the critical radius and energy barrier of a spherical particle of radius, r [66].

2.4.2 Interphase Interfaces in Solids

There are two separate factors that contribute to the energy of solid-solid interphase interfaces. First, there is a structural energy, γ_{St}, due to lattice misfit between the phases. The second factor is the chemical energy term, γ_{Chi}, associated with the sudden change of composition at the boundary on passing from one phase to the other. Thus the interphase boundary energy can be written as $\gamma_{\alpha/\beta} = \gamma_{St} + \gamma_{Chi}$ [69]. On the other hand, the interphase boundaries in solids can be

divided on the basis of their atomic structure into three classes: coherent, semicoherent and incoherent.

A coherent interface, Figure 2.15(a), arises when two crystals match perfectly at the interface plane where the two lattices are continuous across the interface. Due to the low misfit energy, the chemical contribution of the interfacial energy dominates. In this case, the interfacial energy is considered to be equal to the chemical component which is correspondingly low, making the nucleation barrier small. On the other hand, in incoherent and semi-coherent cases, Figure 2.15(b) and (c), respectively, the differences in lattice parameter are taken up by dislocations and other discontinuities in the boundary. These defects greatly increase the energy of the interface and increase the nucleation barrier [63, 69].

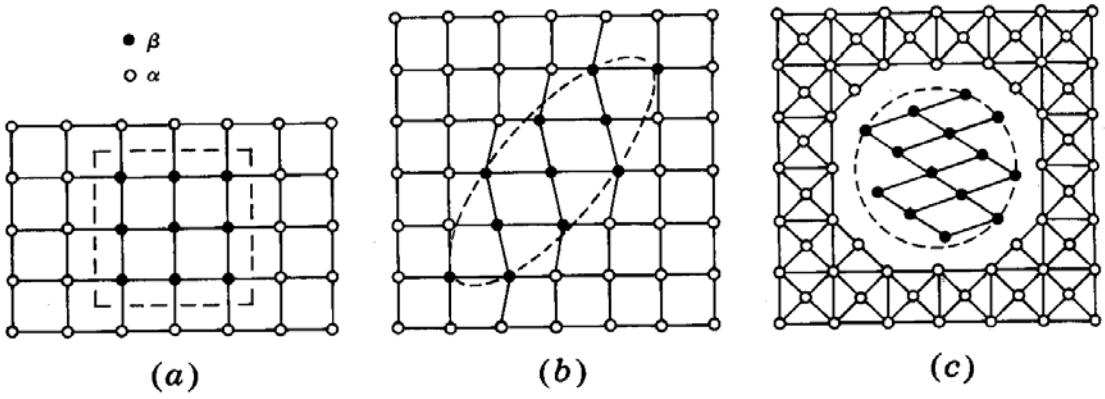

Figure 2.15: Three types of nuclei formation: (a) completely coherent; (b)semi-coherent; (c) Fully incoherent [66].

2.4.3 Homogenous Solid-Solid Nucleation

As mentioned earlier, in homogenous nucleation the new phase nucleates without benefit of pre-existing heterogeneities. In solid state transformation, the changes in atomic configuration are considered since the crystal structure of the new phase is usually different from that of the matrix.

Transformation in the solid phase is different from solidification in three important respects. First, the rate of growth in solidification, due to the heat of fusion, is relatively large compared with the heat of transformation of the solid phase. The second difference is that the solid phase transformations usually involve diffusion which requires time and occurs most rapidly at high temperatures. The third difference is due to the strain energy that opposes the transformation.

When a solid phase nucleates from another solid phase, strain often results due to the misfit between the two crystal structures and volume change. This gives an increase in the overall energy of the system; therefore, the free energy change during nucleation must be modified to include the strain energy term, ΔG_S. Then Equation 2-6 is written as [63]:

$$\Delta G = \Delta G_V + \Delta G_A + \Delta G_S \tag{2-12}$$

where ΔG_S is the strain free energy in the bulk away from the interface. Both ΔG_A and ΔG_S are always positive and are related to the nature of the interfacial energy between the nucleus and the matrix. The magnitude of the interfacial energy is strongly dependent on the interface coherence as discussed previously.

In the case of a spherical nucleus, the free energy of formation is written as [63]:

$$\Delta G_{hom} = 4\pi r^2\gamma + 4/3\pi^3 \, (\Delta G_v + \Delta G_s) \tag{2-13}$$

Similar to Equations 2-9 and 2-10, maximization of the above equation yields the critical radius [63]:

$$r^* = -\frac{2\gamma}{(\Delta G_V + \Delta G_S)} \tag{2-14}$$

and the free energy of activation

$$\Delta G^* = \frac{16\pi\gamma^3}{3(\Delta G_V + \Delta G_S)^2} \tag{2-15}$$

2.4.4 Heterogeneous Solid-Solid Nucleation

As has been reported by several authors [40, 62, 64, 68, 69, 71, 72, 78, 79], nucleation in solids is almost always heterogeneous where a variety of structural defects often act as nucleation sites. Among the preferable nucleation sites are grain boundaries, incoherent twin boundaries, deformation bands, dislocations, stacking faults, inclusions and free surfaces. The presence of these non-equilibrium defects increases the total free energy of the bulk material. Thus, if the formation of a nucleus results in the destruction of a defect, a subsequent release in free energy will accompany the event. This released energy can be used to overcome the activation energy barrier for nucleation, ΔG*.

Among these nucleation sites, grain boundaries are especially potent, since they have larger interfacial energies and faster diffusion rates compared to the bulk material. Moreover, the open structure of the grain boundaries tends to reduce the transformation strain [80].

The optimum shape for an incoherent grain boundary nucleus of the newly formed phase is assumed to be two abutted spherical caps in order to minimize the total interfacial free energy, Figure 2.16. The excess free energy associated with this nucleus is given by [71,72]:

$$\Delta G = V\left(\Delta G_V + \Delta G_S\right) + A_{\alpha\beta}\gamma_{\alpha\beta} - A_{\alpha\alpha}\gamma_{\alpha\alpha} \tag{2-16}$$

where $\gamma_{\alpha\alpha}$ is the interfacial energy between the two α grains and $\gamma_{\alpha\beta}$ is the interfacial energy between the α and β grains which is assumed to be isotropic and equal for both grains. $A_{\alpha\beta}$ is the area of α/β interface created while $A_{\alpha\alpha}$ represents the area of α/α grain boundary consumed during the nucleation process. The energy balance of the system is given by [71, 72]:

$$\gamma_{\alpha\alpha} = 2\gamma_{\alpha\beta}\cos\theta \tag{2-17}$$

From the geometry of Figure 2.16, the volume, V, and the surface areas, $A_{\alpha\beta}$ and $A_{\alpha\alpha}$ are calculated using the following equations [71,72]:

$$V = \frac{2\pi r^3}{3}\left(2+\cos\theta\right)\left(1-\cos\theta\right)^2 \tag{2-18}$$

$$A_{\alpha\beta} = 4\pi r^2\left(1-\cos\theta\right) \tag{2-19}$$

$$A_{\alpha\alpha} = 2\pi r^2 \sin^2\theta \tag{2-20}$$

where r in this case is the radius of curvature of the spherical surface and 2θ is the included spherical caps angles. Substituting the above values into Equation 2-16, the following relation is obtained:

$$\Delta G_{het} = \left\{\frac{4}{3}\pi r^3\left(\Delta G_V + \Delta G_S\right) + 4\pi r^2\gamma_{\alpha\beta}\right\}S(\theta) \tag{2-21}$$

This could be written as:

$$\Delta G_{het} = \Delta G_{\text{hom}} S(\theta) \tag{2-22}$$

where S(θ) is a shape factor given by:

$$S(\theta) = \frac{1}{2}\left(2+\cos\theta\right)\left(1-\cos\theta\right)^2 \tag{2-23}$$

Based on the above equations, the activation energy barrier for heterogeneous nucleation, ΔG^*_{het}, yields the following expression:

$$\frac{\Delta G^*_{het}}{\Delta G^*_{\text{hom}}} = S(\theta) \tag{2-24}$$

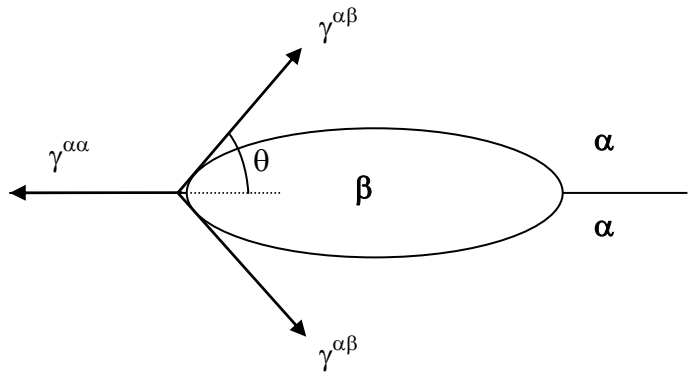

Figure 2.16: Double hemispherical cap model for nucleation of grain boundary allotriomorph [72].

In addition to the nucleation event in the grain boundaries, Cahn [78] showed that the ΔG^*_{het} value could be reduced further if the nucleation event takes place on the edge or corner of the grain. Figure 2.17 shows the dependency of the $\Delta G^*_{het} / \Delta G^*_{\text{hom}}$ ratio on cosθ for the various grain boundary nucleation sites. The ratio of free energy required to form the grain boundary nucleus, ΔG^*_B, to that required to form a homogenous nucleus, ΔG^*_{hom}, decreases with increasing ratio of the grain boundary energy to the interphase boundary energy, $\gamma_{\alpha\alpha} / 2\gamma_{\alpha\beta}$. For all values of cosθ, it is shown that $\Delta G^*_C < \Delta G^*_E < \Delta G^*_B < \Delta G^*_{\text{hom}}$, where the designations C, E and B in the

ΔG* term represent the free energy required to form a grain corner, edge and boundary nucleus, respectively. Hence, grain corners are considered as preferable sites for nucleation.

Subgrain boundaries as well as deformation bands also serve as heterogeneous nucleation sites. Moreover, the interface between the inclusions and the matrix acts as an active interface and could be treated in a manner similar to that of grain boundaries.

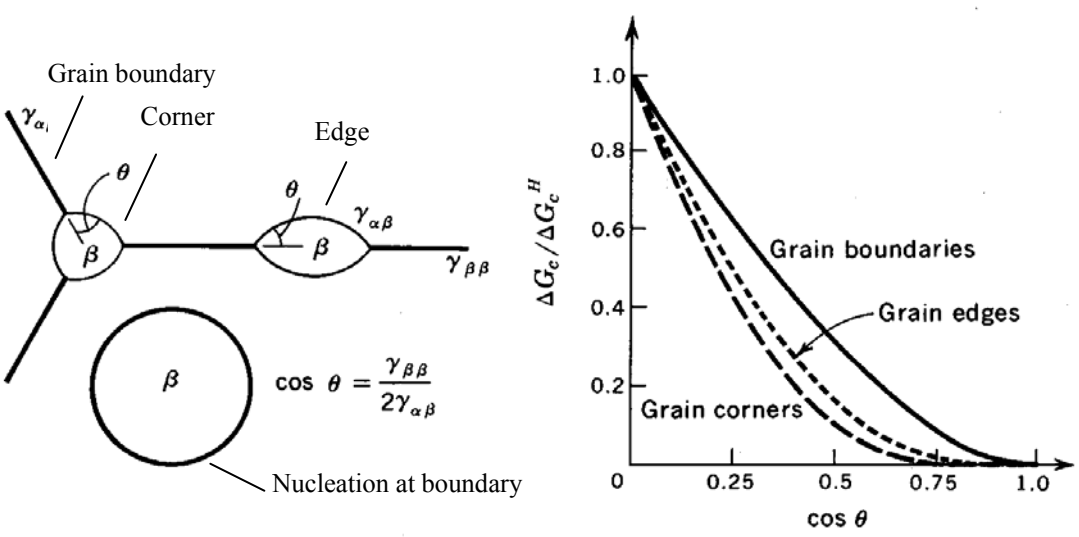

Figure 2.17: Activation energy for nucleation at grain boundaries, faces and edges [78].

2.4.5 Rates of Heterogeneous Nucleation

Based on the revision of the kinetic theory of nucleation [68, 80, 81,82], the rate of nucleation is introduced as a function of two variables. The first is the thermodynamic driving force which is directly related to ΔG*. The second is the atomic migration rate at which atoms jump from the α

matrix to the β embryo which is related to the diffusivity. Both the thermodynamic and the kinetic factors are functions of temperature.

The nucleation rate, I, is defined as the number of embryos that jump over the energy barrier per unit volume, and is determined by multiplying the number of critical nuclei by the rate of growth of these embryos. The equation of nucleation rate is given as [82]:

$$I = s^* v_o \exp\left(-\frac{\Delta G_m}{kT}\right) N_v \exp\left(-\frac{\Delta G^*}{kT}\right) \tag{2-25}$$

where s* is the number of atoms on surface of embryo of critical size, ν_o is the number of times per second an atom tries to jump over the barrier, and it is known as a frequency factor, N_v is the number of atoms per unit volume, ΔG_m is the atomic migration energy which is defined as the activation energy for an atom to cross the surface between two phases, k is the Boltzman factor and T is the temperature.

In the case of heterogeneous nucleation, there are different types of nucleation sites available in the system, therefore, the nucleation rate could be written as [82]:

$$I = \sum_{j=0}^{j=\max} \frac{N_j K_j}{V} \exp\left[-\frac{(\Delta G^*_{\text{hom}} + \Delta G_m - \Delta G_j)}{kT}\right] \tag{2-26}$$

where j refers to a particular heterogeneous nucleation site, Nj/V is the number of j sites per unit volume and $\Delta G_j = \Delta G^*_{\text{hom}} - \Delta G^*_j$, where ΔG^*_j is the activation energy for nucleation of site j. Fine [82] showed that K_j is a function of s*, ν_o, N_v and temperature in addition to the surface energy per unit area of interface.

In conclusion, in addition to the degree of undercooling, the rate of heterogeneous nucleation is a function of number, type and energy associated with each type of the heterogeneous sites.

2.4.6 Growth -vs- Coarsening

Growth is defined as a continuation of the transformational process beyond the nucleation event, where the stable nuclei grow into a new phase. The growth event could occur with or without compositional change. The latter one represents the interface controlled growth event, where the attention is focused on the thermally activated atomic jumping across the interface separating the two phases. When considering the former case, the growth is controlled by diffusion in the parent phase. However, growth could be controlled by a combination of both interfacial and diffusional processes.

Grain growth of a single phase metal is considered as interface controlled growth since it occurs without change in the composition between the product and the parent phases. The surface energy of the grain boundaries is the driving force for the reaction. Boundaries move toward their center of curvature with the rate proportional to the amount of curvature. The overall result of the boundary migration is to reduce the total grain boundary energy through reducing the number of grains per unit area. Grain growth is a thermally activated process depending on time and temperature. The concentration of solute elements and the presence of the second phase particles may affect the migration of the grain boundaries during the growth process.

Hillert [83] has classified grain growth into two types, normal and abnormal growth. Normal or continuous grain growth ends up with grains relatively uniform in size. On the other hand, abnormal or discontinuous growth is characterized by the variation of grain size due to the rapid growth of some grains.

On the other hand, grain coarsening or abnormal grain growth is one of the consequences of the reheating process, and occurs once the transformation is completed. In this case, the thermal energy will activate the boundary migration of large grains toward their center of curvatures and the small ones will be consumed. The overall result of such migration is to reduce the total grain boundary energy through reducing the number of grains per unit volume [83, 84].

In reheating stage of TMP, the control of grain coarsening behavior is an important step to achieve fine grained products. Grain coarsening during reheating in microalloyed steels is characterized by temperature regions of continuous growth at high and low temperatures between which is a narrow temperature range where the abnormal growth of austenite grains occurs and starts to produce a duplex microstructure. Abnormal grain growth occurs at the temperatures which are significantly lower than the microalloying solution temperature. However, the reheating temperature necessary to achieve uniform initial austenite grains varies with the type and amount of MAE, since the abnormal grain growth is controlled by the interaction between the grain boundaries and the precipitated particles [43].

The final ferrite microstructure will be determined based on the nucleation, growth and coarsening events during and after the austenite-ferrite transformation. Microstructural refinement occurs when the nucleation rate, $\acute{N}$, of ferrite during transformation is high while the growth rate, $\dot{G}$, and coarsening rate, $\dot{C}$, are low. Hence, the larger the $\acute{N}/(\dot{G}+\dot{C})$ ratio, the finer will be the D_α produced during transformation process of a given austenite.

2.5 AUSTENITE TO FERRITE (γ/α) TRANSFORMATION

Based on the transformation temperature and cooling rate, the austenite decomposition may occur either through diffusional or shear-dominated, i.e. martensitic, transformation. At a relatively low cooling rate and high transformation temperature, diffusional transformation takes place, where austenite transfers to ferrite or pearlite through the nucleation and growth mechanism. On the other hand, the martensitic transformation takes place at low temperatures and very fast cooling rates where the transformation proceeds through the mechanism of shearing [85].

The final D_α in hot rolled steels is a function of the chemical composition of the austenite, $D\gamma$ prior to transformation and the cooling rate or temperature during transformation [86]. The effects of these variables in the transformation mechanism are discussed in the following sections.

2.5.1 Effect of Austenite Grain Size and Morphology on the γ-α Transformation

As mentioned earlier, refinement of the ferrite grain structure is a direct result of increasing the S_V value prior to the transformation. It has also been shown that the principal nucleation sites of ferrite are the austenite grain boundaries, where the newly formed ferrite grains grow until they impinge on one another. Furthermore, the influence of rolling schedule on the S_V value has also been discussed. This includes reheating temperature, rolling temperature and the amount of deformation.

Kozasu et al.,[2] showed that the nucleation rate increases with increasing the S_V value, where the produced D_α decreases with increasing nucleation rate. Therefore, the controlled rolling processes are applied mainly to increase the nucleation rate of ferrite by increasing the S_V value either by refining the recrystallized austenite grain size or by flattening it to provide a large number of heterogeneous nucleation sites. The effect of recrystallized and deformed austenite on the resulting D_α is given in Figure 2.18. In a similar way, adding of non-metallic inclusions to steel increases the amount of S_V and provides additional nucleation sites to form IGF and refine D_α during transformation.

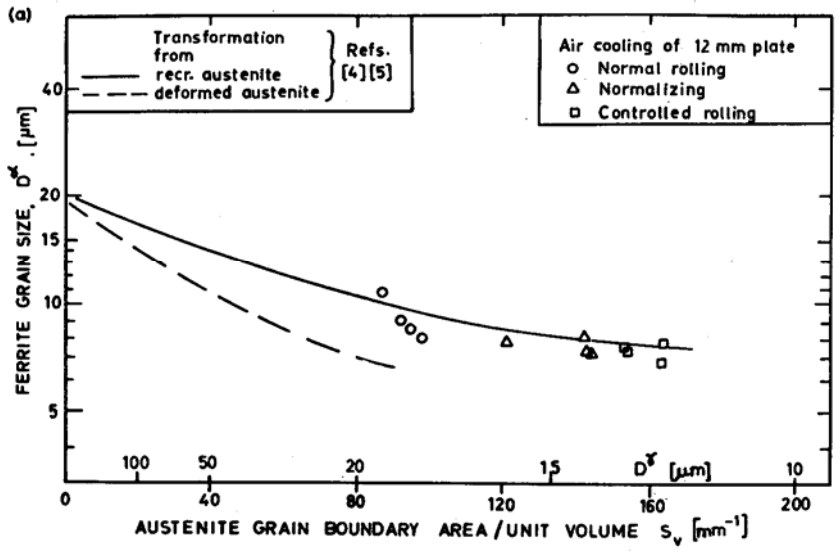

Figure 2.18: Effect of S_V for recrystallized and deformed austenite on ferrite grain size [40,87].

2.5.2 Effect of Cooling Rate on the γ-α Transformation

Dubé et al.,[88] proposed a classification of ferrite morphologies which occur as the austenite-ferrite transformation temperature is lowered. At a very low cooling rate or high transformation temperature, the grain boundary allotriomorphic crystals nucleate at the austenite grain boundaries and grow preferentially along them. Some of these adjacent polygonal ferrite grains with similar orientations coalesce into one grain. As the cooling rate increases, Widmanstätten side plates start to appear. These plates advance into the interior of the austenite grain from the vicinity of its grain boundary. As the cooling rate is further increased, intragranular idiomorphs of equiaxed crystals, in addition to intragranular Widmanstätten plates, could be nucleated within austenite grains. When the super cooling is sufficiently large, i.e., during ACC, acicular ferrite would be formed in addition to the Widmanstätten structure [89,90].

Grain boundary allotriomorphs are the first morphology to appear over the whole range of temperature. The allotriomorphs nucleation has the Kurdjumov-Sachs (K-S) orientation relationship with one austenite grain, which is given as:

$$\langle 111 \rangle_{\gamma} // \langle 011 \rangle_{\alpha}$$

$$[\bar{1}01]_{\gamma} // [\bar{1}1\bar{1}]_{\alpha}$$

When the ferrite is nucleated at the austenite grain boundary, it satisfies one of the available 24 variants of the K-S orientation relationship with one of the adjacent austenite grains. The incoherent α-γ interface with a random orientation relationship grows faster than other boundaries with the K-S relationship.

At lower transformation temperatures, i.e., high cooling rate, the mobility of random α-γ boundaries decreases, while the coherent interfaces with the K-S relationship dominate. In this

case, the refinement of ferrite grains will be achieved through increasing the nucleation events and hindering the growth of existing ferrite. Equivalently, at higher transformation temperatures, the incoherent interface grows due to high diffusivity and the grains become polygonal [85,91].

The effects of the S_V value and the cooling rates are usually interrelated. The relation of $D\gamma$ and cooling rate with the resulting D_α is given in Figure 2.19. During the phase transformation of small $D\gamma$ under slow cooling rates, austenite grains will be decorated with a thin layer of allotriomorphic ferrite, since these boundaries are considered as energetically favorable nucleation sites. This type of ferrite is also known as polygonal or intergranular ferrite. The formation of such ferrite grains will rapidly increase the carbon concentration within the center of the austenite grain, thereby reducing the undercooling and making the subsequent nucleation events more difficult. At some certain point below the eutectoid temperature, depending on the cooling rate, the nucleation of ferrite crystals stop and the remaining untransformed austenite will form other low temperature microconstituents, as shown in Figure 2.20 (a) [92, 93].

In the case of large $D\gamma$ and under slow cooling rates, the rejected carbon from the allotriomorphic ferrites will take time to reach the center of austenite grains. This would provide enough time for nucleation to start on the less favorable intragranular sites. Inclusions and dislocations are considered to be the most suitable heterogeneous nucleation sites to form such intragranular ferrites. The intragranular nucleation of ferrite occurs at lower transformation temperatures than these characteristic of austenite grain boundary nucleation and after nucleation site saturation has occurred at the boundaries [89, 90, 94].

Two types of intragranular ferrites are considered based on the cooling rate. At a low degree of undercooling, equiaxed intragranular ferrite grains nucleate and grow based on the diffusional mechanism. This would be expected in slowly cooled plates and sections. On the other hand,

acicular ferrites will develop under high degrees of undercooling. This would be expected in more rapidly cooled materials such as the coarse grained regions of the fusion zone and heat affected zone of weldments. The plates of acicular ferrite nucleate heterogeneously and grow in different directions and with several orientations within the austenite grain. The acicular ferrites grow based on a shear mechanism, since the diffusion mechanism is limited due to the low transformation temperature and fast cooling rate [92, 95].

At intermediate cooling rates or with coarse Dγ, the growth rate of the allotriomorphic ferrites decrease as they get thicker. This occurs due to increasing the distance over which carbon has to diffuse with time. Accordingly, the normal growth of ferrite may not be able to keep up with the rate of decrease in temperature; therefore, the Widmanstätten plates are developed, as schematically illustrated in Figure 2.20 (b) [92, 93, 96].

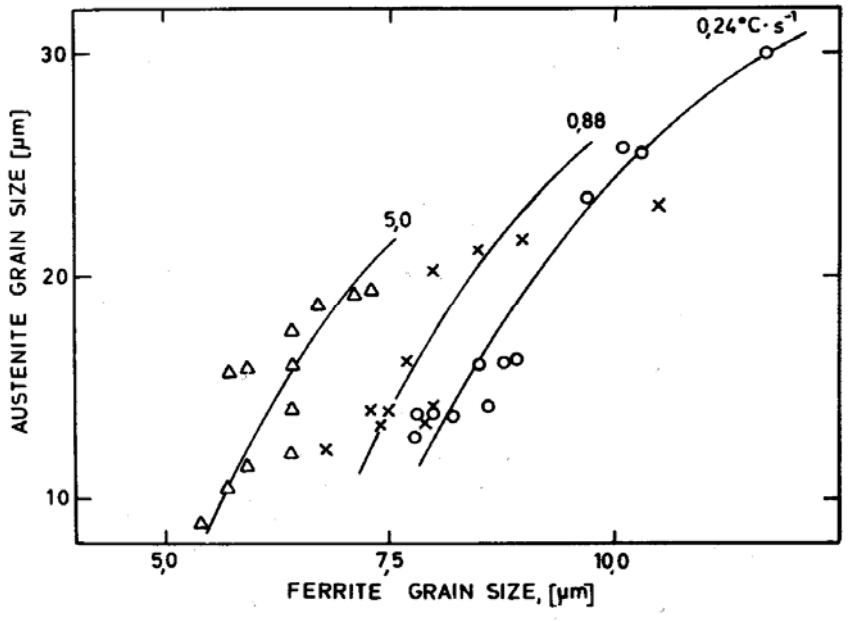

Figure 2.19: Relation between austenite and ferrite grain sizes in microalloyed steels for various cooling rates [97].

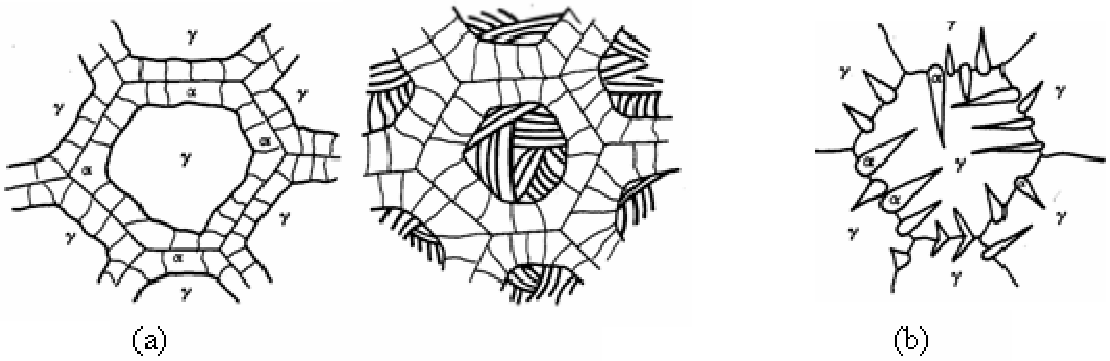

Figure 2.20: Schematic diagram illustrating (a) Nucleation and growth of grain boundary network of α from γ. (b) Widmanstätten growth of α from γ [94].

2.5.3 Effect of Chemical Composition on the γ-α Transformation

The alloying elements can be classified, based on their effects on the equilibrium phase diagram, as austenite or ferrite stabilizers [97]. Those elements that expand the γ loop such as Ni, Mn, C and N stabilize austenite by lowering the Ar_3 temperature and retarding the decomposition of austenite. The other elements such as Si, Al, Ti, V and Nb stabilize ferrite by raising the Ar_3 temperature. On the other hand, these elements also retard the decomposition of austenite by slowing down the diffusivity of carbon in austenite. However, both classes of alloying elements affect the kinetics and the mechanism of the γ/α transformation.

The strong carbide forming elements affect both the transformation kinetics as well as the ferrite microstructure. Among the strong carbide forming elements, MAE such as Ti, V and Nb, have a major influence on the γ/α transformation. This influence is due either to their solubility in austenite or their ability to form stable carbides, nitrides or carbonitrides.

During TMP of microalloyed steels, carbides, nitrides and carbonitrides precipitate in the austenite as the temperature decreases. This precipitation usually takes place on grain boundaries as well as on the subgrain boundaries. These precipitates in austenite control the recovery and recrystallization processes and inhibit the subsequent grain growth. During the γ/α transformation, the MAE precipitates occur predominantly at the γ/α interface and substantially influence the phase transformation kinetics. The MAE precipitates also affect the γ/α transformation by changing the hardenability through solute depletion in austenite [85, 98, 99, 100].

2.6 PARTICLE-STIMULATED NUCLEATION (PSN)

As mentioned earlier, the production of fine D_α from coarse $D\gamma$ in heavy sections required a different approach from the conventional TMP. One of the most effective methods of producing fine D_α out of coarse $D\gamma$ is through the use of PSN which leads to the nucleation of intragranular ferrite inside the austenite matrix. This approach has been studied by several workers [4, 6, 7, 8, 9, 10, 11, 12, 13, 14, 15, 16, 17] who proposed using second phase particles to promote the nucleation of ferrite. The use of non-metallic inclusions as IGF nucleation sites was originally studied to refine D_α from coarse $D\gamma$ in the heat affected zone, HAZ, of weldments [89, 90, 94, 101, 102, 103, 104, 105, 106, 107, 108, 109]. The high density of inclusions present in steel weld deposits ensures a high density of nucleation sites which favors the formation of acicular ferrites during the transformation under high cooling rates. This approach has been also used to nucleate IGF in microalloyed forging steels, where the poor toughness of hot forged microalloyed

products is attributed to their coarse ferrite-pearlite structure, which is caused by forging at high temperatures [12].

The microstructure and mechanical properties of IGF are of interest not only in welded steel, but also for other applications where there is a limitation for the thermomechanical controlled processing (TMCP), and a significant degree of microstructural refinement is needed to optimize strength and toughness. Therefore, the same mechanism could be implemented for the intragranular nucleation of polygonal ferrite in heavy steel sections that are associated with very slow cooling rates during the transformation.

A microstructure in which the ferrite is nucleated at both austenite grain boundaries and intragranular sites tends to be more random. Such a microstructure presents many crystallographic orientations of ferrite per unit volume that could deflect the propagation of cleavage cracks. As a result, toughness could be improved beyond that expected from grain refinement alone [8].

2.6.1 Role of Inclusions in Ferrite Formation

Based on the classical nucleation theory, the primary role of inclusions is to provide heterogeneous nucleation sites for ferrite formation beside those available at the austenite grain boundaries [10, 95]. However, several factors are known to influence the formation of IGF during the phase transformation. These factors include number density of inclusions [90, 94], size [90, 110, 111] and type of inclusions [94, 102, 103], prior austenite grain size [6, 90, 108, 109], hardenability [89, 90] and cooling rate [90].

It is generally believed that increasing inclusion density per unit volume or prior austenite grain size tends to promote the formation of IGF [90, 94]. The degree of inter and intragranular nucleation may change by altering the prior austenite grain size, where the small prior austenite grains may favor the grain boundary reaction, and the intergranular polygonal ferrite will dominate over intragranular ones [8, 13, 14]. Ferrante and Farrar [101] showed that the growth of austenite appears to be controlled by pinning of the grain boundaries by the inclusions. According to Gladman [53], the pinning of austenite grain boundaries could be eliminated and the grain growth would proceeds with increasing the mean size and/or decreasing the volume fraction of the inclusions. According to Ricks et al.[94], coarse inclusions are theoretically expected to be more effective nuclei. This prediction has been confirmed experimentally by several workers [90, 110, 112]. Thewlis et al. [110], showed that inclusions larger than 3μm act as effective nucleation sites for IGF.

Furthermore, if the number density of inclusion is excessively high, the ratio of the intergranular ferrite to the IGF will be increased by two factors. Firstly, the effect of the pinning force on the austenite grain size, and secondly, inclusions located within grain boundaries may promote nucleation at those sites [8, 105].

Considering the type of inclusions, the inclusions that contribute in IGF nucleation usually are not pure phases and have complex multiphase microstructures. Agreement is not complete concerning the identity of the most effective nucleating phase within these inclusions [17]. Some researcher proposed Ti oxides or nitrides to be the most effective nucleation species [17, 103, 104, 106, 107, 108, 109, 113], while others suggested MnS [12, 90, 102, 103] or emphasized the role of aluminum rich inclusions [104, 114] or rare earth metal oxides [104]. Farrar and Harrison [89] indicated that the role of composition on the formation of IGF depends upon the direct

influence the element has on the basic hardenability of steel; therefore, they considered Mn, Si and C among the most effective elements that increase the hardenability and stabilize the austenite.

The major influence of the cooling rate is to determine the degree of supercooling prior to the transformation, which directly affects the thermodynamic driving force for the austenite-ferrite transformation. The transformation temperature decreases as the cooling rates increase and encourage the formation of intragranular acicular ferrite, while at very slow cooling rates, the dominant transformation products would be coarse polygonal ferrite [89]. Moreover, the decrease in transformation temperature caused a change in the morphology of IGF from idiomorphic ferrite to acicular ferrite [113, 115].

2.6.2 IGF Nucleation Mechanisms

Although the mechanism by which inclusions nucleate both acicular and polygonal IGF is yet unclear, there have been four suggested mechanisms for nucleation [15, 17, 116]: 1) Simple heterogeneous nucleation at inclusions; 2) Lattice disregistry or energy effects; 3) Nucleation assisted by volumetric strain; 4) Nucleation assisted by local solute depletion effects.

2.6.2.1 Heterogeneous Nucleation at Inclusions According to the classical theory of heterogeneous nucleation, inclusions are considered to act as internal substrates that reduce the free energy barrier to nucleation [94, 101]. Below the Ar3 temperature, the transformation of austenite to ferrite will proceed at a number of sites depending on the degree of undercooling. At a small degree of undercooling, ferrite nucleates preferentially at the corners and edges of high

angle grain boundaries and grows with the advancement of a planar front where carbon is redistributed [68, 78]. According to Enomoto [14], the temperature of ferrite formation at grain boundaries and intragranular inclusions differs by 20 to 50 °C. The activation energy barriers for ferrite nucleation at various heterogeneous sites have been calculated as shown in Figure 2.21 [110]. It is evident that grain boundary sites have significantly lower free energy barrier to ferrite nucleation than intragranular inclusions. Moreover, large intragranular inclusions are more efficient in nucleating ferrite than small inclusions. Accordingly, ferrite transformation is expected to begin at the austenite grain boundary sites, and as transformation proceeds, intergranular inclusions sites activated.

The efficiency of inclusions as substrates for nucleation has been examined using classical nucleation theory while considering the inclusions to be inert, incoherent and non-deformable [71, 94, 117]. The major findings of this investigation in Figure 2.22 confirm that regardless of the inclusion size, nucleation at inclusion is always energetically less favorable than nucleation at austenite grain boundaries for a given driving force. Hence, after the saturation of the grain boundary surfaces with allotriomorphic ferrite, other nucleation sites such as inclusions become active at greater undercooling [84]. This fact was further explained by Bhadeshia [116] who indicated that the large spherical non-metallic inclusions are more effective for heterogeneous nucleation than the smaller ones, where the newly formed embryo will have smaller curvature at the surface of large inclusions. Therefore, the flat surface of austenite grains is expected to be a more potent heterogeneous nucleation site than a large spherical inclusion. Moreover, the interfacial energy between the ferrite and the inclusion is likely to be larger than the one between the ferrite and the austenite grain surface.

The simple heterogeneous mechanism of nucleation is seems to be not sufficient for the promotion of IGF since many large inclusions do not induced the nucleation, therefore, other factors are additionally required [115].

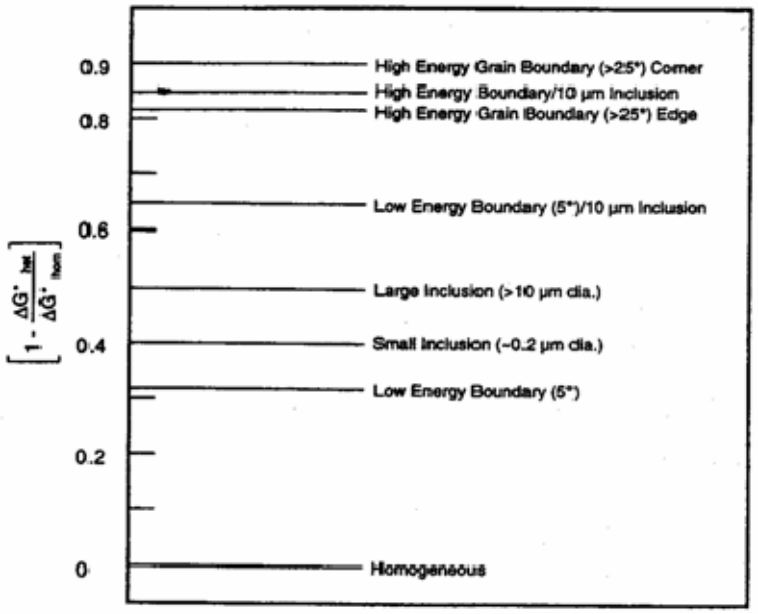

Figure 2.21: Normalized activation energy barriers for nucleation (1 - $\Delta G^*_{het}/\Delta G^*_{hom}$) at various heterogeneous sites [110].

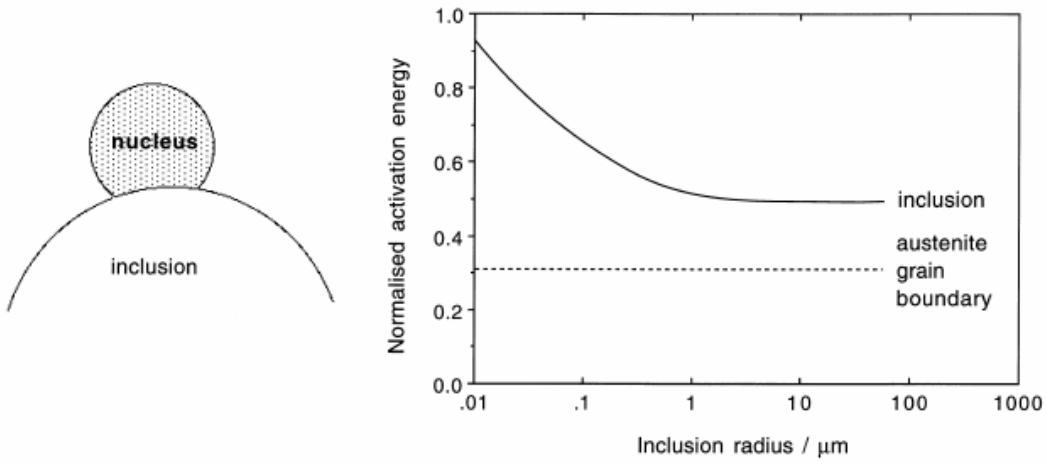

Figure 2.22: Variation of activation energy for nucleation ΔG* normalized with respect to activation energy of heterogeneous nucleation ΔG^*_h, as a function of inclusion radius I. The γ/γ interfacial energy was assumed to be similar to γ/α interfacial energy, i.e., the inclusion/α and inclusion/γ interfacial energies are identical [94, 116].

2.6.2.2 Lattice Disregistry Since IGF transformation is nucleation at the γ/inclusion interphase boundary, Furuhara et al.[118], indicated that the energy balance of the α/inclusion/γ interphase boundaries affects greatly the nucleation kinetics of IGF. This approach to explaining enhancement of IGF nucleation by second phase particles is often traced back to the work of Bramfitt [119], who concluded that the controlling factor in nucleation was interfacial free energy at the nucleating interface.

The lattice disregistry approach has been proposed by several workers [9, 10, 13, 103, 120]. In this approach the IGF is assumed to nucleate on the inclusion which has the best lattice match with ferrite [14, 95] and easily produces an epitaxial growth of the phase on the nucleating particle. Mills et al.[103] and Ishikawa et al.[9, 10] showed that a low lattice misfit of the inclusion surface layers with ferrite coupled with closely spaced inclusions would seem to be key

factors of IGF nucleation. In addition to the lattice disregistry, Mills et al.[103] mentioned the importance of inclusion volume fraction and size distribution in the development of a large volume fraction of IGF. Table 2-2 shows their calculated values of misfit between ferrite matrix and several inclusions. However, most of these values are considered to be high and not typical for coherency, which is closer to 0.5% misfit.

Table 2-2: Misfit values between different substrates and ferrite [103].

Inclusion	Lattice Parameter (Å)	Plane of Epitaxy $\{hkl\}_{\alpha}//\{hkl\}_{Inclusion}$	Misfit (%)
TiO	4.18	{100}//{100}	3.0
γ-Al_2O_3	7.85	{100}//{100}	3.2
Al_2O_3 MnO (Galaxite)	8.27	{100}//{100}	1.8
TiN	4.24	{100}//{100}	4.6
BN	3.62	{111}//{110}	6.5
CuS	5.57	{111}//{111}	2.8
MnS	5.23	{111}//{111}	8.8

Furuhara et al. [121] and Madariaga and Gutierrez [112] indicated that the energy barrier for nucleation at inclusions is a function of the difference between inclusion/γ and inclusion/α interfacial energies assuming the differences in the interfacial energy associated with the relative lattice matching between the involved phases. The improvement in the energetic balance of the nucleation at inclusions that is resulted from replacing high energy inclusion/γ interface with low energy inclusion/α interface can favor IGF nucleation at inclusions, as shown in Figure 2.23 Based on the misfit theory, the change in the interfacial energy and the driving force for ferrite nucleation from different inclusions were calculated and shown in Figure 2.24 [6].

Although the allotriomorphs ferrite has the K-S orientation relationship with one austenite grain, it has been revealed, by electron backscatters diffraction pattern (EBSP) analysis, that there is no specific orientation relationship between the IGF and the austenite matrix [119].

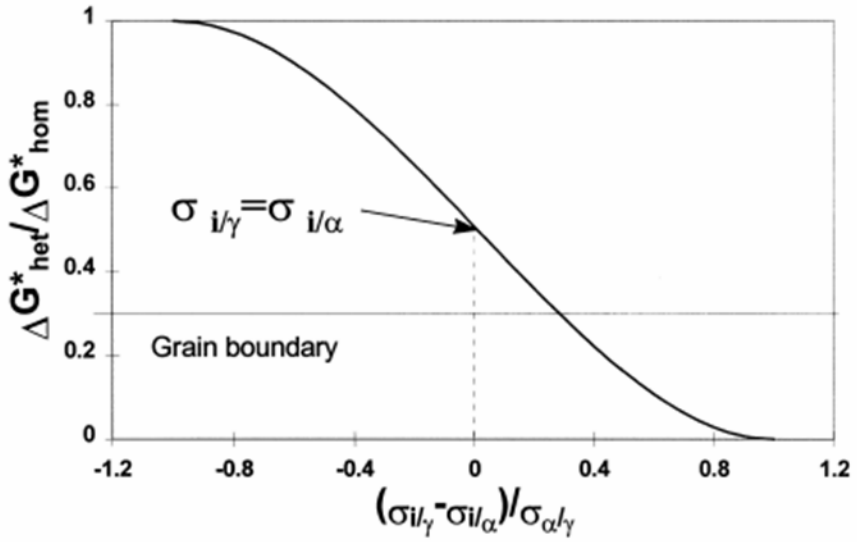

Figure 2.23: Energy barrier with heterogeneous nucleation as a function of the deference between austenite/inclusion and ferrite/inclusion interfacial energy per unit area of interface [112].

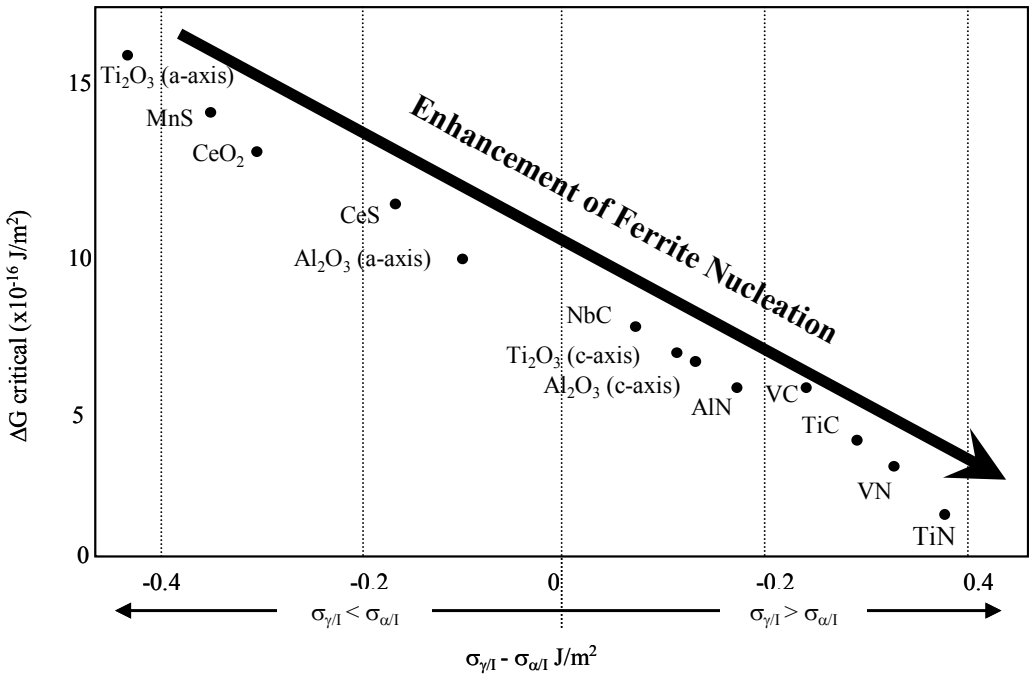

Figure 2.24: Change in interfacial energy and driving force for ferrite nucleation from various inclusions. Where $\sigma_{\gamma/I}$ = interfacial energy between γ and inclusion, and $\sigma_{\alpha/I}$ = interfacial energy between α and inclusion [6].

In contrary, it has been concluded by several workers [94, 102, 122] that interfacial energy due to lattice disregistry is not significant in IGF nucleation. This conclusion is based on several observations. Firstly, several others considered MnS [14, 123, 124], TiO [103, 111] and Ti_2O_3 [14, 115, 125, 126] as effective ferrite nucleation sites, while TiN [115, 127] is less effective, yet the planar disregistries are 8.8%, 3.0%, 26.8% and 4.6%, respectively. Moreover, as shown in Table 2-2, there are some other particles like galaxite and γ-Al_2O_3 have good lattice matching but are considering as inert inclusions [128]. Secondly, the perfect lattice orientation between IGF and inclusions could not be detected experimentally in several cases [102, 118, 121]. Finally, the inclusions, which usually form in liquid steel, are randomly oriented but the IGF usually exhibits

the K-S orientation relationship with prior austenite so it results that the inclusion/ferrite orientation relation must be random, Figure 2.25 [116]. In contrast, Grong et al.[120] showed that the δ-ferrite nucleate on the inclusion in the melt and during the transformation via the austenite, the acicular ferrite then could have an orientation relationship with inclusions.

The former mechanism appears to be inadequate to explain the IGF nucleation on inclusions since some particles with good lattice register do not nucleate IGF effectively, therefore, other factors or mechanisms are additionally required.

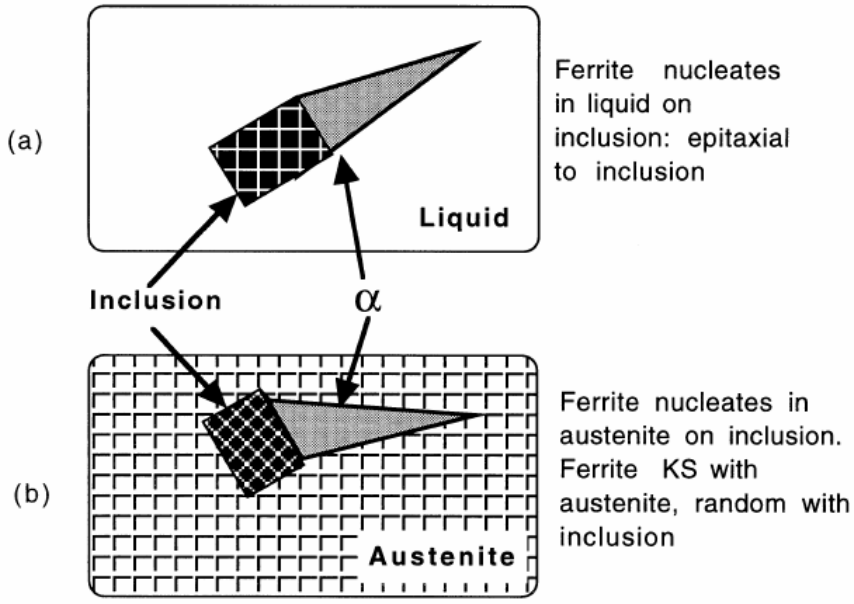

Figure 2.25: Illustration of the orientation relationship that might develop between acicular ferrite an inclusion. (a) When δ-ferrite nucleates on an inclusion in the melt; ferrite could adopt a favored orientation relationship. (b) The inclusion, which grows from liquid, is randomly oriented to the austenite. The acicular ferrite, which has fixed K-S relation with the austenite, must therefore be randomly oriented to the inclusion [116].

2.6.2.3 Nucleation Assisted by Volumetric Strain It has been proposed by several workers [9, 89, 90, 95, 102, 103, 106, 112, 121] that inclusions can develop large thermally induced stresses due to the differences in the thermal expansion coefficients compared with matrix. The presence of these stress-strain fields can then provide favorable sites for acicular ferrite nucleation. Liu and Olson [129] have reported that the strain energy contribution to the total free energy of austenite decomposition due to the differential thermal contraction effect is insignificant when compared with the austenite to ferrite transformation volume free energy. Abson [130] also proposed that the matrix straining is not the determining mechanism. Furthermore, in the case of slow cooling rates, the effect of volumetric strain will be negligible. In addition, this theory will not be able to explain the potency of Ti-oxide in nucleating the IGF while it has an expansion coefficient closer to austenite [17].

2.6.2.4 Local Solute Depletion Effects Solute depletion in the matrix around inclusions is considered as a possible factor that could assist the IGF nucleation. Many authors [115, 123, 125, 126, 131] assumed the Mn depletion zone (MDZ) around the inclusions as a most active nucleation site of IGF in the austenite matrix.

Generally, there are two different views to explain the formation of MDZ around Ti-O. The first one is that MDZ is formed by the precipitation of MnS at Ti-O particle within austenite grains at high temperature, where MnS acts as a direct nucleation site for IGF [123, 125]. The second view is that Ti-oxide itself absorbs neighboring Mn atoms from the matrix, thus the MDZ being formed around it [128].

Tomita et al.[126] studied the effect of TiN on steels and claimed that the formation of a MDZ around TiN-MnS particles was an essential part of the mechanism of IGF nucleation. The

size of the MDZ is estimated at 0.35 - 3.5 μm. On the other hand, Yamamoto et al. [122, 125] have proposed that nucleation of acicular ferrite is enhanced on Ti_2O_3 because MnS and TiN precipitation on the surface. Precipitation of MnS forms MDZ at the Ti_2O_3/γ interface, which increases chemical free energy changes for ferrite nucleation, while precipitation of TiN decreases interfacial energy for ferrite nucleation. It was calculated that the Mn depletion would be between 0.02 to 0.2 wt% Mn less than the bulk composition in the region of 0.1 μm depth. Experimentally, Byun et al. [15] showed that Mn depletion ranged from 0.4 to 1.0 wt% in the MDZ in a region of 0.25 μm. In contrast, by using electronic probe microanalyzer (EPMA), Lee and Pan [106] indicated that the examination across inclusions did not revealed any MDZ.

In conclusion, despite various experimental investigations of different types of inclusions, there has been virtually no conclusive experimental confirmation of such a manganese depleted layer near nucleating particles in weld metals [90], or in plate steels [106].

While it is clear that the key role of inclusions is to provide heterogeneous nucleation sites for ferrite nucleation, the detailed mechanisms of inclusion remain unclear. However, based on the previous discussion it seems that the most likely mechanism that appears to promote the intragranular nucleation of ferrite depends on simple heterogeneous mechanism. While, the lattice disregistry seems to achieve the energy balance of the α/inclusion/γ interphase.

2.6.3 Decomposition of Austenite

During the decomposition of austenite under a slow cooling rate, the first ferrite grain often form as coarse proeutectoid ferrite at the prior austenite grain boundaries, α-GB. As transformation proceeds and site saturation occurs, fine intragranular ferrite may be nucleated at suitable

intragranular sites [7, 110]. DeArdo, et al.[7] have identified the intragranular nucleation of ferrite to take place at three different locations. One of these locations is known as α-I where the ferrite nucleates directly on the inclusion, while the other two locations are on the new existing γ/α boundaries. One of these latter locations is known as α/α-GB or type A site and the other type is known as α/α-I or type B site. In the A site the new ferrite grain nucleates at the interface of the ferrite grain that had previously nucleated at the austenite grain boundary, γ/γ GB. On the other hand, in the B site, the new ferrite grain nucleates at the interface of the ferrite that had formed at the inclusion surface, α-I. For simplicity, these nucleation sites are schematically illustrated in Figure 2.26.

With further cooling, the nucleation of ferrite at the γ/α boundaries and inclusions, γ/I, occurs simultaneously. In this case, the surface of inclusions become an active nucleation site for ferrite grains after the saturation of the prior austenite grain boundaries with α-GB ferrite [7, 10, 11, 12, 95]. It has been considered that the interface energy of γ/α and γ/I sites is of the same order of magnitude [132, 133].

Lee and Pan [108, 134] have shown that the minimum austenite grain size of approximately 50μm is required for the IGF formation. DeArdo et al.,[7] have confirmed this result suggesting that the minimum austenite grain size required is about 100 μm. Moreover, DeArdo et al., [7] showed that in the coarse Dγ (about 300 μm), with an insufficient number of inclusions, the newly formed γ/α interfaces (sites A and B) can be the dominant sites for further phase transformation.

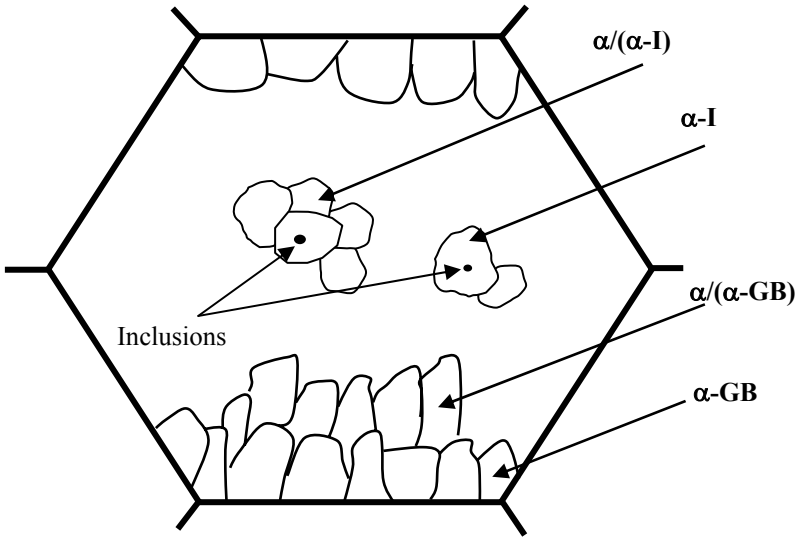

Figure 2.26: Schematic diagram of the γ-α transformation with particle-stimulated nucleation [7].

2.6.4 Theoretical Prediction of D_α

As discussed previously, the final D_α is directly related to the $D\gamma$ and morphology prior to the transformation which in turn is related to the chemical composition and rolling schedule. There have been a number of approaches developed by several workers [135, 136, 137, 138] to predict the D_α in hot rolled steels. In addition to the prior austenite grain size (D_γ) and cooling rate ($\dot{T}$), the retained strain in the austenite prior to transformation (ε_r) is considered to predict the ferrite grain size. The retained strain is the amount of strain accumulated below the recrystallization stop temperature. Therefore, in the recrystallization controlled rolling the ε_r value is considered as zero. Sellars [136] and Saito [135] have proposed the most realistic relations where both

equations give similar results up to 130 μm of prior austenite, Figure 2.27. The Saito's [135] equation is given as:

$$\ln D_{\alpha} = 0.92 + 0.44 \ln D_{\gamma} - 0.17 \ln \dot{T} - 0.88 \tanh(10\varepsilon_r) \tag{2-27}$$

And the Sellers and Beynon [136] equation is given as:

$$D_{\alpha} = (2.5 + 3.0\dot{T}^{-0.5} + 20(1 - \exp(-0.015 D_{\gamma}) - 0.1)(1 - 0.45\varepsilon_r^{0.5}) \tag{2-28}$$

Tamura et al.,[85] were tried to predict the ferrite grain size during the continuous cooling based on the S_V value, nucleation and growth rates. Beside the complication in calculating the nucleation and growth rates, no simple relationship was found to link ferrite grain size with the S_V value [86].

These equations consider only the formation of polygonal or intergranular ferrite that nucleates at the austenite grain boundaries. Jones and Bhadeshia [8] developed a model that considers the competitive growth of ferrite nucleated both at austenite grain boundaries and intragranularly on inclusions. This model depends mainly on the calculation of both nucleation and growth rate during the transformation. In the same area of interest, Gao, et al.,[139] have developed and equation that considering the effect the intragranular inclusions in the final ferrite grain size. This relation is based on the Saito empirical equation and given as:

$$D_{\alpha} = \left(1 / D_{\alpha 0}^{2} + \beta \cdot V_f / D_P^{2}\right)^{-1/2} \tag{2-29}$$

where $D_{\alpha o}$ is the mean ferrite grain size based on the Saito equation, D_p is the mean particles size, β is the number of ferrite grains that could be nucleated from one inclusion and V_f is the volume fraction of particles. The derivation of this equation is shown in details in Appendix A.

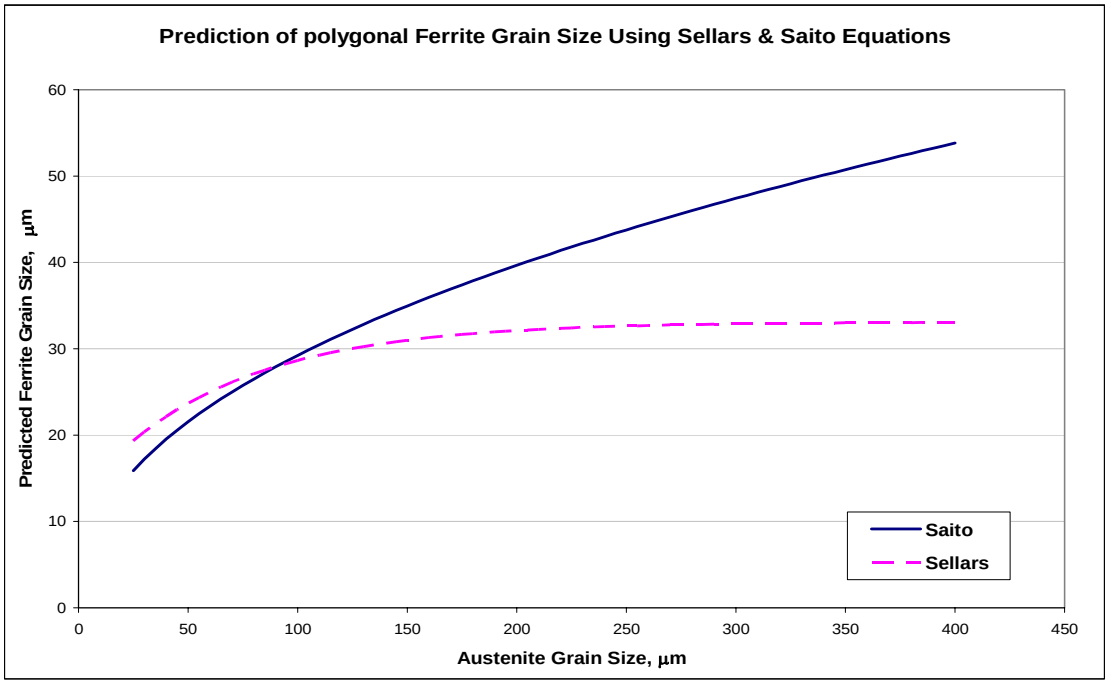

Figure 2.27: Prediction of the ferrite grain size based in the Saito and Sellars equations where the cooling rate was selected as 0.08 °C/sec.

2.6.5 Effect of the S_V Value on the IGF Nucleation

Lee's [105] approach for the evaluation of nucleation potential of IGF is considered in this study. It is assumed that the intragranular inclusions are effective nucleation sites for IGF, while the polygonal ferrite nucleates at grain boundaries. The relationship among the volume fraction of IGF (V_{IGF}), the volume fraction of grain boundary nucleating ferrite (V_{GB}), the available surface area of intragranular inclusions (S_{VI}), and the total available surface area of grain boundaries (S_{VGB}) is written as [105]:

$$\frac{V_{IGF}}{V_{GB}} = \frac{E_I}{E_B} \cdot \frac{S_I}{S_B} = P \cdot \frac{S_I}{S_B} \qquad (2\text{-}30)$$

where E_I and E_B are the nucleation effectiveness of intragranular inclusions and boundary surfaces, respectively, and P is relative nucleation potential of intragranular to grain boundary nucleation.

The total grain boundary surface area (S_{VGB}) available for nucleation in unit volume is a summation of grain boundary surface (S^B_B) and surfaces of inclusions which are located at grain boundaries (S^I_B), which written as [105]:

$$S_{VGB} = S_B^I + S_B^B \tag{2-31}$$

The (S^B_B) value is a parameter which indicates the density of nucleation sites on the grain boundary and is given as [105]:

$$S_B^B = \frac{2}{D_\gamma} \tag{2-32}$$

The (S^I_B) value depends on the geometric relation between the inclusion and the grain boundaries, and considers as [105]:

$$S_B^I = \frac{\pi D_I{}^2 N_V^B}{2} \tag{2-33}$$

where N^B_V is the number of grain boundary inclusions in a unit volume. Usually up to 20% of inclusions could be trapped by grain boundaries for austenite grain sizes ranging from 100 to 180 μm [105, 106, 109]. However, only intragranular inclusions (N^I_V) contribute to the formation of IGF, and are given by [105]:

$$N_V^I = N_V - N_V^B \tag{2-34}$$

where N_V is the total number of inclusions per unit volume.

The available surface area for intragranular nucleation (S_{VI}) is determined by number, size and shape of intragranular inclusions. Assuming a spherical shape of inclusions, the (S_{VI}) is determined as a function of (N^I_V) and inclusion mean size (D_I), and written as [105]:

$$S_{VI} = \pi N_V^I D_I^2 \tag{2-35}$$

The total available nucleation area per unit volume (S_V) for both inter granular and intragranular ferrite is given by [105, 140]:

$$S_V = S_{VI} + S_{VGB} \tag{2-36}$$

Capdevila et al., [140] have shown that the ratio of (S_{VI}/ S_{VGB}) increases with increasing the prior austenite grain size. Therefore, the potential of the IGF nucleation sites become more important as the austenite grain size increases.

3.0 STATEMENT OF OBJECTIVES

The broad aim of this study is to investigate the feasibility of refining the ferrite microstructure in heavy steel sections using the particle-stimulated nucleation, PSN, mechanism to enhance the nucleation of the intragranular ferrite, IGF.

The achievement of the stated goal was proposed to be studied through five separated stages concerning the IGF nucleation. The first stage was to investigate the effect of the TMP on a typical commercial heavy section steel, A572 grade 50, and to provide an understanding of the austenite grain size behavior prior to transformation under different deformation schedules.

The second stage was to investigate the effect of the non-metallic inclusions, specifically MnS and TiO, on refining the ferrite microstructure under very slow cooling rates. The effect of the grain refinement on the strength and toughness was planned to be investigated.

The third stage of this research was aimed to study the effect of size and volume fraction of different types of inclusions in the formation of IGF. This part of the research was expected to yield information regarding the effective size and chemistry of inclusions.

Since the mechanism by which inclusions nucleate IGF is as yet unclear, the fourth stage of this study was designed to investigate the real mechanism of this type of ferrite nucleation.

Based on the allotriomorphic and idiomorphic nucleation rates, the final stage of this research was planned to develop a mathematical relationship which would describe the effect of PSN on the ferrite grain size.

4.0 EXPERIMENTAL PROCEDURE

4.1 MATERIALS SELECTION

A typical ASTM A572 grade 50 steel (Jumbo steel) was selected to be the reference material in this investigation since it is on of the most used structural steel grade today. The Jumbo steel samples were prepared from a commercial continuous casting slab.

Based on the chemical composition of the Jumbo steel, two different steels were designed to have high volume fraction of two particular types of inclusions; MnS and Ti-oxides. Both types of inclusions have been reported as being highly effective sites for intragranular ferrite, IGF, nucleation [14, 103, 115, 122, 123, 124, 125, 126]. The laboratory TiO and MnS steels ingots were designed to verify the effect of particle-stimulated nucleation, PSN, on the nucleation of IGF. The chemical compositions of these three steels are listed in Table 4-1.

Due to their high affinity to oxygen, both Al and Si contents in the TiO steel were designed to be as low as possible to allow oxygen–titanium reaction to form sufficient amount of Ti-oxide inclusions. On the other hand, the sulfur content in the Jumbo steel is hypostoichiometric, therefore, adding more sulfur increased the volume fraction of the MnS particles in the MnS steel. The sulfur content in the MnS steel was increased ten times over the Jumbo steel to assure high volume fraction of MnS inclusions.

Table 4-1: Chemical composition of the Jumbo, TiO and MnS steels.

Steel	Elements (wt %)											
	C	Si	Mn	P	S	Al	Cu	N	O	Nb	Ti	V
Jumbo	0.08	0.3	1.42	0.008	0.003	0.034	0.31	0.005	-	0.003	0.003	0.132
TiO	0.095	0.03	1.22	0.008	0.003	0.003	0.28	0.004	0.022	-	0.02	0.14
MnS	0.086	0.32	1.57	0.008	0.037	0.028	0.27	0.005	0.002	-	-	0.137

4.2 EXPERIMENTAL APPROACH

The main stated objectives of this work were to be achieved through the following studies.

4.2.1 Grain Coarsening Studies

In order to ascertain the grain coarsening behavior of austenite as a function of temperature, isothermal reheating studies were conducted on steel samples cut from as-cast ingots. Prior to each austenitizing treatment, specimens were encapsulated in evacuated quartz tubes back-filled with dry argon (99.9% purity) to minimize any oxidation effects.

Samples of 12 x 12 x 6 mm were heated and held for 60 minutes at temperatures starting from 900 ºC and ending at 1300 ºC at increments of 100 ºC. Then the samples were water quenched in an ice brine bath to retain the austenite grain size formed at those temperatures. As

illustrated in the reheating schedule in Figure 4.1, samples were subjected to a slow heating rate of 5ºC/min within the austenite range to allow diffusion of the dissolved elements and to simulate as closely as possible the reheating schedule used in industry.

Following the heat treatments, specimens were longitudinally cut in half and then tempered at 500°C for 24 hours or more to help reveal the austenite grain boundaries when etching with picric acid. Following tempering, specimens were prepared for metallographic analysis using optical microscopy to determine the grain coarsening temperature (T_{GC}) by analyzing the D_{γ} and morphology of the austenite grain boundaries from each temperature. The reheating temperature for further heat treatment of each type of steels was determined based on the results of grain coarsening study.

All austenitizing and tempering treatments were accomplished in a Lindberg/Blue M box furnace that is equipped with a type (R) thermocouple. The temperature accuracy was cross checked by using an external thermocouple positioned close to the samples. The approximate accuracy of the thermocouples was ± 2 °C with applying slow heating rates.

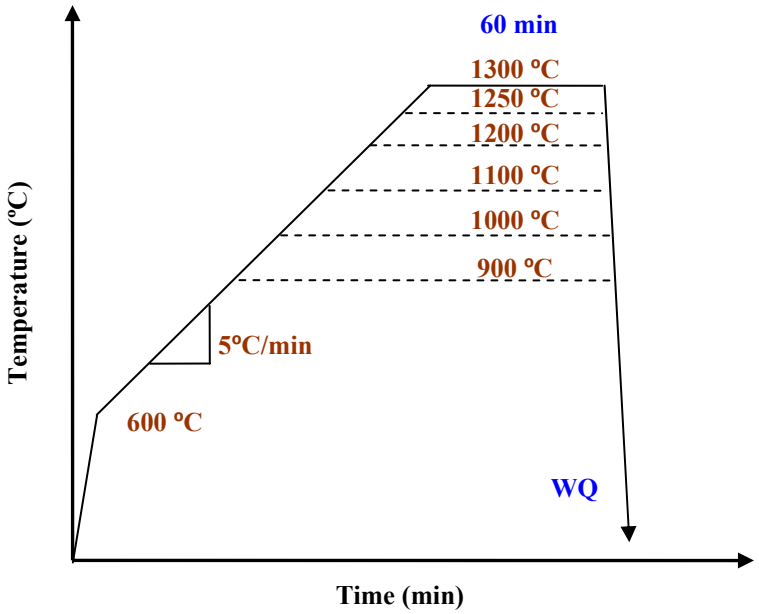

Figure 4.1: Heat treatment schedule to obtain T_{GC}.

4.2.2 TMP Studies

A TMP schedule was selected to simulate as close as possible the industrial hot rolling practice for heavy steel sections. This study was applied only for the Jumbo steel to investigate the effect of the deformation parameters on the behavior of austenite and subsequent transformation. Accordingly, the austenite grain size prior to the phase transformation was determined for different deformation schedules to study the effect of deformation temperatures and cooling rates on the grain size and, hence, on the ferrite nucleation behavior.

4.2.2.1 MTS Hot Compression Testing System The deformation tests were conducted using computer controlled MTS-458 hot compression testing system shown in Figure 4.2. The MTS machine is equipped with a radiation furnace with 12 Sylvania 1200 W halogen quartz infrared bulbs. The capabilities of the furnace are 1250°C maximum reheating temperature.

4.2.2.2 MTS Sample Preparation The compression tests were applied on cylindrical samples 19.1 mm in height and 12.7 mm in diameter. In order to monitor the specimen temperature during the deformation sequence and cooling path, a hole of 1.6 mm in diameter and depth of approximately 5.0 mm was drilled into each cylinder at mid-height. The compression specimen is shown in Figure 4.3. This is known as modified Rastegave's [141] design where an additional modification was made to the geometry of the cylinders to retard the barreling effects through retaining lubricants during deformation to minimize die-specimen friction effects.

Initially, specimens were encapsulated in evacuated quartz tubes and austenitized in a box furnace at 1250 ºC for 1 hour then water quenched in an ice brine bath to retain the composition and grain size of austenite at that temperature. This initial reheating stage was applied to allow the majority of reheating to occur in the box furnace in order to extend the life of the radiation furnace of the MTS machine. In the second reheating stage, specimens were again reheated to 1250ºC in the MTS machine and held for 2 minutes prior to starting the deformation schedules. This technique has been used extensively in previous studies giving an excellent correspondence between the austenite grain size and distribution resulting from the reheating in the box furnace and the MTS reheating step.

Prior to the reheating in the open air radiation furnace, the as-quenched specimens were nickel-coated to prevent further oxidation. The nickel coating procedure to prevent oxidation

consisted of cleaning the specimens of any surface contamination and immersing them in an acid solution containing 20g of nickel sulfate, 27g of sodium hypophosphite and 16g of sodium succinate in one liter of distilled water. A thin layer (10 μm) of nickel was deposited uniformly over the surface of the specimens after soaking in this solution for 1 hour at 98°C [142].

Figure 4.2: MTS hot compression system at BAMPRI labs in the University of Pittsburgh.

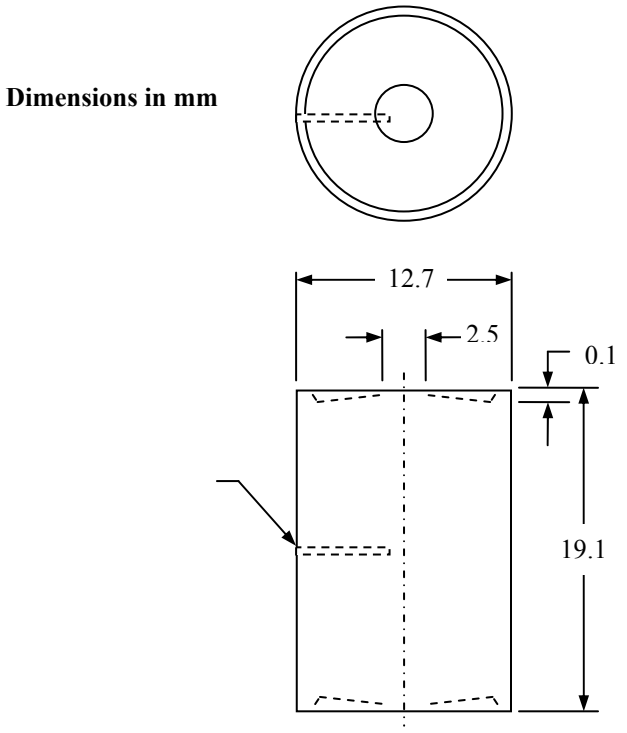

Figure 4.3: Compression specimen geometry [141].

4.2.2.3 TMP Simulation The time-temperature schematic diagram shown in Figure 4.4 illustrates a deformation series of 16 passes starting at 1225 ºC and finishing at three different temperatures (1200, 1100 and 880 ºC). All temperatures were selected to be in the fully recrystallized region of austenite. Furthermore, the highest temperature was selected to be above the grain coarsening temperature of the Jumbo steel. The deformations were conducted under constant strain rate (έ) of 10 sec-1, where the true strain (ε) per pass is 0.05 and the interpass time is 55 second.

In order to study the effect of deformation temperature on the austenite grain size and to monitor the subsequent grain growth during the cooling process, one set of samples was water quenched just after the deformation. Additionally, to study the effect of cooling rates on the austenite grain size behavior prior to the transformation, another set of deformed samples were cooled to the transformation temperature at fast and slow (controlled) cooling rates and then water quenched. The fast cooling rate was selected to be 1.4 ºC/sec, while in the controlled cooling the samples were cooled initially to 800 ºC at a rate of 0.24 ºC/sec and subsequently cooled through the transformation temperature at a rate of 0.08 ºC/sec. A third set of deformed samples was cooled down to room temperature with the controlled cooling rate to measure the final ferrite grain size. This technique allows following the nucleation and growth of ferrite microstructure using different TMP schedules. Following the TMP, samples were prepared for metallographic analysis using optical microscopy to determine the prior austenite grain size at each specific case.

The phase transformation temperature (A_{r3}) of the deformed Jumbo was geometrically derived from the time-temperature curves that were recorded during the cooling process after deformation schedules in the MTS machine. Changes in the microstructure due to the phase transformation were revealed as variations in the slope of the curve. The time-temperature curve for Jumbo steel cooled through the austenite to ferrite transformation after deformation is shown in Figure 4.5.

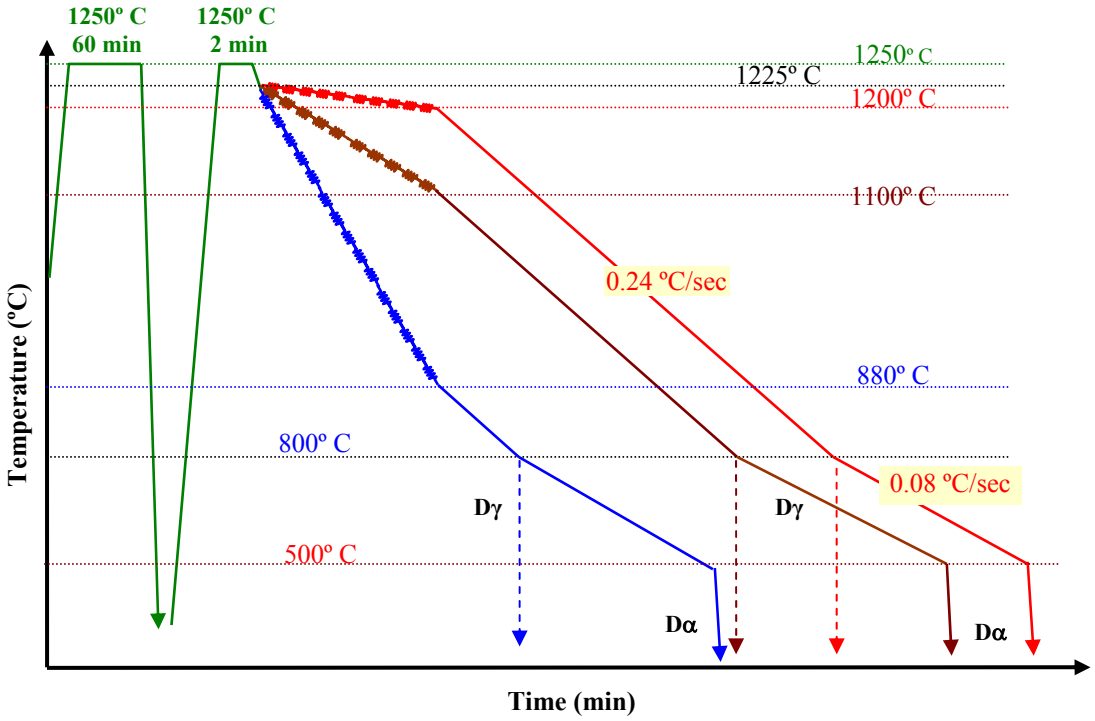

Figure 4.4: Time-temperature schedule diagram of TMP.

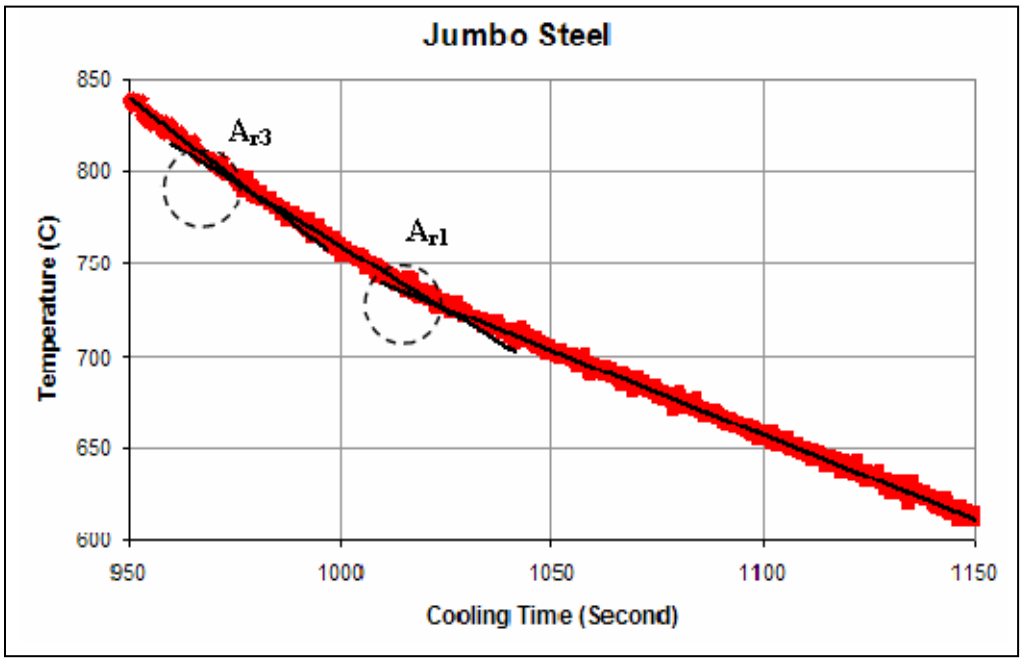

Figure 4.5: Time-temperature cooling curve for deformed Jumbo samples showing the phase transformation temperatures. The Ar_3 for this sample = 780°C and the Ar_1 = 720 °C.

4.2.3 Thermal Processing Studies

The thermal processing or heat treatment study was preformed to compare the evolution of austenite and ferrite microstructures in both TMP deformed and non-deformed materials. Unlike the TMP, the thermal processing schedules, Figure 4.6, were considered to focus the study on the IGF nucleation behavior and to eliminate all other variables related to the deformation schedule.

Specimens were initially encapsulated in evacuated quartz tubes and austenitized in a box furnace at pre selected temperatures for 1 hour then water quenched to retain the composition and grain size of austenite at those temperatures. The reheating temperature for each steel was selected based on the results of the grain coarsening study. Prior to the second reheating, the as-quenched samples were nickel-coated to prevent further oxidation. In the second reheating stage, specimens were held for 2 minutes prior to starting the cooling schedules. Due to the limitation of the radiation furnace of the MTS machine, the reheating processes were accomplished in a box furnace from which the samples transferred immediately to the radiation furnace for the subsequent controlled cooling process.

During the slow cooling procedure, samples were water quenched at different temperatures starting from 800 ºC and ending at 500 ºC at 10 ºC intervals within this range. These temperatures were selected to reveal the nucleation and growth of the allotropic and idiomorphic ferrite. The quenched specimens were longitudinally cut in half and metallographically prepared for further analysis. Furthermore, a sample of each type of steel was cooled down to room temperature to measure the final ferrite grain size and to evaluate the refining of the ferrite microstructure using the PSN technique.

The phase transformation temperatures of the three steels, with the controlled cooling rate, were determined experimentally using the Theta Dilatronic II dilatometer. Cylindrical samples 30.0 mm in length and 3.0 mm in diameter were used in this investigation. These samples were heat treated before machining in order to minimize the experimental time in the dilatometer. The experiments were preformed in an inert environment of dry argon to minimize any oxidation effects. The results were evaluated theoretically using the materials property simulation package, JMatPro-3.0 software.

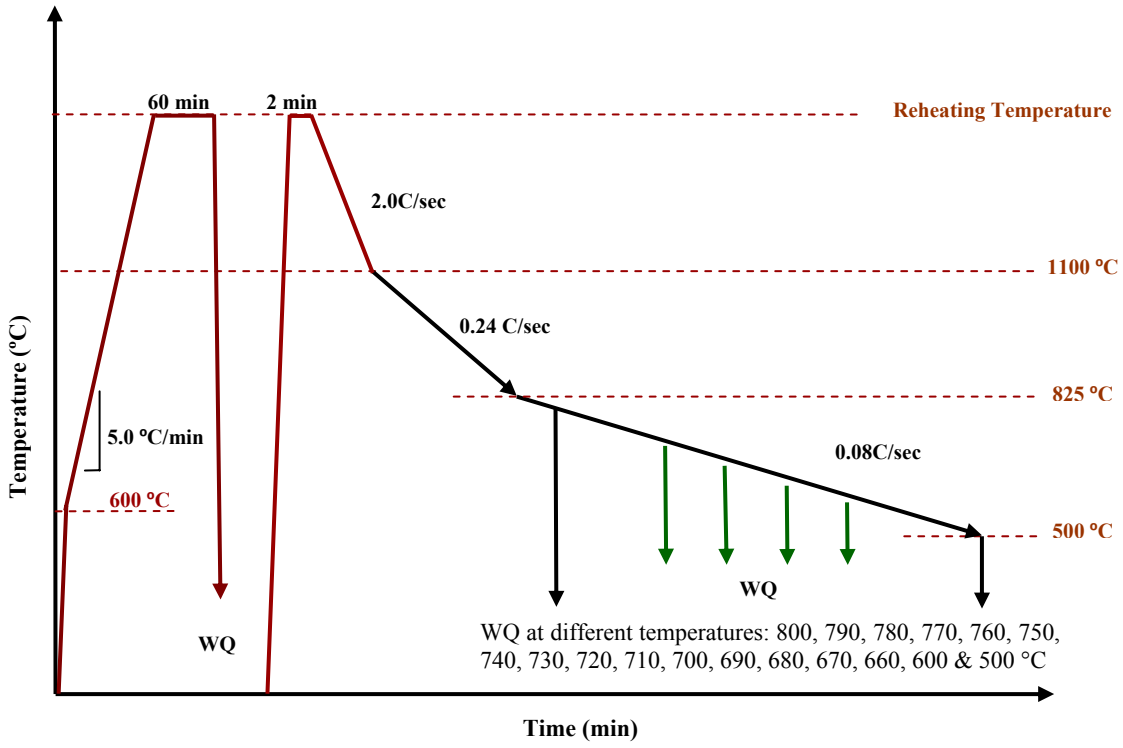

Figure 4.6: Time-temperature schedule diagram of thermal processing.

4.3 MICROSTRUCTURAL ANALYSIS

Several types of metallographic techniques, including optical microscopy, scanning electron microscopy (SEM) and scanning transmission electron microscopy (STEM) were used in this study.

4.3.1 Optical Microscopy

Optical metallogaphy samples in this study were prepared using standard techniques by grinding on 180, 240, 320, 400 and 600 grit silicon carbide papers in this order, and then polishing with 1.0μm and 0.05μm alumina. Two different etching procedures were used to reveal the ferrite-pearlite and prior austenite microstructures.

The ferrite-pearlite microstructure of the heat treated samples was revealed using a 2% nital etching solution at room temperature for 10-15 seconds.

Etching of the as-quenched specimens from the TMP and grain coarsening studies to reveal the prior austenite grain boundaries was relatively more difficult. The etching technique in this study started with tempering the quenched specimens at 500°C for 24 hours in evacuated quartz tubes filled with argon. This tempering process allows phosphorus in solution to segregate towards the prior austenite grain boundaries and aid the optical metallographic techniques by revealing sharp and clear austenite grain boundaries when etching with picric acid [143].It has been shown experimentally (Appendix B) that the image quality of the grain boundaries' details improves with increasing tempering time.

The prior austenite grain boundaries were revealed by a special reagent consisting of 100 ml of saturated aqueous picric acid, in addition to 1 ml of HCl and 10g of dodecylbenzene sodium

sulfonate as a wetting agent. Specimens were immersed into this solution at 80°C where the surface of the specimen was swabbed to maintain fresh etchant over it. Depending on the composition of the material and the solution temperature, the etching cycle ranged between 30 and 90 seconds. However, several polishing and etching cycles were required to achieve optimum results.

The austenite and ferrite grain sizes were measured using a computer controlled Bioquant IV image analysis system attached to an optical microscope. The systematic manual point count test method [144] was applied to determine the ferrite volume fraction of heat treated samples that were quenched at different temperatures.

4.3.2 Scanning Electron Microscopy

Scanning electron microscopy (SEM) and energy dispersive x-ray (EDX) spectroscopy were used for the characterization of the microstructures and for qualitative microanalysis. The analyses were conducted using a Phillips XL 30 field emission gun (FEG) scanning electron microscope (SEM) operated at 10 - 15 kV (accelerating voltage). This instrument was interfaced to a EDAX energy dispersive x-ray spectrometer and analysis system. The microstructure, surface morphology, and qualitative chemical analysis of the steels and inclusions were examined using secondary electron (SE) and backscatter electron (BSE) imaging techniques. Samples for SEM analysis were prepared using the same technique used for optical microscopy analysis.

The BSE image was used to identify the second phase particles and to determine the volume fraction of inclusions in steels. Approximately 5 to 10 mm^2 polished surface area of the

specimen at 2000 x magnification was analyzed. Any inclusion 0.1 μm in size or larger was measured and individually tallied.

The steel microstructure was characterized using the secondary electron imaging mode of the SEM to examine the various microconstituents. The compositions of inclusions and the surrounding matrix were analyzed semi-quantitatively using EDX microanalysis.

4.4 QUANTITATIVE METALLURGY

4.4.1 Grain Size

Measuring the ferrite grain size of the heat treated samples and the austenite grain size of the grain coarsening and TMP samples was performed using a computer controlled Bioquant IV image analysis system attached to an optical microscope.

Grains were measured by manually tracing of the grain boundaries on the screen to obtain the length of the grain boundary in X and Y directions of each individual grain in the measured area. The equivalent diameter or the grain size was automatically calculated based on the grain shape that determined by the relationship between the X and Y measurements. Regardless of the magnification, approximately 500 grains were measured for each sample. By using Microsoft Excel software, the average grain size and the statistical standard deviation were calculated for each sample. All results were established according to mean, standard deviation and relative error values for 95% confidence limit.

4.4.2 Ferrite Volume Fraction ($V_{f\alpha}$)

The systematic manual point count method [144] was applied for estimating statistically the ferrite volume fraction of thermal processed samples that were quenched at different temperatures.

A transparent sheet with a square test grid of 10x10 points was attached on the computer screen and superimposed over the image of the microstructure. The number of test points falling within the ferrite phase on the i^{th} field (P_i) were counted and divided by the total number of grid points (P_T) yielding the point fraction (P_{fi}) expressed as a percentage and written as follow:

$$P_{fi} = \frac{P_i}{P_T} \times 100 \tag{4-1}$$

The average point fraction for (n) number of measured fields gives an estimate of the volume fraction of the ferrite phase is expressed as:

$$\bar{P}_f = \frac{1}{n} \sum_{i=1}^{n} P_{fi} \tag{4-2}$$

During the measurement process, any point falling inside the ferrite phase was counted as one while any points that fell on the ferrite grain boundary or any doubtful points were counted as one half.

The degree of precision for the measurement depends on the number of measured fields. As per the ASTM E 562 standard [144], a minimum of 30 fields should be measured in order to have a 95% confidence limit for the average point fraction. Whenever less than 30 fields were

used, tabled correction factors were used to calculate the confidence limit based on the number of fields.

4.4.3 Particle Size Analysis

In considering the determination of particle size, it is important to mention that the SEM was used in the analysis. A similar technique to determine the grain size was used to measure the size of inclusions. The SEM backscatter electron micrographs were analyzed using the Bioquant IV image analysis system to find the diameter of inclusions which considers as spherical particles. For each material, approximately 5 to 10 mm^2 polished surface area of the specimen at 2000 x magnification was analyzed to determine the inclusions size.

The particles are effectively sectioned by the plane of polish Figure 4.7. The mean particles diameter was used to derive a relationship between observed and absolute dimensions of a distribution of spherical particles. This could eliminate the errors where large particles contribute circles of all smaller sizes than the true diameter to the plane of polish. The particles were divided into an arbitrary number of size groups according to the diameters that were observed on the plane of polish, (D_i). The mean of the reciprocals of the particle diameters (M) was found to be:

$$M = \frac{\sum n_i / D_i}{\sum n_i} \tag{4-3}$$

where D_i was taken as the diameter at the mid-point of each size group and n_i represents the frequency of each group.

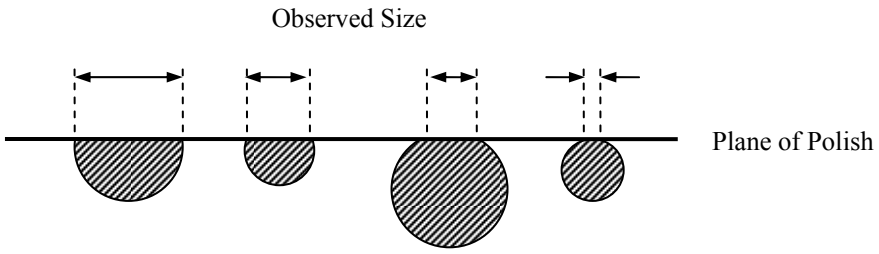

Figure 4.7: Schematic illustration of the different in particle sizes observed by SEM and optical microscopy.

4.4.4 Inclusion Volume Fraction (V_f)

The V_f of the inclusions was obtained by determining area fraction of the particles (A_f) where all V_f, A_f and P_f are equal. For more accurate results, the samples were viewed under the SEM for the particle A_f analysis. As per the ASTM E 45 standard [145], several fields of the specimen were viewed to find the total area of inclusions (A_I) per total viewed areas (A_T) of the specimen. The A_f of inclusions expressed as a percentage and written as follow:

$$A_f = \frac{A_I}{A_T} \times 100 \qquad \textbf{(4-4)}$$

4.4.5 Surface Area per Unit Volume (S_v)

The basic equation for obtaining the area of surfaces in a volume was derived by Saltykov [146], and then by Smith and Guttman [147] as a function of the number of point intersection per unit length of test line (P_L). This equation is written as:

$$S_V = 2P_L \ (\mathrm{mm^2/mm^3}) \tag{4-5}$$

The above equation is valid for systems of interconnected surfaces, i.e., austenite grain boundaries, as well as systems of discontinuous surfaces, i.e., inclusions in the matrix phase. The treatment accorded dispersed particles in a matrix is no different in principle from that of the interconnecting system. Alternatively, instead of counting intersections of interfaces, the number of interceptions of particles per unit length of test line (N_L) was counted in this case. In terms of N_L, the above equation becomes:

$$S_{V\alpha} = 2P_L = 4N_L \tag{4-6}$$

where $S_{V\alpha}$ refers to the total particle interface area per unit volume of the total system which includes α particles and the matrix. In the case of the spherical particles, the $S_{V\alpha}$ value is equal to the average particle surface area multiplied by the number of particles per unit test volume (N_V)[41]:

$$S_{V\alpha} = \pi D^2 \, . \, N_V = 4N_L \tag{4-7}$$

The pertinent measurement and equations for determining the S_V in different systems are given Figure 4.8.

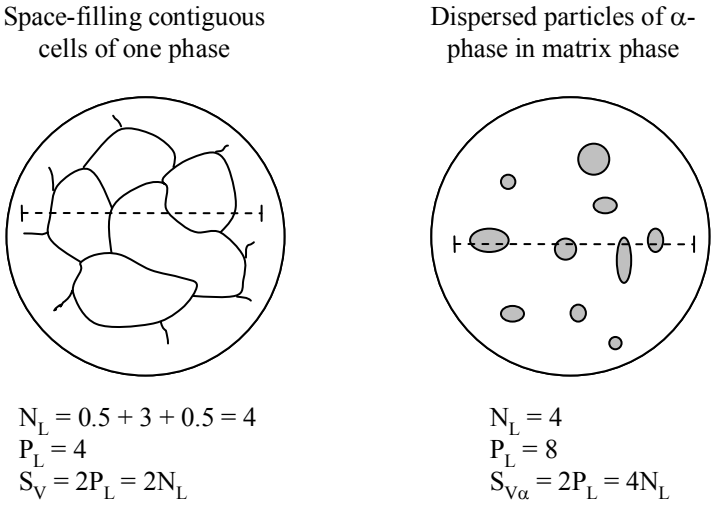

Figure 4.8: Techniques for measuring the S_V value in interconnected and discontinuous systems [41].

4.4.6 Number of Particles per unit Volume (N_V)

The number of particles per unit area (N_A) was obtained by considering a cubic sample of side (L) containing particles of average diameter (D). The probability that a particle was sectioned by the plane of polish is D/L. Therefore, the total number of particles appearing of plane area L^2 is given by [41]:

$$N_A L^2 = N_V L^3 . D/L \quad \text{or} \quad N_A = N_V . D \tag{4-8}$$

However, this relation is strictly true only when all particles are of constant shape independent of their size. In the case of uniform sized spherical particles of volume (V), the particle volume fraction, (V_f) is, given by [41]:

$$V_f = N_V V = N_V . \pi D^3/6 \tag{4-9}$$

From Equations 4-8 and 4-9:

$$N_V = \frac{\pi N_A^2}{4N_L} = \frac{N_A}{D} \tag{4-10}$$

However, the mean values of the particle parameters were calculated for the spherical particles of non-uniform size using Equation 4-3. According to Fullman [148], equations for calculating the mean diameter and N_V are as follow:

$$D = \pi / 2M \tag{4-11}$$

and

$$N_V = 2MN_A / \pi \tag{4-12}$$

5.0 RESULTS

5.1 AS-RECEIVED MATERIAL CONDITION

The optical microstructures of the three steels in the as-received condition are shown in Figure 5.1. While both TiO and MnS steel ingots were from laboratory, the Jumbo steel samples were from a commercial continuous casting slab.

The optical micrograph of the Jumbo steel, Figure 5.1 (a), exhibits the proeutectoid ferrite delineating the prior austenitic grain structures. The inside of the austenite grains contains non-polygonal ferrite and other low temperature, high carbon microconstituents.

On the other hand, Figure 5.1 (b) and (c) illustrate the large polygonal ferrite and pearlite microstructure of the TiO and MnS steels, respectively. The dendritic structures, shown in Figure 5.2, illustrated the differences in terms of the width and size of the dendrites through the thickness of the ingots. The average secondary dendrite arm spacing, (SDAS), at sub-surface, quarter-thickness and center positions was quantitatively measured and plotted in Figure 5.3 for comparison. As expected, the finest SDAS was indicated near the surface, which experienced the highest cooling rates. The SDAS increased as moving towards the center of the ingots se a result of decreasing the cooling rate. The difference in the SDAS observed in each steel ingot may be attributed to the effect of the type and volume fraction of non-metallic inclusions. MnS inclusions seem to be more effective in reducing the SDAS than are the TiO particles.

(a) Jumbo

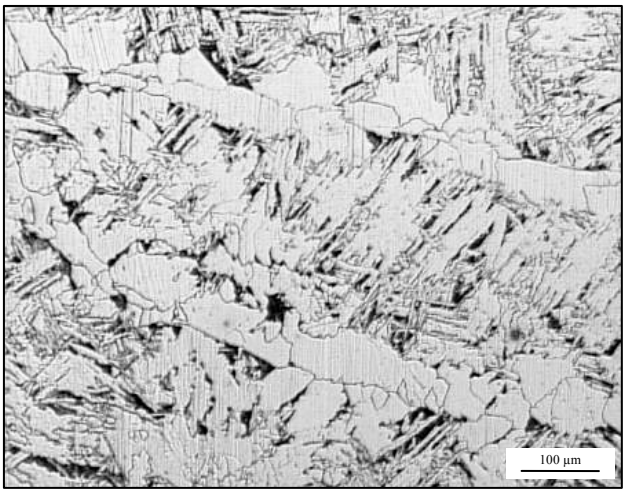

(b) TiO

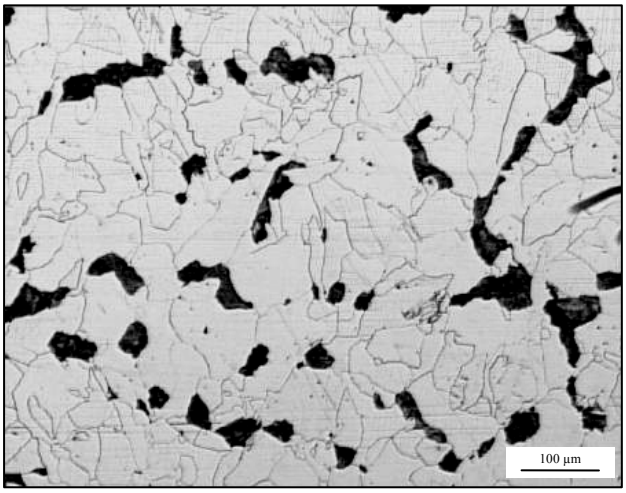

(c) MnS

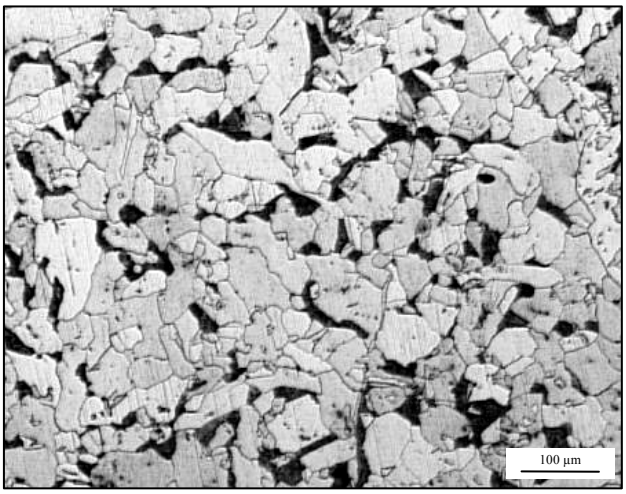

Figure 5.1: Optical micrographs showing the as received microstructures of the slab materials: (a) Jumbo steel, (b) TiO-steel and (c) MnS-steel.

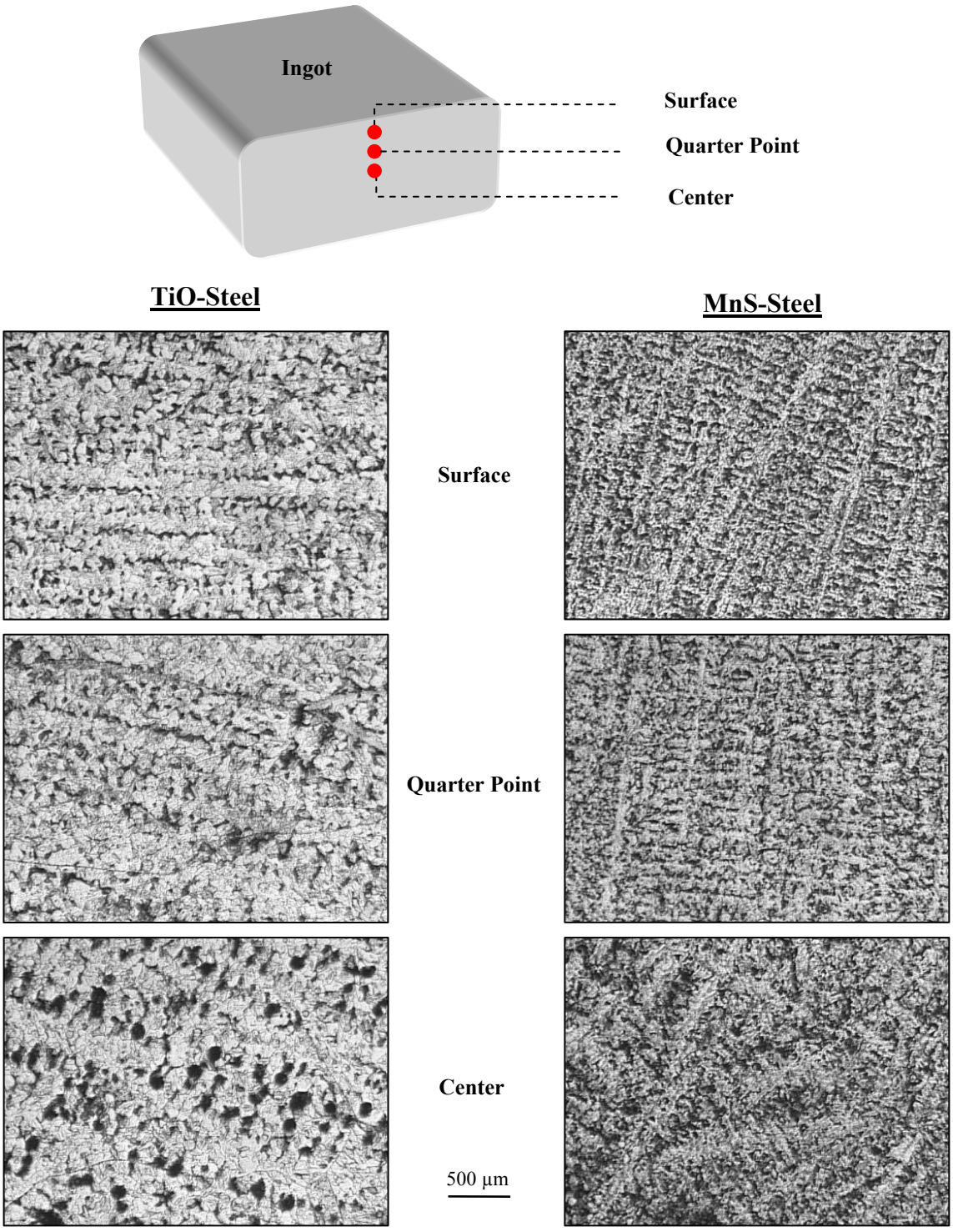

Figure 5.2: Dendritic structure of TiO and MnS steels through slab thickness.

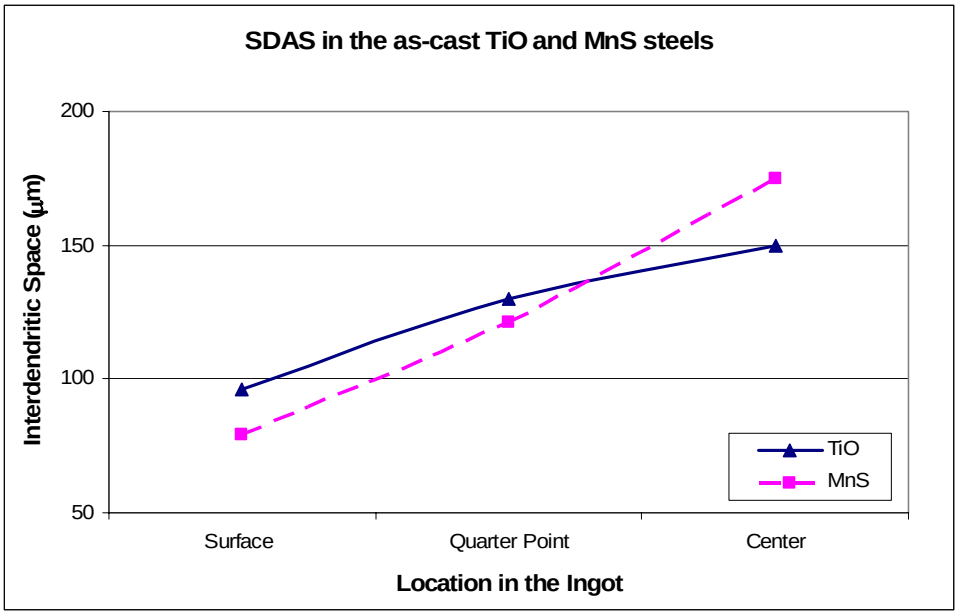

Figure 5.3: Secondary dendritic arm spacing of TiO and MnS steels as a function of the ingot thickness.

5.2 INCLUSION CHARACTERIZATION

The as-received materials were examined using optical and scanning electron microscopy to characterize the non-metallic inclusions. In the following, the major results from the inclusion analysis are presented in order to reveal their morphology, size distribution, volume fraction and chemical composition.

5.2.1 Inclusion Morphology, Volume Fraction and Size distribution

The SEM micrographs, Figure 5.4, illustrate the morphology, distribution and size of inclusions in the as-received condition of the Jumbo, TiO and MnS steels. Although the volume fraction, size and distribution vary widely, the majority of the inclusions in the three steels have a spherical shape, Figure 5.5. Clearly, the Ti-oxide inclusions have rough and porous surface, while the MnS inclusions in the Jumbo and MnS steels have smooth surface.

The quantitative analysis of inclusions in these three steels, including the volume fraction, mean size and the number of particles per unit area and per unit volume, is listed in Table 5-1.

The major goal of this work was to study the effect of the types of inclusions on the refinement of ferrite and the elimination of high carbon low temperature transformation microstructural products. Therefore, the alloys design was not optimized to improve the mechanical properties. Hence, in order to study the IGF nucleation behavior, the volume fraction of inclusions was increased from 0.00012 in the Jumbo steel to 0.00146 and 0.00332 in the TiO and MnS steels, respectively. The mean size of inclusions in the Jumbo steel was 1.37 ± 1.08 μm and the size ranged from 0.18 to about 6.0μm. In the TiO steels, the mean size of inclusions decreased to 1.08 ± 1.51μm while the size range expanded between 0.12 and 21.0 μm. In the MnS steel, the mean size of inclusions was 1.33 ± 0.97μm while the size range extended between 0.16 and 10.0 μm. In both the Jumbo and MnS steels, approximately 50% of the inclusions were smaller than 1.0 μm, while the majority, 75%, of the inclusions in the TiO steel was smaller than 1.0μm. The overall size distribution of the Jumbo, TiO and MnS steels are graphically represented in Figure 5.6, 5.7 and 5.8, respectively. The data were derived from heat treated samples that were water quenched from 800°C after reheating and slow cooling to determine the

amount of inclusion prior to transformation. The quantitative analysis showed that there was no difference in the inclusion size between materials in the as-cast and heat treated conditions.

The amount of coarse inclusions that are larger than 6.0 μm is limited in all three materials. It only corresponds to 1.3% and 0.15% of the total observed inclusion sizes in both TiO and MnS steels, respectively. All observed inclusions in the Jumbo steel are smaller than 6.0 μm. Therefore, only inclusions that are less than or equal to 6.0μm were considered in this study in order to eliminate the variation on the mean size. The overall size distribution of the three steels for inclusions up to 6.0μm are shown in Figure 5.9. Based on this consideration, the mean size of particles in the TiO steels changed form 1.08 ± 1.51 to 0.96 ± 1.0 μm, while the mean size of the MnS steel particles did not change. However, due to the low percentage of large inclusions, the number of particles per unit area, (N_A), and per unit volume, (N_V), is slightly changed as shown in Table 5-1. Regardless of the volume fraction of the inclusions, the MnS particles in both Jumbo and MnS steels have similar mean size and size distribution.

(a) Jumbo

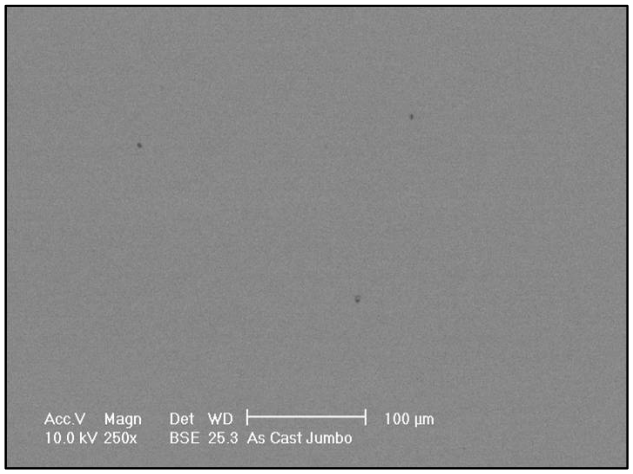

(b) TiO

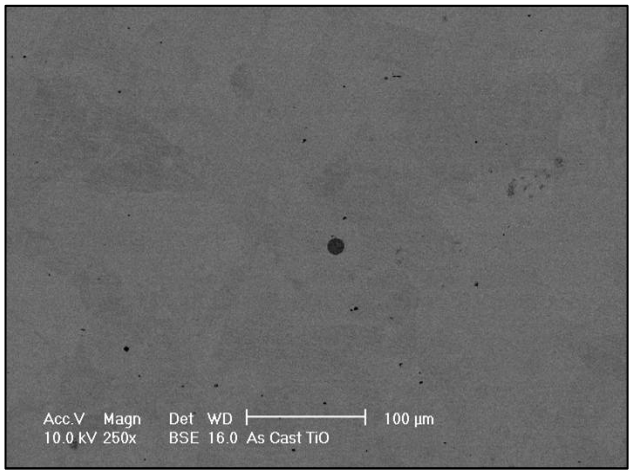

(c) MnS

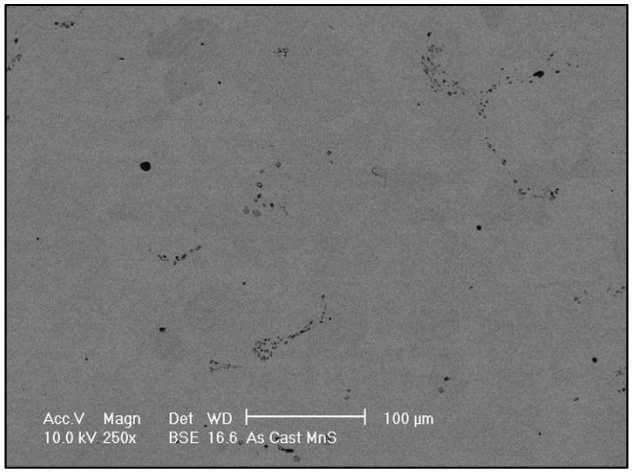

Figure 5.4: SEM micrographs showing the morphology, size and distributions of inclusions in the as-received microstructures of the slab materials: (a) Jumbo steel, (b) TiO-steel and (c) MnS-steel.

(a) Jumbo

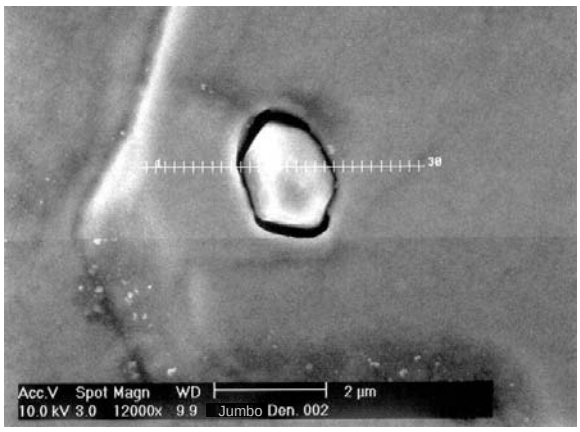

(b) TiO

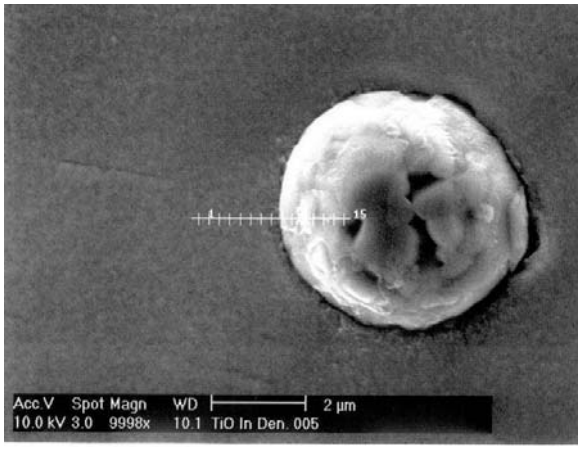

(c) MnS

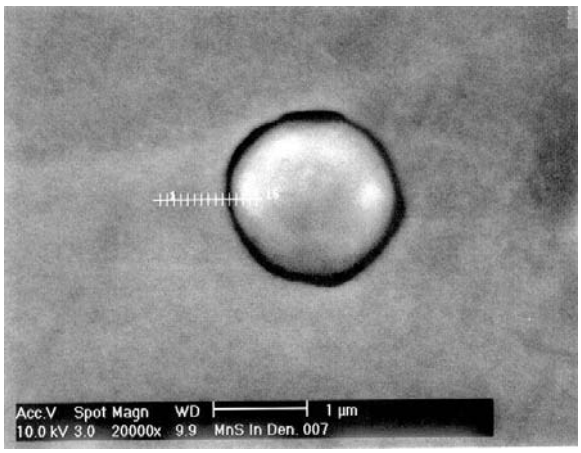

Figure 5.5: SEM micrographs showing the morphology of inclusions in the as-received materials: (a) Jumbo steel, (b) TiO-steel and (c) MnS-steel. Inclusions in the three materials have a spherical shape.

Table 5-1: Quantitative analysis of inclusions in the three steels.

Inclusions	Materials		
	Jumbo	TiO	MnS
Inclusion Type	MnS Mainly	Complex Compounds (Mn, MnS, Ti-oxides and Al-oxides) Mainly Ti-oxides	MnS Mainly
Mean size (μm)	1.37 ± 1.08	1.08 ± 1.51	1.33 ± 0.97
Inclusions < 1.0μm	46 %	74 %	47 %
Volume fraction (Vf)	$1.2x10^{-4}$ = 0.012 %	$1.46x10^{-3}$ = 0.146 %	$3.32x10^{-3}$ = 0.332 %
Number density per unit area (N_A, μm^{-2})	$5.1x10^{-5}$	$5.41x10^{-4}$	$1.56 x10^{-3}$
Number density per unit volume (N_V, μm^{-3})	$3.72x10^{-5}$	$5.01x10^{-4}$	$1.17 x10^{-3}$
Inclusions with size ≤ 6.0μm			
Mean size (μm)	1.37 ± 1.08	0.96 ± 1.0	1.32 ± 0.93
Volume fraction (Vf)	$1.2x10^{-4}$ = 0.012 %	$8.0x10^{-4}$ = 0.08 %	$3.18x10^{-3}$ = 0.318 %
Number density per unit area (N_A, μm^{-2})	$5.1x10^{-5}$	$5.34x10^{-4}$	$1.56 x10^{-3}$
Number density per unit volume (N_V, μm^{-3})	$3.72x10^{-5}$	$5.56x10^{-4}$	$1.18 x10^{-3}$

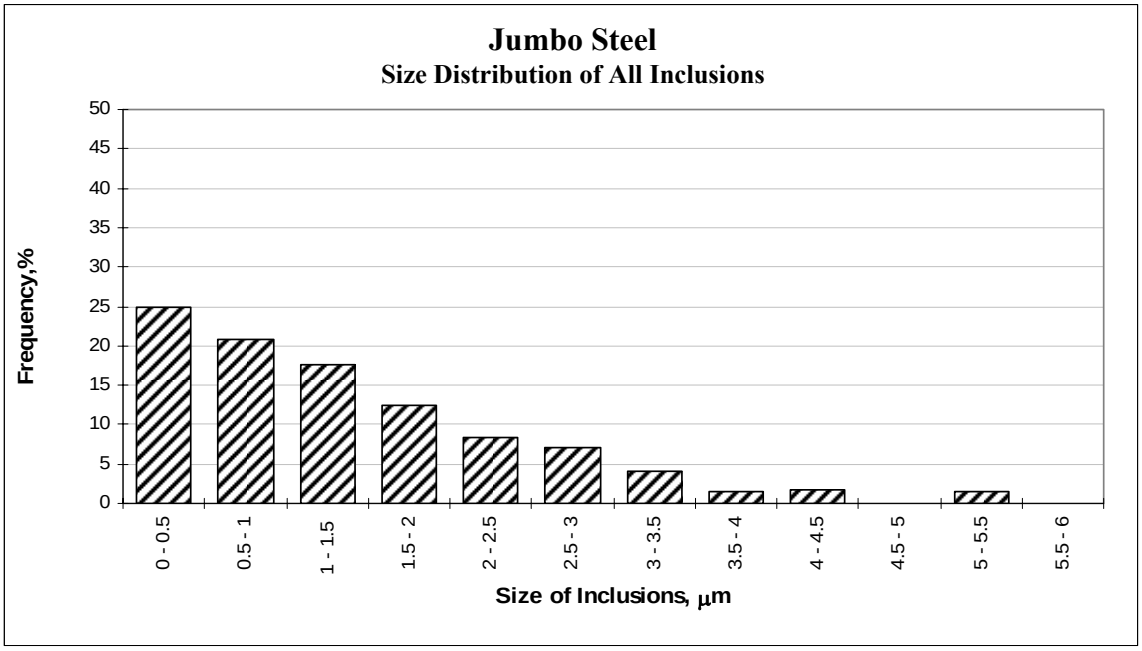

Figure 5.6: Size distribution of all inclusions in the Jumbo steel. Inclusions ranged from 0.18 to 5.5 μm with mean size 1.37 ± 1.08 μm.

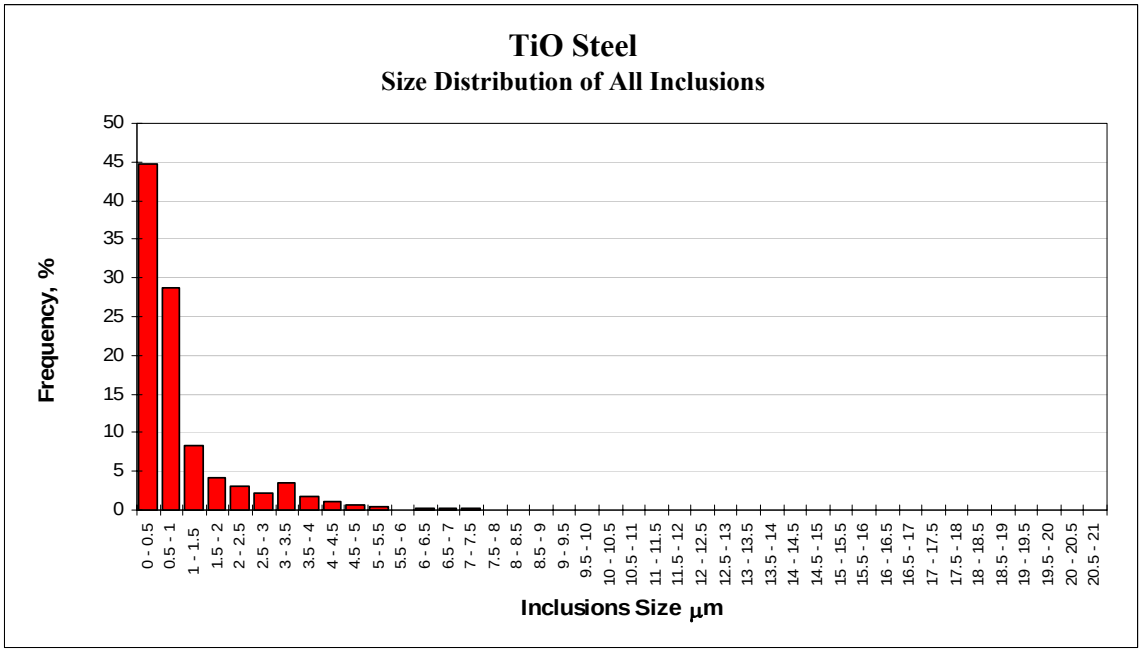

Figure 5.7: Size distribution of all inclusions in the TiO steel. Inclusions ranged from 0.12 to 21 μm with mean size 1.08 ± 1.51 μm.

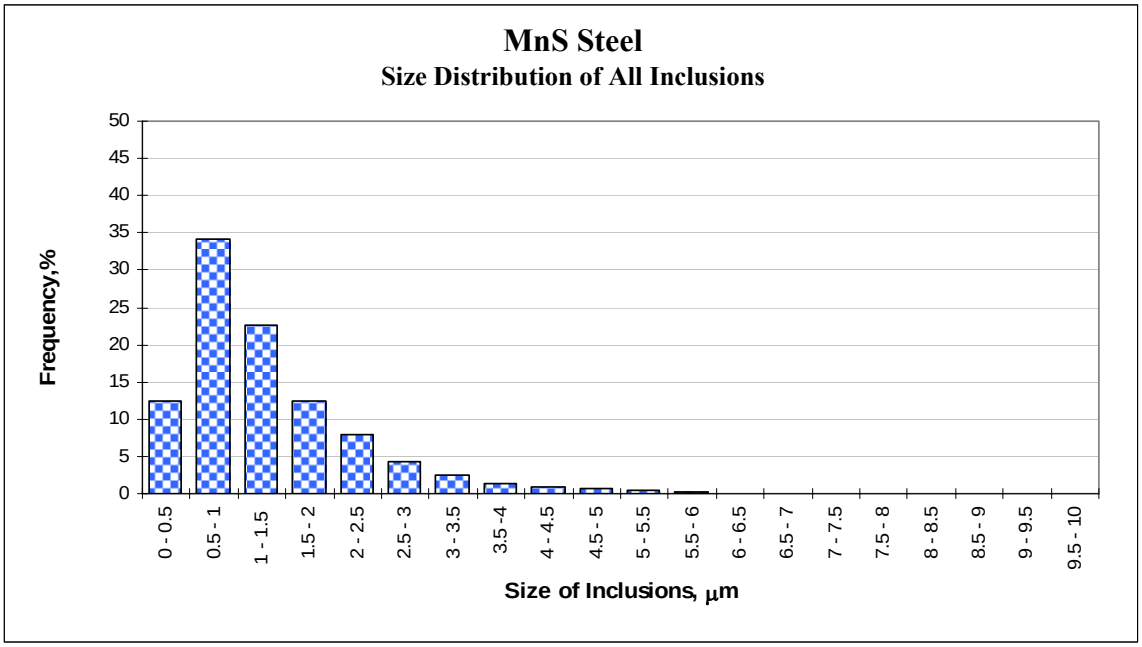

Figure 5.8: Size distribution of all inclusions in the MnS steel. Inclusions ranged from 0.16 to 10 μm with mean size 1.44 ± 0.97 μm.

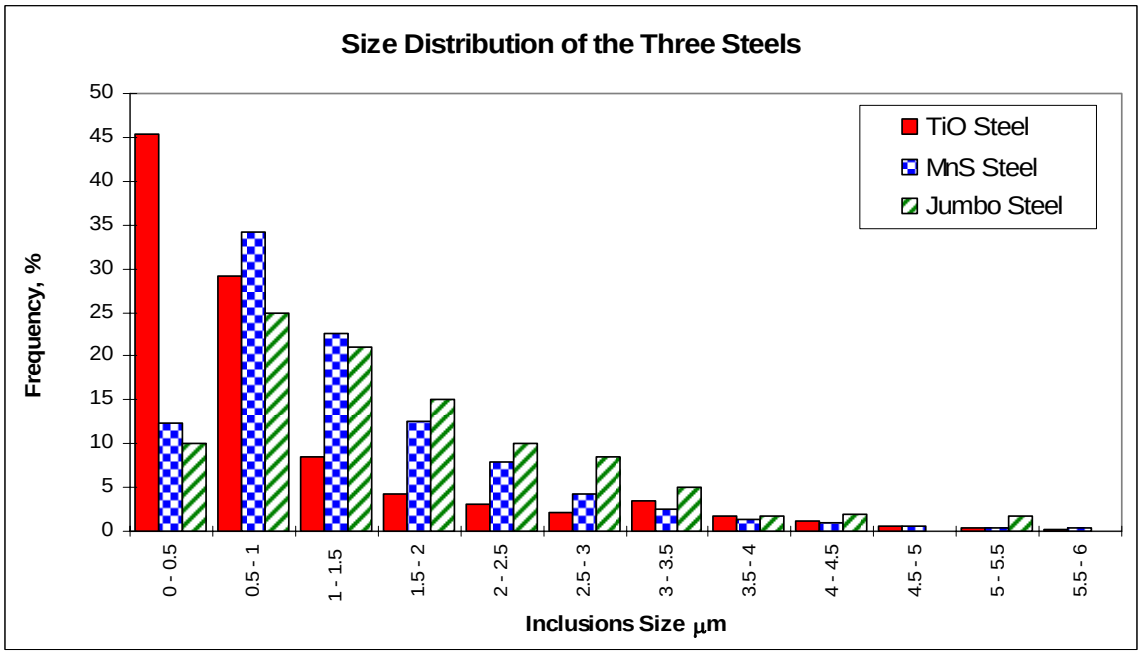

Figure 5.9: Size distribution of the three steels with inclusions ≤ 6.0μm.

5.2.2 Chemical Analysis of Inclusions

Two main types of inclusions were found in the TiO steel. The first type consists of small inclusions that ranged from 0.12 to 3.0 μm in size, while the other type consists of inclusions larger than 3.0 μm. The EDX spectrum in Figure 5.10 shows that the majority of the small inclusions present in this steel are mainly Ti-oxide with small amounts of Mn. In addition to the Ti-oxide, the EDX spectrums in Figure 5.11 (a-c) show that the large inclusions usually contain complex compounds such as Mn, MnS and Al-oxides. The amount of these complex compounds varied widely from one particle to the other and even within the same particle. Therefore, an average composition or a single area analysis would not reflect comprehensively the accurate chemical nature of an inclusion.

Clearly, Figure 5.11(a), (c) and (b) show the appearance of different phases in large inclusions localized in the TiO steel. Theses micrographs show that the oxide inclusions core contain rod-shape Al rich phase in addition to Ti and Mn. The Al-oxide trapped in the Ti-oxide matrix and did not mix with Ti-Mn-oxide. Moreover, MnS was detected in several events on the surface of the inclusion. These observations are consistent with those reported by other workers [149, 150, 151]. The formation of inclusion, as a function of temperature and composition, could be understood based on the thermodynamic stability of the different compounds.

On the other hand, the EDX analysis of the particles in the Jumbo MnS steels shows that the majority of inclusions presented in these steels are mainly MnS. The EDX spectrum of the inclusions in the Jumbo and MnS steel is shown in Figure 5.12 and Figure 5.13, respectively.

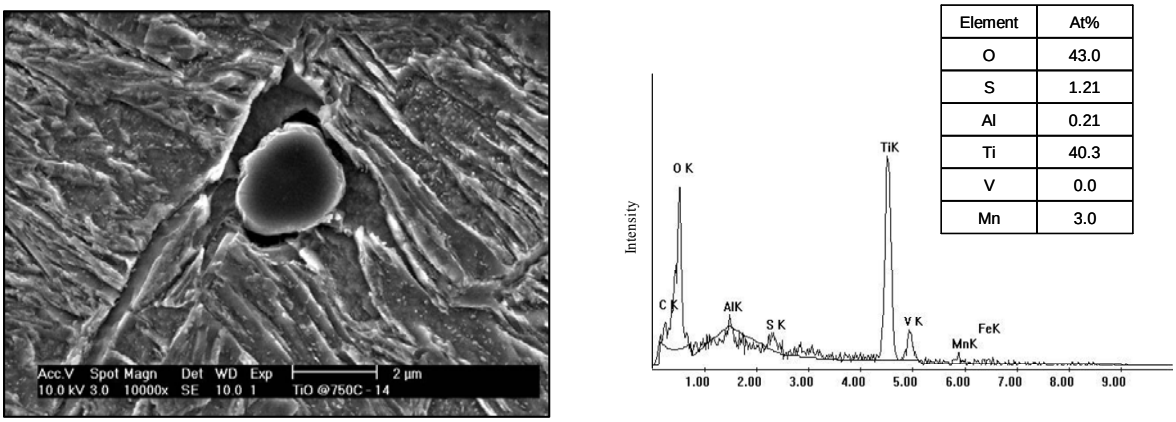

Element	At%
O	43.0
S	1.21
Al	0.21
Ti	40.3
V	0.0
Mn	3.0

Figure 5.10: SEM-EDX analysis of the TiO steel inclusions (Ti-oxide inclusion < 3.0 µm). Sample was controlled cooled and water quenched at 750°C.

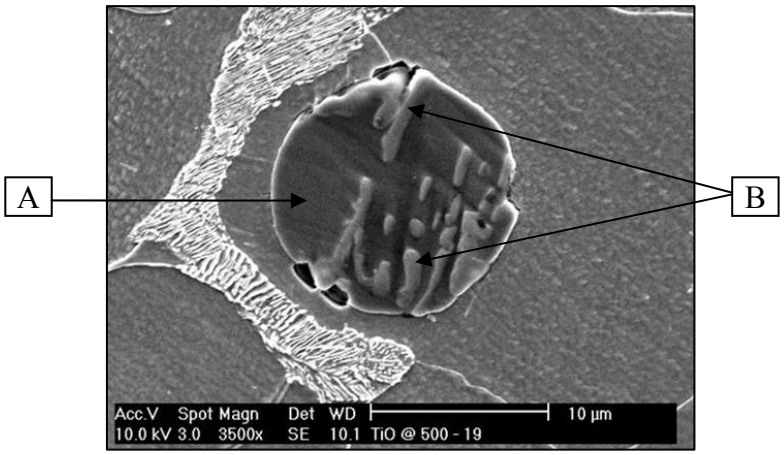

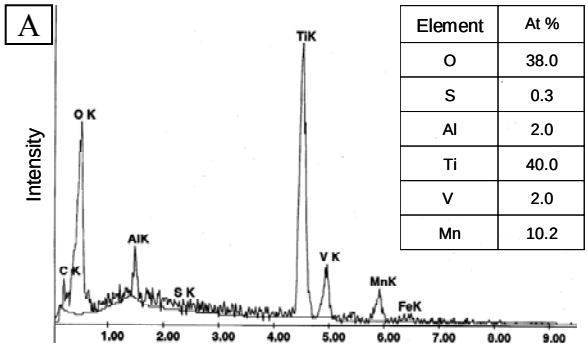

Element	At %
O	38.0
S	0.3
Al	2.0
Ti	40.0
V	2.0
Mn	10.2

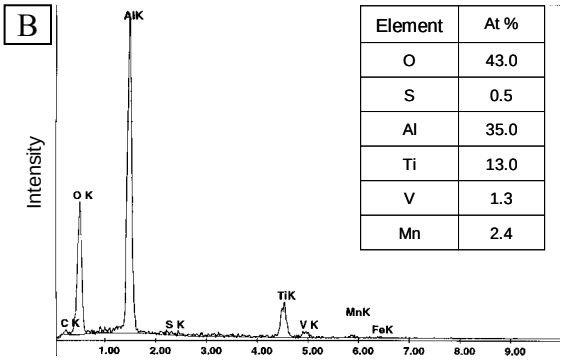

Element	At %
O	43.0
S	0.5
Al	35.0
Ti	13.0
V	1.3
Mn	2.4

Figure 5.11 (a): SEM-EDX analysis of the TiO steel inclusions (Ti-oxide inclusion > 3.0 µm). Complex compounds. Sample was controlled cooled and water quenched at 500°C.

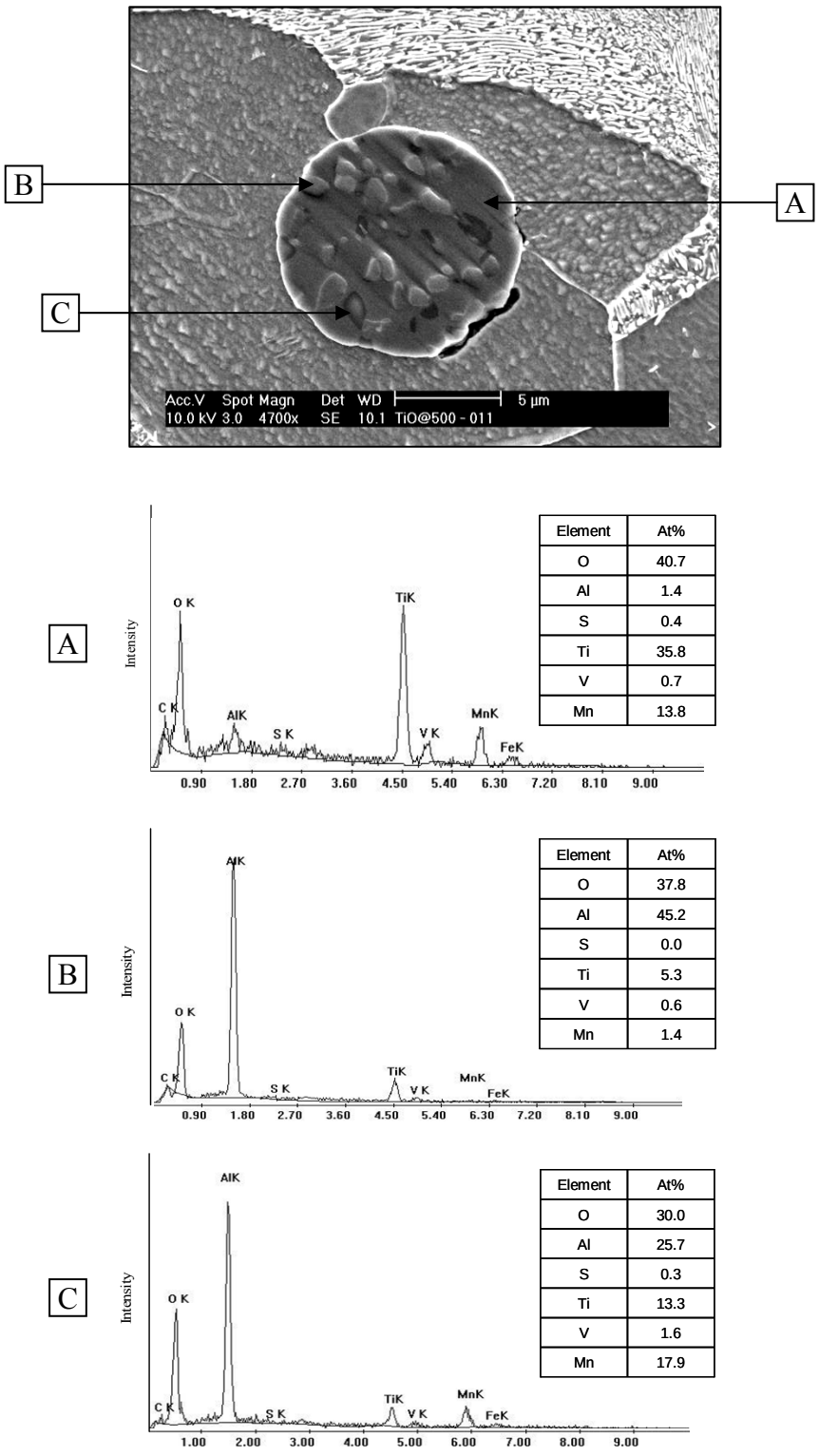

Figure 5.11 (b): SEM-EDX analysis of the TiO steel inclusions (Ti-oxide inclusion > 3.0 µm). Complex compounds. Sample was controlled cooled and water quenched at 500°C.

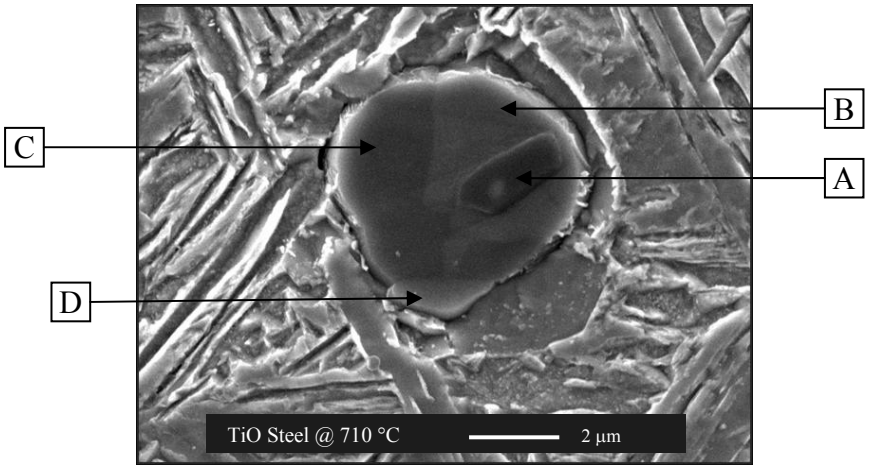

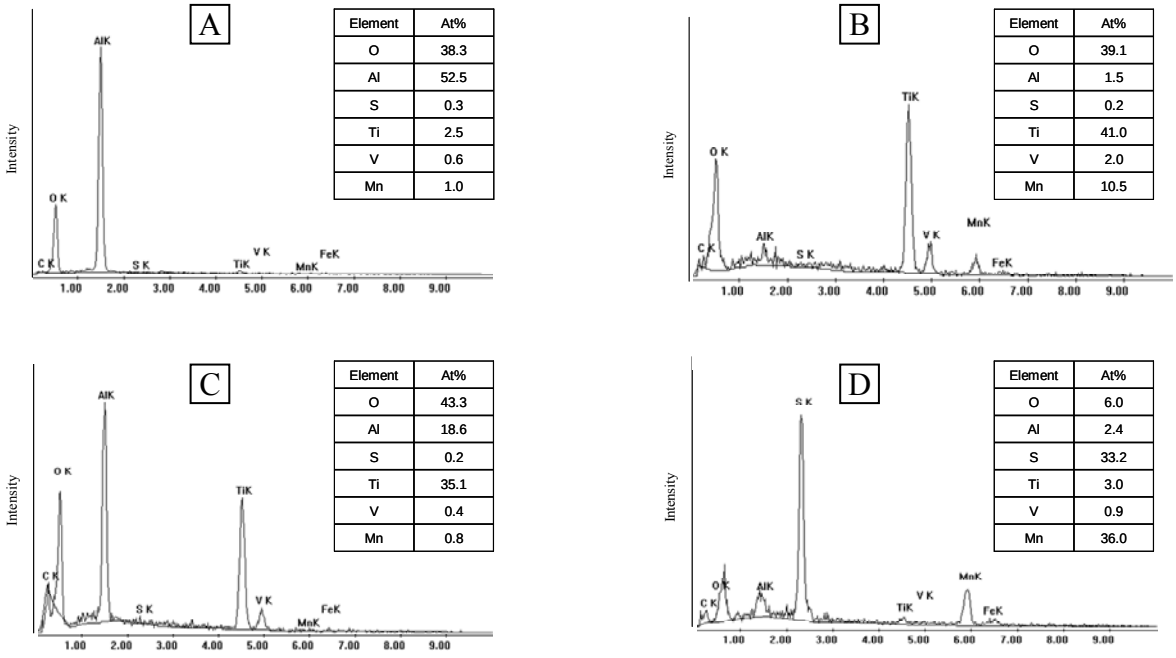

Element	At%
O	38.3
Al	52.5
S	0.3
Ti	2.5
V	0.6
Mn	1.0

Element	At%
O	39.1
Al	1.5
S	0.2
Ti	41.0
V	2.0
Mn	10.5

Element	At%
O	43.3
Al	18.6
S	0.2
Ti	35.1
V	0.4
Mn	0.8

Element	At%
O	6.0
Al	2.4
S	33.2
Ti	3.0
V	0.9
Mn	36.0

Figure 2.11(c): SEM-EDX analysis of the TiO steel inclusions (Ti-oxide inclusion > 3.0 µm) Complex compounds. Sample was controlled cooled and water quenched at 750°C.

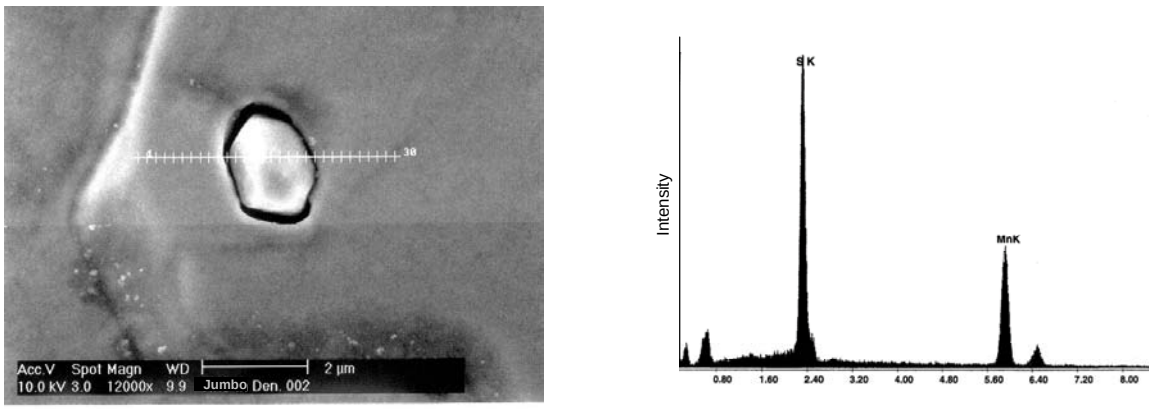

Figure 5.12: SEM-EDX analysis of the Jumbo steel inclusions in the as-cast condition.

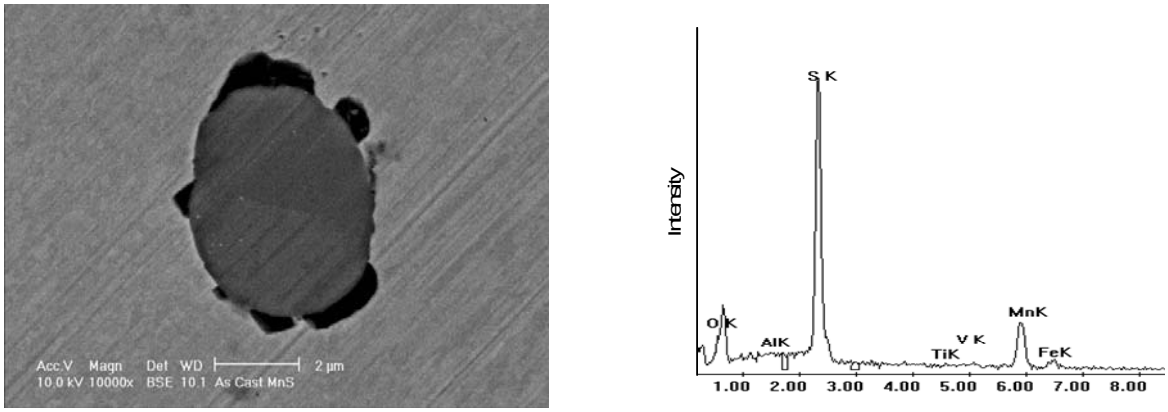

Figure 5.13: SEM-EDX analysis of the MnS steel inclusions in the as-cast condition.

5.3 GRAIN COARSENING BEHAVIOR

Isothermal reheating studies were performed on all three steels. The prior austenite grain size as a function of reheating temperature for the Jumbo, TiO and MnS steels is shown in Figure 5.14, Figure 5.15 and Figure 5.16, respectively. The austenite microstructures were obtained after reheating and holding samples at particular temperatures for 60 minutes before quenching in an ice brine bath. The micrographs indicate that, as expected, the prior austenite grain size increases with increasing temperature. This behavior is quantitatively represented in Table 5-2 and graphically shown in Figure 5.17.

The grain coarsening study shows that the austenite grain size in the Jumbo and TiO steels vary discontinuously with the reheating temperature. The discontinuous grain coarsening behavior indicates the occurrence of the abnormal grain growth or secondary recrystallization which is a common behavior in microalloyed steels. The abnormal grain growth occurs when the first-formed austenite grains are kept to a small size by the pinning force of a fine dispersion of precipitates. The discontinuity in the austenite grain size is observed with further reheating to and slightly above the grain coarsening temperature (T_{GC}). The bimodal grain distribution can occur over various temperatures depending on the type, size and volume fraction of the microalloy carbides and nitrides [34, 40]. In addition to the effect of microalloying elements, the high volume fraction of fine TiO particles (75% of inclusions < 0.1 μm) in the TiO steel hinder grain coarsening to higher temperatures. The result of the present study shows that the T_{GC} of the TiO steel (~1150°C) is higher than that of the Jumbo steel (~1100°C). Above the T_{GC} region, the austenite grain size increases continuously with temperature.

On the other hand, the MnS steel exhibited different behavior. Due to the high amount of fine MnS inclusions (50 % of inclusions < 0.1 μm), the austenite microstructure pinned effectively up to 1300 °C. Insignificant continuous growth of the austenite microstructure was observed in that range of reheating temperatures. Significant austenite grain coarsening took place above 1300 °C where the driving force of the grain coarsening overcame the pinning force.

The difference between the driving and pinning forces on the grain boundaries, in addition to the critical size of inclusions, was calculated based on the Gladman equations [52, 53, 58]. The calculated data are listed in Table 5-3. It is clearly shown that the grain coarsening temperature increased with the increasing difference between the driving and pinning force of the grain boundaries. Furthermore, the grain coarsening increased with a decrease in the difference between the particles size, (r), and the critical size of particles, (r_C), that effectively counteract the driving force for austenite grain coarsening.

The reheating temperatures of the three steels were selected based on the results of the T_{GC} study. The temperatures were selected to coarse austenite microstructure during the further process in order to increase the possibility of IGF nucleation events [140]. The austenite grain size at 1250, 1300 and 1350 °C was 375, 207 and 195 μm for the Jumbo, TiO and MnS steels, respectively.

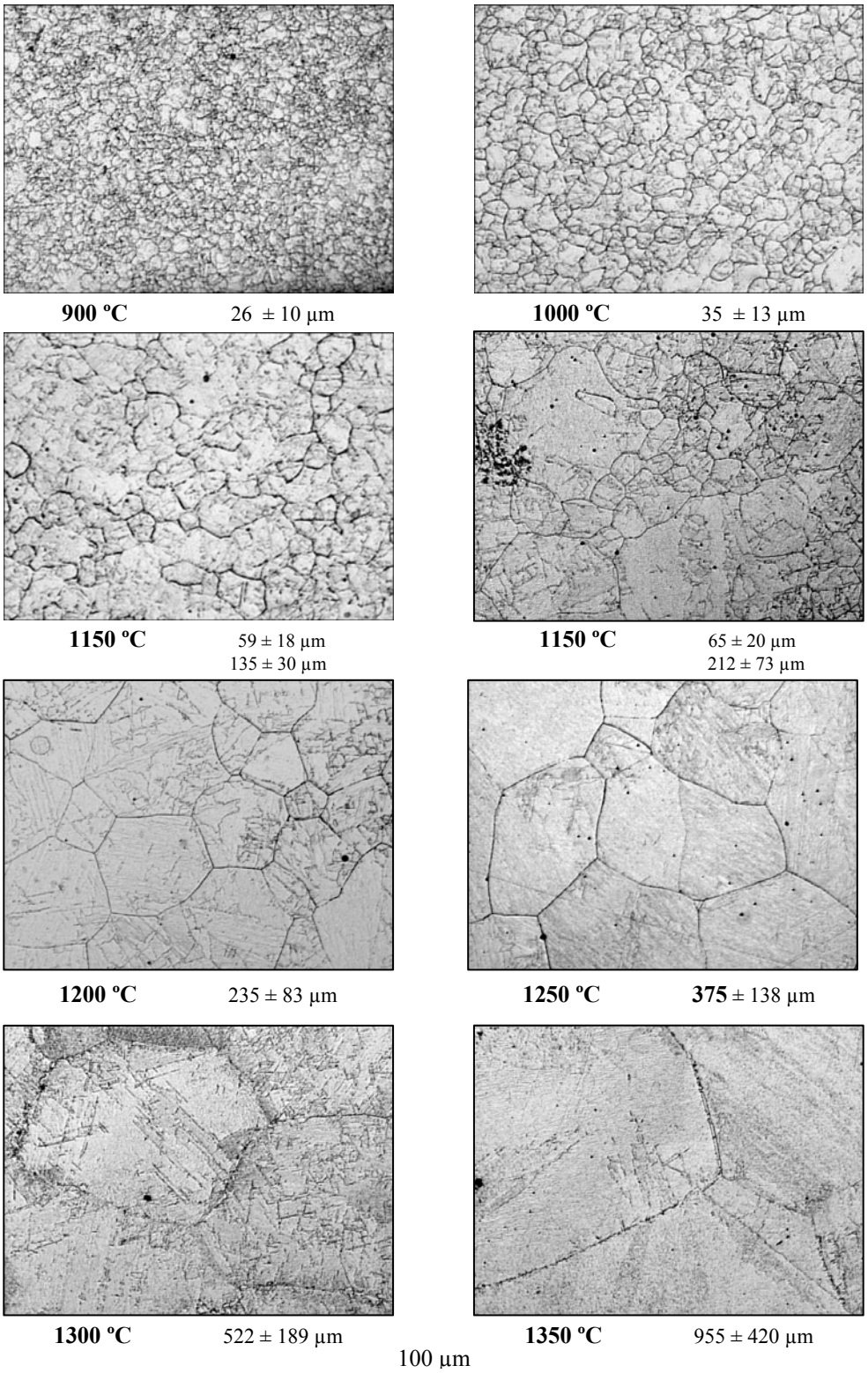

Figure 5.14: Prior austenite grains for Jumbo steel after isothermally reheating to different temperatures and water quenching.

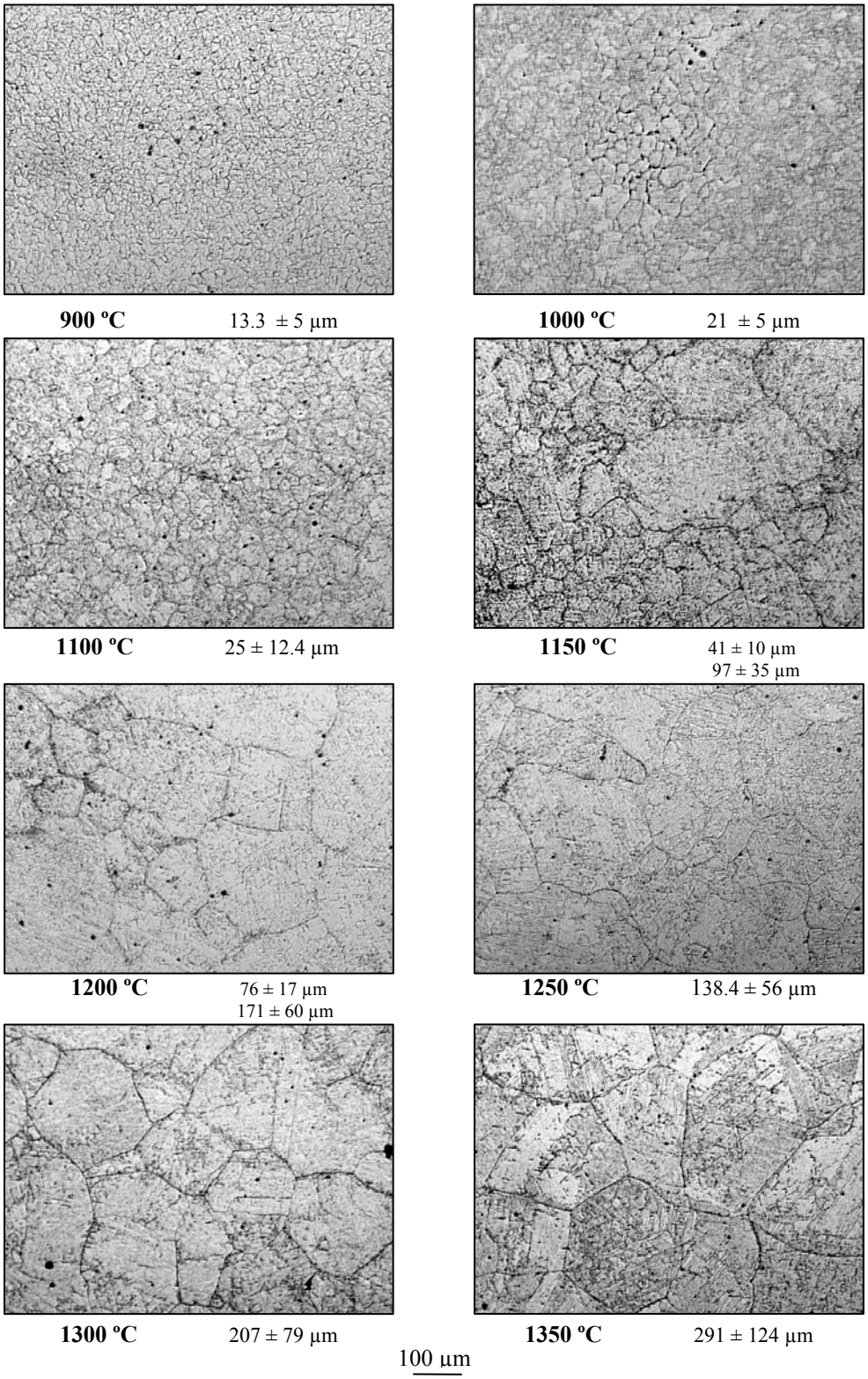

Figure 5.15: Prior austenite grains for TiO steel after isothermally reheating to different temperatures and water quenching.

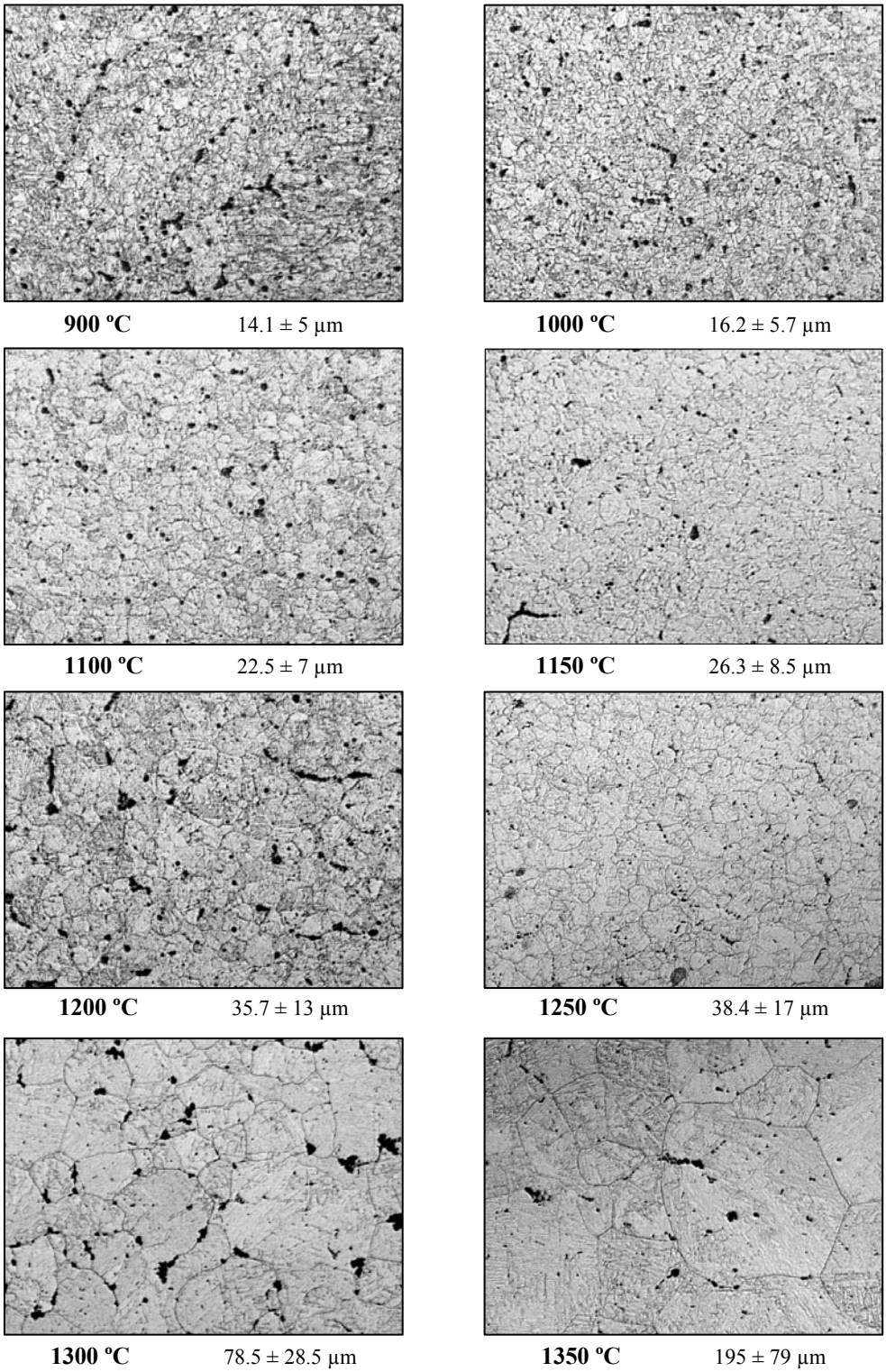

Figure 5.16: Prior austenite grains for MnS steel after isothermally reheating to different temperatures and water quenching.

Table 5-2: Average austenite grain size for all steels after isothermally reheating to different temperatures and water quenching.

Reheating Temperature (°C)	Austenite Grain Size (μm)		
	Jumbo (A572)	TiO	MnS
900	26 ± 10	13.3 ± 5	14.1 ± 5
1000	35 ± 13	21 ± 5	16.2 ± 5.7
1100	59 ± 18 135 ± 30	25 ± 12.4	22.5 ± 7
1150	65 ± 20 212 ± 73	41 ± 10 97 ± 35	26.3 ± 8.5
1200	235 ± 83	76 ± 17 171 ± 60	35.7 ± 13
1250	375 ± 138	139± 56	38.4 ± 17
1300	522 ± 189	207 ± 79	78.5 ± 28.5
1350	955 ± 420	291 ± 124	195 ± 79

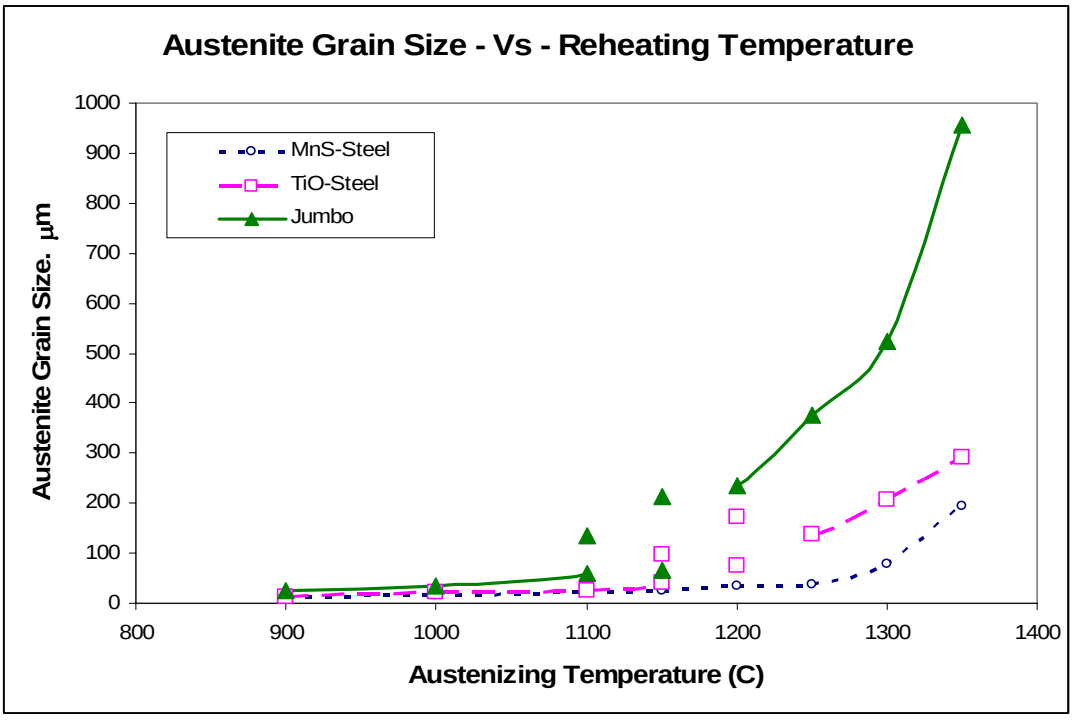

Figure 5.17: Average austenite grain size as a function of reheating temperatures for Jumbo, TiO and MnS steels.

Table 5-3: Calculated pinning and driving forces for the grain coarsening in the three steels.

Variables	Steel		
	Jumbo	TiO	MnS
V_f	1.2×10^{-4}	1.46×10^{-3}	3.32×10^{-3}
N_A (μm^{-2})	5.1×10^{-5}	5.41×10^{-4}	1.56×10^{-3}
$Ro = D_\gamma/2$ (μm)	188	104	95
$r = D_l/2$ (μm)	0.685	0.540	0.665
$r_C = 6R_oV_f / \pi(3/2 - 2/Z)$ (μm)	0.260	1.740	3.730
$F_{PIN} = 4\ r\ \sigma\ N_A$ (Pa)	111	935	3320
$F_D = (2/Z - 3/2)\sigma/R_o$ (Pa)	710	1285	1365
T_{GC} (°C)	1100	1150	1300
- The interfacial energy per unit area of austenite grain boundary, $\sigma = 0.8$ J/m^2 - The ratio of the radii of growing and matrix grains, Z is assumed as 1.5			

5.4 TMP ANALYSIS

This study was only preformed on the Jumbo steel in order to investigate the effect of different deformation temperatures and subsequent cooling rates on austenite grain size prior to γ-α transformation. The results of the TMP study are presented in the following sections.

5.4.1 Effect of Deformation Temperatures on Dγ

The austenite grain size was determined in the beginning of the TMP in order to observe the effect of the subsequent processing on the austenite microstructure. A sample was water quenched just after the second reheating stage and prior to the deformation process. In this reheating stage, a sample was held for 2 minutes at 1250°C in the radiation furnace of the MTS machine. The average austenite grain size prior to deformation in the Jumbo steel was 430 ± 172μ m.

The effect of the deformation temperature on the austenite microstructure was determined through measuring the austenite grain size at the end of each deformation schedule (1200, 1100 and 880 °C). The deformed samples were water quenched immediately after the final pass in each schedule. The quantitative measurement showed that the austenite grain size decreased as a function of decreasing deformation temperatures. The average austenite grain size for the 1200, 1100 and 880°C deformation schedules was 160 ± 62, 102 ± 43 and 75 ± 33 μm, respectively. The relation between the austenite grain size and deformation temperature is graphically depicted in Figure 5.18. It is clearly shown that processing the material above the grain coarsening temperature provided the necessary thermal energy for grain coarsening. The relatively large interpass time (55 sec) eliminates the grain refining recrystallization effect of each deformation pass through facilitating the grain coarsening between passes.

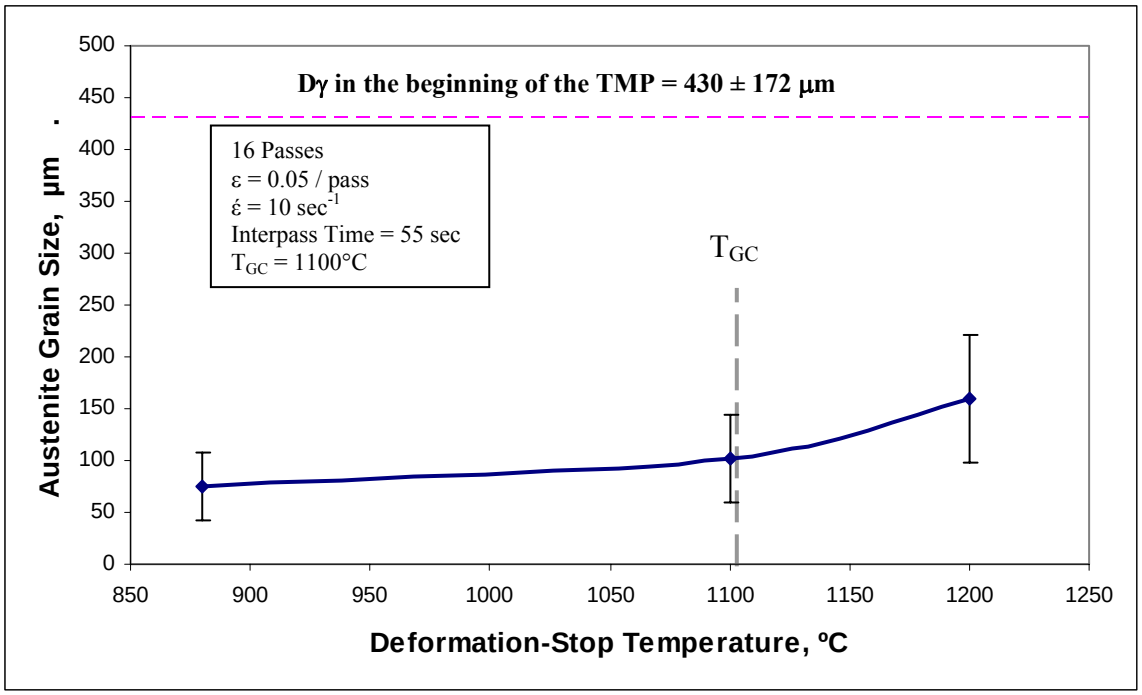

Figure 5.18: The variation of austenite grain size as a function of deformation-stop temperature.

5.4.2 Effect of Cooling Rates on D_γ

The deformed materials were subjected to two different cooling schedules to study the effect of the cooling rate on the austenite microstructure prior to the phase transformation and on the subsequent ferrite microstructure. During controlled cooling, the deformed samples were cooled to 800 ºC at a rate of 0.24 ºC/sec and then cooled to the transformation temperature, (Ar_3), at 0.08 ºC/sec. This cooling schedule was selected to simulate as close as possible the industrial process for heavy steel sections. During fast cooling, the deformed samples were cooled to A_{r3} at 1.4 ºC/sec then water quenched.

In order to study the austenite decomposition behavior, the Ar_3 for each deformation schedule was determined through analyzing the time-temperature data of the TMP. These data were

recorded automatically upon deformation in the MTS machine. The Ar_3 in addition to the finishing transformation temperatures of austenite, (Ar_1), were measured at a fast cooling rate (1.4 ºC/sec). Both transformation temperatures are quantitatively represented, in Table 5-4, and graphically shown in Figure 5.19, as a function of austenite grain size. The results show that the Ar_3 and Ar_1 temperatures increase with decreasing the deformation temperature, i.e., with increasing the prior austenite grain size. This behavior is expected since the nucleation sites per unit volume decrease with increasing austenite grain size. Based on the above results, the water quenching temperature for each deformation schedule was selected to be just above the phase transformation temperature, Ar_3.

The variation of $D\gamma$ as a function of different cooling conditions is illustrated in Figure 5.20. This behavior is shown quantitatively in Table 5-5. It is clearly shown that the $D\gamma$ increases approximately 15% for all deformation schedules by applying the 1.4 ºC/sec cooling rate after deformation. It is also shown that grain coarsening increases with further decrease in the cooling rate. With the controlled cooling process, $D\gamma$ increases about 30 % for both the 1100 and 880 ºC deformation schedules whereas the increase is approximately 100% for that of the 1200 ºC.

The abnormal coarsening of the 1200°C schedule is due to the completion of the deformation series 100°C above the grain coarsening temperature. This deformation schedule, in combination with the controlled cooling rate, provides enough time and thermal energy for the secondary recrystallization to occur. To eliminate the coarsening effect after the deformation at elevated temperature, a set of samples was deformed at 1150ºC and subjected to the same cooling conditions of other schedules. The variation of $D\gamma$ as a function of cooling rates for the 1150 ºC schedule is shown in Figure 5.20 and the quantitative values are added to Table 5-5. The results indicate that the majority of the grain coarsening takes place above 1150 ºC where the time and

thermal energy are sufficient to activate the migration of austenite grain boundaries and coarsen the grains.

Table 5-4: Measured phase transformation temperatures of deformed Jumbo steel with different schedules at the cooling rate of 1.4 °C/sec.

Deformation Stop Temperature (°C)	**Dγ** (μm)	**γ - α Transformation Temperature** (°C)	
		A_{r3}	**A_{r1}**
880	75 ± 33	780	720
1100	102 ± 43	728	677
1200	160 ± 62	722	672

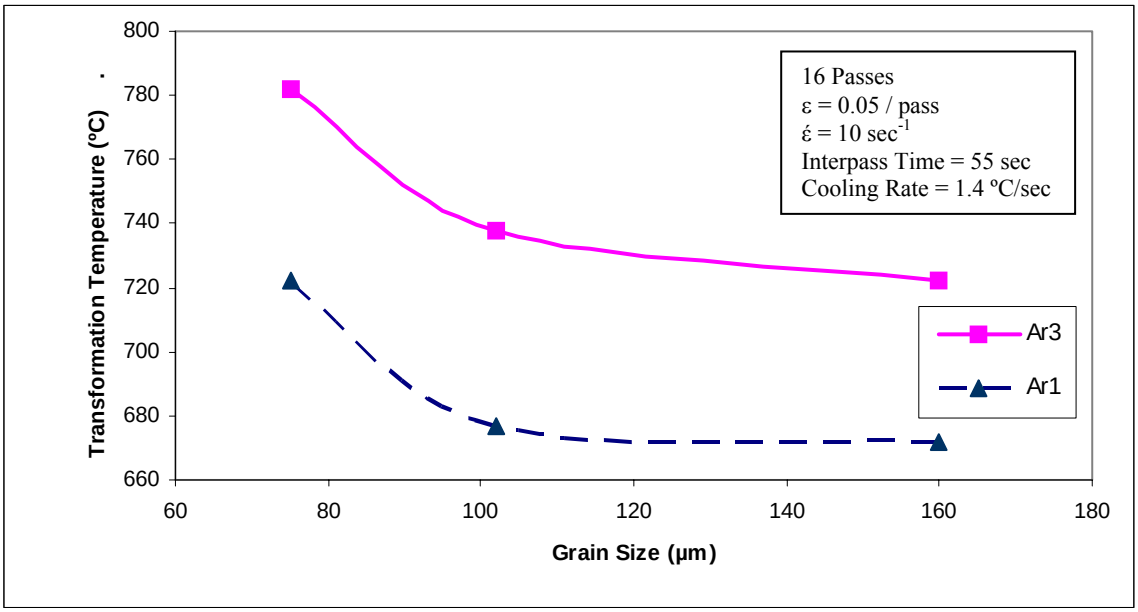

Figure 5.19: The variation of the transformation temperatures as a function of austenite grain size.

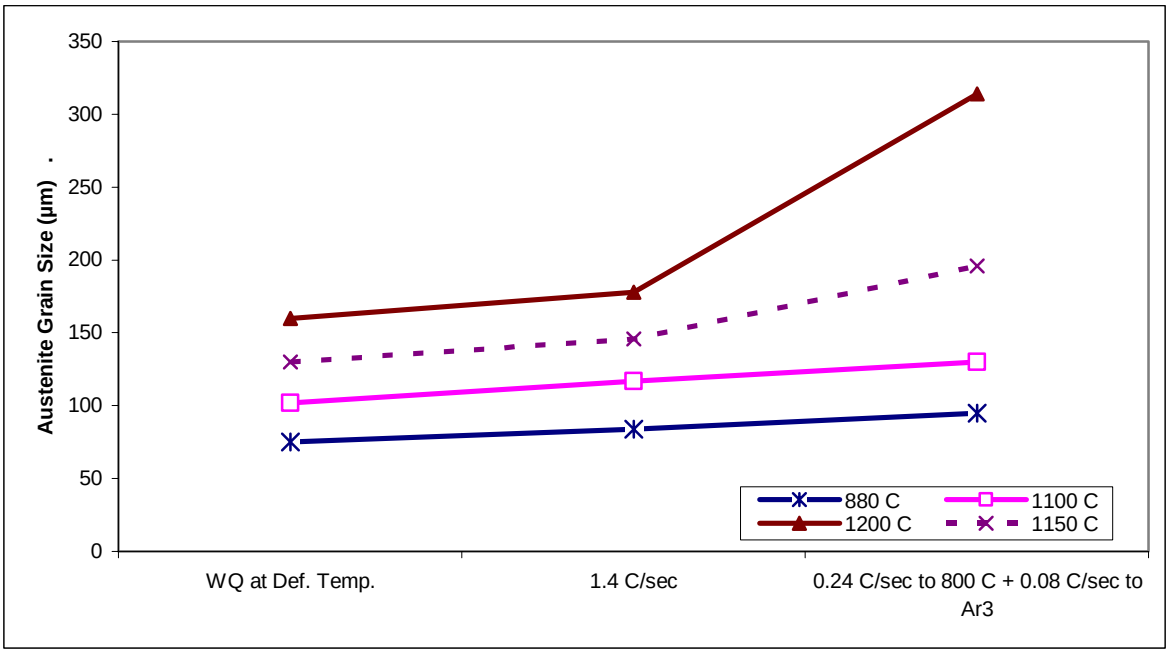

Figure 5.20: The variation of the austenite grain size at different deformation schedules as a function of different cooling conditions.

Table 5-5: Austenite grain size as a function of different cooling conditions and deformation schedules.

Deformation Stop Temperature (ºC)	**Ar_3** (ºC)	**Dγ (µm)**		
		At Deformation Temp.	**Cooling Rate 1.4 ºC/sec**	**Controlled Cooling 0.24 ºC/sec at 800 ºC + 0.08 ºC/sec to Ar_3**
880	780	75 ± 33	95 ± 38	100 ± 40
1100	728	102 ± 43	117 ± 31	130 ± 73
1150	725	129 ± 64	143 ± 69	196 ± 81
1200	722	160 ± 62	178 ± 71	314 ± 120

5.4.3 Austenite Decomposition Behavior Based on the TMP Study

The decomposition of austenite during the controlled cooling and the nucleation of ferrite grains are shown in Figure 5.21. The series of micrographs demonstrates the nucleation and growth of the ferrite microstructure as a function of controlled cooling temperature for the 1200°C deformation schedule. Noticeably, and as expected, the ferrite grains start to nucleate preferentially at γ/γ the prior austenite grain boundaries at the beginning of the transformation. With decreasing transformation temperatures, the favorable nucleation sites in the austenite grain boundaries are consumed and nucleation of ferrite starts simultaneously at the γ/α boundaries and other available interfaces, such as non-metallic inclusions, γ/I. The findings of this investigation confirm that nucleation at inclusion is always energetically less favorable than nucleation at austenite grain boundaries for a given driving force. Hence, after the saturation of the grain boundary surfaces with allotriomorphic ferrite, other nucleation sites such as inclusions become active at greater undercooling [84, 116].

The relation between the prior austenite and the final ferrite grain sizes is quantitatively shown in Table 5-6. Evidently, the presented data confirm that the refining of the ferrite microstructure improves with decreasing the prior austenite grain size. The data is graphically illustrated in Figure 5.22, and compared with the suggested values based on the empirical relations of Saito [135] and Sellars [136]. Clearly, Saito equation gives more accurate prediction for the ferrite grain size based on the prior austenite grain size and the cooling rate, hence, this equation is considered in the rest of this study. However, this congruity is only in the case of the allotriomorphic ferrite without considering the effect of the particle-stimulated nucleation, PSN. Moreover, the Saito and Sellars equations were proposed to predict the ferrite grain size in TMP

plates where the prior austenite grain size in the range of 100 μm and the cooling rate is grater than 0.1°C/sec.

The results of the 1200°C TMP schedule show that the gained refinement during the deformation process was approximately eliminated prior to the phase transformation due to the controlled cooling process. At the end of the high temperature deformation process, the austenite microstructure was refined from 430 ± 172 μm to 160 ± 62 μm. The refinement effect was eliminated during the controlled cooling process and the austenite microstructure coarsens back to 314 ± 120 μm prior to the γ-α transformation. Based on this observation, it was decided to process the steels without deformation and compare the results. However, similar coarsening effect was found when the samples were thermal processed without deformation. That is the size of austenite grains prior to the transformation were similar in size to those obtained after deformation controlled cooling prior to the phase transformation.

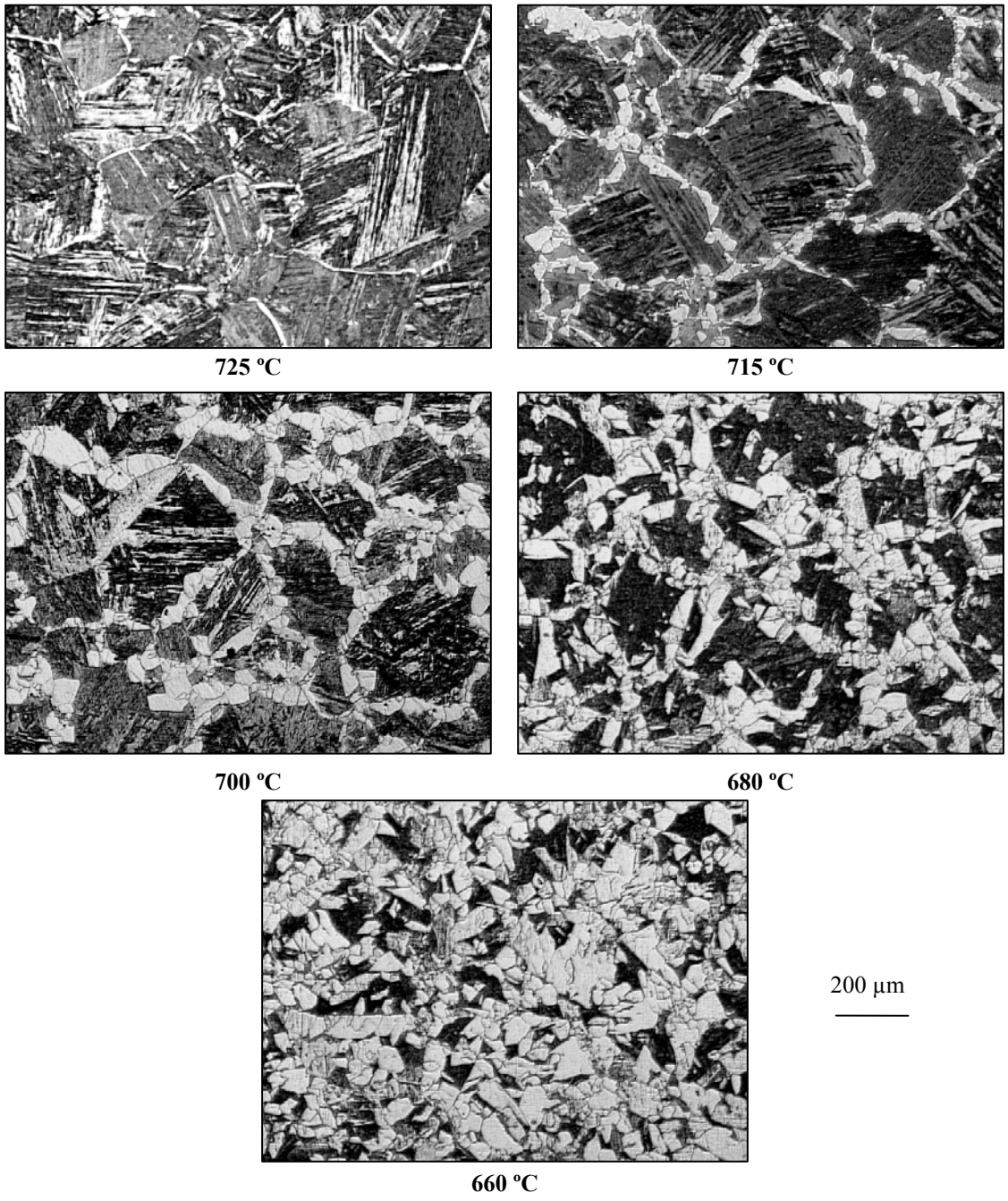

Figure 5.21: Nucleation of ferrite grains on the prior austenite grain boundaries as a function of time. Samples were subjected to 1200 °C deformation schedule and cooled to 800°C at 0.24°C/sec and then at 0.08°C/sec then water quenched at different temperatures

Table 5-6: The relation between the prior austenite and the nucleated ferrite grain sizes as a function of deformation schedules with controlled cooling process.

Deformation Stop Temperature (°C)	Grain Size (μm)	
	Dγ	Dα
880	100 ± 40	29.7 ± 11.2
1100	130 ± 37	34 ± 11
1200	314 ± 120	47 ± 15

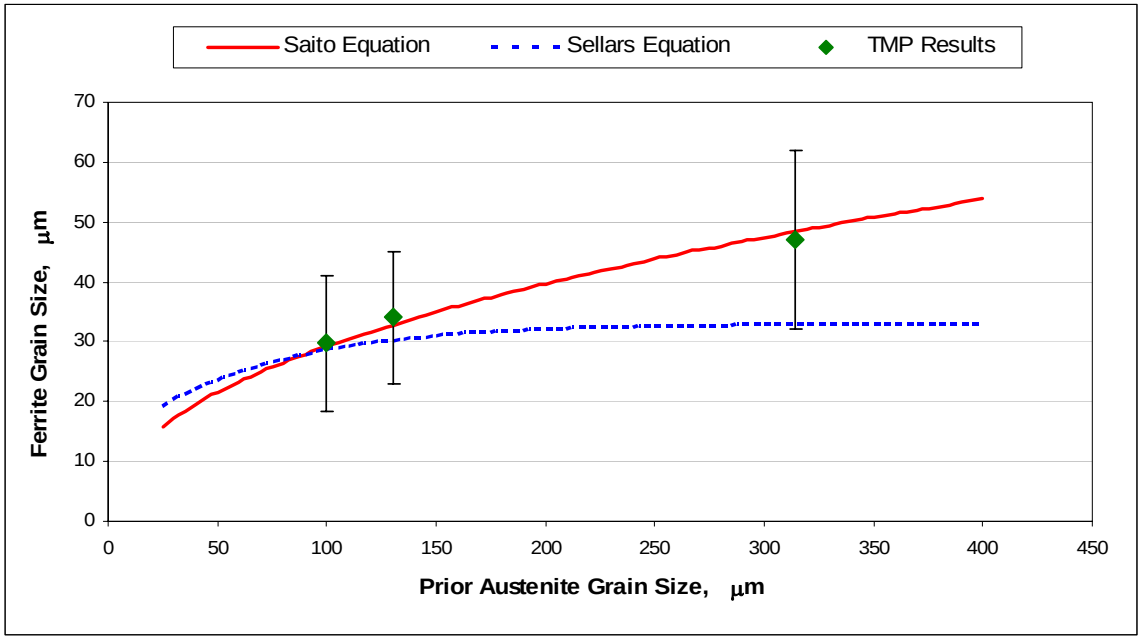

Figure 5.22: The variation of ferrite grain size as a function of prior austenite grain size for the TMP Jumbo steel with controlled cooling rate of 0.24 + 0.08 °C/sec. Comparison of the experimental results with the Saito and Sellars empirical equations.

5.5 THERMAL PROCESSING ANALYSIS

The thermal processing study was performed to investigate the effect of the PSN in the refining of ferrite microstructure in the absence of a deformation process. The thermal processing schedule focused on the study of the IGF nucleation behavior. The deformation schedule was eliminated during thermal processing because most of the austenite refinement due to the deformation was lost during the cooling process. The nucleation rate of ferrite was determined based on the decomposition behavior of the prior austenite microstructure during the controlled cooling schedule. The results of the thermal processing study are presented in the following sections.

5.5.1 Austenite Grain Size Prior to the Phase Transformation

In the beginning of the thermal processing study, the prior austenite grain size for the three steels was determined. Samples were water quenched just after the second reheating stage and prior to controlled cooling, Figure 4.6. Samples were held for 2 minutes in the radiation furnace at 1250, 1300 and 1350°C for the Jumbo, TiO and MnS steels, respectively. The average austenite grain sizes prior to the controlled cooling process are 430 ± 175, 219 ± 97 and 184 ± 75 μm for the Jumbo, TiO and MnS steels, correspondingly. The austenite grain size prior to the phase transformation temperature was measured for each material to determine the relation between the decomposed austenite and nucleated ferrite grain sizes. The average austenite grain sizes just before the phase transformation, at 825°C, are 372 ± 160, 240 ± 106 and 230 ± 87 μm for the

Jumbo, TiO and MnS steels, respectively. However, the measured value of the transformation temperatures for the Jumbo, TiO and MnS steels was 805, 805 and 810 °C, respectively.

In the Jumbo steel, the average austenite grain size prior to the phase transformation was 372 ± 160 μm which is approximately similar to the austenite grain size in the TMP, 314 ± 120 μm. This behavior was explained in section 5.4.3.

The austenite grain size of the three steels at different stages of the thermal processing process prior to the phase transformation, in addition to the final ferrite grain size, are quantitatively shown in Table 5-7. Due to the increasing nucleation sites per unit area, the refining of the ferrite microstructure improves as the prior austenite grain size decreases. The relation between the austenite grain size prior to the transformation and the final ferrite grain size is graphically illustrated in Figure 5.23, and compared with the suggested values of the empirical relations of Saito [135] and Sellars [136]. Due to the similar prior austenite and final ferrite grain sizes in TMP and thermal processing, the Jumbo steel has kept the same relationship with the Saito equation. Both TiO and MnS steels were shifted below Saito's curve by 25 and 35%, respectively. The Saito equation does not account for the additional nucleation sits produced by the presence of inclusions. Hence, the significant differences are considered as the effect of inclusions on the refining of microstructures.

Table 5-7: The prior austenite and the final ferrite grain size as a function of the thermal processing.

Steel	Grain Size (μm)		
	Dγ At Reheating Temp.	Dγ At 825 °C	Dα
Jumbo	**430 ± 175**	**372 ± 160**	**54.2 ± 28.5**
TiO	**219 ± 97**	**240 ± 106**	**33.3 ± 16.5**
MnS	**184 ± 75**	**230 ± 87**	**27.2 ± 18**

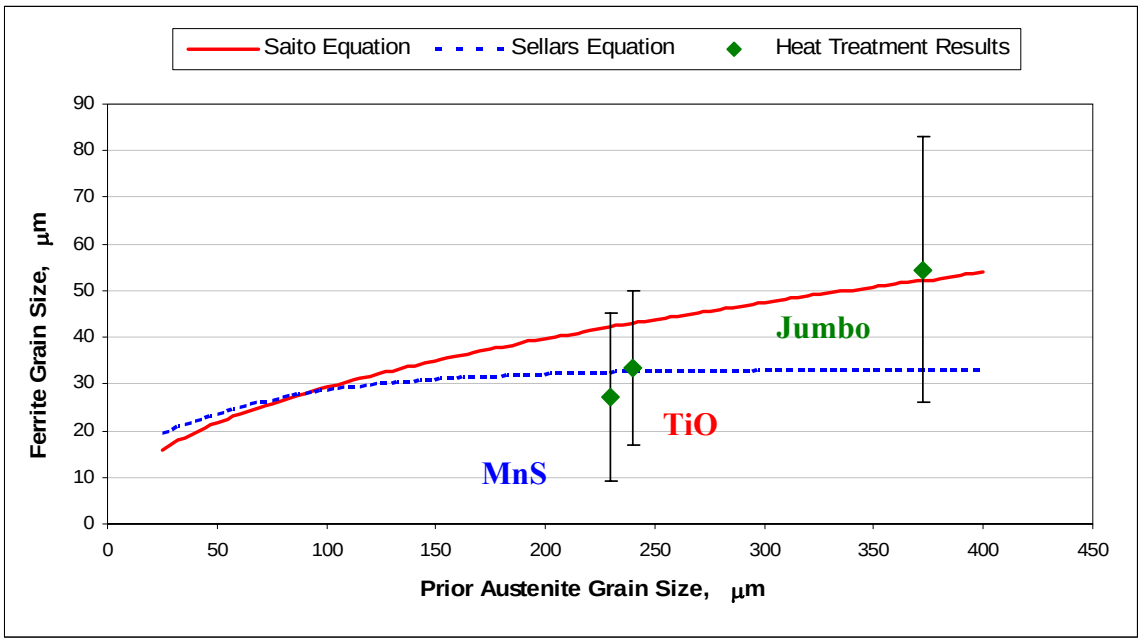

Figure 5.23: Variation of ferrite grain size as a function of prior austenite grain size for the heat treated steels. Comparison of the experimental results with the Saito and Sellars empirical equations.

5.5.2 Austenite Decomposition Behavior during the Thermal Processing Study

A series of optical micrographs depicting the decomposition behavior of the prior austenite microstructure and the formation of the ferrite microstructure as a function of the cooling temperature for Jumbo, TiO and MnS steels are shown in Figure 5.24, Figure 5.25 and Figure 5.26, respectively. During the controlled cooling process, the materials were water quenched from different temperatures in the 800 to 500 °C range to depict the sequence of the austenite decomposition to ferrite. Although the optical micrographs show that the phase transformation of all steels started just above 800 °C, each material behaved differently during the transformation.

In the Jumbo steel, Figure 5.24, the quenched sample at 770°C shows the consumption of all available austenite grain boundaries with nucleated proeutectoid ferrite. There was no evidence of IGF formation at this temperature. Upon quenching from 750°C, additional nucleation and growth of ferrite along and perpendicular to the austenite grain boundaries was observed. Simultaneously, the IGF started to take place as a second layer of ferrite that nucleated at the γ/α interface. The growth of the primary nucleated ferrite grains at austenite grain boundaries continued and more IGF formed as the temperature decreased. Due to the low inclusion content, the majority of the observed IGF in the Jumbo steel was nucleated at the γ/α interface, while few nucleation events were observed within the austenite grains. The transformation appeared to be completed around 600°C, where the volume fraction and grain size of ferrite did not change considerably with subsequent reduction in the temperature. The formation of polygonal ferrite grains rapidly increased the carbon concentration within the center of the austenite grain, thereby reducing the undercooling making the subsequent nucleation events more difficult. At some certain point below the eutectoid temperature, the nucleation of ferrite grains stopped and the

remaining untransformed austenite formed other low temperature microconstituents, as shown clearly in the optical micrographs of 600 and 500 °C.

The change of ferrite volume fraction as a function of cooling temperatures in the Jumbo steel is presented graphically in Figure 5.27. These curves were drawn based on the point counting technique for the nucleated ferrite at different stages throughout the cooling process. The curve of the grain boundary ferrite represents the volume fraction of ferrite that nucleated at the grain boundary. It is clearly shown that the saturation of grain boundary sites occurred at 770°C. The growth of the ferrite, in the addition to the nucleation and growth of the ferrite at the γ/α interfaces are represented in the nucleation and growth curve which continuously proceeded up to 660°C. On the other hand, the IGF curve started at 690°C and represents the volume fraction of ferrite that nucleated intragranularly on the inclusions. Evidently, the volume fraction of the IGF observed is very limited due to the low amount of inclusions in the Jumbo steel. The probability error in detecting the IGF increases at lower temperatures with increasing the volume fraction of intergranular and intragranular ferrite. In some cases it was difficult to distinguish between the two events nucleating of ferrite.

The prior austenite microstructure in both TiO and MnS steels decomposed in a very similar manner. In the TiO steel, Figure 5.25, the consumption of the available prior austenite grain boundaries is observed around 760 °C. Further nucleation and growth of ferrite along and perpendicular to the austenite grain boundaries were observed with cooling to 750°C. At this temperature, in addition to nucleation of ferrite at the γ/α interface, ferrite started to nucleate intragranularly at inclusions inside the austenite grains. On the other hand, the utilization of the available austenite grain boundaries was completed around 750°C in the MnS steel, Figure 5.26. The further nucleation and growth of ferrite along the prior austenite grain boundaries were

observed with cooling to 730°C. The differences between the MnS and TiO steels transformation temperatures could be explained due to the high content of Mn and Ti in these materials, respectively. While the Mn is considered as austenite stabilizer, the Ti is classified as a ferrite stabilizer [99]. Therefore, a higher degree of undercooling was required in the MnS steel to achieve a similar transformation effect on the TiO steel.

With continuous cooling below 710 °C, inclusions in both steels acted as effective nucleation sites for IGF while the growth of the primary nucleated ferrite grains at austenite grain boundaries continued. Due to the high inclusion content, the volume fraction of ferrite grains increased remarkably between 710 and 690 °C in both cases. The higher activity of the grain boundaries nucleation sites is due to its lower free energy barrier to ferrite nucleation than intragranular inclusions [110]. However, the transformation appeared to be completed at approximately 670 °C, where the volume fraction and grain size of ferrite did not change much with subsequent reduction in the temperature. The low temperature microconstituents were not observed at low temperatures due to the relatively small austenite grain size and high inclusion volume fraction in both materials.

The changes of ferrite volume fraction as a function of cooling temperatures in the TiO and MnS steels are graphically presented in Figure 5.28 and Figure 5.29, respectively. Due to the high amount of inclusions, both steels revealed remarkably high volume fraction of IGF over the grain boundary and γ/α interfaces ferrite. In the TiO steel, although the IGF nucleation was started at 740°C, the volume fraction of IGF was dramatically increased between 710 and 670°C. Unlike the TiO steel, the IGF nucleation in the MnS steel started at 720°C. The 10 °C shift in the start of the IGF nucleation between the TiO and MnS steels could be related to the differences in the hardenability effect of the γ/I interface between both steels. However, the volume fraction of

IGF in the MnS steel increased significantly between 710 and 680 °C, similar to the behavior of the TiO steel. Due to the higher amount of inclusions per unit volume, MnS steels showed better refinement in ferrite than the TiO steel.

Graphs of the variations of the total ferrite volume fraction as a function of cooling temperatures in the three steels are depicted in Figure 5.30. The comparison between the three curves exhibited the similarity in the decomposition behavior of the TiO and MnS steels. The obvious differences between the decomposition curve of the Jumbo steel and the curves of the PSN materials reflect the significant effect of the inclusions in the kinetics of the decomposition behavior of austenite in the three steels.

Regardless of the similarity and differences between the decomposition behaviors, each curve was divided, by its nature, into four major stages. The first stage is defined as the γ/γ grain boundary saturation, where the ferrite grains nucleated preferentially on the prior γ/γ grain boundaries and absolutely consumed them. In addition to the growth of the ferrite at grain boundaries, the second stage contained nucleation of new ferrite at the γ/α interfaces with the simultaneous nucleation of few events of IGF at the active austenite-inclusion, γ/I, interfaces. In this stage, the growth process is dominated due to the high diffusion rate and small undercooling that associated with high temperature. In the third stage, growth of the nucleated ferrite, in addition to the nucleation of IGF was accomplished. The fourth stage contained the rest of the ferrite growth and the low temperature transformation for the untransformed austenite. These regions are shown in Figure 5.31 for the Jumbo steel and in Figure 5.32 for both TiO and MnS steels.

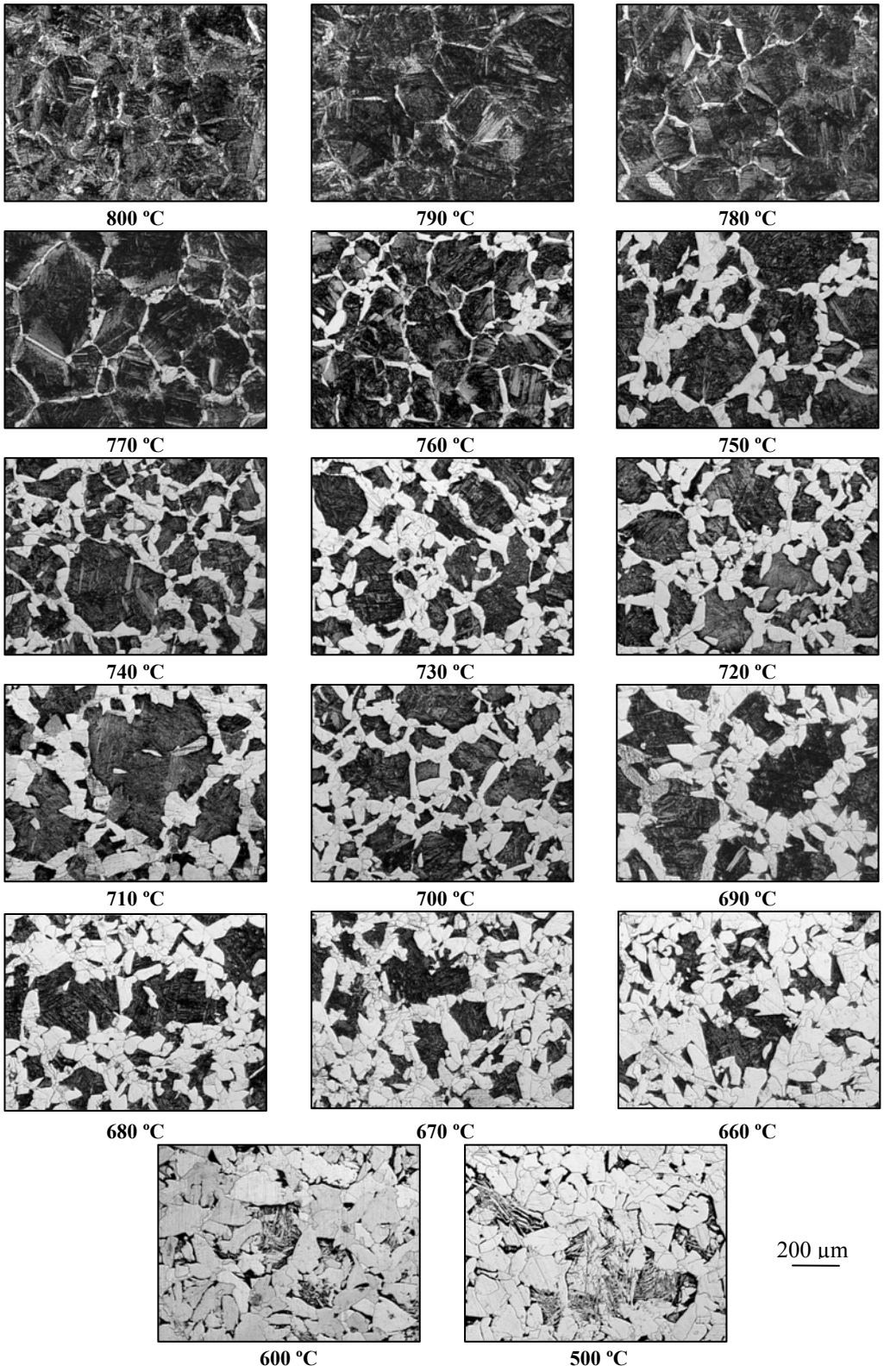

Figure 5.24: Decomposition behavior of the prior austenite microstructure in the Jumbo steel as a function of cooling temperature.

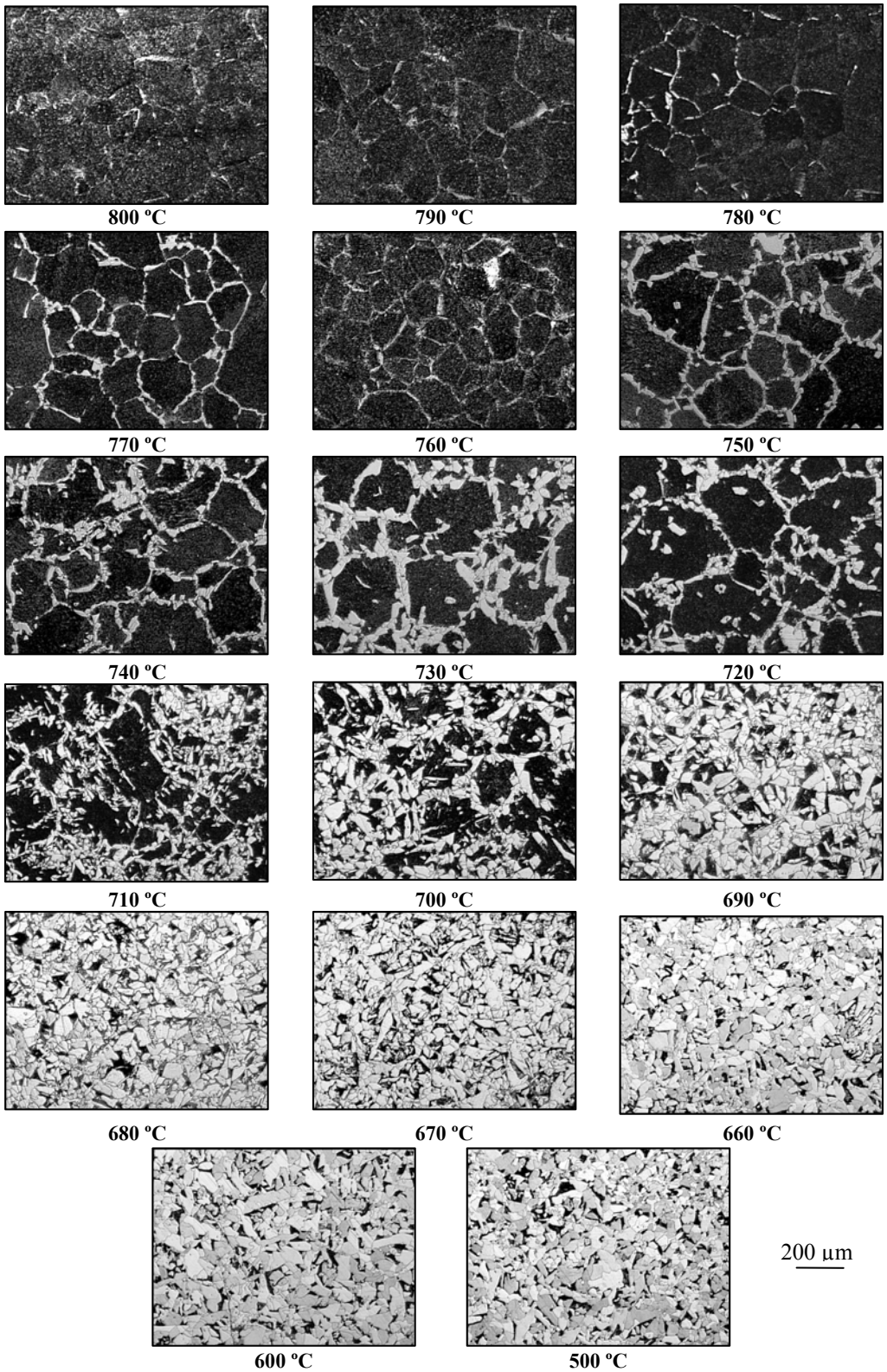

Figure 5.25: Decomposition behavior of the prior austenite microstructure in the TiO steel as a function of cooling temperature.

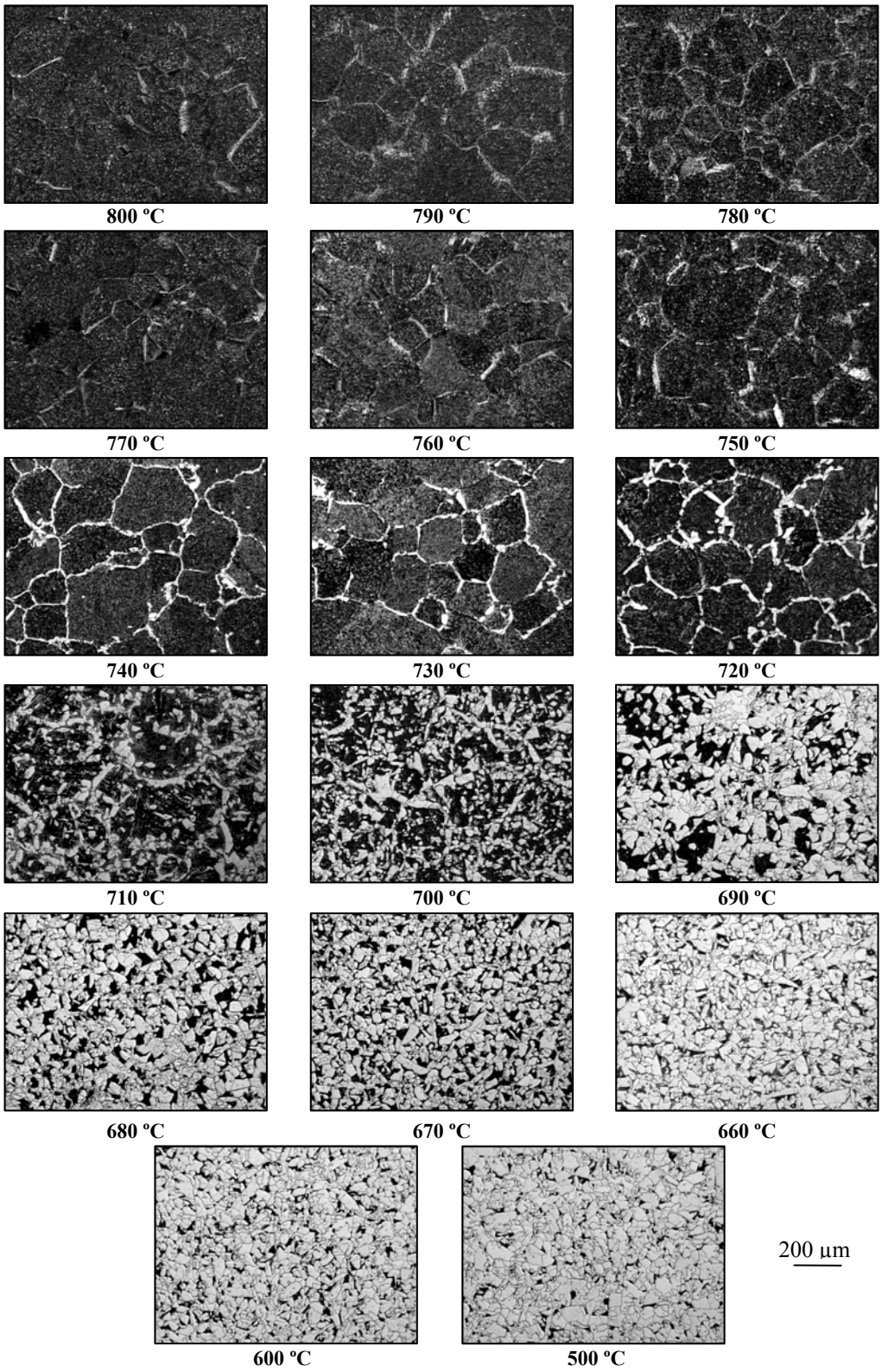

Figure 5.26: Decomposition behavior of the prior austenite microstructure in the MnS steel as a function of cooling temperature.

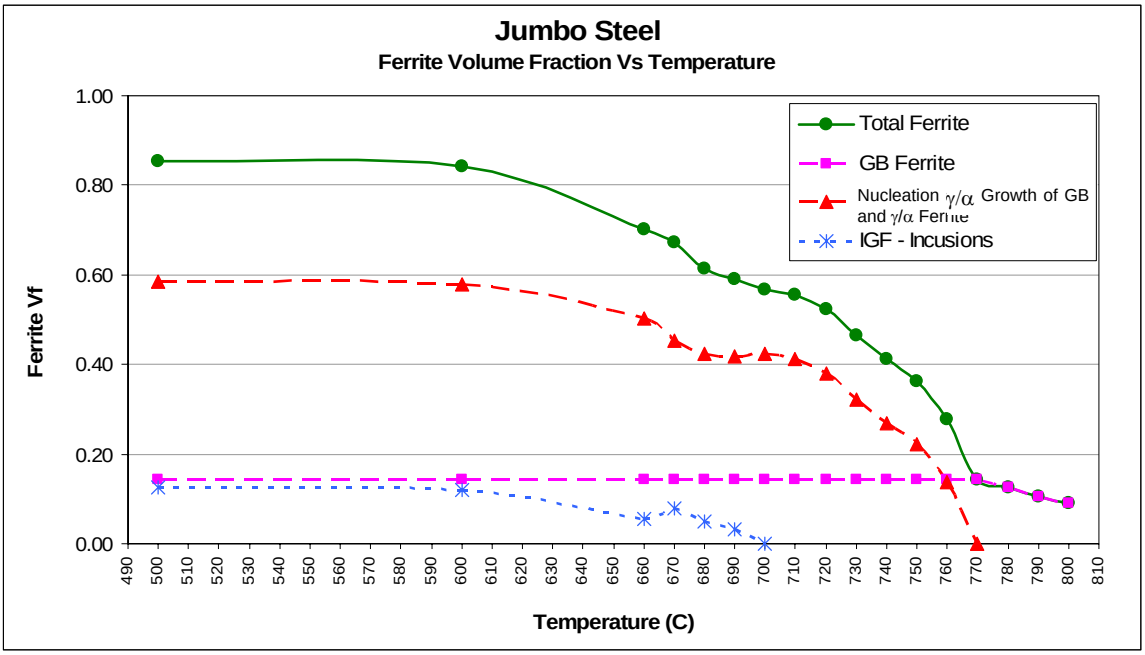

Figure 5.27: The variation of ferrite volume fraction as a function of cooling temperature in the Jumbo steel. Samples were cooled from 1250 to 825°C at 0.24°C/sec and then at 0.08°C/sec.

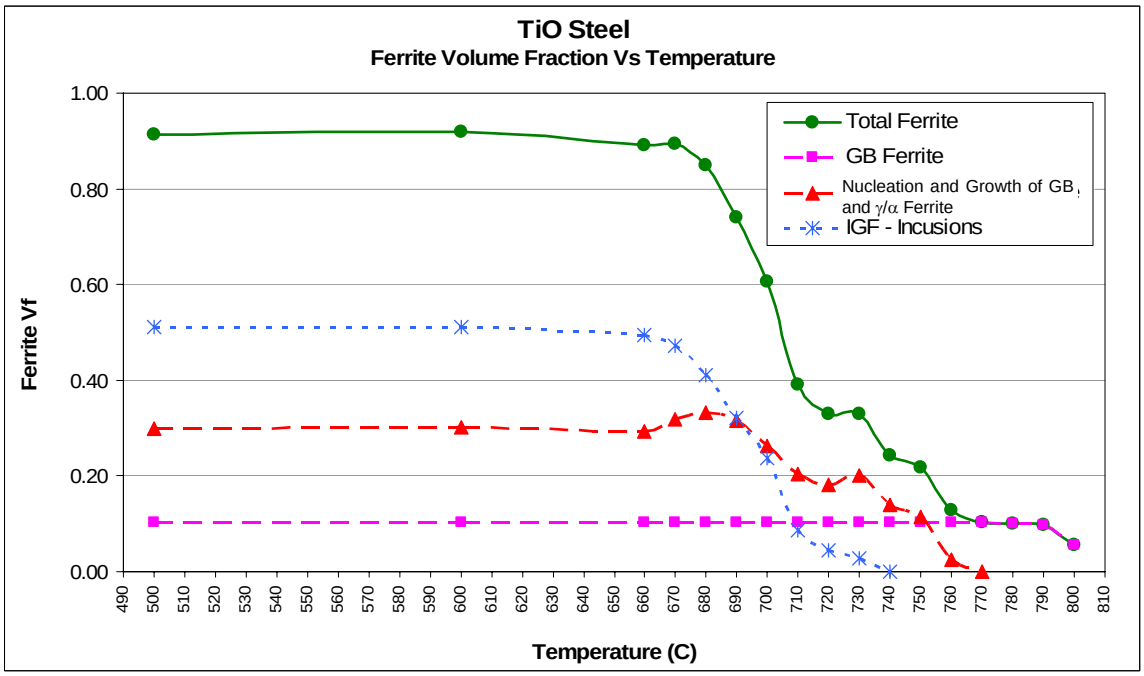

Figure 5.28: The variation of ferrite volume fraction as a function of cooling temperature in the TiO steel. Samples were cooled from 1300 to 825°C at 0.24°C/sec and then at 0.08°C/sec.

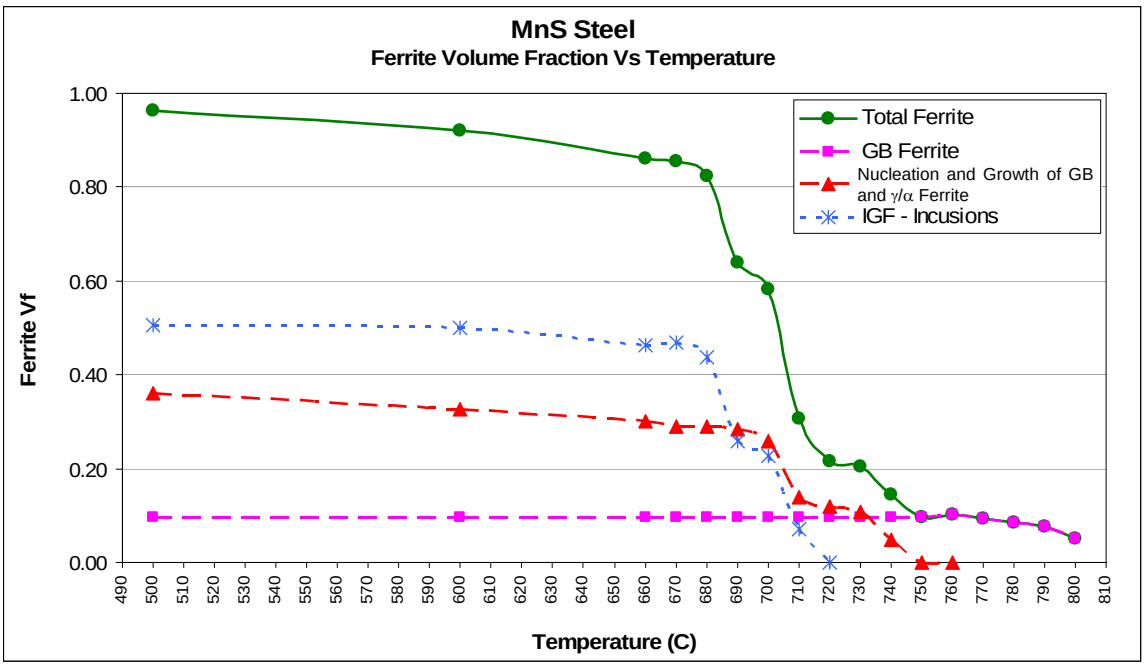

Figure 5.29: The variation of ferrite volume fraction as a function of cooling temperature in the MnS steel. Samples were cooled from 1350 to 825°C at 0.24°C/sec and then at 0.08°C/sec.

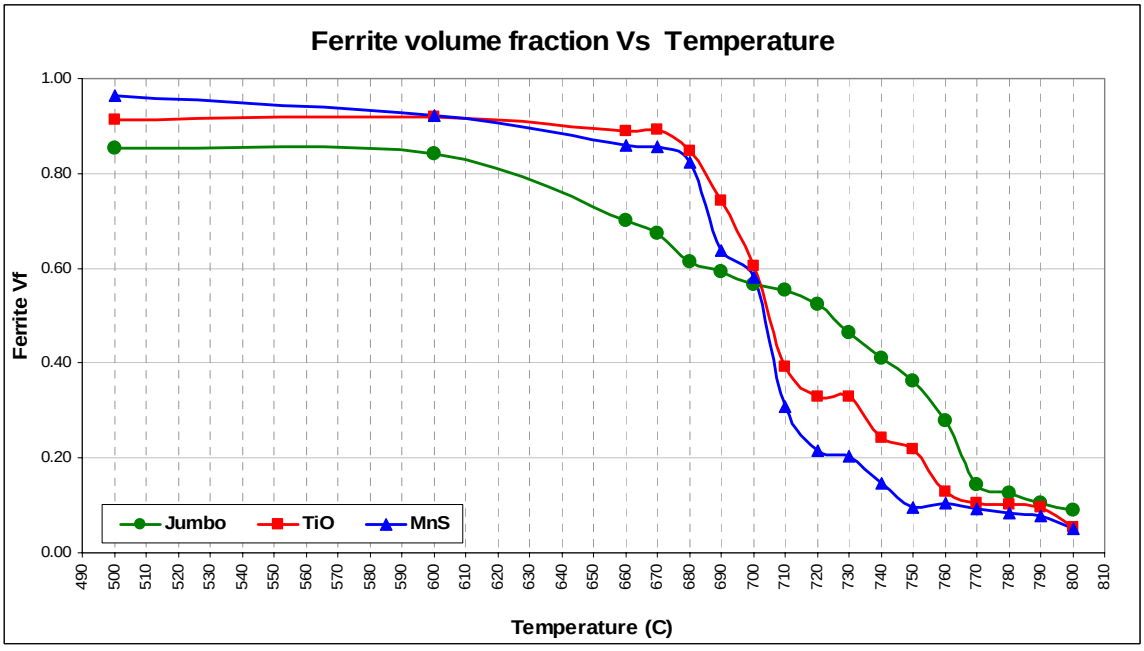

Figure 5.30: The variation of total ferrite volume fraction as a function of cooling temperature in the three steels. Samples were cooled from 1250, 1300 and 1350 to 825°C at 0.24°C/sec and then at 0.08°C/sec for the Jumbo, TiO and MnS steels, respectively.

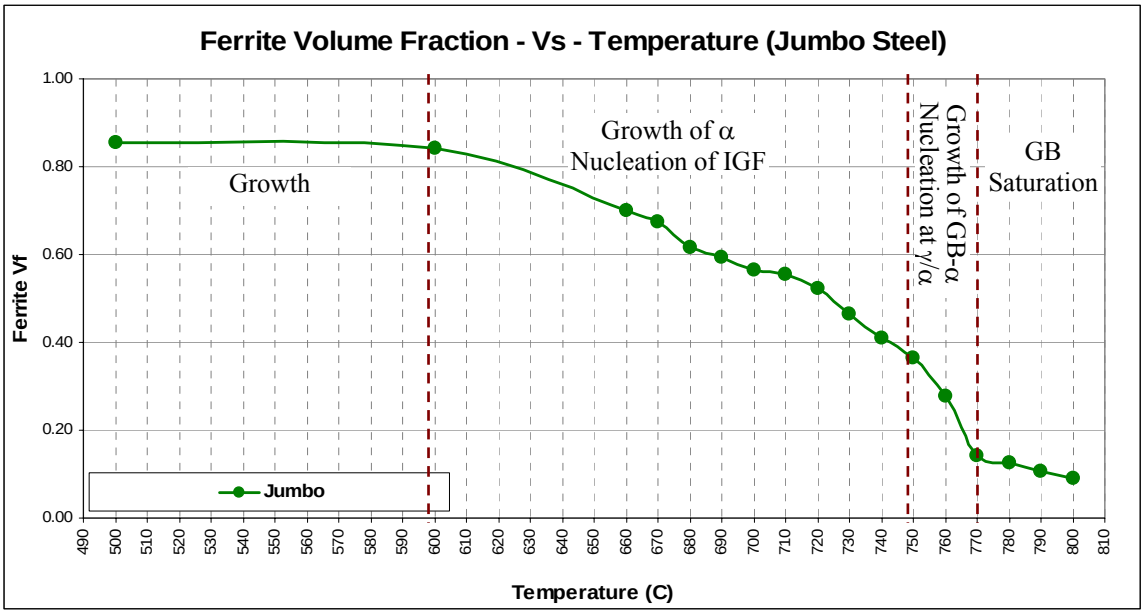

Figure 5.31: Austenite decomposition regions in the Jumbo steel. Samples were cooled from 1250 to 825°C at 0.24°C/sec and then at 0.08°C/sec.

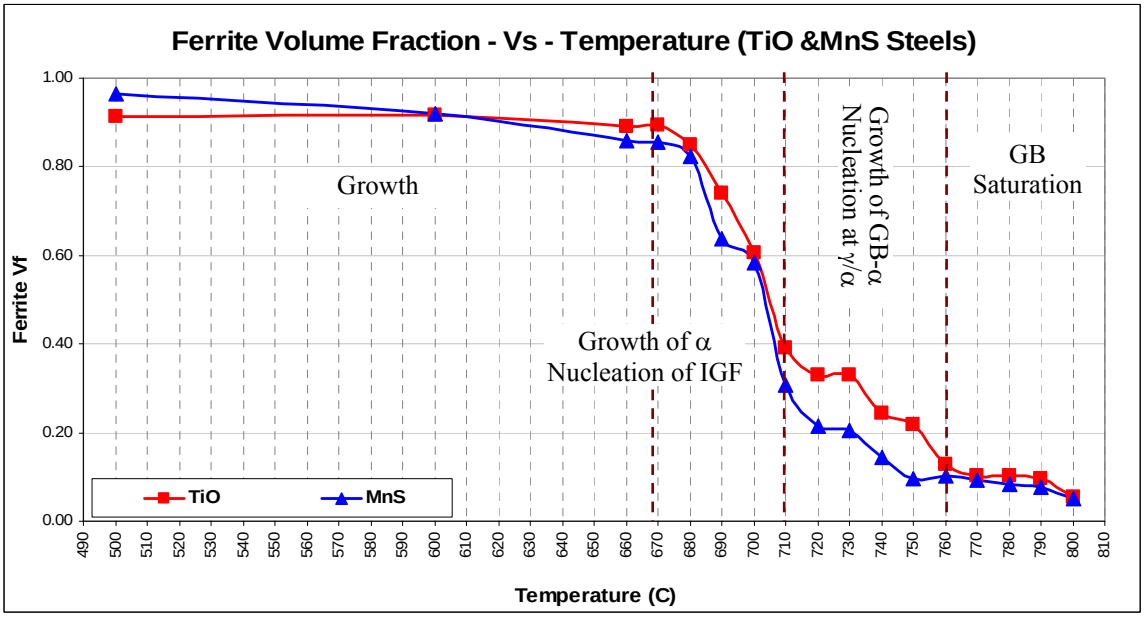

Figure 5.32: Austenite decomposition regions in the TiO and MnS steels. Samples were cooled from 1300 and 1350 to 825°C at 0.24°C/sec and then at 0.08°C/sec for the TiO and MnS steels, respectively.

5.5.3 Nucleation Sites of Ferrite

Based on the previous four stages of the austenite decomposition, three types of nucleation sites for ferrite were identified. The first nucleation site is located at the prior austenite grain boundaries (γ/γ-GB). Austenite grain boundaries are considered as the most effective nucleation sites due to the nature of the interface between grains. The second nucleation site is located at the (γ/I) interface, while the third nucleation site is located at the interface of the ferrite that had previously nucleated at the (γ/γ-GB) and/or (γ/I) interfaces and defined as (γ/α) sites. The nucleation sites are depicted in the optical microstructure shown in Figure 5.33.

The variation of the ferrite volume fraction as a function of the nucleation sites is listed quantitatively in Table 5-8 and presented graphically in Figure 5.34. The variation of ferrite volume fraction with the nucleation sites in the three steels confirms the similarity between the MnS and TiO steels. The volume fraction of grain boundary nucleating ferrite (V_{GB}) is about the same in the three steels. However, by considering the difference in the ferrite grain size between the steels, the number density of ferrite per unit area for MnS and TiO steels is higher than that of the Jumbo steel. The volume fraction of IGF (V_{IGF}) is approximately equal for the TiO and MnS steels despite that the amount of inclusions in the TiO steel is one half that of the MnS steel. This behavior indicates that the TiO inclusions are remarkably more active than the MnS inclusions. However, due to the higher contents of the inclusions, the V_{IGF} of the TiO and MnS steels is four times higher than the V_{IGF} of the Jumbo steel.

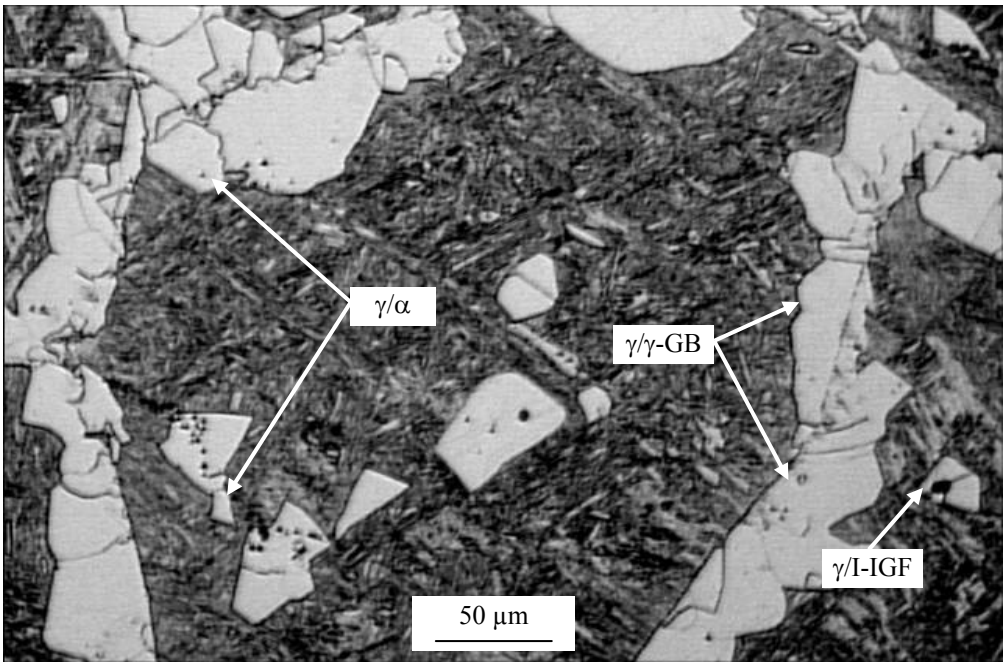

Figure 5.33: Ferrite nucleation sites in the MnS steel. Sample was cooled from 1350 to 825°C at 0.24°C/sec and then at 0.08°C/sec before water quenched at 710°C.

Table 5-8: The variation of the ferrite volume fraction as a function of the nucleation sites in the three steels.

Steel	Volume Fraction of Ferrite in Different Nucleation Sites		
	γ/γ-GB	γ/α	γ/I-IGF
Jumbo	0.142	0.585	0.127
TiO	0.103	0.300	0.511
MnS	0.096	0.362	0.506

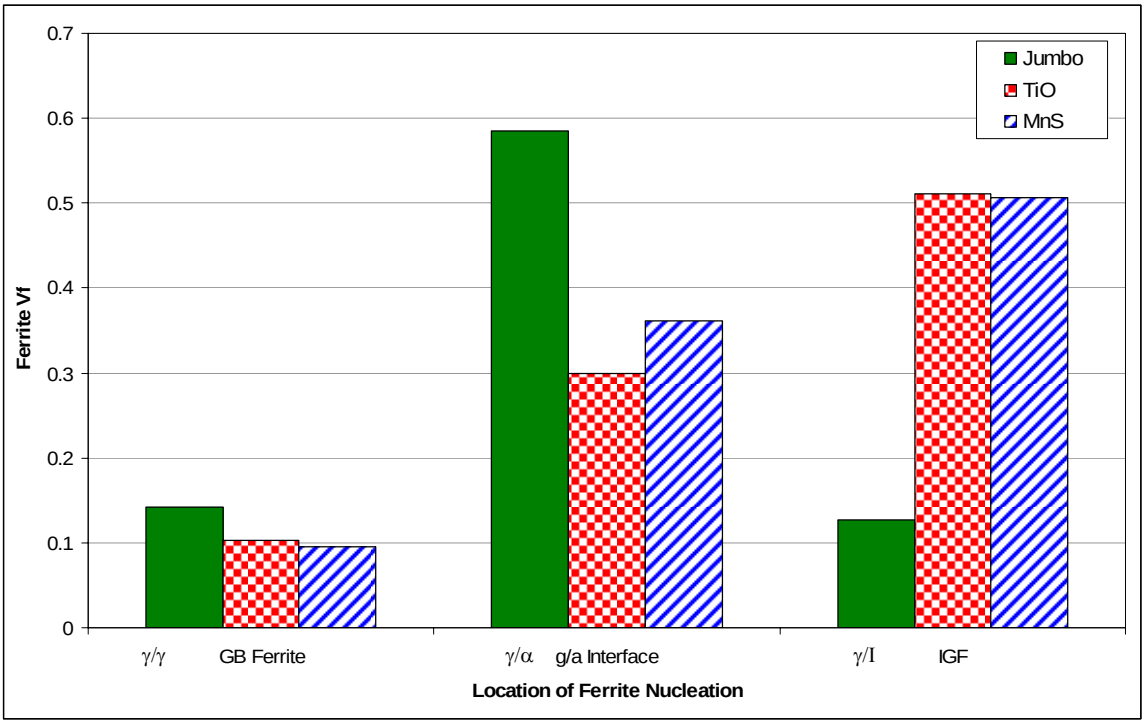

Figure 5.34: Comparison of the volume fraction of ferrite nucleated at different sites in the end of the decomposition behavior of the three steels.

5.5.4 Nucleation and Growth Rates of Ferrite

The nucleation and growth rates at the four different stages of the austenite decomposition process were determined based on the variation of the ferrite volume fraction within each stage. The change of the ferrite volume fraction as a function of time was drawn based on the relation between the ferrite volume fraction and the cooling temperatures. The volume fraction-time curves for Jumbo, TiO and MnS steels are shown in Figure 5.35, Figure 5.36 and Figure 5.37, respectively. The nucleation and growth rate at each stage was represented by the slope of the curve at that stage. The data is quantitatively shown in Table 5-9.

Noticeably, the TiO and MnS steels have similar nucleation and growth rates in all stages. However, the nucleation and growth rates for the three materials were approximately equal in the first and fourth stages. In the first stage, the nucleation and growth rate for the MnS steel was slower than the other two materials due to the higher hardenability. In the second stage, the nucleation and growth rates of the jumbo steel are twice the rates of the TiO and MnS steels. This could be interpreted as a result of the earlier austenite grain boundary saturation in the Jumbo steel which allows more growth at high temperatures comparing to the other two steels. Moreover, the availability of the inclusions in the TiO and MnS steels favor the IGF nucleation and decrease the opportunity of the growth at this stage. Due to the high content of inclusions, the third stage of the TiO and MnS steels showed significantly higher nucleation rates which were five times higher than the nucleation rate of the Jumbo steel. All the three steels showed similar behavior as the temperature decreased in the forth stage where the nucleation was terminated and the growth rates were hindered as a result of low diffusivity.

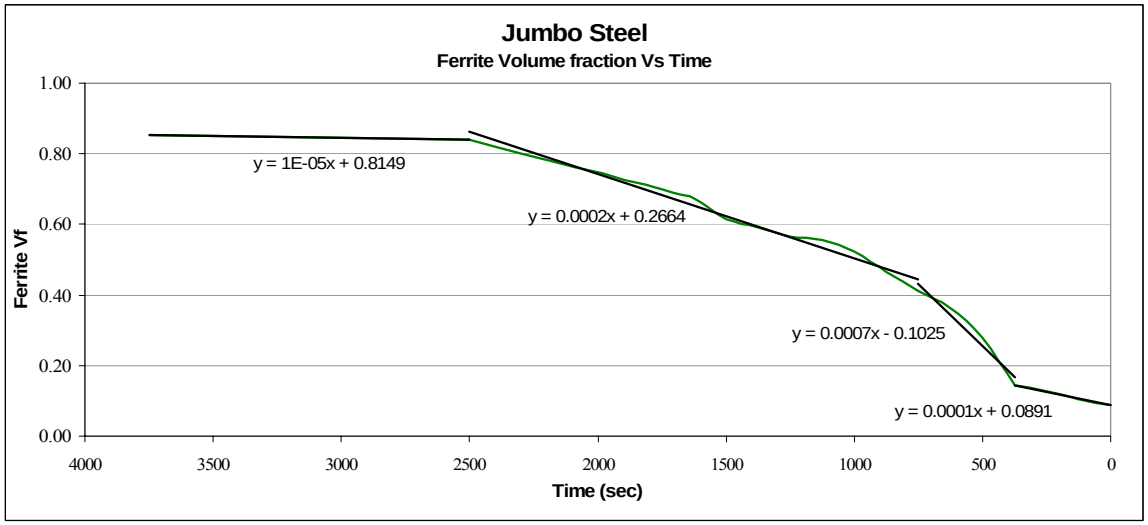

Figure 5.35: The variation of ferrite volume fraction as a function of time in the Jumbo steel.

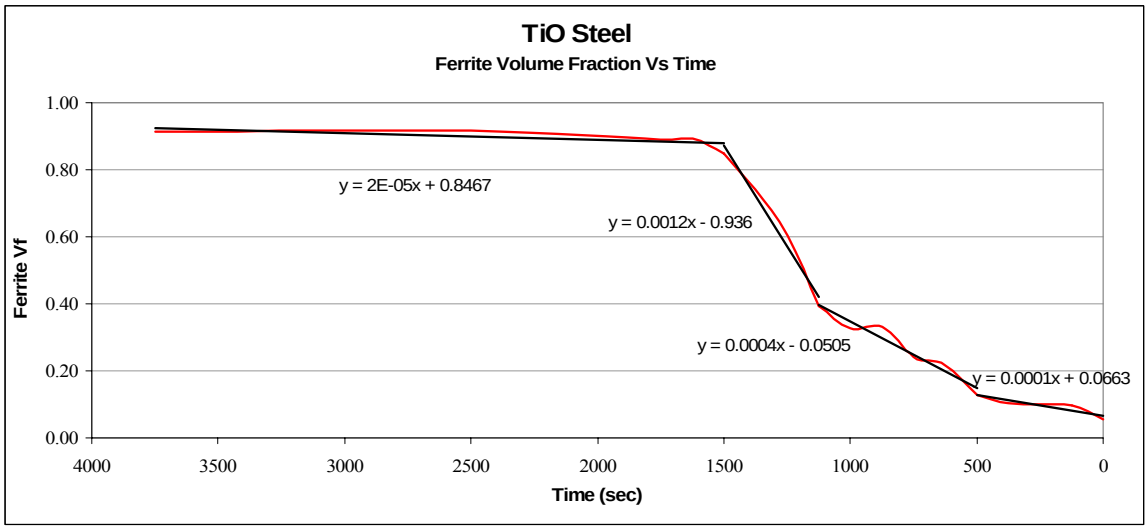

Figure 5.36: The variation of ferrite volume fraction as a function of time in the TiO steel.

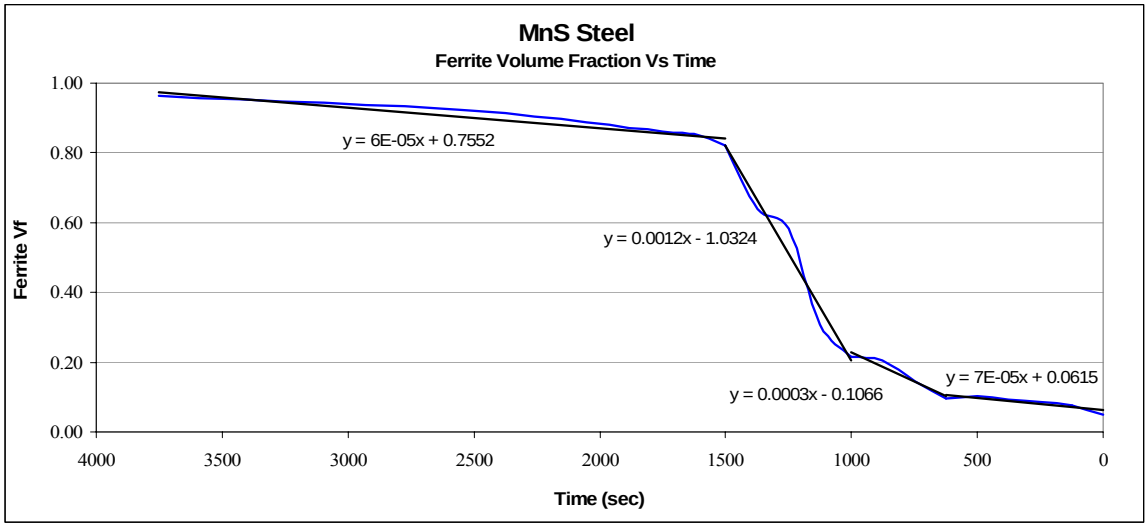

Figure 5.37: The variation of ferrite volume fraction as a function of time in the MnS steel.

Table 5-9: Ferrite nucleation and growth rates of the three steels.

Steel	Ferrite Nucleation an Growth Rates (mm^{-2} sec^{-1})			
	Regions in the ferrite volume fraction – time curve			
	(1) GB Saturation γ/γ	**(2)** Growth of GB-α Nucleation at γ/α	**(3)** Growth of α Nucleation of IGF	**(4)** Growth
Jumbo	140	885	251	10
TiO	122	395	1200	25
MnS	72	345	1240	58

5.6 FERRITE NUCLEATION MECHANISMS

5.6.1 IGF Nucleation Behavior

The study of the decomposition behavior of the austenite during the controlled cooling process confirmed that the nucleation of IGF was significantly stimulated below 720 °C for TiO and MnS steels. However, the insightful investigation of the IGF nucleation behavior showed that the nucleation at the γ/I interfaces was started at higher temperatures. As the optical and SEM micrographs shown in Figure 5.38, the first IGF nucleation event in the TiO and MnS steels was noticed at 750 and 740 °C, respectively. At these temperatures, the nucleation of IGF was noticed at the large inclusions that ranged above 10.0 μm in the TiO steels and above 4.0 μm in

the MnS steel. Due to the small surface curvature, the large inclusions are usually more effective in heterogeneous nucleation than the smaller ones.

It was noticed that the large Ti-oxide inclusions (> 3.0 μm) usually associated with nucleation of more than one ferrite grain, while the small inclusions are commonly nucleated one ferrite grain. This could be a result of the large surface area of the large inclusions which provide sufficient nucleation sites for more than one ferrite grain. However, the characterization of the inclusions in the TiO steel showed that the size range expanded between 0.12 and 21.0 μm, and approximately 9.0% of the inclusions were larger than 3.0 μm. The optical micrographs of IGF nucleation events at different temperatures in the TiO steel are shown in Figure 5.39.

On the other hand, MnS inclusions were occasionally associated with more than one ferrite grain. The characterization of the inclusions in this steel showed that the size range expanded between 0.16 and 10.0 μm, and about 6.3 % of the MnS inclusions were bigger than 3.0 μm. The nucleation of IGF at different temperatures in the MnS steel is shown in Figure 5.40.

Moreover, there is evidence that nucleation occurs preferentially at pairs or groups of particles as shown in Figure 5.41. This may occur even if the individual particles are below the critical size of nucleation. This type of nucleation was noticed in the MnS steel due to the inhomogeneous distribution of the particles.

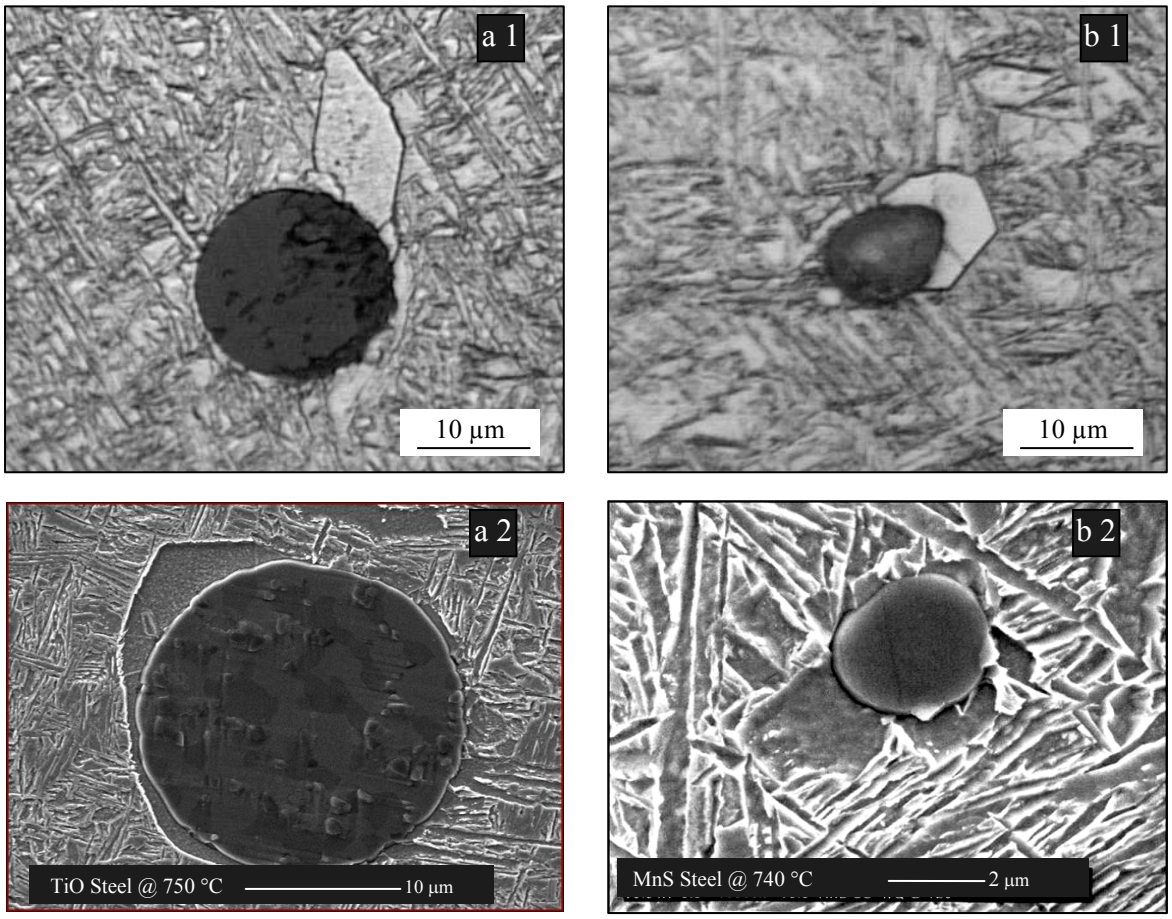

Figure 5.38: IGF nucleation at the (γ/I) interface in: a) Ti-oxide inclusions at 750°C in the TiO steel, (a1) optical) and (a2) SEM. b) MnS inclusion at 740°C in the MnS steel, (a1) optical) and (a2) SEM. Samples were cooled to 825°C at 0.24°C/sec and then at 0.08°C/sec before water quenched.

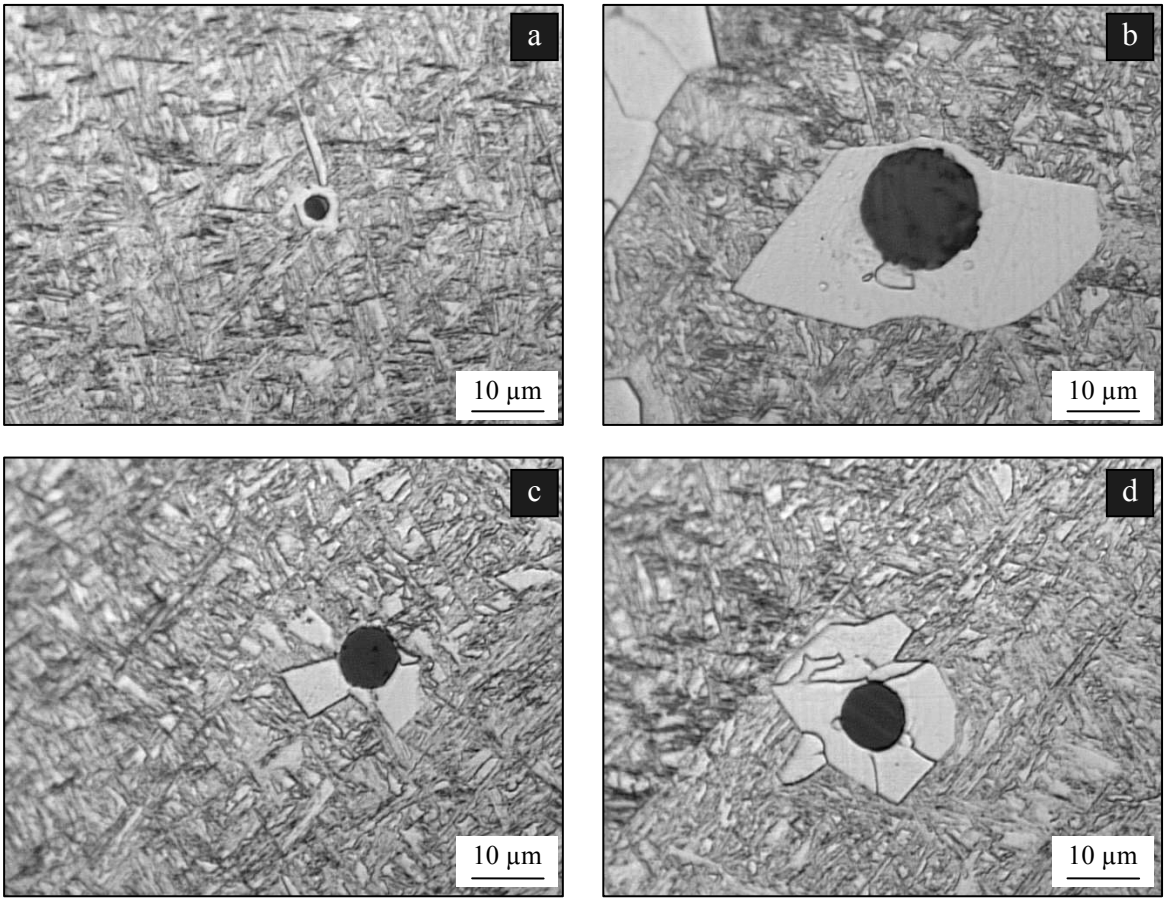

Figure 5.39: Nucleation of IGF at the Ti-oxide inclusions in the TiO steel. a) Small inclusion (2.5 µm) nucleated one ferrite grain at 730 °C. b) Large inclusion (13.8 µm) nucleated one ferrite grain at 740°C. c) Large inclusion (7.1 µm) nucleated two ferrite grains at 740 °C. d) Large inclusion (8.3 µm) associated with more than three ferrite grains at 740 °C. Samples were cooled from 1300 °C to 825°C at 0.24°C/sec and then at 0.08°C/sec before water quenched.

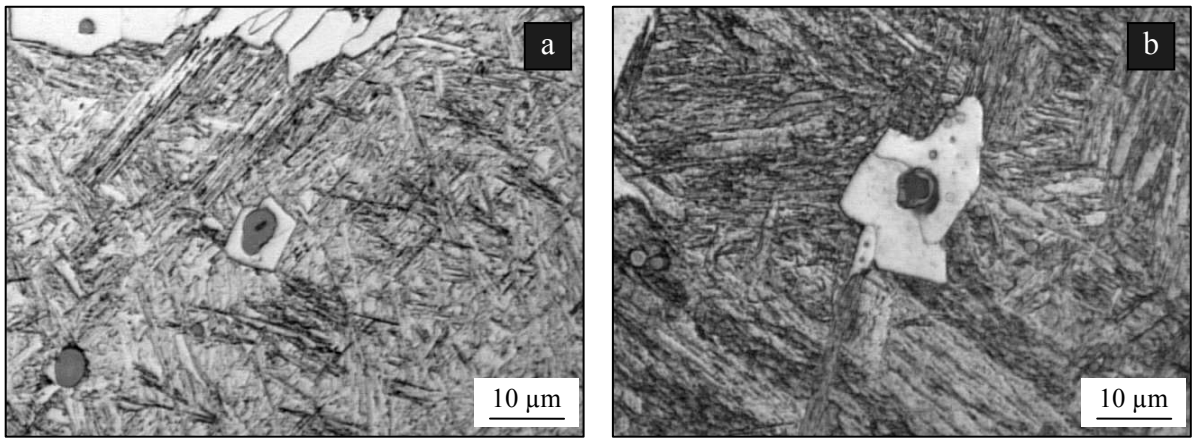

Figure 5.40: Nucleation of IGF at the MnS inclusions in the MnS steel. a) Inclusion (4.7 μm) nucleated one ferrite grain at 740 °C. b) Inclusion (4.5 μm) nucleated two ferrite grains at 720 °C. Samples were cooled from 1350 °C to 825°C at 0.24°C/sec and then at 0.08°C/sec before water quenched.

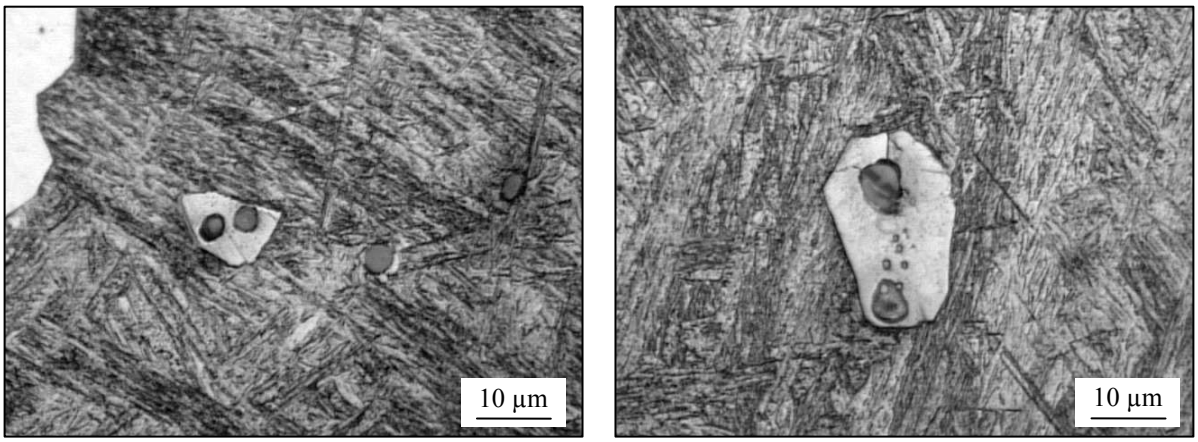

Figure 5.41: Nucleation IGF at a cluster of MnS particles in the MnS steel at 720 °C. Samples were cooled from 1350 °C to 825°C at 0.24°C/sec and then at 0.08°C/sec before water quenched.

5.6.2 Effect of the Inclusion size

During the study of the austenite decomposition behavior, it has been observed that the nucleation of IGF was notably stimulated in temperatures ranged from 720 to 680°C for the TiO and MnS steels. SEM investigation of the samples that were cooled within this range of temperatures showed that only specific sizes were strongly active within the IGF nucleation region. This range of sizes varied according to the type of inclusions. Therefore, the effect of the inclusion size was studied as a function of the cooling temperature. In each particular temperature within this range, only the inclusions that definitely participate in the IGF nucleation event were considered in this analysis. Examples of the active inclusions at different temperatures are shown in Figure 5.42

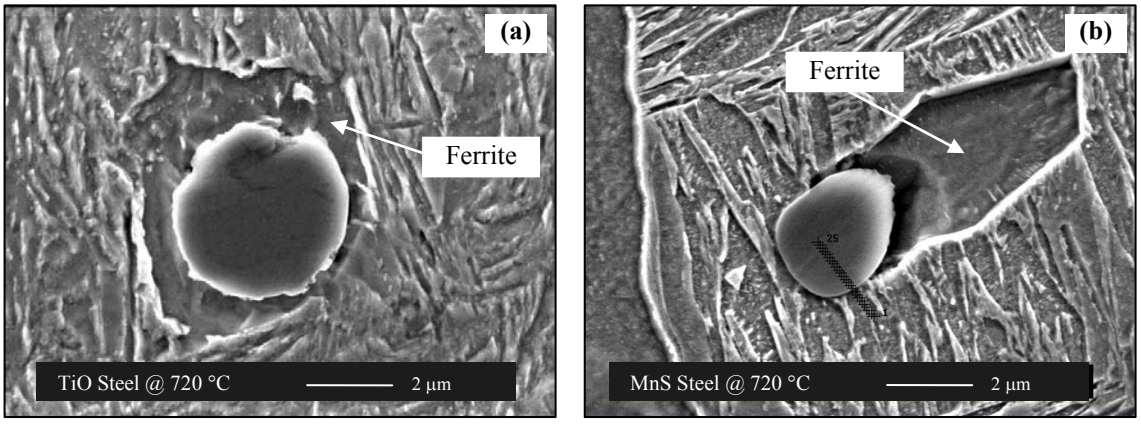

Figure 5.42: SEM micrographs show the nucleation of ferrite intragranularly at the γ/I interface in the: (a) TiO and (b) MnS steels. Samples were cooled to 825°C at 0.24°C/sec and then at 0.08°C/sec before water quenched.

The analysis of the TiO steel showed that the most active size of Ti-oxide particles was above 2.0 μm. Although the volume fraction of this range of sizes was only about 14% of the total volume fraction of available inclusions, more than 95% of the intragranular nucleation events were found in that range of sizes. The relation between the inclusion size distribution and the size of active inclusions is shown in Figure 5.43. The cumulative curve shows that the majority of IGF nucleation events occurred in inclusions larger than 2.0 μm. For comparison purposes with the MnS steel, the curves were redrawn eliminating the effect of inclusions larger than 6.0 μm as shown in Figure 5.44. Clearly, the Ti-oxide inclusions ranging in size 2.0 to 6.0 μm were responsible for more than 60% of IGF nucleation events in the TiO steel. The total number of particles per unit area for the active inclusions (>2.0 μm) was 7.6×10^{-5} μm^{-2}, which forms only about 14% of the total number of particles per unit area of all available inclusions (5.41×10^{-4} μm^{-2}). Hence, only 14% of the total number of inclusions was active in the nucleation of IGF.

The relation between the size distribution of active inclusions and the cooling temperature is shown in Figure 5.45. Within the active range of sizes (>2.0 μm), the nucleation of IGF started at 720°C on the large inclusions that have an average size of 4.3 μm. The smallest active inclusion at this temperature was greater than 2.5μm, while the largest one was about 20.0 μm. With decreasing the temperature, finer inclusions started to contribute in the IGF nucleation event. At 680°C, the average size of active inclusions decreased to 3.6 μm. However, the smallest active inclusion that observed within this range of temperatures (720- 680°C) was 0.8 μm. In general, the average size of active inclusions decreased as the degree of undercooling increased and the number of available large particles decreased. The cumulative curves show that the 60 to 80 % of the IGF nucleation took place within the 2.0 to 6.0 μn inclusions range.

On the other hand, the analysis of the MnS steel showed that the most active size of MnS particles was above the 1.0 μm. The volume fraction of this range of sizes was approximately 53% of the total volume fraction of available inclusions. However, approximately 90% of the intragranular nucleation events were found in that range of sizes (1.0 - 6.0 μm). The relation between the MnS inclusion size distribution and the size of active inclusions is shown in Figure 5.46. Within the active range of sizes, the IGF nucleated preferentially on the inclusions that have average size of 1.0 to 3.5 μm. More than 70 % of IGF nucleation events in the MnS steel took place at that range. The total number of particles per unit area for the active inclusions (>1.0 μm) was 8.3×10^{-4} μm^{-2}, which forms around 53% of the total number of particles per unit area of all available inclusions (1.56×10^{-3} μm^{-2}). Hence, only 53% of the total number of inclusions was active in the nucleation of IGF.

The relation between the size distribution of active inclusions and the cooling temperature is shown in Figure 5.47. Within the active range of sizes (>1.0 μm), the nucleation of IGF occurred in inclusions that have an average size ranged from 2.1 to 2.6μm. The largest active inclusion (8.5μm) was observed at 720 °C, while the finest one (0.6μm) was observed at 680 °C.

In conclusion, the above results confirmed that Ti-oxides inclusions are more active than MnS inclusions in nucleating IGF. A similar degree of refinement was achieved in the TiO steel with using significantly less number of inclusions than the MnS steel. In TiO steel, only 14% of available inclusions were involved in the nucleation of IGF with total volume fraction of 2.04×10^{-4} and the total number of inclusions per unit area was 7.6×10^{-5} μm^{-2}. On the other hand, about 53% of inclusions were participating in the IGF nucleation in the MnS steel, with total volume fraction of 1.76×10^{-3} and the total number of inclusions per unit area was 8.3×10^{-4} μm^{-2}.

In other word, the number of MnS inclusions per unit area was eleven times larger than the number of Ti-oxide inclusions.

However, two main facts must be noticed regarding the Ti-oxide particles. The first one is that the majority of the large particles (> 3.0 μm) were observed nucleating multi-ferrite grains. This definitely improves the efficiency of the large Ti-oxides in nucleating IGF. The second fact is that the large inclusions contain complex compounds, which could enhance the ability of the particles in nucleating IGF.

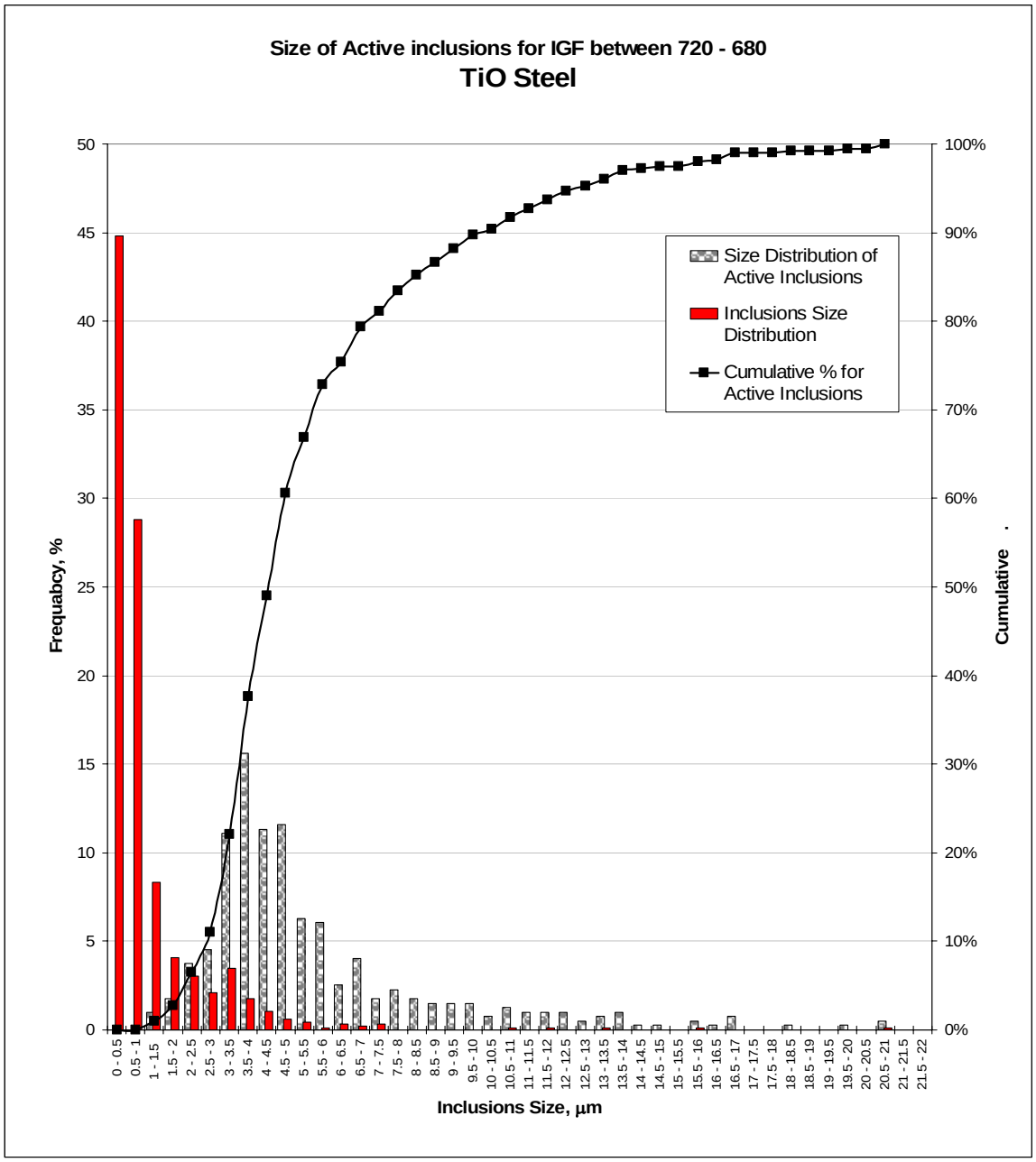

Figure 5.43: The relation between the inclusions size distribution and the size of active inclusions in IGF nucleation in the TiO steel.

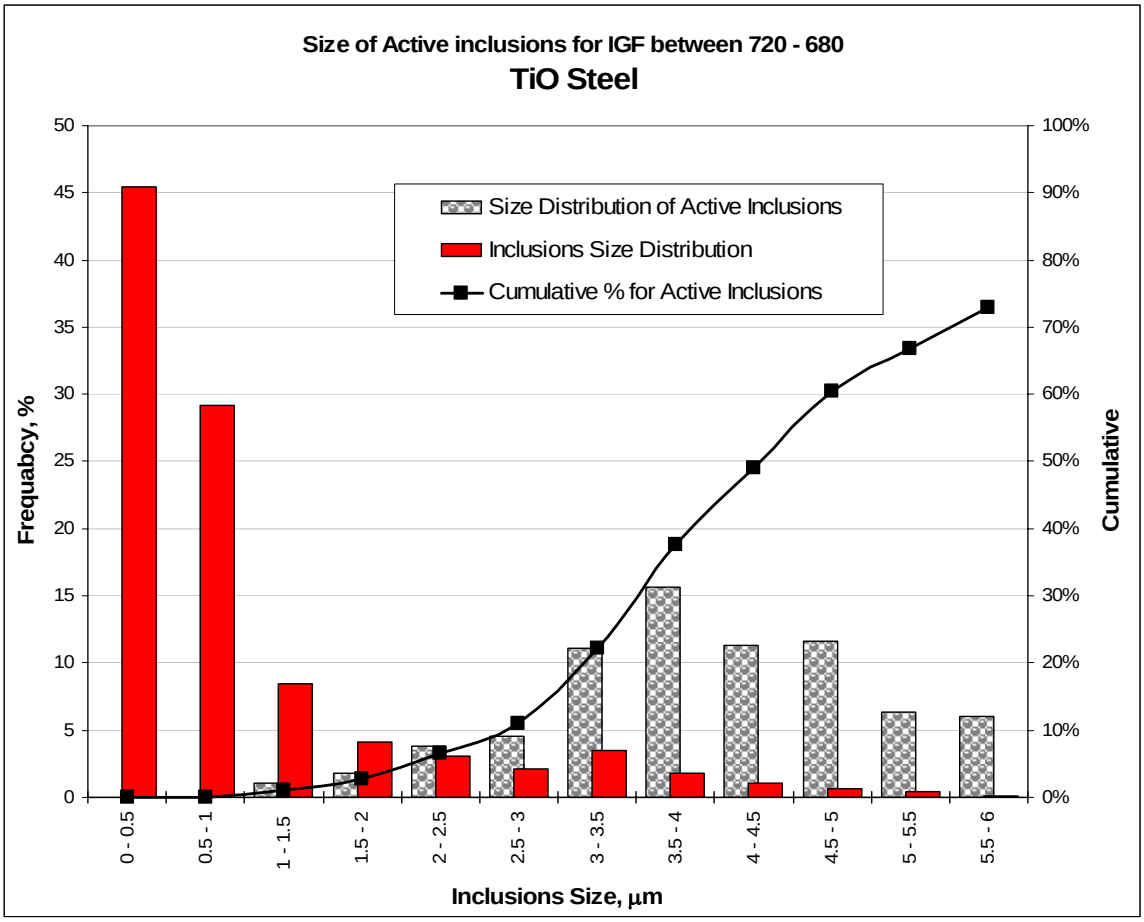

Figure 5.44: The relation between the inclusions size distribution and the size of active inclusions for particles less than or equal 6.0 μm in the TiO steel.

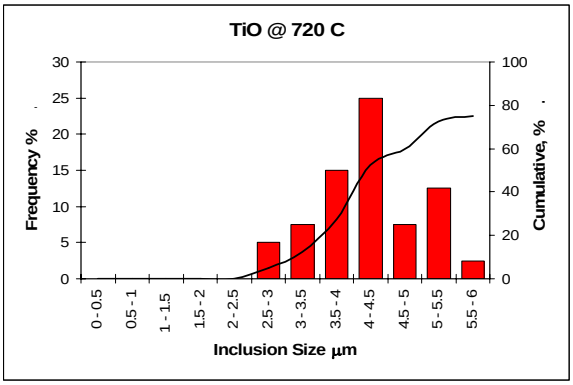

Ave. Inclusion Size = 4.26 ± 0.74 μm

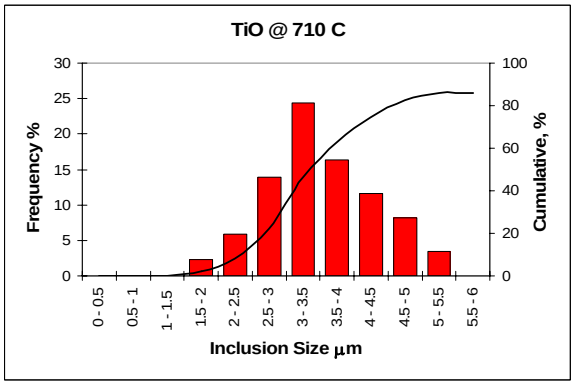

Ave. Inclusion Size = 3.55 ± 0.80 μm

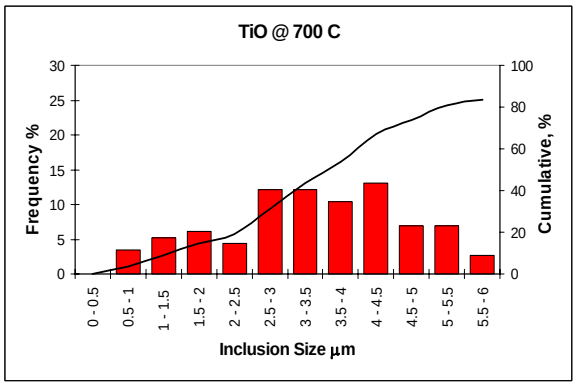

Ave. Inclusion Size = 3.42 ± 1.26 μm

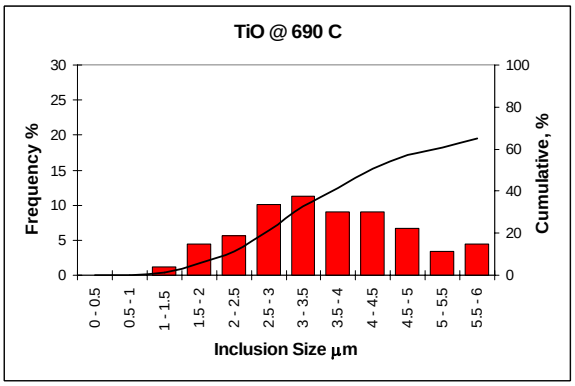

Ave. Inclusion Size = 3.6 ± 1.15 μm

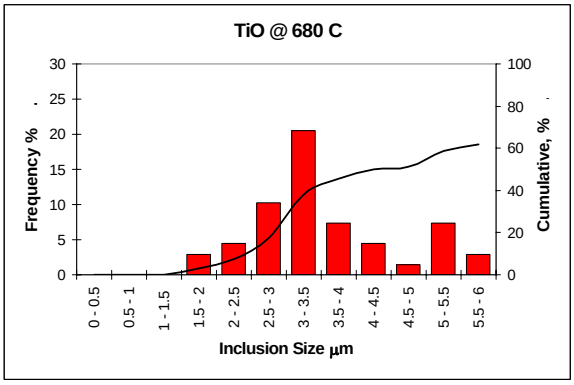

Ave. Inclusion Size = 3.58 ± 1.05 μm

Figure 5.45: The relation between the size distribution of active Ti-oxide and the cooling temperature in the TiO steel. Only inclusions size <6.0 μm was considered.

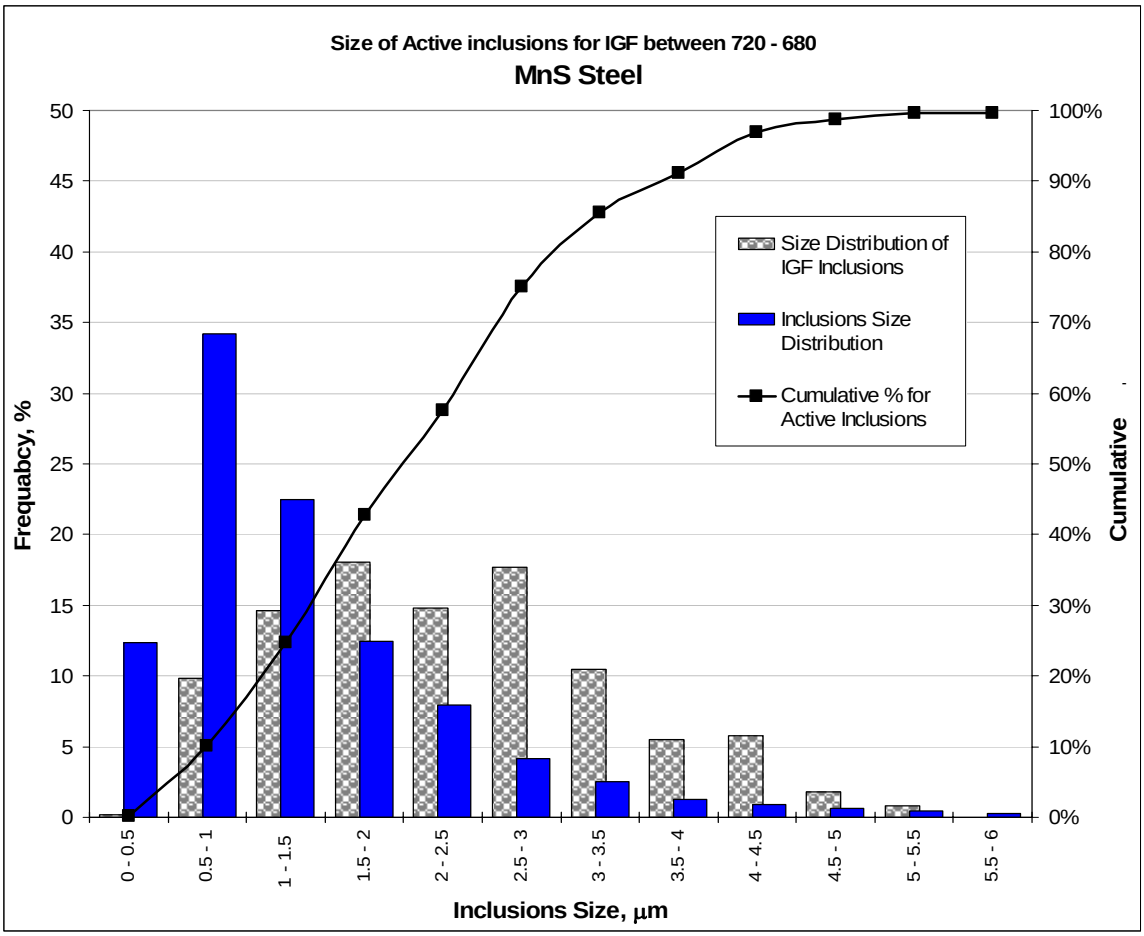

Figure 5.46: The relation between the inclusions size distribution and the size of active inclusions for particles less than or equal 6.0 μm in the MnS steel.

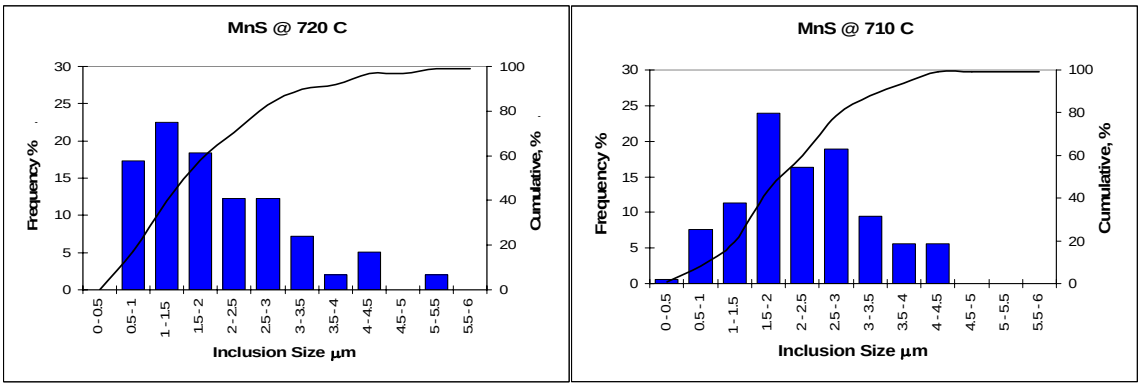

Ave. Inclusion Size = 2.10 ± 1.24 µm

Ave. Inclusion Size = 2.32 ± 1.0 µm

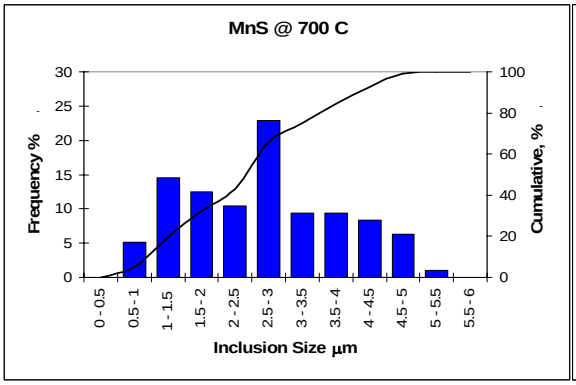

Ave. Inclusion Size = 2.67 ± 1.13 µm

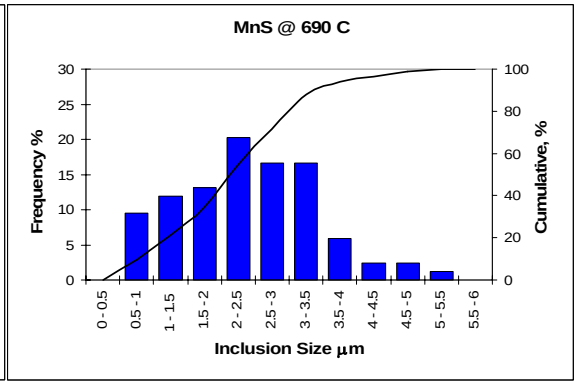

Ave. Inclusion Size = 2.44 ± 1.02 µm

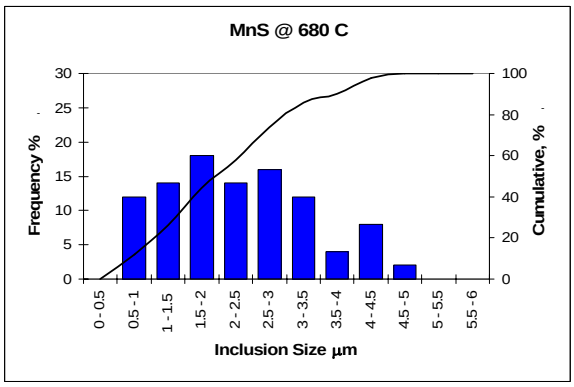

Ave. Inclusion Size = 2.31 ± 1.10 µm

Figure 5.47: The relation between the size distribution of active MnS inclusions and the cooling temperature in the MnS steel. Only inclusions size <6.0 µm was considered.

5.6.3 Effect of the S_V Value on the IGF Nucleation

The total available area per unit volume for ferrite nucleation, (S_V), and relative nucleation potential of intragranular to grain boundary nucleation, (*P*), were calculated based on Lee's [105] equations. The calculation of (*P*) values for the three steels showed that the Jumbo and MnS steels have approximately equal potential. This similarity is attributable to the effect of the MnS inclusions present in both materials. Due to the high efficiency of the Ti-oxide inclusions as the IGF nucleation sites, the TiO steel showed higher (*P*) values. The effectiveness of Ti-oxides inclusions is two times more than that of the MnS inclusions. This finding could be confirmed through considering the number of active particles per unit area for both steels. The amount of active MnS inclusions was eleven times above the amount of active Ti-oxide inclusions and both gave similar refining effect. The calculated values are quantitatively listed in Table 5-10.

The austenite grain sizes for the three steels were calculated with considering the contribution of the available surface area of intragranular inclusions (S_{VI}). The activity of the γ/I sites was assumed to be equal to the γ/γ-GB sites, therefore (S_{VI}) was considered as a (S_{VGB}). The corrected sizes of the austenite grain boundaries for the Jumbo, TiO and MnS steels were calculated as 356, 195 and 132 μm, respectively. However, this corrected value did not consider the volume fraction of the effective inclusion size for the TiO and MnS steels, which was remarkably below the total volume fraction. The measured and calculated values of the prior austenite grain size were compared with the Saito and Sellars approaches in Figure 5.48.

Table 5-10: Calculated value of the surface area per unit volume and the relative nucleation potential of intragranular to grain boundary nucleation for the three steels.

Calculated Values	Steel		
	Jumbo	TiO	MnS
D_γ (μm)	372	240	230
D_I (μm)	1.37	1.08	1.33
N_V (μm^{-3})	3.72×10^{-5}	5.01×10^{-4}	1.17×10^{-3}
$S_{VGB} = 2/D_\gamma$ (mm^{-1})	5.4	8.4	8.7
$S_{VI} = \pi N_V D_I^2$ (mm^{-1})	0.22	1.84	6.5
$S_V = S_{VGB} + S_{VI}$ (mm^{-1})	5.62	10.24	15.2
$D\gamma = 2 / S_V$ (μm)	356	195	132
S_{VI}/ S_{VGB}	0.041	0.22	0.75
V_{IGF}/V_{GB}	0.39	4.48	5.27
$P = V_{IGF}/V_{GB} . S_{VGB}/S_{VI}$	9.51	20.36	7.03

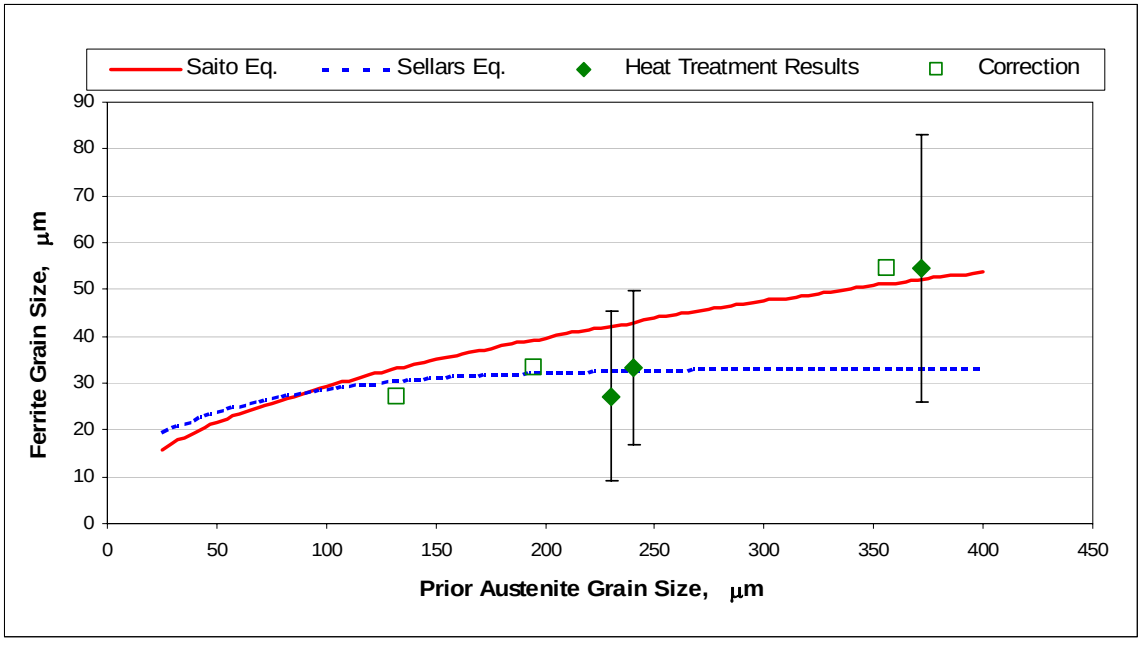

Figure 5.48: Variation of the measured and calculated values of the prior austenite grain size related to the Saito and Sellars approaches.

5.6.4 Effect of the Chemical Depletion Zone

There are numerous reports in the literature concerning the possible existence and role of the MDZ in enhancing ferrite nucleation at inclusions. [114, 122, 111, 125, 130] Therefore, the TiO and MnS steels were examined using energy dispersive x-ray microanalysis in the SEM to determine whether there was a pronounced Mn-depleted zone (MDZ) surrounding the inclusions. Both inclusions that acted as nucleation sites for ferrite and those inert inclusions that did not nucleate ferrite were examined for the TiO and MnS steels. Energy dispersive x-ray (EDX) microanalysis in the SEM was used obtain a semi-quantitative indication as to whether there is a significant zone surrounding the inclusion which has a reduced Mn level. Even though the MDZ, around the inclusions was considered as an effective factor that could assist the IGF nucleation, no clear evidence was found in this study to support this view. However, it must be noted that the spatial resolution of the microanalysis technique used in this study would only be capable of detecting significant depletion (~50% relative) over a distance of ~1 μm. For a more accurate quantitative analysis of the region <~0.5 μm from the inclusion interface, it would be necessary to perform quantitative STEM-EDS microanalysis using thin (~100 nm or less) foils.

Two examples of SEM-EDX semi-quantitative analysis of the region around the Ti-oxide inclusions in the TiO steels are shown in the EDS profiles in Figure 5.49 and Figure 5.50. The results indicate that the MDZ, if it exists, is less than the spatial resolution of the SEM-EDS technique. The profiles shown in Figure 5.50 do not show measurable Mn depletion, although the profile in (b) has a minimum at the interface, which may be related to the present of Al_2O_3 phase with the inclusion. Similar results were obtained from the MnS steel. The semi-

quantitative SEM-EDX linescan analysis of the MDZ around the MnS inclusions is shown in Figure 5.51. The wide variation in published results using SEM-EDX microanalysis, electron probe microanalysis (EPMA) and STEM-EDS microanalysis most likely reflect the pronounced difference in spatial resolution for analysis, ranging from ~0.5 to 1 micron (depending upon accelerating voltage for SEM-EDX and EPMA) to ~20 nm (STEM-EDS). Also, the ability to obtain quantitative microanalytical data is dependent upon the technique employed (and quantification procedure). Clearly, the optimum microanalytical data would be obtainable using field emission gun – scanning transmission electron microscopy (FEG-STEM) EDS microanalysis, where the attainable spatial resolution can be on the order of ~10 nm. It is also important that the specimen for analysis be on the order of ~100 nm or less in thickness. Thus, the wide variation in published results most likely reflects the wide range of techniques employed, and the very broad range of spatial resolution capabilities and quantification procedures used.

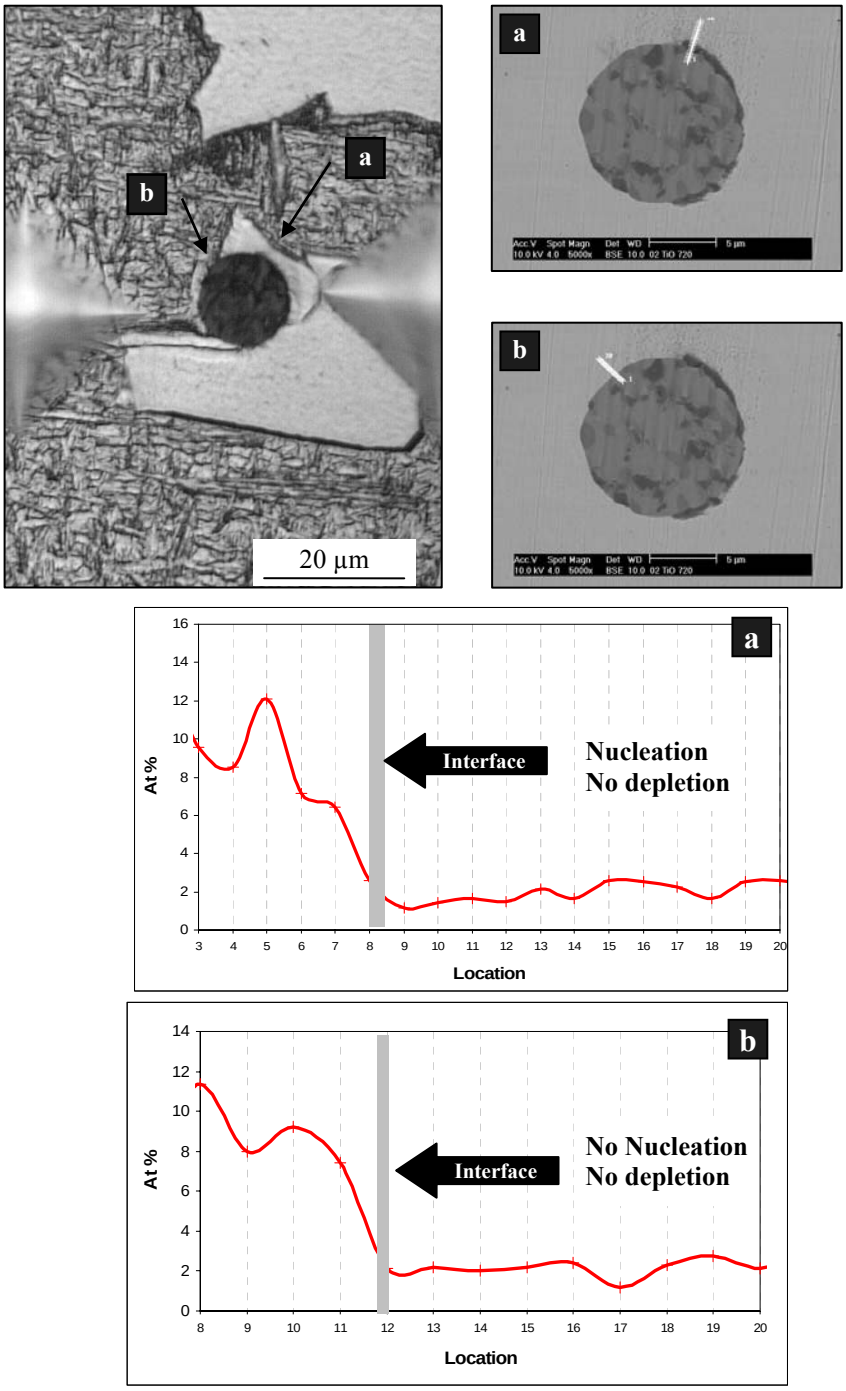

Figure 5.49: SEM-EDX semi-quantitative linescans analysis for Ti-oxide inclusion in the TiO steel.

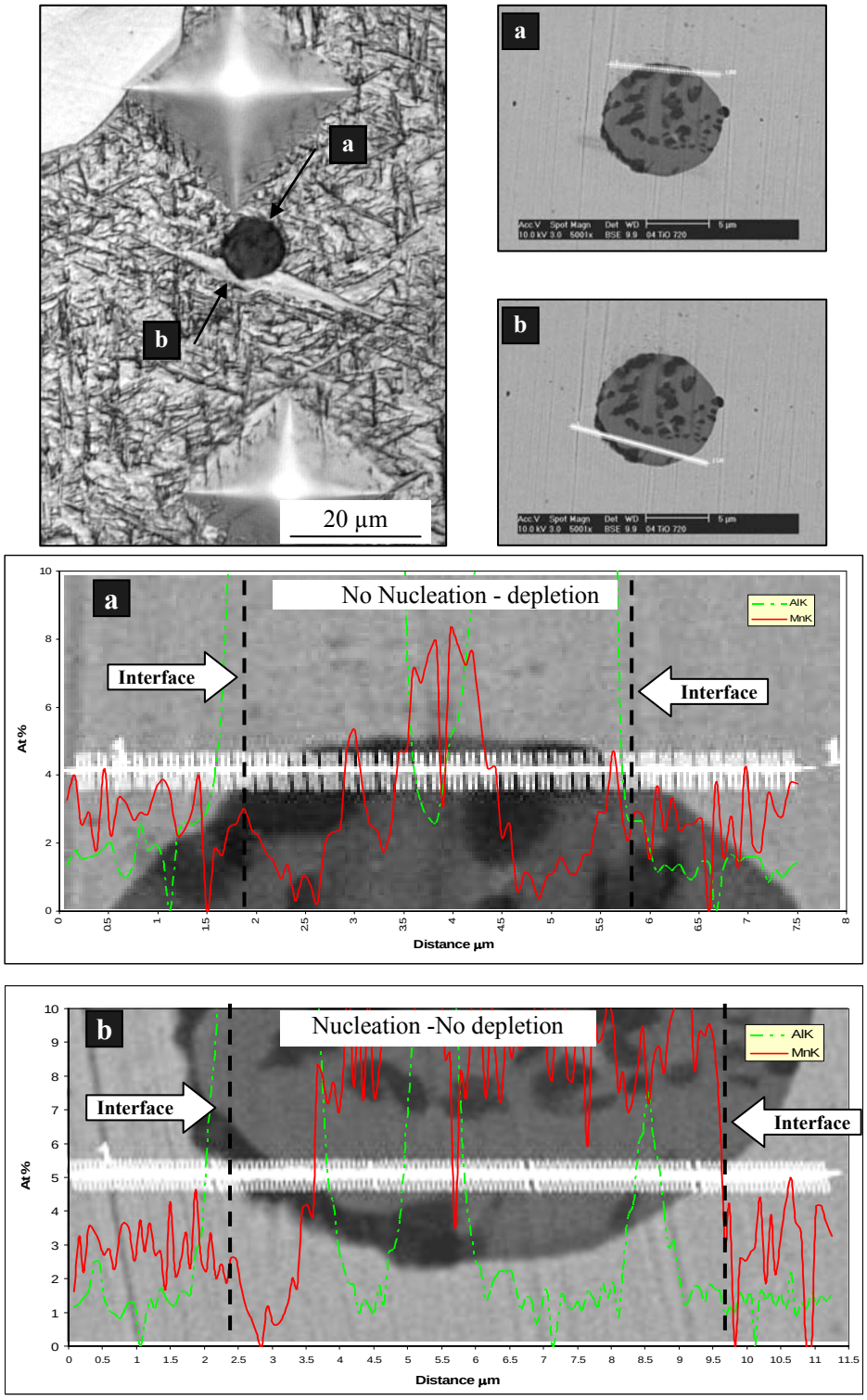

Figure 5.50: SEM-EDX semi-quantitative line analysis for Ti-oxide inclusion in the TiO steel.

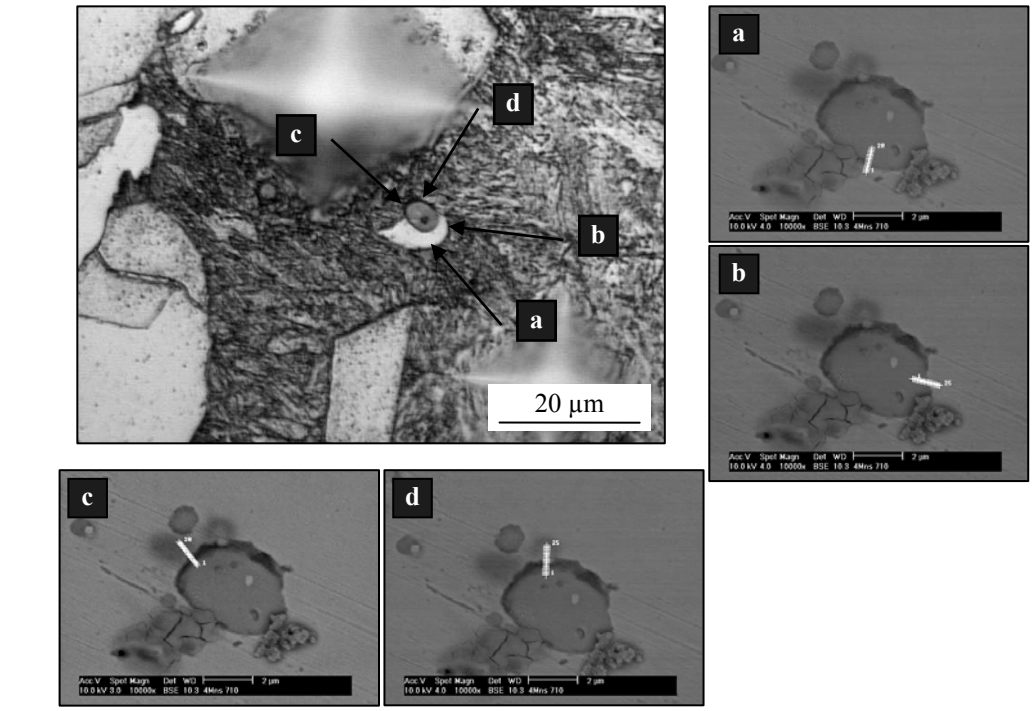

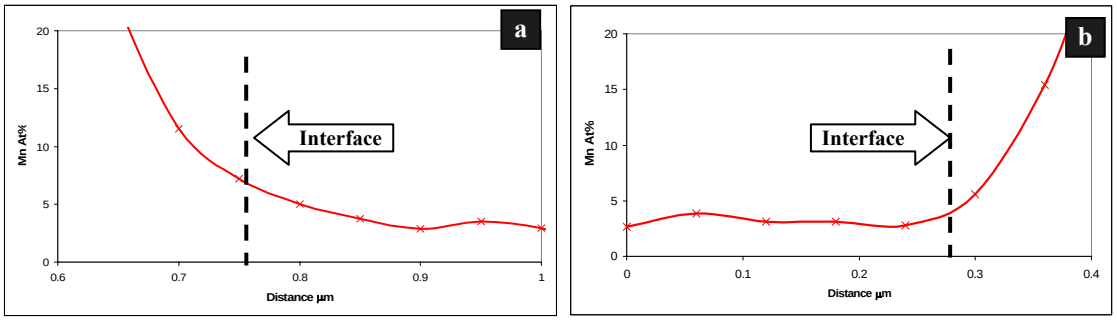

Nucleation No depletion

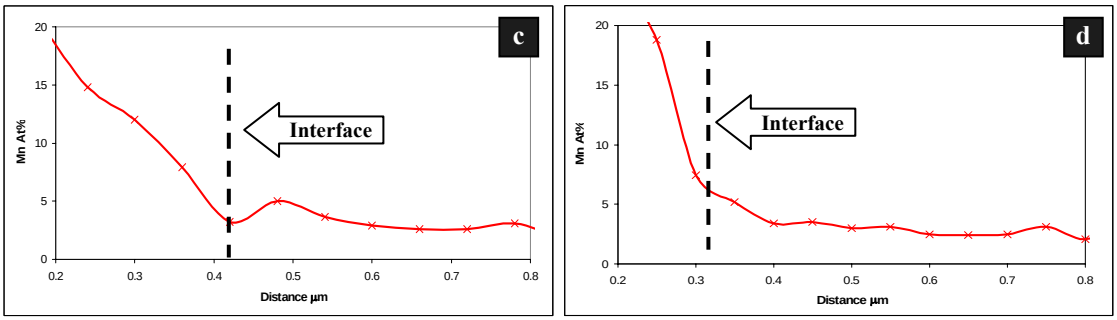

No Nucleation – No depletion

No Nucleation – No depletion

Figure 5.51: SEM-EDX semi-quantitative line analysis for MnS inclusion in the MnS steel.

6.0 DISCUSSION

6.1 CONDITIONING OF AUSTENITE PRIOR TO THE PHASE TRANSFORMATION

The conditioning of austenite prior to the phase transformation aims to give the thermomechanical processed austenite the proper microstructure and composition to allow the desired final ferrite microstructure. Therefore, maximizing the density of the most preferable ferrite nucleation sites per unit volume, (S_V), just prior to the phase transformation, will increase the nucleation rate of ferrite and consequently refine the final microstructure [2, 7, 39, 40, 41]. However, the austenite grain boundaries are considered to be the most preferable sites for ferrite nucleation [40, 62, 64, 68, 71, 78, 79]. There are many factors that can affect the conditioning of austenite in the heavy steel sections. This conditioning includes the as-cast condition, reheating temperature, thermomechanical processing (TMP) and the cooling path during the transformation, in addition to the particle-stimulated nucleation (PSN) mechanism, which is the issue of this study. The influence of these variables on the conditioning of the austenite is discussed below.

6.1.1 Formation of Non-Metallic Inclusions

In steel casting, three types of inclusions occur: primary, secondary and exogenous inclusions. Primary inclusions form before solidification and secondary inclusions form in the supersaturated melt in the interdendritic regions while exogenous inclusions originate from out side the melt.

During the solidification process, microsegregation and solute partitioning can produce significant compositional variation throughout the as-cast products. Except for the size and distribution of non-metallic inclusions, most of the negative aspects related to the casting process can be eliminated during the further processing of the as-cast material. The non-metallic inclusions differ from precipitates in that they are usually form and are present in the liquid steel, while precipitates form during solidification. Therefore, any control of the volume fraction, size and distribution of the non-metallic inclusions must be accomplished during the secondary metallurgy and casting process.

In this study, high volume fractions of Ti-oxide and MnS inclusions were added intentionally to the reference material, i.e., Jumbo steel, to promote the IGF nucleation mechanism. Both types of inclusions have been recognized as highly effective sites for IGF nucleation [14, 103, 115, 122, 123, 124, 125, 126]. However, there was no control over the size and distribution of the inclusions during the casting process in the TiO and MnS steels. The primary concern was to have a sufficient volume fraction of each inclusion type to investigate the IGF nucleation behavior and mechanism.

According to Figure 5.11 (a-c), the sequence of complex inclusion formation in the TiO steel with decreasing temperature could be predicted. Due to the high thermodynamic stability of the

Al-oxide, the rod-shaped Al rich phase forms prior to solidification. During solidification process, Ti-oxide become stable and traps the Al-oxides to form the oxide core of the inclusion. In the final stage of solidification process, MnS will precipitate both on the surface of the existed oxides and in the interdendritic regions to form pure MnS inclusions.

Eijk et al., [149, 150] showed similar sequence based on detailed thermodynamic analysis using Termo-Calc. This sequence is shown in Figure 6.1. Prior to solidification, Al as a strong deoxidizer reacts with dissolved oxygen in the liquid steel to form the core of inclusions on which the Ti-oxides grow epitaxially during solidification. During the final stage of solidification MnS precipitation occurs in the interdendtritic regions due to element partitioning, where the remaining S precipitates on the oxides as MnS in the solid state. At lower temperatures TiN becomes a stable phase and may form on the inclusions. The amount of TiN phase is limited since most of the available Ti is consumed in oxide formation.

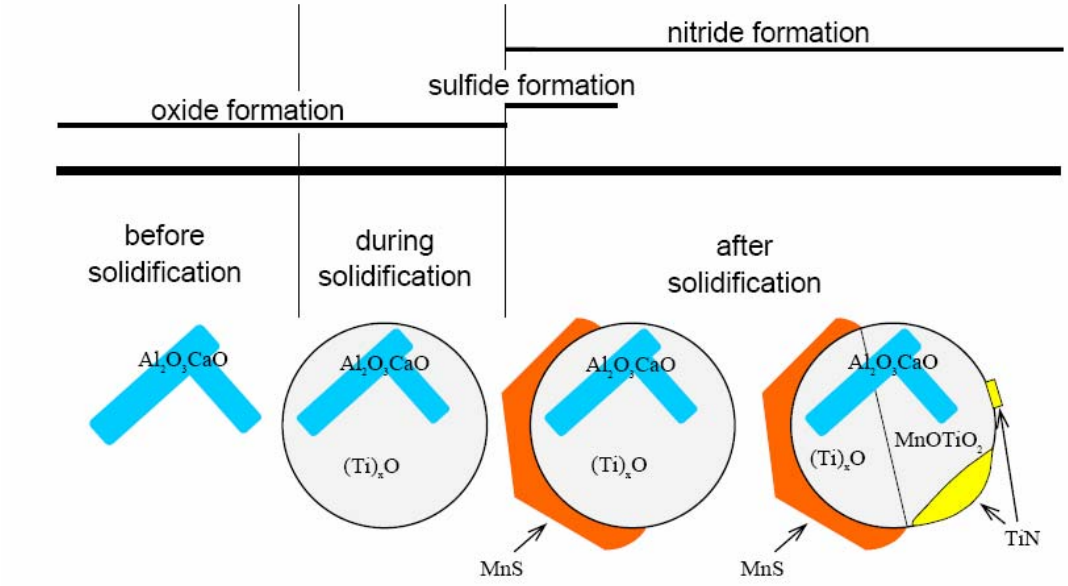

Figure 6.1: Schematic representation of the sequence of inclusion formation in TiO steel [150].

6.1.2 Microstructure of Austenite during Reheating

The grain coarsening behavior of the Jumbo and TiO steels shows typical grain coarsening behavior of the microalloyed austenite during reheating. This behavior has been widely investigated in microalloyed steels [34, 40, 143]. Below the grain coarsening temperature, T_{GC}, fine and uniform distributed austenite grains were observed due to the presence of the second phase particles, which suppressed the austenite grain growth. Based on the Gladman equation [52, 53, 58], the abnormal grain growth could be initiated when the fine precipitates coarsen, due to Ostwald ripening, and have an average radius (r) greater than the critical radius (r_c). Therefore, the abnormal growth progresses as the number of these precipitates per unit volume decreases.

In the addition to the effect of microalloying elements, the high volume fraction of fine Ti-oxide inclusions in the TiO steel could hinder the grain coarsening to higher temperatures. Although more than 75% of the Ti-oxide inclusions in the TiO steel are less than 1.0 μm, the calculated pinning and driving forces, Table 5-3, show that the driving force for the grain coarsening is slightly higher than the pinning force of the particles. This indicates that the grain coarsening behavior in the TiO steel is affected more with the presence of microalloying precipitates.

On the other hand, the grain coarsening behavior in the MnS steel exhibited different behavior than the microalloyed steels. The austenite microstructure is pinned effectively to elevated temperatures due to the significantly high volume fraction of the MnS inclusions. Approximately 50 % of the MnS inclusions are below 1.0 μm. The calculated pinning and

driving forces, Table 5-3, show that the pinning force of the particles is about three times higher than the driving force for the grain coarsening. Therefore, a significant amount of thermal energy is required to stimulate the austenite grain boundaries to overcome the pinning effect of the inclusions.

Regardless of the significantly high T_{GC} of the TiO and MnS steels, samples were reheated further above the grain coarsening temperatures to produce coarse austenite grains. This condition will favor the formation of the IGF. Increasing the prior austenite grain size is promoting the IGF nucleation through reducing the number of nucleation sites at the prior γ/γ grain boundaries, hence promoting nucleation of ferrite at the γ/I interface within the matrix.

6.1.3 Evolution of Austenite Microstructure during the TMP

The principal objective of the TMP is to condition the austenite microstructure prior to the phase transformation to insure the finest ferrite microstructure. The austenite grain refinement in the TMP is obtained from controlling the recrystallization and subsequent grain coarsening in a multi-pass rolling schedule [1, 34, 44, 45]. Generally, the desirable ferrite microstructure in thin plate and strip products is achieved through the controlled rolling process followed by interrupted accelerated cooling. In the case of heavy steel sections and plates over 40 mm thick, the effects of controlled rolling and accelerated cooling will not be spread equally over the whole thickness of the plate. Moreover, the special case of heavy steel sections rolled in the universal rolling mills creates a special environment of high deformation temperature with small reduction per pass, long interpass time and large number of passes. All these processing parameters contribute to coarsening the equiaxed recrystallized austenite grains prior to the transformation.

The results of the current TMP investigation in this study showed that the refining effect of the deformation at elevated temperatures was approximately eliminated prior to the phase transformation due to the coarsening process that associated with the slow cooling rate. Based on the results of the TMP study, the austenite grain coarsening could be eliminated through three techniques. The first one is to complete the deformation schedule at lower temperature, just above the T_{GC}, while keeping the same controlled cooling rate, i.e., cooling at 0.24 °C/sec to 825°C and then at 0.08 °C/sec to room temperature. In the 1150°C deformation schedule, the average austenite grain size prior to the transformation was 196 ± 81 μm which is approximately 120 μm below the austenite grain size obtained from applying the 1200°C deformation schedule (314 ± 120 μm). The second proposed technique is to apply fast cooling rates after finishing the deformation process at elevated temperatures. In the 1200°C deformation schedule with 1.4 °C/sec cooling rate, the average austenite grain size prior to the transformation was 178 ± 71 μm which is about 140 μm finer than the austenite grains that were obtained with controlled cooling rate (314 ± 120 μm). The third way of refining austenite microstructure could be through applying a combination of low deformation temperature and fast cooling rates. The average austenite grain size prior to the transformation was refined to 143 ± 69 μm with applying fast cooling rate (1.4 °C/sec) after ending the deformation at 1150°C. This combination process gives more than 100% ferrite refinement comparing to the typical process.

Due to the limitation of processing the heavy sections, it seems to be nearly impossible to produce fine ferrite microstructures in heavy sections by using the conventional TMP approach which depends on the effective austenite conditioning and accelerated cooling. Hence, none of the above refining methods could be applied in the universal-type rolling mills. Therefore, another approach is proposed to refine the final ferrite structure. The new approach proposes

using particle-stimulated nucleation, PSN, which leads to the formation of IGF. Adding active second phase particles to steel increases the S_V value and provides additional nucleation sites to form fine D_α during transformation [4, 6, 7, 8, 9, 10, 11, 12, 13, 14, 20]. The new proposed approach consists of a combination between the TMP at elevated temperatures and the PSN technique during the phase transformation. The role of the TMP in this approach is limited to the geometrically shaping of the material and gives a homogenous austenite microstructure through recrystallization, while the PSN technique provides extra nucleation sites for IGF.

6.2 DECOMPOSITION BEHAVIOR OF AUSTENITE

The interrupted cooling experiments conducted in this study show that the dynamics of the austenite to ferrite transformation follow quite clear patterns. The decomposition behavior of austenite grains during the controlled cooling in the TMP and thermal processing samples was very similar.

At high temperatures where diffusion rates are high but the driving force for nucleation is low, ferrite nucleation and growth is largely confined to the prior austenite grain boundary sites. The austenite grain boundaries are considered as energetically favorable nucleation sites due to their high interfacial energy [64, 78, 94]. Therefore, in the first stage of the phase transformation, a thin layer of allotriomorphic (intergranular) ferrite nucleated on the prior austenite grain boundaries. At the same time, the rejected carbon from the newly nucleated allotriomorphic ferrites made the subsequent nucleation event at the γ/α interface more difficult; therefore, more undercooling was required for further nucleation and growth.

The amount of the allotriomorphic ferrite is related to the available nucleation sites, i.e., grain boundaries area per unit volume, (S_V). Therefore, the nucleation of allotriomorphic ferrite was accomplished at earlier stages of the phase transformation in the three steels due to the consumption of these active sites. Although the phase transformation temperature (Ar_3) of the three steels was similar, the grain boundaries site saturation temperatures were different due to the variation of the S_V value in addition to the different hardenability of each material. The S_V values of the Jumbo, TiO and MnS steels were calculated as 5.4, 8.4 and 8.7 mm^{-1}, while the site saturation temperatures were found experimentally to be 770, 760 and 750 °C, respectively. However, the site saturation temperatures of the austenite grain boundary were confirmed by applying the Johnson-Mehl-Avrami-Kolmogorov (JMAK) equation, which can be written as[152]:

$$X_V = 1 - \exp\left(\frac{-f\dot{N}G^3t^4}{4}\right) \tag{6-1}$$

where $\acute{N}$ and G are the nucleation and growth rates of ferrite, respectively, and f is a shape factor which is considered as ($4\pi/3$) for austenite grains. X_V is the fraction of formed ferrite or site saturation that rises rapidly with time, t.

The nucleation and growth rates during the site saturation period were obtained as a single value, (η), based on the slope of the time-ferrite volume fraction curves in Figure 5.35, 5.36 and 5.37 for the Jumbo, TiO and MnS steels, respectively. It was not possible to differentiate between the nucleation and growth rates in the measured values. Therefore, a modification factor was assumed to be applied in the JMAK equation. Therefore, the $\acute{N}$ and G values in the JMAK equation were replaced by the measured nucleation and growth rate, η. The assumption was built on the fact that the growth rate at high temperatures is greater than the nucleation rate due to the

high diffusivity and small driving force for nucleation. Therefore, an empirical factor of η^X was used instead of the $\acute{N}G^3$ in the JMAK equation. The X value of 2.6 was selected based on the site saturation temperature of the Jumbo steel, which was experimentally considered to be 770°C, as shown in Figure 5.24 and Figure 5.27. The $\eta^{2.6}$ factor was applied to the other two steels and gave results that are in good agreement with the experimental results. Based on the JMAK relation, the site saturation curves for the three materials are drawn in Figure 6.2 considering the differences in the Ar_3 between the steels. Based on the saturation curves, the 99 % saturation levels for TiO and MnS steels were found to be 764 and 752 °C, respectively.

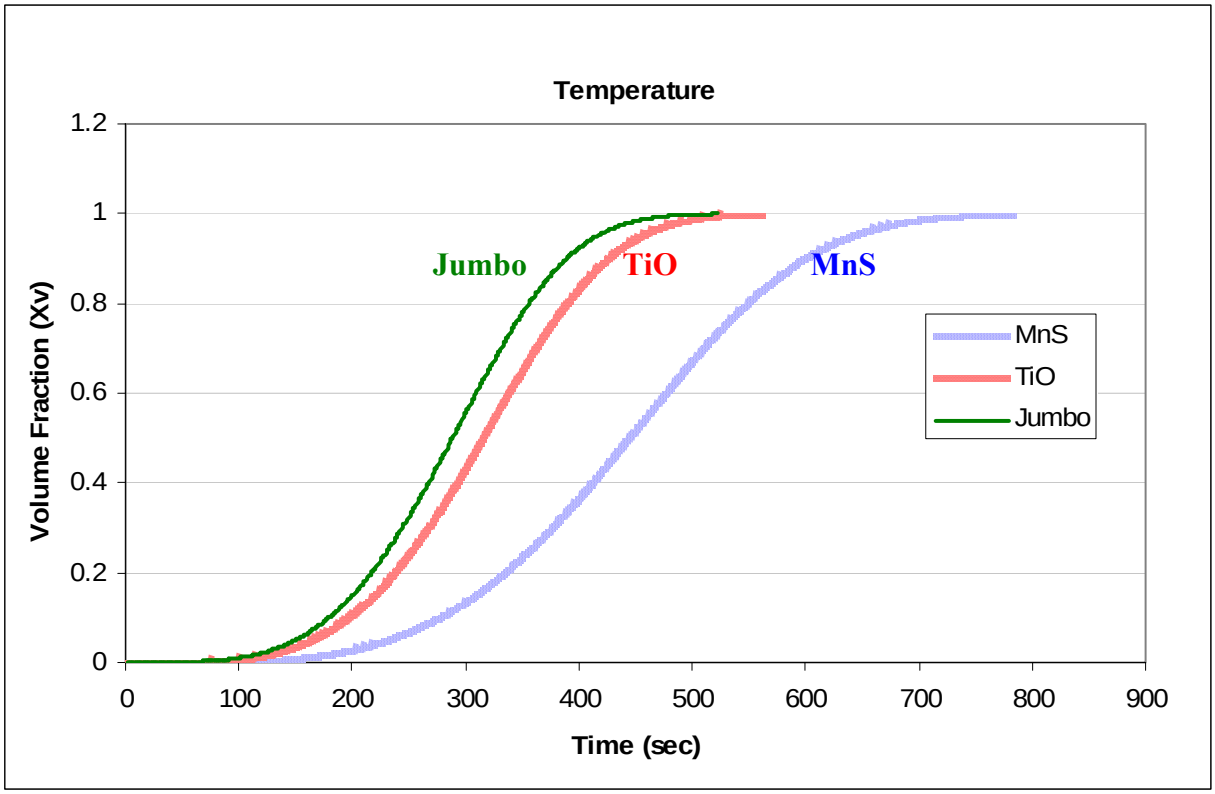

Figure 6.2: An Avrami simulation with site saturation for the three steels.

As the temperature is lowered and the driving force for ferrite formation increases, the interrupted quenched samples show that large intragranular inclusions in the TiO and MnS steels become active as nucleation sites. The ferrite initially forms small caps on specific regions of the γ/I interface. This nucleation of IGF is clearly evident at 750°C in the TiO steels and 740°C in the MnS steels. The difference between the IGF nucleation temperatures in these steels is due to the high hardenability of the MnS steel in addition to the availability of larger inclusions in the TiO steel. The experimental results show that IGF nucleation at the γ/I interfaces start approximately 20°C below the grain boundaries site saturation temperature. Similar results were reported by Enomoto [14], showed that the nucleation temperature of allotriomorphic and idiomorphic (intragranular) ferrite differs by 50 to 20 °C.

On further cooling, the driving force for ferrite nucleation increases and the small intragranular inclusions become operative as nucleation sites. However, due to the low cooling rates, the ferrite morphology at the prior austenite grain boundaries and on the inclusions, is observed to have similar polygonal shape.

Due to the lack of the intragranular nucleation sites in the large austenite grains of the Jumbo steel, the formation of allotriomorphic ferrite grains increased the concentration of carbon within the austenite grain without forming IGF. At lower temperature, the nucleation of ferrite crystals stops and the remaining untransformed austenite forms high-carbon low temperature microconstituents.

Based on the observation of the thermal processing study, it is evident that the main nucleation sites and the sequence by which they become active are arranged as:

1) Prior austenite grain boundaries, γ/γ interfaces.
2) Large intragranular inclusions, γ/I_{Large} interfaces, then

3) Small intragranular inclusions, γ/I_{small} interfaces.

These observations are inconsistent with the way in which the critical energy barrier for the ferrite nucleation changes with nucleation site, shown by Thewlis et al. [110], in Figure 2.21. Moreover, the variation of the volume fraction of IGF (V_{IGF}) to the volume fraction of intergranular ferrite (V_{GB}) in the three steels confirms the effectiveness of the PSN mechanism in improving the nucleation of IGF. The V_{IGF}/ V_{GB} ratio increased from 0.39 in the jumbo steel to 4.48 and 5.27 in the TiO and MnS steels.

6.3 EFFECT OF INCLUSIONS ON THE IGF NUCLEATION

Since inclusions are assumed to provide IGF nucleation sites, variation in inclusion type, volume fraction and size distribution may significantly influence the dynamics of the austenite to ferrite transformation process. These effects are discussed in the following sections.

6.3.1 Effect of Particle Size and Volume Fraction

It is clearly shown in this study that the large inclusions have a pronounced effect on the IGF nucleation. This result is consistent with other published work [94, 110, 112, 114]. The large inclusions become active at slightly lower temperatures than the grain boundaries. This temperature was approximately 20°C below the grain boundary saturation temperature. A similar result was reported by Enomoto [14] during the formation of acicular ferrite. This fact was explained by Bhadeshia [116] who suggested that the large spherical, non-metallic, inclusions

are more effective for heterogeneous nucleation than the smaller ones, where the newly formed embryo will have smaller curvature at the surface of large inclusions. Thus, decreasing the wetting angle would improve the heterogeneous nucleation. This fact is schematically illustrated in Figure 6.3 .Therefore, the flat surface of austenite grains is expected to be a more potent heterogeneous nucleation site than a large spherical inclusion.

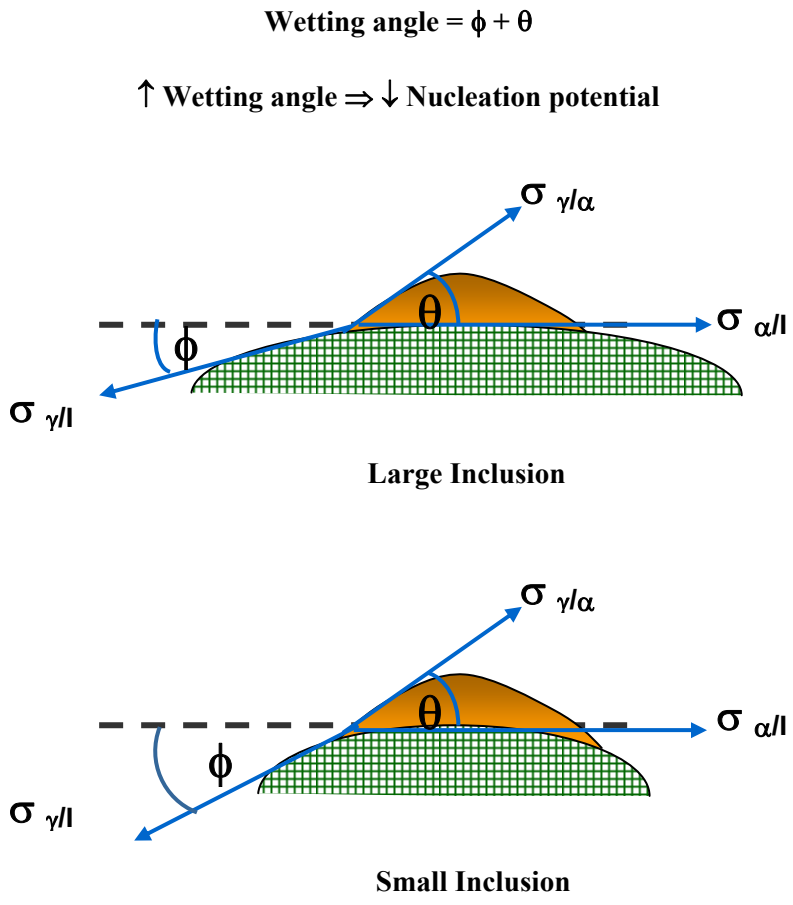

Figure 6.3: Schematic illustration of the effect of large and small inclusions in the wetting angle.

The amount of large inclusions in both TiO and MnS steels is very limited. Figure 5.44 and Figure 5.46 show that the large inclusions are relatively uncommon in both steels. The number of large inclusions (> 2.0 μm) per unit area in the TiO steel, is $7.6x10^{-5}$ μm^{-2}, while the number of inclusions that are less than 2.0 μm, is $4.65x10^{-4}$ μm^{-2}. In other words, the amount of large inclusions only forms 14% of the total available particles. Similarly, in the MnS steel, the number of large inclusions (> 1.0 μm) per unit area is $8.3x10^{-4}$ μm^{-2}, while the numbers of inclusions less than 1.0 μm is $7.3x10^{-4}$ μm^{-2}. Therefore, approximately 53% of the total available particles are considered as large inclusions. Clearly, the Ti-oxide inclusions are a more potent since the same degree of refinement was achieved with eleven times less number of particles than MnS. It is important to mention that all inclusions smaller than 0.6 μm are considered as inert substrates. In both steels, no IGF nucleation event was observed below this size.

Considering the volume fraction of inclusions, the results indicate that the similar refinement effect could be achieved in the TiO steel with having only $2.04x10^{-4}$ of the current volume fraction ($1.46x10^{-3}$) of Ti-oxide inclusions if the particle sizes are controlled to be larger than 2.0 μm. On the other hand, the similar refining effect could be achieved in the MnS steel by decreasing the volume fraction of inclusions from $3.32x10^{-3}$ to $1.76x10^{-3}$ and controlling the inclusion size to be larger than 1.0 μm. This means the required volume fraction of the MnS inclusions to achieve the similar degree of refinement is eight times grater than that of the Ti-oxide particles. Therefore, the Ti-oxide inclusions approach would be preferred because it may produce cleaner steel.

Ferrite associated with large inclusions is observed to nucleate on localized areas on the inclusion surface. This fact is related to the orientation relationship of the newly nucleated ferrite grain with the inclusion and the austenite matrix. Several workers [94, 103, 104, 110, 120]

showed that the inclusion nucleation could be promoted further if the ferrite adopts a rational orientation relationship with both the austenite and polycrystalline substrate, i.e., inclusion.

Moreover, it has been observed that multi-nucleation events of ferrite took place preferentially at large Ti-oxide inclusions (> 3.0 μm). In addition to the orientation relationship, this fact is due to the availability of the complex compounds in these inclusions. Because the large inclusions are multiphase, there is a high probability that many high surface energy regions exist on an inclusion and nucleate several ferrite grains. Similar observations have been made by Dowling et al., [102] and Zhang and Farrar [104].

6.3.2 Particle Activity

The results of this study show that the TiO and MnS steels start the decomposition process with similar austenite grain size and end with similar ferrite grain size. Although the refining effect was approximately the same in both materials, the number of Ti-oxide inclusions is significantly less than the number of MnS inclusions. It is clearly indicated that the potential of Ti-oxides particles in the nucleation of IGF is significantly higher than that of the MnS inclusions. The effectiveness of the Ti-oxide particles could be attributed to the following five factors:

1) The availability of significantly large inclusions in the TiO steel. The measurement of particles size shows that approximately 1.3% of Ti-oxide particles are above 6.0 μm, while only 0.15% of the MnS inclusions are above this range. The effect of the inclusion size has been confirmed by several workers [90, 94, 110, 112, 114,].
2) The hardenability effect [89, 99]. Ti-oxide particles promote the nucleation of ferrite since the Ti is classified as a ferrite stabilizer.

3) Availability of the complex compounds in the Ti-oxide inclusions such as aluminum oxides which also consider as a ferrite former [102].
4) Multi-nucleation events at large Ti-oxide particles, where one inclusion could nucleate several ferrite grains [102, 104]. This type of nucleation is rarely observed in the MnS steel.
5) The rough and porous surface of the Ti-oxide inclusions could enhance the nucleation of IGF through decreasing the wetting angle in a similar manner to the heterogeneous nucleation in mould-wall cracks [63].

The calculation of the relative nucleation potential of intragranular to grain boundary nucleation, (*P*), for both Ti-oxides and MnS inclusions, Table 5-10, shows the high potential of Ti-oxide inclusions in IGF nucleation. The activity of these particles is twice the activity of the MnS inclusions. This finding was confirmed through considering only the number of active particles per unit area for both steels. In this case, the activity of Ti-oxide particles was eleven times the activity of the MnS particles. Therefore, the relative nucleation potential was recalculated based on the effective size and number of particles per unit volume, as shown in Table 6-1. In this new approach, the relative nucleation potential of Ti-oxide particles is increased from two to four times above the MnS potential. The relative nucleation potential for MnS inclusions has the same value for both Jumbo and MnS steels.

Table 6-1: Calculated value of the surface area per unit volume and the relative nucleation potential of intragranular to grain boundary nucleation for the three steels based on the active inclusion size and volume fraction.

Calculated Values	Steel		
	Jumbo	TiO >2.0 μm	MnS >1.0 μm
D_γ (μm)	372	240	230
D_I (μm)	1.37	3.88	1.94
N_V (μm^{-3})	3.72×10^{-5}	2.0×10^{-5}	4.3×10^{-4}
$S_{VGB} = 2/D_\gamma$ (mm^{-1})	5.4	8.4	8.7
$S_{VI} = \pi N_V D_I^2$ (mm^{-1})	0.22	0.96	5.08
$S_V = S_{VGB} + S_{VI}$ (mm^{-1})	5.62	9.36	13.78
$D\gamma = 2 / S_V$ (μm)	356	213	145
S_{VI}/ S_{VGB}	0.04	0.11	0.58
V_{IGF}/V_{GB}	0.39	4.48	5.27
$P = V_{IGF}/V_{GB} . S_{VGB}/S_{VI}$	9.51	40.73	9.10

6.4 EFFECT OF PSN ON THE FERRITE GRAIN SIZE

The final ferrite grain size, in a specific material, is a function of the microstructural state of the austenite prior to the transformation and the cooling rate during the phase transformation [86]. Therefore, all the empirical equations, which are reviewed in this study, for predicting ferrite grain size, consider these two variables [135, 136, 137, 138].

The results of this study show that the ferrite grain sizes for both TMP and thermal processed Jumbo steel are very similar since the prior austenite grain sizes and cooling schedules are alike. In the TMP, the average austenite grain size of 314 ± 120 μm is transferred to 47 ± 15 μm average ferrite grain sizes. Similar results were obtained by Gao et al., [139] where 337 ± 147μm average austenite grain size was transferred to 48.4 ± 28.5 μm ferrite under the same deformation and cooling conditions. In the thermal processing, with applying the same cooling schedule of the TMP, the average austenite grain of size 372 ± 160 μm is transferred to 54.2 ± 15 μm ferrite. In addition to the similarity in these three cases, the results were in agreement with Saito's equation. This equation is considered, in this work, as the most appropriate relation for predicting the formation of allotriomorphic ferrite in a coarse austenite microstructure. All the results of the TMP and thermal processing in addition to the Gao et al., [139] results, are listed in Table 6-2 and compared to the Saito curve in Figure 6.4.

It is evident from Figure 6.4 that the Saito equation exhibits a better fit to predict the final ferrite grain size without considering the effect of the PSN. While all the readings of the Jumbo steel lie on Saito's curve, the TiO and MnS readings are 25 to 35 % below the curve. This shifting from the Saito equation is considered as an effect of the PSN. Therefore, another approach is suggested to consider the effect of the PSN mechanism in the final ferrite microstructure. In the Gao et al., [139] approach, Equation 29, gives perfect results only if the effective size of inclusions and volume fraction are considered, as shown in Figure 6.5. The equation is applied to the TiO steel considering the inclusions larger than 2.0 μm which have a volume fraction of 2.04×10^{-4}. Similarly, the equation is applied to the MnS steel for particles larger than 1.0 μm that have 1.76×10^{-3} volume fraction. Based on the observation in the TiO

steel, each Ti-oxide particle is assumed to nucleate two ferrite grains on average, while the MnS inclusions are considered to be associated with only one ferrite grain.

Table 6-2: The relation between the prior austenite and the nucleated ferrite grain sizes as a function of processing technique. All samples were subjected to the same controlled cooling process.

Steel	Conditioning	Grain Size (μm)	
		Dγ	**Dα**
Jumbo	TMP 880	100 ± 40	29.7 ± 11.2
	TMP 1100	130 ± 37	34 ± 11
	TMP 1200	314 ± 120	47 ± 15
	TMP Gao et al.,[139]	337 ± 147	48.4 ± 28.5
	Thermal Processing	372 ± 160	54.2 ± 28.5
TiO	Thermal Processing	240 ± 106	33.3 ± 16.5
MnS	Thermal Processing	230 ± 87	27.2 ± 18

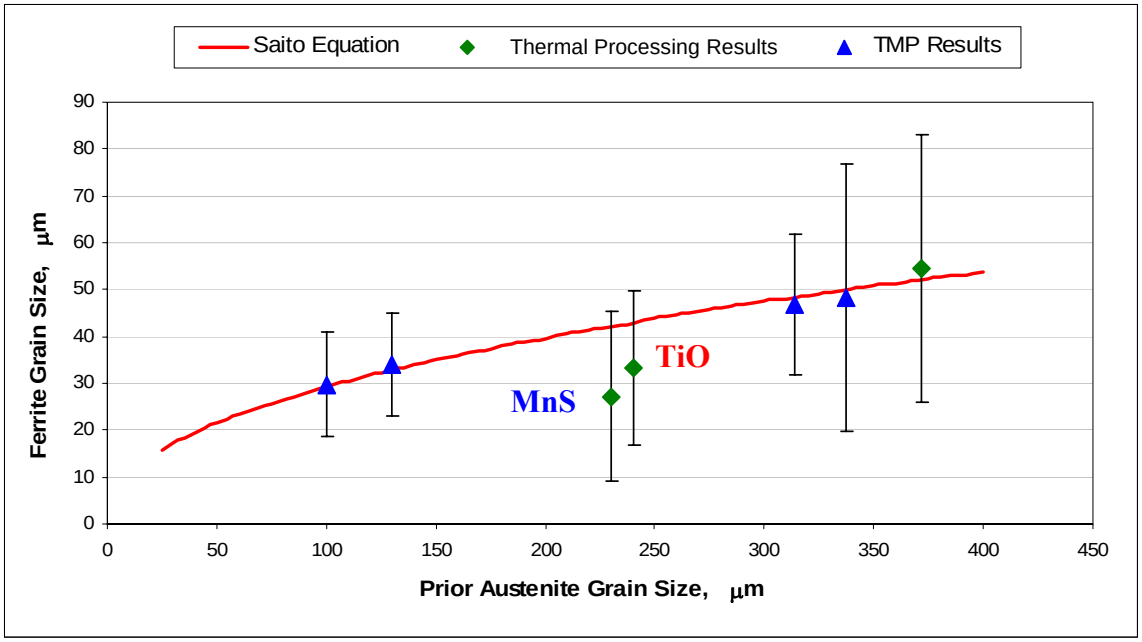

Figure 6.4: Variation of ferrite grain size as a function of prior austenite grain size for the TMP and thermal processed samples with the Saito empirical equations.

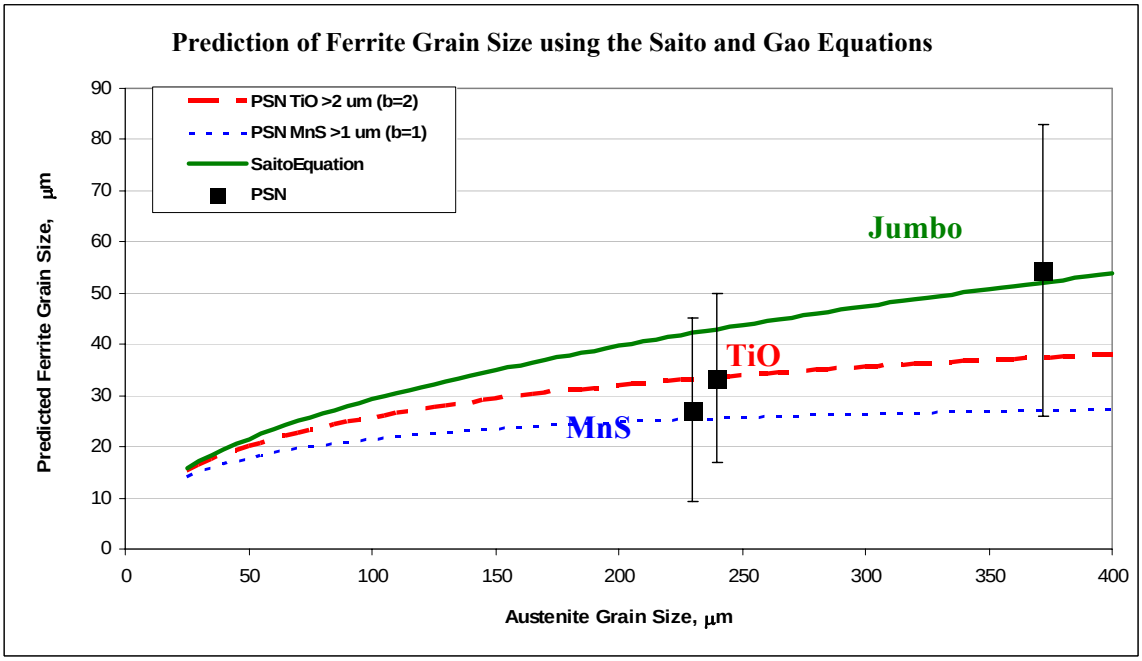

Figure 6.5: Predicting the ferrite grain size in the thermal treated steels based on the Gao equation with only considering the active inclusions size and volume fraction.

6.5 IGF NUCLEATION MECHANISM

Four possible mechanisms have been proposed [17, 102, 104, 115, 128] regarding the nucleation of the IGF at non-metallic inclusions. These mechanisms are: a) simple heterogeneous, b) volumetric strain, c) local depletion zone, and d) lattice mismatch.

It is possible that volumetric strain occurring from the differences in the thermal expansion coefficient between inclusions and austenite matrix contribute to IGF nucleation [9, 89, 90, 95, 102, 103, 106, 112, 121]. However, this mechanism is supposed to be effective with fast cooling rates where the effect of the thermal expansion is obvious. Therefore, the effect of volumetric strain is unlikely to be a major factor stimulating the nucleation of IGF in the present study [17, 115, 129, 130].

It has been reported [15, 113, 114, 115, 122, 111, 125, 130] that the Mn depleted zone (MDZ) around the inclusions forms active nucleation sites of IGF in the austenite matrix. Generally, despite various experimental investigations of different types of inclusions, there has been no conclusive experimental confirmation of such a manganese depleted layer near nucleating particles in weld metals [90], or in plate steels [106].

Yamamoto et al., [125] have postulated that the precipitation of MnS on Ti-oxide causes a depletion of manganese around the inclusion. This local chemical variation would lead to an increase in transformation temperature, thereby promoting the formation of IGF. Byun et al. [15] and Shim et al. [113, 115] showed that the MDZ is formed by the manganese absorption by Ti_2O_3 during austenitization heat treatment.

The measurement of Mn concentration in the steel/Ti_2O_3 interface has been reported using several techniques. The existence of MDZ was reported by Byun et al., [15] using scanning transmission electron microscopy (STEM) - energy-dispersive x-ray (EDS) analysis, and also by Shim et al. [113] and Kim et al. [131] using electron probe microanalysis (EPMA). Shim et al. [115] used SEM/EDX analysis to evaluate the presence of the MDZ. However, these results contradict those of Ricks et al. [94] and Lee and Pan [106] in which both STEM/EDS and EPMA techniques were employed. In the latter studies, no detectable variation in Mn was measured around the Ti-oxide inclusions. Clearly, high spatial resolution quantitative microanalysis – such as FEG-STEM EDS microanalysis – is required in order to conclusively document the presence and extent of any Mn depletion associated with the inclusions. Based on the data reported in the literature and the results of this study, any Mn depleted zone must be very narrow (<50 nm).

However, in the present study, it was not possible to adequately measure any variation in Mn content in the vicinity of the inclusions using SEM-based EDX microanalysis. It was observed, however, that the microstructures developed in the vicinity of some inclusions contained some non-uniformly distributed regions of fine pearlite. This may be interpreted as not supporting a MDZ. Nucleation of IGF could occur with or without forming the MDZ in Ti-oxide and MnS inclusions. Similar results have been reported by Lee and Pan [106].

It should also be noted that the postulated Mn-depleted zone should form during the formation of the inclusions. Subsequent heat treatments will permit diffusion of solute elements, such as Mn, so that any depletion that might occur during inclusion formation could be eliminated. This may also be a factor in explaining the contradictory reports in the literature.

It has been suggested that the inclusion surface may assist the formation of IGF by simple heterogeneous nucleation [94, 101]. The results of the present study show that IGF nucleation is

enhanced with increasing nucleation sites per unit volume. However, the Ti-oxide and MnS inclusions exhibit the similar effect in IGF nucleation, while the surface area per unit volume of the active intragranular inclusions (S_{VI}) varies significantly between the two types of inclusions. The S_{VI} values for the Ti-oxide and MnS inclusions are 0.96 and 5.08, respectively. Additionally, some relatively large inclusions do not induce nucleation. Therefore, it seems that the simple heterogeneous nucleation mechanism is not sufficient, on its own. It seems that the promotion of IGF nucleation requires heterogeneous nucleation in addition to other mechanisms.

Since the nucleation of IGF occurs at the γ/inclusion interphase, several workers [9, 10, 13, 14, 103, 117, 118, 119, 120, 121] studied the energy balance of the α/inclusion/γ interphase boundaries and its effect on the nucleation kinetics of IGF. In general, it has been shown that the inclusion nucleation could be promoted further if the ferrite adopts a rational orientation relationship with both the austenite and the inclusion.

In conclusion, in this study, it is clear that the key role of inclusions is to provide heterogeneous nucleation sites for IGF nucleation, In addition, the lattice disregistry seems to achieve the energy balance of the α/inclusion/γ interphase.

7.0 CONCLUSIONS

From the present study, the following conclusions can be made:

- The conventional TMP could not be applied as an austenite conditioning mechanism in the heavy steel sections.
- The refining of ferrite microstructure is achieved, successfully, through enhancing the IGF nucleation with implementing of the particle-stimulated nucleation, PSN mechanism.
- The refinement of ferrite microstructure with the addition of inclusions could be due to the effect of the S_V value through: 1) Decreasing the $D\gamma$ as a result of the pinning force effect, and 2) Increasing the IGF nucleation sites where the particles act as a heterogeneous nucleation sites.
- The nucleation of ferrite on localized areas on the inclusion surface could be due to the correct crystallographic orientation with the polycrystalline substrate.
- Ferrite nucleation and growth starts at prior γ/γ grain boundaries at high temperatures. With increased undercooling, the nucleation of ferrite at γ/α interfaces and at large intragranular inclusions occurs simultaneously. With additional increase in the undercooling, smaller inclusions are activated.

- The efficiency of the inclusion as a nucleation site is mainly related to the inclusion size and type. Less than 14 and 50 % of the total number of inclusion per unit area is contributing to the IGF nucleation in the TiO and MnS steels, respectively.
- The high activity of Ti-oxide particles in nucleating IGF could be attributed to their: a) large size, b) complex compounds, c) hardenability, d) multi-nucleation characteristics, and e) surface morphology.
- An accurate prediction of final ferrite grain size, with considering the effect of the PSN, was achieved with applying the modified form of Saito's equation by considering the volume fraction of the active size of inclusions and the average number of nucleation events per particle.

8.0 FUTURE WORK

The following research fields are recommended to be pursued:

- Study the IGF nucleation behavior through designing new steels by controlling the size and volume fraction of the inclusions based on the results of the current study.
- Study the effect of non-metallic inclusions, size and volume fraction, on the mechanical properties of the steel (advantages and disadvantages).
- Investigate the orientation relationship between the inclusion/austenite, inclusion/IGF and austenite/IGF. This study is suggested to be achieved using the EBSD analysis.
- More work should be performed to assess the MDZ using high spatial resolution microanalysis techniques such as FEG-STEM EDS microanalysis.
- Study the effect of other non-metallic inclusions.

APPENDIX A

Theoretical Prediction of Ferrite Grain Size: Gao Model of PSN

Gao, et al., [139] have developed an equation that considers the effect of the intragranular inclusions in prediction of the final ferrite grain size. This relation is based on the Saito[135] empirical equation which considers only the formation of intergranular ferrite that nucleates at the austenite grain boundaries, and given as:

$$\ln D_{\alpha o} = 0.92 + 0.44 \ln D_{\gamma} - 0.17 \ln \dot{T} - 0.88 \tanh(10\varepsilon_r) \qquad \text{(A-1)}$$

The derivation of Gao's model is as follow:

- For the inherent transformation of an austenite grain structure to a ferrite grain structure, the following relation is considered:

$$\pi \,.\, [(D_{\gamma 0}/2)]^2 = N_{\alpha 0} \,.\, \pi \,.\, [(D_{\alpha 0}/2)]^2 \qquad \text{(A-2)}$$

  where $D_{\gamma 0}$ is the mean austenite grain size, $D_{\alpha 0}$ is the mean ferrite grain size, $N_{\alpha 0}$ is the nucleation factor. The nucleation factor for the inherent austenite to ferrite transformation can be expressed as:

$$N_{\alpha 0} = D_{\gamma 0}^2 / D_{\alpha 0}^2 \qquad \text{(A-3)}$$

- When particles are added to the steel, N_P particles are assumed to be trapped in a certain austenite grain $D_{\gamma 0}$, and written as:

$$(N_A)_p = N_P / [\pi (D_{\gamma 0}^2/4)] \qquad \text{(A-4)}$$

where $(N_A)_p$ is the particle number density in a particular grain, and N_p is the number of particles in this grain.

- The relation between the volume fraction (F_V) and the $(N_A)_p$ is written as:

$$F_v = F_A = (N_A)_p \bullet [\pi (D_p^2/4)] \quad \text{(A-5)}$$

where D_p is the particle size. Based on equations (A-4) and (A-5), the following relation is derived:

$$N_P = F_v \bullet D_{\gamma 0}^2 / D_p^2 \quad \text{(A-6)}$$

- In the case of PSN, β ferrite grains are assumed to be nucleated from one particle. Therefore, the number of ferrite grains nucleated in one austenite grain is given by:

$$N_{PSN} = \beta \bullet N_p \quad \text{(A-7)}$$

where N_{PSN} is the number of the ferrite grains nucleated on the intragranular particles. ß is coefficient related to interfacial energies, strain energies, particle size, cooling rate. Assuming the change of $N_{\alpha 0}$ is negligible with the addition of second phase particles, then the total number of ferrite nucleation $(N_\alpha)_{mix}$ is given as:

$$(N_\alpha)_{mix} = N_{\alpha 0} + \beta \bullet N_{PSN} \quad \text{(A-8)}$$

Therefore, assuming a homogeneous mixture of inherent nuclei with the particle stimulated nuclei:

$$\pi[(D_{\gamma 0}/2)]^2 = (N_\alpha)_{mix} \bullet \pi[(D_\alpha /2)]^2 \quad \text{(A-9)}$$

where D_α is the final ferrite grain size.

- Based on equation (A-7), the follow relation is written:

$$D_{\gamma 0}^2 = (N_{\alpha 0} + \beta \bullet N_{PSN}) \bullet D_\alpha^2 \quad \text{(A-10)}$$

And from equations (A-3) and (A-6), the follow relation is derived:

$$D_{\gamma 0}^2 = (D_{\gamma 0}^2 / D_{\alpha 0}^2 + \beta \bullet F_v \bullet D_{\gamma 0}^2 / D_p^2) \bullet D_\alpha^2 \qquad \text{(A-11)}$$

- Finally, the ferrite grain size, D_α , is expressed as:

$$D_\alpha = \left(1 / D_{\alpha 0}^2 + \beta \cdot V_f / D_P^2\right)^{-1/2} \qquad \text{(A-12)}$$

APPENDIX B

Effect of the Tempering Time in Revealing the Prior Austenite Microstructure

Revealing the prior austenite grain boundaries in as-quenched steel is considered as a relatively difficult task. However, it was found that the as-quenched material responds positively to the etching solution after tempering the specimen prior to the etching process. This tempering process allows phosphorus in solution to segregate towards the prior austenite grain boundaries and aid the optical metallographic techniques by revealing sharp and clear austenite grain boundaries when etching with picric acid [143].

The effect of the tempering time was studied at constant temperature, 490 °C, for three different steels. The chemical compositions of these three steels are listed in Table B-1. In this study, specimens were encapsulated in evacuated quartz tubes and austenitized at 1250 ºC for 1 hour then water quenched in an ice brine bath. Following the heat treatment process, specimens were tempered for 12, 24, 48 and 72 hours before they were prepared for metallographic analysis using optical microscopy. Samples were etched using special reagent consisting of 100 ml of saturated aqueous picric acid, in addition to 1 ml of HCl and 10g of dodecylbenzene sodium sulfonate as a wetting agent. Specimens were immersed into this solution at 80°C for about 60 seconds, where the surface of the specimen was swabbed to maintain fresh etchant over it.

The tempered specimens were compared with the as-quenched (non-tempered) specimens to study the effect of the tempering time. The sequences of the optical micrographs for the three

steels are shown in Figure B-1, B-2 and B-3. Noticeably, the image quality of the grain boundaries' details improves with increasing tempering time.

Table B-1: Chemical composition of the three steels.

Steel	Elements (wt %)											
	C	**Si**	**Mn**	**P**	**S**	**Al**	**Cu**	**N**	**Cr**	**Nb**	**Ti**	**V**
Jumbo	0.08	0.3	1.42	0.008	0.003	0.034	0.31	0.005	0.018	0.003	0.003	0.132
High Nb	0.09	0.01	1.14	0.018	0.008	0.03	0.023	0.005	0.023	0.052	0.002	0.003
Low Nb	0.05	0.21	0.50	0.01	0.002	0.03	0.10	0.008	0.01	0.025	0.004	0.008

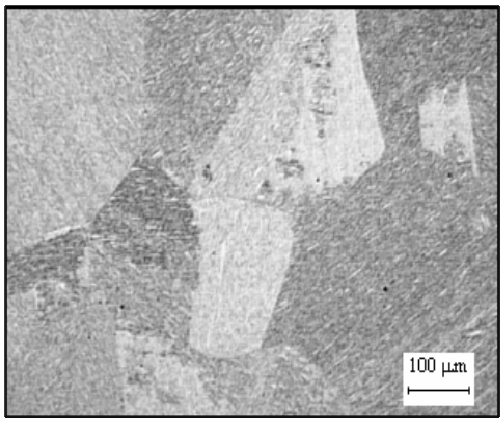

As-Quenched

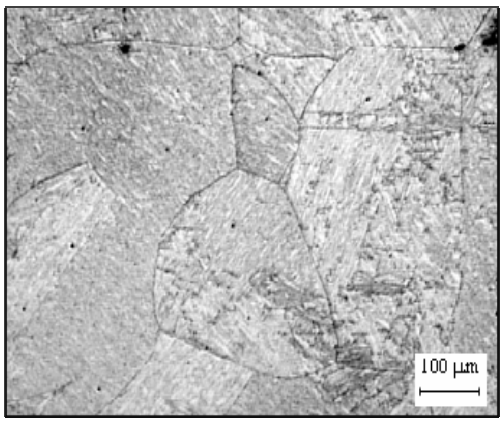

12 hr. @ 490 °C

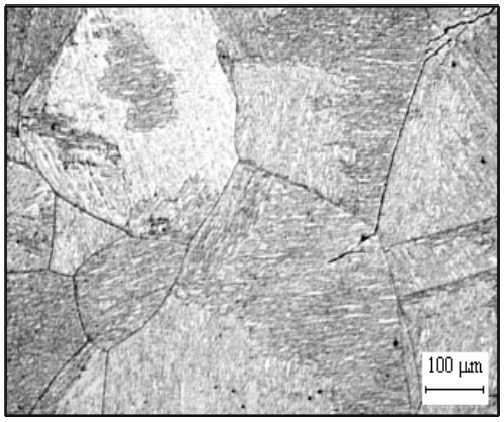

42 hr. @ 490 °C

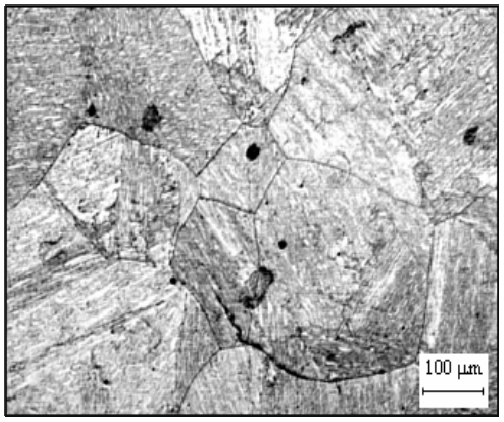

48 hr. @ 490 °C

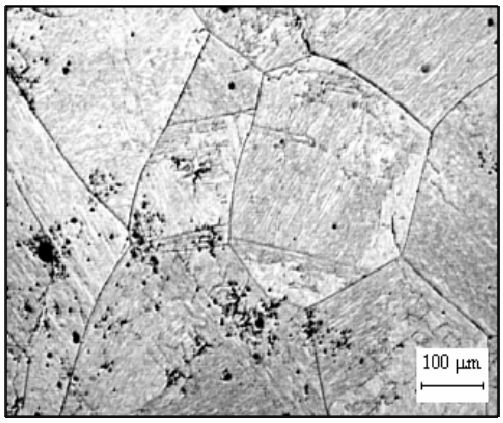

72 hr. @ 490 °C

Figure B.1: Jumbo steel. Samples were austenitized at 1250 ºC for 1 hour before quenched and tempered.

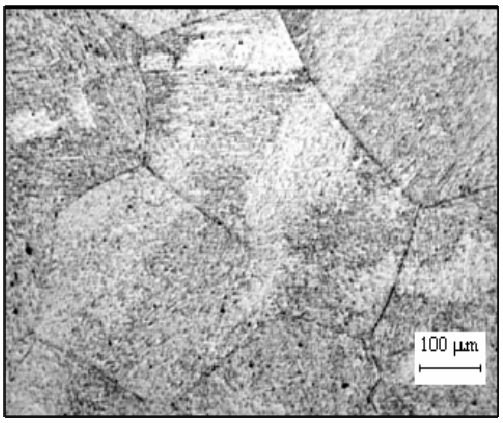

As-Quenched

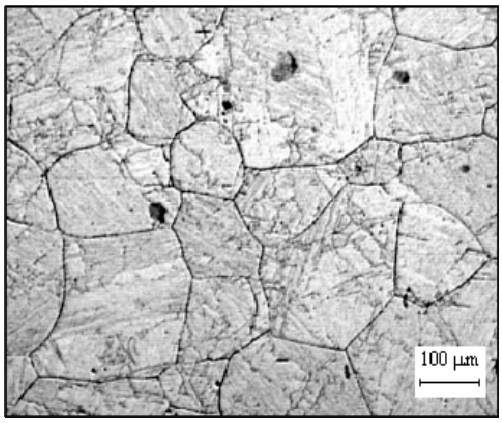

12 hr. @ 490 °C

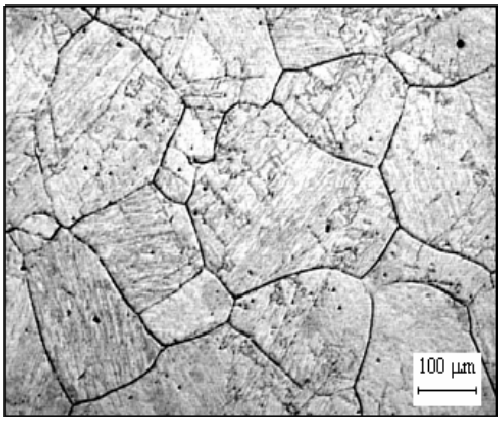

42 hr. @ 490 °C

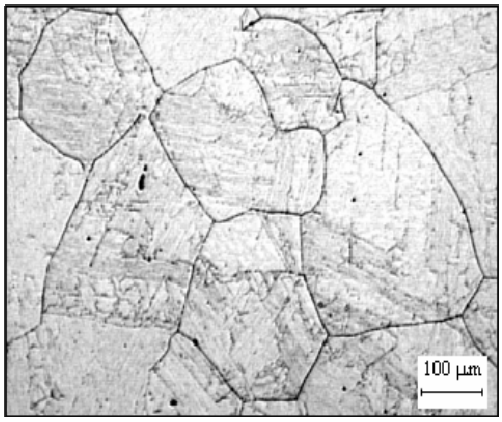

48 hr. @ 490 °C

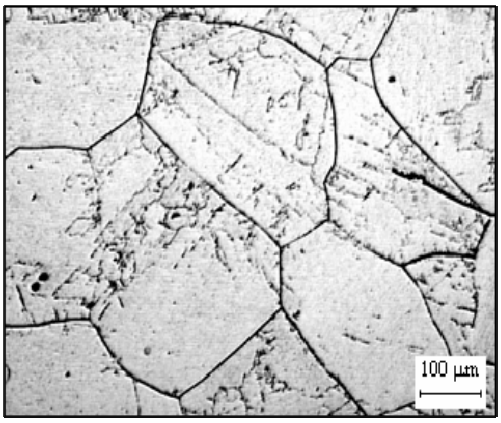

72 hr. @ 490 °C

Figure B.2: High Nb steel. Samples were austenitized at 1250 ºC for 1 hour before quenched and tempered.

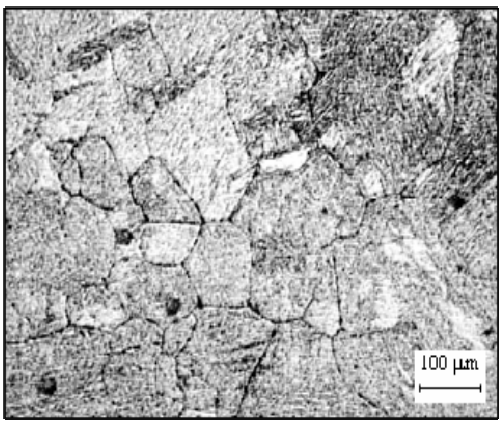

As-Quenched

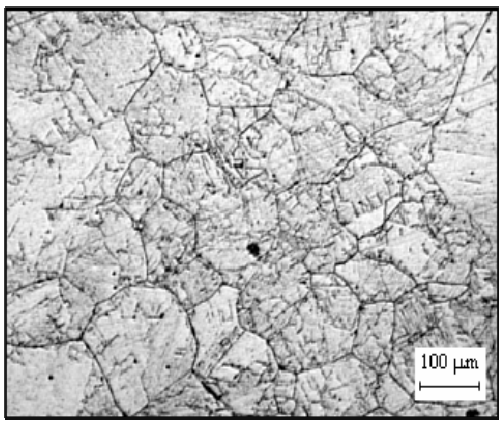

12 hr. @ 490 °C

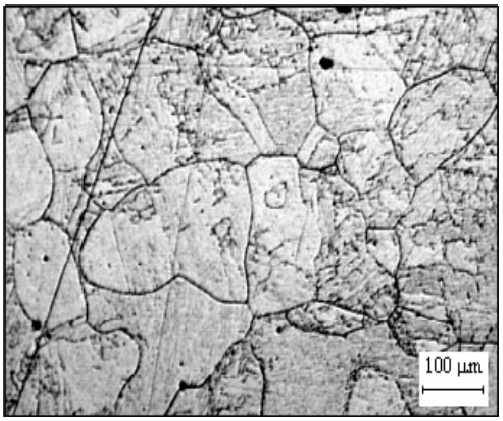

42 hr. @ 490 °C

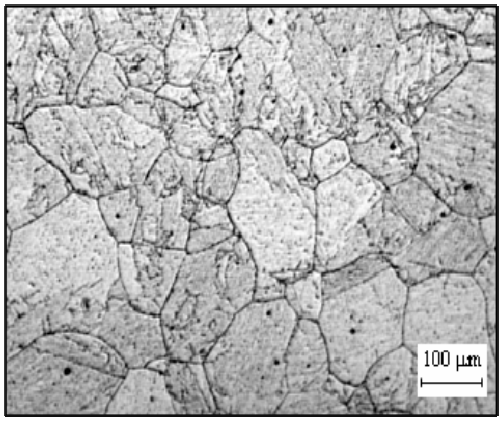

48 hr. @ 490 °C

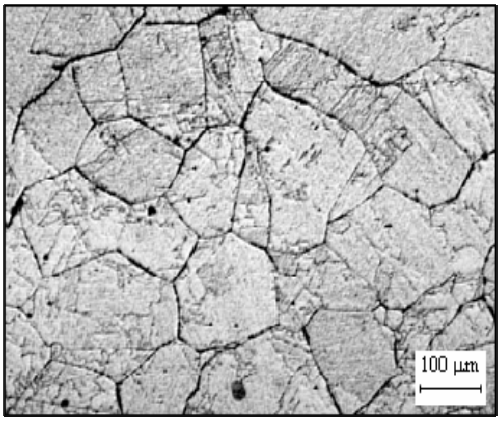

72 hr. @ 490 °C

Figure B.3: Low Nb steel. Samples were austenitized at 1250 ºC for 1 hour before quenched and tempered.

BIBLIOGRAPHY

1. Tanaka, T., "Science and Technology of Hot Rolling Process of Steel", Microalloying `95, Pittsburgh, Published by ISS, 1995, pp 165-181.

2. Kozasu, I., Ouchi, C., Sampei, S. and Okita, T., "Hot Rolling as a High-Temperature Thermo-Mechanical Process", Microalloying `75, (Washington, D.C. October1-3, 1975),Union Carbide Corp. New York, 1977, pp 120-135.

3. Tanaka, T., Tabata, N., Hatomura, T. and Chiaki, S., "Three Stages of the Controlled Rolling Process", Microalloying `75, (Washington, D.C. October1-3, 1975), Union Carbide Corp. New York, 1977, pp 107-119.

4. Satoh, H., Yoshida, S., Yamamoto, K. and Kurokawa, M., "Thermo-Mechanical Control Process for H-shapes and Its Characteristics", 41th MWSP (Mechanical Working and Steel Processing) Conference Proc., ISS, Vol. XXXVII, 1999, pp. 911-922.

5. Tamura, I., Ouchi, C., Tanaka, T. and Sekine, H., "Thermomechanical Processing of High Strength Low Alloy Steels", Butterworth & Co. (Publishers) Ltd, 1988, pp. 182-186.

6. Kimura, T., Kawabata, K., Amano, A., Ohmori, M., Okatsu, M. and Uchida, K., "Heavy Gauge H-Shapes with Excellent Seismic-Resistance for Building Structures Produced by the Third Generation TMCP", Steel for Fabricated Structures, ASM, International Conference, 1999, pp. 165-171.

7. DeArdo, A. J., Garcia, C. I., Gao, W. and Hua, M., "Thermomechanical Processing of Microalloyed Steels: Grain Refinement Revisited", International Conference on Thermomechanical Processing: Mechanics, Microstructure and Control, The University of Sheffield, England, 2002, pp. 97-106.

8. Jones, S. J. and Bhadeshia, H. K. D. H., "Competitive Formation of Inter-and Intragranularly Nucleated Ferrite", Metallurgical and Materials Transaction A, Vol. 28A, Oct. 1997, pp 2005-2013.

9. Ishikawa, F. and Takahashi, T., "The formation of Intragranular Ferrite Plates in Medium-Carbon Steels for Hot-forging and Its Effect on the Toughness", ISIJ International., Vol. 35, 1995, pp. 1128-1133.

10. Ishikawa, F., Takahashi, T. and Ochi, T., “Intragranular Ferrite Plates in Medium-Carbon Vanadium Steels”, Metallurgical and Materials Transaction A, Vol. 25A, May. 1994, pp 929-936.

11. Hanamura, T., Shibata, H., Waseda, Y., Nakajima, H., Torizuka, S., Takahashi, T and Nagai, K., “In-Situ Observation of Intragranular Ferrite Nucleation at Oxide Particles”, ISIJ International, Vol. 39, 1999, pp. 1188-1193.

12. Ochi, T., Takahashi, T. and Takada, H., “Improvement of the Toughness of Hot Forged Products through Intragranular Ferrite Formation”, Iron & Steelmaker, Vol. 16, Feb. 1989, pp 21-28.

13. Kimura, T., Ohmori, A., Kawabata, F. and Amano, K., “Ferrite Grain Refinement through Intragranular Ferrite Transformation on VN Precipitates in TMCP of HSLA Steels”, THERMEC’97, International Conference on TMP of Steels & Other Materials, Edited by Chandra, T. and Sakai, T., The Minerals, Metals & Materials Society, 1997, pp. 645-651.

14. Enomoto, M., “The Mechanisms of Ferrite Nucleation at Intragranular Inclusions in Steels”, THERMEC’97, International Conference on TMP of Steels & Other Materials, Edited by Chandra, T. and Sakai, T., The Minerals, Metals & Materials Society, 1997, pp. 427-433.

15. Byun, J. S., Shim, J. H., Cho, Y. W. and Lee, D. N., "Non-metallic Inclusions and Intragranular Nucleation of Ferrite in Ti-Killed C-Mn Steel", Acta Materialia, Vol. 51, 2003, pp. 1593-1606.

16. Jin, H. H., Shim, J. H., Cho, Y. W. and Lee, H. C., "Formation of Intragranular Acicular Ferrite Grains in a Ti-containing Low Carbon Steel", ISIJ International, Vol. 43, 2003, No. 7, pp. 1111-1113.

17. Barbaro, F. J. & Krauklis, P, “Intragranular Ferrite in Inoculated Low-Carbon Steels”, Materials Forum, Vol. 23, 1999, pp 77-104.

18. Henry, P. “The importance of Molybdenum in Heavy Steel Sections”, Climax Molybdenum Ltd., London, 1969, pp. 17-18.

19. Technical report of Coarse Construction and Industrial, “Jumbo Section: Helping you to Shape the World”, United Kingdom, 2004.

20. Bjorhovde, R., Engstrom, M. F., Griffis, L. G., Kloiber, L. A. and Malley, J. O., “Structural Steel Selection Considerations: A Guide for students, Educators, Designer and Builders”, Structural Engineering Institute, ASCE (American Society of Civil Engineers), 2001, pp 55- 61.

21. Pickering, F. B., "Physical Metallurgy and the design of the steels", Applied Science Publishers, London, 1978, pp. 1-88.

22. Morcinek, P., Smid, V., Heczko, T. and Prnka, T., "Structural Steels with Acicular Ferrite", Microalloying `75, (Washington, D.C. October1-3, 1975), Union Carbide Corp. New York, 1977, pp 272-278.

23. Tanaka, T., Tabata, N., Hatomura, T. and Chiaki, S., "Three Stages of the Controlled Rolling Process", Microalloying `75, (Washington, D.C. October1-3, 1975), Union Carbide Corp. New York, 1977, pp 107-119.

24. Hertzberg, R.W., "Deformation and Fracture Mechanics of Engineering Materials", John Wiley and Sons, 1976, pp 39-48.

25. Fletcher, E. E., "High-Strength, Low –Alloy Steels: Status, Selection and Physical Metallurgy", Battelle Press, 1979, pp. 111-134.

26. Ginzburg, V. B., "Steel-Rolling Technology: theory and Practice", Marcel Dekker, Inc., 1989, pp. 107-123.

27. Leslie, W.C., "Iron and its Dilute Substitutional Solid Solutions", Metallurgical Transactions, Vol. 3, 1972, pp 5-26.

28. Gladman, T., "The Physical Metallurgy of Microalloyed Steels", The Institute of Materials, 1997, pp 47-54.

29. Gladman, T., Dulieu, D. and McIvor, I. "Structure property relationships in High-Strength Microalloyed Steels", Microalloying `75, (Washington, D.C. October1-3, 1975),Union Carbide Corp. New York, 1977, pp 32-58.

30. Meyers, M. and Chawla, K., "Mechanical Metallurgy, Principles and Applications" Prentice-Hall, Inc., 1984, pp 402-437.

31. Verhoeven, J. D., "Fundamentals of Physical Metallurgy", John Wiley and Sons, 1975, pp 515-517.

32. Hall, E. O., "The Deformation and Aging of Mild Steel: III Discussion of results", Proceedings, Physics Society, Series B, vol. 64, 1951, pp 747-753.

33. Petch, N. J., "The cleavage Strength of Polycrystals", Journal of the Iron and Steel Institute, vol. 174, 1953, pp 25-28.

34. DeArdo, A. J., "Modern Thermomechanical Processing of Microalloyed Steel: A Physical Metallurgy Perspective", Microalloying `95, Pittsburgh, Published by ISS, 1995, pp 15-33.

35. Cohen, M. and Hansen, S. S., "On the Fundamentals of HSLA Steels", HSLA Steels: Metallurgy and Applications, Conference Proceeding, ASM International, Beijing, China, 1986, pp 61- 71.

36. Cohen, M. and Hansen, S. S., "Microstructure Control in Microalloyed Steels", MiCon 78: Optimization of Processing, Properties and Service Performance Through Microstractural Control, ASTM STP 627, Edits by: Abrams, H., Maniar, G. N., Nai, D. A. and Solomon, H. D., ASTM, 1979, pp 34 -52.

37. Gray, J. M. and DeArdo, A. J., "Austenite Conditioning Alternatives for Microalloyed Steels Products", HSLA Steels: Metallurgy and Applications, Conference Proceeding, ASM International, Beijing, China, 1986, pp 83- 96.

38. Umemoto, M., Tamura, I. and Guo, Z. H., " The Effect of Austenite Grain size on the Isothermally Formed Ferrite Grain Size", HSLA Steels: Metallurgy and Applications, Conference Proceeding, ASM International, Beijing, China, 1986, pp 97- 102.

39. Cuddy, L. J., "Microstructure Development during Thermomechanical Treatment of HSLA Steels", Metallurigical Transaction A, Vol. 12A, July 1981, pp 1313 -1320.

40. Speich, G. R., Cuddy, L. J., Gordon, C. R. and DeArdo, A. J. "Formation of Ferrite from Control-Rolled Austenite", Proc. Phase Transformations in Ferrous Alloys, Edited by Marder, A. R. and Goldstein, J. I., TMS-AIME, Warrendale, PA, 1984, pp 341-390.

41. Underwood, E. E., "Quantitative Stereology" Addison-Wesley Publishing Co. Inc., Reading, Mass., 1970 pp 1-38.

42. Llewellyn, D. T., "Steels: Metallurgy and Applications", Butterworth-Heinemann, 1992, pp 64-122.

43. "The Making, Shaping and Treading of Steel", Association of Iron and Steel Engineers AISE, Edits by: Lankford, W. T., Samways, N. L., Craven, R. F., McGannon. H. E., 10th edition, 1985, pp 782- 785.

44. Pickering, F. B., "Physical Metallurgy and the design of the steels", Applied Science Publishers, London, 1978, pp. 1-88.

45. Pickering, F. B., "High-Strength, Low-Alloyed Steels – A Decade of Progress", Microalloying `75, (Washington, D.C. October1-3, 1975),Union Carbide Corp. New York, 1977, pp 9-31.

46. Ginzburg, V. B., "Steel-Rolling Technology: theory and Practice", Marcel Dekker, Inc., 1989, pp. 454-462.

47. Palmiere, E. J., Garcia, C. I. and DeArdo, A. J., "The Influence of Niobium Supersatureation in Austenite on the Static Recyrstallization Behavior of Low Carbon Microalloyed Steels", Metallurgy and Materials Transactions A, Vol. 27A, 1993, pp 951-960.

48. Sekine, H. and Maruyama, T., "proceeding", 3rd International Conference on the Strength of Metals and Alloys, London, Iron and Steel Institute, 1973, pp 85-94.

49. Palmiere, E. J., Garcia, C. I. and DeArdo, A. J., "Composition and Microstructural Changes which Attend Reheating and Grain Coarsening in Steel Containing Niobiom", Metallurgy and Materials Transactions A, Vol. 25A, February, 1994, pp 277-286.

50. Palmiere, E. J., "Precipitation Phenomena in Microalloyed Steels", Microalloying' 95 conference, Pittsburgh, USA, Published by ISS, 1995, pp 307-320.

51. Zener, C., privet communication to Smith, C. S., Trans. AIME, vol. 175, 1949, p 15.

52. Gladman, T., "On the Theory of Precipitate Particles on Grain Growth in Metals", Proc. Roy. Soc., Vol. 294 A, 1966, pp 298-309.

53. Gladman, T., "Grain Refinement in Multiple Microalloyed Steels", HSLA Steels, Processing, Properties and Applications, Edit by, Tither, G., TMS, 1992, pp 4-6.

54. Hansen, S. S., Vander Sande, J. B. And Cohen, M., "Niobium Carbonitride Precipitation and Austenite Recrystallization in Hot-Rolled Microalloyed Steels", Metallurgical Transactions A, Vol. 11A, pp 387-402.

55. Cuddy, L. J., "Austenite Microstructures Developed During Simulated Hot Rolling", Recrystallization and Grain Growth of Multi-Phases and Particale Containing Materials: 1st RISO international Symposium on Metallurgy and Material Science, Denmark, Septemper 8 – 12 1980, Eds, by Hansen, S., Jones, A. R. and Leffers, T., 1980, pp 317-329.

56. Cuddy, L. J., "The Effect of Microalloy Concentration on the Recrestallization of Austenite during Hot Deformation", Thermomechanical Processing of Microalloyed Austenite, Warrandel, PA: TMS-AIME, 1984, pp 129-140.

57. Hillert, M., "On the Theory of normal and Abnormal Grain Growth", Acta Metall., Vol. 13, 1965, pp. 227-238.

58. Glagman, T., "Second phase Particles Distribution and Secondary Recrystallization", Scripta Metallurgica et Materialia, Vol. 27, 1992, pp 1569-1573.

59. Cuddy, L. J. and Raley, J. C., “Austenite Grain Coarsening in Microalloyed Steels”, Metallurgical Transactions A, Vol. 14A, 1983, pp 1989-1995.

60. DeArdo, A. J., Garcia, C. I. and Palmiere, E. J., “Thermomechanical Processing of Steels”, ASM Handbook, Heat Treating, Vol. 4, 1991, pp. 237-255.

61. Uhlmann, D. R. and Chalmers, B., “The Energetics of Nucleation”, Symposium on Nucleation Phenomena, Washington, D.C., 1965, publication of American Chemical Society, 1966, pp. 1-13.

62. Hilliard, J. E., “Nucleation within Crystalline Phase”, Symposium on Nucleation Phenomena, Washington, D.C., 1965, publication of American Chemical Society, 1966, pp 79-85.

63. Porter, D. A. and Easterling, K. E., “Phase transformations in Metals and Alloys”, Second edition, published in 1992 by Chapman and Hall, Reprinted by Stanley Thornes (Publishers) Ltd., 2000, pp. 185-198.

64. Ibid., pp.263-275.

65. Reed-Hill, R. E. and Abbaschian, R., “Physical Metallurgy Principles”, Third Edition, Pws Publishing Company, Boston, 1994, pp.479-506.

66. Shewmon, P. G., “Transformation in Metals”, McGraw-Hill Inc., 1969, pp 156-166.

67. Ibid., pp 209-216.

68. Christian, J. W., “The Theory of Transformations in Metals and Alloys: Equilibrium and General Kinetic Theory-Part I”, Publish at Pergamon Press, London, 1975, pp. 448-462.

69. Chadwick, G. A., “Metallography of Phase Transformations”, Butterworth & Co (Publishers) Ltd, 1972, pp. 160-202.

70. Pound, G. M. and Mehl Medalist, R. F., “Perspectives on Nucleation”, Metallurgical Transactions A, Vol. 16A, 1985, pp. 487-502.

71. Johnson, W. C., White, C. L., Marth, P. E., Ruf, P. K., Stuominen, S. M., Wade, K. D., Russell, K. C. and Aaronson, H. I., "Influence of Crystallography on Aspects of Solid-Solid Nucleation Theory", Metallurgical Transactions A, Vol. 6A, 1975,pp. 911-919.

72. Clemm, P. J. and Fisher, J. C., "The Influence of Grain Boundaries on the Nucleation of Second Phases", Act Metallurgica, Vol. 3, 1955, pp. 70-73.

73. Gibbs, J. W., "On the Equilibrium of Heterogeneous Substances", collected works, Vol. I, New Haven: Yale University Press, 1948, pp. 105-115.

74. Volmer, M. and Weber, A., "Nucleation Theory", Physical Chemistry Journal, Vol. 19, 1929, pp. 277- 280.

75. Recker, R. and Döring, W., "Classical Nucleus Model", Physical Chemistry Journal, Vol. 24, 1935, pp. 719- 721.

76. Turnbull, D. and Fischer, J. C., "Rate of nucleation in Condensed Systems", Journal of Chemical Physics, Vol. 17, 1949, pp. 71- 73.

77. Hollomon, J. H. and Turnbull, D., "Nucleation", Progress in Material Physics, Vol. 4, 1953, pp. 333-388.

78. Cahn, J. W., "The kinetics of Grain Boundary Nucleated Reactions", Acta Metallurgica, Vol.4, 1956, pp. 449-459.

79. Cahn, J. W., "Nucleation of Dislocation", Acta Metallurgica, Vol.5, 1957, pp. 169-172.

80. Doremus, R. H., "Rates of Phase Transformations", Academic Press, Inc., 1985, pp.67.

81. Russell, K. C. and Aaronson, H. I., "Sequences of Precipitation nucleation", Journal of Materials Scince, vol. 10, 1975, pp. 1991-1999.

82. Fine, M. E., "Introduction to Phase Transformations in Condensed Systems", McMillan, NY, 1964, pp.7- 44.

83. Hillert, M., "On the Theory of Normal and Abnormal Grain Growth", Acta Metallurgica, Vol. 13, 1965, pp. 227-238.

84. Porter, D. A. and Easterling, K. E., "Phase transformations in Metals and Alloys", Second edition, published in 1992 by Chapman and Hall, Reprinted by Stanley Thornes (Publishers) Ltd., 2000, pp. 130-131.

85. Tamura, I., Ouchi, C., Tanaka, T. and Sekine, H., "Thermomechanical Processing of High Strength Low Alloy Steels", Butterworth & Co. (Publishers) Ltd, 1988, pp. 17-48.

86. Gibbs, R. K., Parker, B. A. and Hodgson, P. D., " The Prediction of Ferrite Grain Size in Niobium Microalloyed Controlled Rolled Steels", International Symposium on Low-Carbon Steels for the 90's, Edit by Asfahani, R. and Tither, G., The Minerals, Metals and Materials society, 1993, pp. 173- 179.

87. Roberts, W. Lidefelt, H. and Sandberg, A., "Mechanism of Enhanced Ferrite Nucleation from Deformed Austenite in Microalloyed Steels", Proc. Hot Working and Forming Processes, Edited by Ellars, C. M. and Davies, G. J., Metals Socitey, London, 1980, pp. 38-42.

88. Dubé, C. A., Aaronson, H. I. and Mehl, R. F., Reviewed Metallurgia, Vol. 55, 1958, p. 201.

89. Farrar, R. A. and Harrison, P. L., "Acicular Ferrite in Carbon –Manganese Weld Metals: an Overview", Journal of Materials Science, Vol. 22, 1987, pp 3812-3820.

90. Barbaro, F. J., Krauklis, P. and Easterling, K., "Formation of Acicular Ferrite at Particles in Steel", Materials science and technology, Vol. 5, 1989, pp 1057-1077.

91. Honeycombe, R. W. K. and Bhadeshia, H. K. D. H., "Steels: Microstructure and Prosperities", Second edition, Edward Arnold, London, 1995, pp. 30-41.

92. Porter, D. A. and Easterling, K. E., "Phase transformations in Metals and Alloys", Second edition, published in 1992 by Chapman and Hall, Reprinted by Stanley Thornes (Publishers) Ltd., 2000, pp. 317-322.

93. Chadwick, G. A., "Metallography of Phase Transformations", Butterworth & Co (Publishers) Ltd, 1972, pp. 231-234.

94. Ricks, R. A., Howell, P. R. and Barritte, G. S., "The Nature of Acicular Ferrite in HSLA Steel Weld Metals", Journal of Materials Science, Vol. 17, 1982, pp 723-740.

95. Honeycombe, R. W. K. and Bhadeshia, H. K. D. H., "Steels: Microstructure and Prosperities", Second edition, Edward Arnold, London, 1995, pp. 140-150.

96. Ibid., pp. 280-289.

97. Bain, E. C., "Function of alloying Elements in Steel", First edition, American Society for Metal, Cleveland, Ohio, 1939, pp. 8-12.

98. Honeycombe, R. W. K., "Carbide Precipitation in Ferrite",Proc. Phase Transformations in Ferrous Alloys, Edited by Marder, A. R. and Goldstein, J. I., TMS-AIME, Warrendale, PA, 1984, pp 259-280.

99. Honeycombe, R. W. K. and Bhadeshia, H. K. D. H., "Steels: Microstructure and Prosperities", Second edition, Edward Arnold, London, 1995, pp. 60-82.

100. Honeycombe, R. W. K., "Carbide Precipitation in HSLA Steels", Proc. Processing, Microstructure and Properties of HSLA Steels, Edited by DeArdo, A. J., The Minerals, Metals and Materials Society, , 1988, pp 1-13.

101. Ferrante, M. and Farrar, R. A., "The Role of Oxygen rich inclusions in determining the Microstructure of Weld Metal Deposits", Journal of Materials Science, Vol. 17, 1982, pp 3293-3298.

102. Dowling, J.M., Corbett, J. M. and Kerr, H. W., "Inclusion Phases and the Nucleation of Acicular Ferrite in Submerged Arc Welds in High Strength Low Alloy Steels", Metallurgical Transactions A, Vol. 17 A, 1986, pp 1611-1623.

103. Mills, A. R., Thewlis, G. and Whiteman, J. A., "Nature of Inclusions in Metals and their Influence on Formation of Acicular Ferrite", Materials Science and Technology, Vol. 3, 1987, pp. 1051-1061.

104. Zhang, Z. and Farrar, R. A., "Role of Non-Metallic inclusions in Formation of Acicular Ferrite in low Alloy Weld Metals", Materials Science and Technology, Vol. 12, 1996, pp. 237-260.

105. Lee, J. L., "Evaluation of the Nucleation Potential of Intragranular Acicular Ferrite in Steel Weldments", Acta. Metall, Mater. Vol. 42 (10), 1994, pp. 3291-3298.

106. Lee, J. L. and Pan, Y. T., "Effect of Sulfur Content on the Microstructure and Toughness of Simulated Heat-Affected Zone in Ti-Killed Steels", Metallurgical Transactions A, Vol. 24 A, 1993, pp 1399-1408.

107. Lee, J. L. and Pan Y. T., "Effect of Silicon Content on the Microstructure and Toughness of Simulated Heat-Affected Zone in Ti-Killed Steels", Materials Science and Technology, Vol. 8, 1992, pp. 236-244.

108. Lee, J. L. and Pan Y. T., "Microstructure and Toughness of Simulated Heat-Affected Zone in Ti-Killed Steels", Materials Science and Engineering, Vol. 136 A, 1991, pp. 109-119.

109. Lee, J. L. and Pan Y. T., "The Formation of Intragranular Acicular Ferrite in Simulated Heat-Affected Zone", ISIJ International, Vol. 35, 1995, pp. 1027-1033.

110 . Thewlis, G., Whiteman, J. A. and Senogles, D. J., "Dynamics of Austenite to Ferrite Phase Transformation in Ferrous Weld Metals", Materials Science and Technology, Vol. 13, 1997, pp. 257-274.

111. St-Laurent, S. and Esperance, G., "Effects of Chemistry, Density and size Distribution of Inclusion on the Nucleation of Acicular ferrite of C-Mn Steel Shielded-Metal-Arc-Welding Weldments", Materials Science and Engineering, Vol. A 149, 1992, pp. 203-216.

112. Madariaga, I. and Gutierrez, I., "Role of the Particle-Matrix Interface on the Nucleation of Acicular Ferrite in a Medium Carbon Microalloyed Steel", Acta Materialia, Vol. 47, No. 3, 1999, pp. 951-960.

113. Shim, J. H., Cho, Y. W, Chung, S. H., Shim, J. D. and Lee, D. N., "Nucleation of Intragranular Ferrite at Ti2O3 Particle in Low Carbon Steel", Acta Materialia, Vol. 47, No. 9, 1999, pp 2751-2760.

114. Takamura, J. and Mizoguchi, S, "Roles of Oxides in Steels Performance – Metallurgy of Oxide in Steels", Proceding of the sixth International Iron and Steel Congress, Nagoya, ISIJ, 1990, pp 591-597.

115. Shim, Y. J. Oh, J. H., Suh, J. Y. Cho, Y. W, Shim, J. D., Byun, J. S. and Lee, D. N., "Ferrite Nucleation Potency of Non-Metallic Inclusions in Medium Carbon Steels", Acta Materialia, Vol. 49, 2001, pp 2115-2122.

116. Bhadeshia, H. K. D. H., "Bainite in Steels", Institute of Materials, London, 1992, Ch 10, pp237-276.

117. Aaronson, H. I. and Wells, C., "Sympathetic Nucleation of Ferrite", Trans. A. I. M. E., Vol. 206, 1956, p1216.

118. Furuhara, T., Shinyoshi, G., Miyamoto, G., Yamaguchi, J., Sugita, N, Kimura, N, Takemura,. N and Maki, T., "Multiphase Crystallography in the Nucleation of Intragranular Ferrite on MnS+V(C,N) Complex Precipitate in Austenite", ISIJ international, Vol. 43, No.12, 2003, pp 2028-2037.

119. Bramfit, B. L., "The Effect of Carbide and Nitride Additions on the Heterogenous Nucleation Behavior of Liquid Iron", Metallurgical Transactions, Vol. 1, 1970, pp 1987-1995.

120. Grong, O., Kluken, A. O., Nylund, H. K., Dons, A. L. And Hjelen, J., "Catalyst Effects in Heterogeneous nucleation of Acicular Ferrite", Metall. and Mater. Trans. A, Vol. 26 A, 1995, pp. 525-534.

121. Furuhara, J., Yamaguchi, N., Sugita, N., Miyamoto, G. and Maki, T., "Nucleation of Proeutectoid Ferrite on Complex Precipitates in Austenite", ISIJ International, Vol. 43, No. 10, 2003, pp. 1630-1639.

122. Yamamoto, K., Matsuda, S., Haze, T., Chijiiwa, R. and Mimura, H., "A Newly developed Ti-Oxide Bearing Steel Having High HAZ Toughness", Residual and Unspecified Elements in Steel, ASTM STP 1042, A. S. Melilli and E. G. Nisbett, Eds., American Society for Testing and Materials, Philadelphia, 1989, pp 266-284.

123. Mabuchi, H., Uemori, R. and Fujioka, M., "The Role on Mn Depletion in Intragranular Ferrite Transformation in the Heat Affected Zone of Welded Joints with Large Heat Input in Structural Steels", ISIJ International, Vol. 36, No. 11, 1996, pp. 1406-1412.

124. Furuhara, T. and Maki, T., "Acceleration on Intragranular Nucleation of Ferrite and Pearlite at Inclusions by Hot Deformation of Austenite", J.J. Jonas Symposium, Thermomechanical Processing of Steels, Edited by Yue, S. and Es-sadiqi, E., Ottawa, Canada, 2000, pp 465-473.

125. Yamamoto, K., Hasegawa, T. and Takamura, J., "Effect of Boron on Intragranular Ferrite Formation in Ti-Oxide Bearing Steels", ISIJ International, Vol. 36, 1996, pp. 80-86.

126. Tomita, Y., Saito, N., Tsuzuki, T., Tokunaga, Y. And Okamoto, K., "Improvment in HAZ Toughness of Steel by TiN-MnS addition", ISIJ International, Vol. 34, 1994, pp. 829-835.

127. Zhang, S., Hattori, N., Enomoto, M. And Tarui, T., "Ferrite Nucleation at Ceramic/Austenite Interfaces", ISIJ International, Vol. 36, 1996, pp. 1301-1309.

128. Gregg, J. M and Bhadeshia, H. K. D. H., "Solid-state nucleation of acicular ferrite on minerals added to molten steel", Acta Materialia, Vol. 45, 1997, PP 739-748.

129. Liu, S., and Olson, D. L., "The role of inclusions in controlling HSLA steel weld microstructures", Welding Journal, Vol. 65, No. 6, 1986, pp 139-149.

130. Abson, D. J., Dolby, R. E., and Hart, P. M. H., "The role of nonmetallic inclusions in ferrite nucleation in carbon steel weld metals", Procedure of International Conference on Trend in Steel and Consumables for Welding, The Welding Institute, London, 1978, pp 75–101.

131. Kim, H., Lee, H. Oh, K., "MnS Precipitation in Association with Manganese Silicate Inclusion in Si/Mn Deoxidized Steel", Metallurgy and Materials Transactions A, Vol. 32A, 2001, pp 1519-1525.

132. Liu, Y. C., Sommer, F. and Mittemeijer, "Abnormal Austenite–Ferrite Transformation Behavior in Substitutional Fe-Based Alloys", Acta Materialia, Vol. 51, 2003, pp. 507-519.

133. Kempen, A. T., Sommer, F. and Mittemeijer, "The Kinetics of the Austenite–Ferrite Phase Transformation of Fe-Mn: Differential Thermal Analysis during Cooling", Acta Materialia, Vol. 50, 2002, pp. 3545-3555.

134. Lee, J. L. and Pan Y. T., "Effect of Killing Time on the Microstructure and Toughness of the Heat-Affected Zone in Ti-Killed Steels", Materials Science and Engineering, Vol. 136 A, 1991, pp. 2818-2822.

135. Saito, Y., Tanaka, M., Sekine, T. and Nishizaki, H., "Mechnical Properties control in Controlled Rolling and Accelerated Cooling of HSLA Steels", Proc. High Strength Low Alloy Steels, University of Wollongong, Wollongong. Australia, 1985, pp. 28-32.

136. Sellars, C. M., "The Physical Mettalurgy of Hot working", International Conference, Hot Working and Forming Processes, Edit by Sellars, C. M. and Davies, G. J The Metals Society, Sheffield, 1980, p 3.

137. Perdrix, C., Chamont, B., Amoris, E. and Biausser, H., "A Model for Mechanical Properties of Thermomechanically Treated Plates", International Conference on Physical Metallurgy of Thermomechanical Processing of Steels and Other Metals, THERMEC-88, Vol. 2, ISIJ, Tokyo, Japan, 1988, pp. 807-814.

138. Anelli, E., Ghersi, M. and Mascanzoni, A., "Plate Rolling of HSLA Steels With Control of Microstructure", HSLA Steels: Metallurgy and Applications, Conference Proceeding, ASM International, Beijing, China, 1986, pp 693-698.

139. Gao, W., Garcia, C. I. and DeArdo, A. J., "Study of the Refinement of Final Ferrite Grain Size during Heavy Section Rolling", Special report, BAMPRI- University of Pittsburgh, 2002.

140. Capdevila, C., Caballero, F and Garcia de Andres, C., "Competition between Allotriomorphic and Idiomorphic Ferrite Transformation Kinetics", The Minerals, Austenite Formation and Decomposition, Metals and Materials Society, 2003, pp 81- 95

141. Herbertz, R. and Wiegels, H., "Ein Verfahren Zur Verwirklichung des Reibungsfreien Zylinderstauchversuches für die Ermittlung von Fließkurven", Stahl und Eisen, Vol. 101, 1984, pp 29.

142. Vander Voort, G. F., "Metallography Principles and Practice", ASM International, 1999, Appendix D, pp 538-539.

143. Santella, M. L., "Grain Growth and High-Temperature Hot Rolling Behavior of Low Alloy Steel Austenite", Ph.D. Thesis, University of Pittsburgh, 1981, pp 49-52.

144. "Standard Test Methods for Determining Volume Fraction by Systematic Manual Point Count", ASTM Designation E562-89, Annual Book of ASTM Standards, ASTM.

145. "Standard Test Methods for Determining the Inclusion Content of Steel", ASTM Designation E45-97 (Reapproved 2002), Annual Book of ASTM Standards, ASTM.

146. Saltykov, S. A., "Sterometric Metallography", Second edition, Metallurgizdat. Moscow, 1958, p 446.

147. Smith, C. S. and Guttman, L., "Measurement of Internal Boundaries in Three-Dimensional Structures by Random Sectioning", A.I.M.E Transaction, vol. 197, 1953, p 81-90.

148. Fullman, R. L., "Measurement of particle sizes in opaque Bodies", A.I.M.E Transaction, vol. 197, 1953, pp 447- 452.

149. Van der Eijk, C., Grong, Ø., Babu, S. S. and David, S. A., "Effect of Interactive Particles on Steel Weldability", 5th International Conference on Trends in Welding Research, Georgia, 1998.

150. Van der Eijk, C., Grong, Ø. and Walmsley, J., "Effects of Deoxidation Practice on the Inclusion Formation in Low Alloy Structural Steels", Sixth International Conference on Molten Slags, Fluxes and Salts Stockholm, Sweden-Helsinki, Finland 12-17 June 2000.

151. Takamura, J. and Mizoguchi, S., "Role of Oxides in Steels Performance-Metallurgy of Oxides in Steels", Proc. of the Sixth International Iron and Steel Congress, Nagoya, ISIJ, 1990, pp 591-597.

152. Johnson, W. and Mehl, "Reaction kinetics processes of nucleation and growth", Trans. AIME, Vol. 135, 1939, pp 416-441.